



All Theses and Dissertations

2013-12-12

Synthesis, Characterization, and Application of High Surface Area, Mesoporous, Stabilized Anatase TiO₂ Catalyst Supports

Rebecca Elizabeth Olsen
Brigham Young University - Provo

Follow this and additional works at: <https://scholarsarchive.byu.edu/etd>

 Part of the [Biochemistry Commons](#), and the [Chemistry Commons](#)

BYU ScholarsArchive Citation

Olsen, Rebecca Elizabeth, "Synthesis, Characterization, and Application of High Surface Area, Mesoporous, Stabilized Anatase TiO₂ Catalyst Supports" (2013). *All Theses and Dissertations*. 3884.
<https://scholarsarchive.byu.edu/etd/3884>

This Dissertation is brought to you for free and open access by BYU ScholarsArchive. It has been accepted for inclusion in All Theses and Dissertations by an authorized administrator of BYU ScholarsArchive. For more information, please contact scholarsarchive@byu.edu, ellen_amatangelo@byu.edu.

Synthesis, Characterization, and Application of High Surface Area, Mesoporous, Stabilized
Anatase TiO₂ Catalyst Supports

Rebecca Elizabeth Olsen

A dissertation submitted to the faculty of
Brigham Young University
in partial fulfillment of the requirements for the degree of
Doctor of Philosophy

Brian F. Woodfield, Chair
Juliana Boerio-Goates
Branton Campbell
Roger G. Harrison
Matthew R. Linford

Department of Chemistry and Biochemistry

Brigham Young University

December 2013

Copyright ©2013 Rebecca Elizabeth Olsen

All Rights Reserved

ABSTRACT

Synthesis, Characterization, and Application of High Surface Area, Mesoporous, Stabilized, Anatase TiO₂ Catalyst Supports

Rebecca Elizabeth Olsen
Department of Chemistry and Biochemistry, BYU
Doctor of Philosophy

Nanomaterials have attracted substantial attention in the area of catalysis due to the unique properties they exhibit such as high surface areas, intricate pore networks and unique morphologies. TiO₂ has attracted attention as a catalyst since the discovery of its high photocatalytic activity by Fujishima and Honda in 1972. Given its high thermal stability, low cost, low environmental impact, and versatility, TiO₂ is a widely used commercial catalyst and catalyst support. TiO₂ is used in many applications such as photocatalysis and is also an excellent support material for noble metals in a number of oxidative synthesis and pollution-control reactions. Though TiO₂ is a widely used catalyst support, currently available commercial titanias often have low surface area and poor thermal and hydrothermal stability. While several methods reported in literature produce materials of higher surface area and more ideal porosity relative to commercially available titanias, these procedures generally involve inherent drawbacks including time-consuming, complicated, and expensive processes that are not industrially viable. Cost-effective, large-scale preparations of stable, high surface area, mesoporous TiO₂ need to be developed.

The work in this dissertation focuses on (1) producing high surface area stabilized TiO₂ supports of controlled pore diameters and (2) the preparation of well dispersed Pt on these supports using industrially viable processes. The effects of dopants Al, La, Si, and Zr on the stability, surface area, and porosity of anatase TiO₂ supports were investigated. Results show that dopants increased the surface area and thermal stability of anatase through structural modifications and grain growth inhibition. Stabilized titanias produced by this method demonstrated equivalent or higher thermal stability and surface area compared with pure anatase and previously reported materials after treatment at 400°C and 700°C including 22 mol% Al-TiO₂ calcined at 400°C which had a surface area of 479 ± 39 m²/g, a pore volume of 0.46 ± 0.04 cm³/g, and a pore diameter of 2.9 ± 0.2 nm. Ten synthesis variables were examined and optimized using statistically designed experiments (DOEs). Equations were developed to predict the conditions to obtain the highest surface area and pore volume at the desired pore diameter and predict the pore diameter range that may be obtained for aluminum-modified anatase TiO₂. Confirmation trials closely matched predicted surface areas, pore volumes, and pore diameters in all but one trial, demonstrating the power of DOEs in identifying and controlling synthesis variables in relatively few experiments.

The structure of Al-modified anatase TiO₂ was analyzed to determine the mechanism of Al stabilization. Surface Al stabilized TiO₂ by lowering anatase surface energy, stabilizing planes of high surface energy which would otherwise join to achieve stabilization. Al in TiO₂ lattice vacancies stabilized TiO₂ through increasing lattice strain and limiting mass transport

necessary for grain growth. Results demonstrate the importance of structure analysis of doped nanomaterials in the development of stabilized catalysts and catalyst supports.

An industrially viable, one-pot synthesis of Pt supported on 22 mol% Al-modified anatase is presented. Pt dispersions as high as 54% (one-pot method) and 59% (DI method) have been obtained. Results show that this one-pot method and the DI method using our Al-modified supports are promising syntheses of highly dispersed Pt catalysts and demonstrate that the alumina-stabilized anatase support is superior to other many available anatase supports.

Keywords: TiO₂, anatase, catalyst support, high surface area, thermal stability, statistical design, DOE, synthesis, Pt supported catalyst, controlled porosity

ACKNOWLEDGEMENTS

Throughout my graduate experience I was fortunate to work with incredible advisors. I would like to thank Brian, my official advisor, for all the time and energy spent sharing ideas and encouraging me to try new things. Your big dreams and excitement led me to accomplish more than I would have tried on my own. Thank you Julie for being a wonderful role model and showing me what a woman in science can accomplish. I would like to thank Cal for introducing me to catalysis and for the endless hours spent planning experiments and discussing ideas. Your questions led to new discoveries and pushed me to explore deeper.

I would like to thank my committee members, Branton, Roger and Matt, for the years of support and guidance, new ideas and excellent suggestions. I would also like to thank Lynn and Cosmas Inc. for providing equipment, funding, and ideas for new research. I would like to thank Jeff Farrer and the BYU microscopy laboratory for hours spent imaging and interpreting TEM micrographs. Two nanometer particles can be difficult; thanks for being excited instead of frustrated Jeff.

My time at BYU has been spent working with wonderful undergraduates and fellow graduate students Stacey, Baiyu, Maryam, and Jacob. Thank you all for the friendship and fun we have shared. I could not ask for a better working environment.

I would like to thank my wonderful family who has encouraged me, supported me, and never missed a magic show.

I would like to thank the most wonderful man in the world, Owen, who has encouraged me to follow my dreams, supported me through this entire process, edited many papers, and even helped make many samples. If you ever need a new hobby, you would be a great chemist.

TABLE OF CONTENTS

Chapter 1: Introduction.....	1
1.1 Introduction	1
1.2 TiO ₂ Crystal Structures	2
1.3 Morphologies	5
1.3.1 Nanomaterials	6
1.4 Synthesis of TiO ₂	7
1.4.1 Heat Treatment.....	7
1.4.2 Solution Methods	8
1.4.3 Gas Phase Methods	11
1.4.4 Other Specialized Methods.....	12
1.4.5 Industrial Techniques.....	12
1.4.6 Synthesis of Supported Catalysts.....	12
1.5 Dopants.....	16
1.5.1 Transition and Rare Earth Metal Dopants	17
1.5.2 Noble Metal Dopants	18
1.5.3 Non-metal and Anion Dopants	19
1.6 Applications in Catalysis.....	19
1.6.1 Photocatalysis	21
1.6.2 Solar Cells.....	26

1.6.3	Sensors	27
1.6.4	Lithium Ion Batteries	27
1.6.5	Catalyst Supports	27
1.7	Dissertation Overview	29
1.7.1	Chapter Abstracts	30
1.8	References	33
Chapter 2: Characterization Techniques		50
2.1	Introduction	50
2.2	X-ray Diffraction	51
2.3	X-ray Absorption Spectroscopy	58
2.3.1	XANES	62
2.3.2	EXAFS	64
2.4	Transmission Electron Microscopy (TEM)	66
2.5	Adsorption	76
2.5.1	Physisorption	77
2.5.2	Chemisorption	86
2.6	References	92
Chapter 3: Synthesis and Characterization of Pure and Stabilized Mesoporous Anatase Titanias		97
3.1	Introduction	97

3.2	Experimental	99
3.2.1	Sample Preparation	99
3.2.2	Sample Characterization	100
3.3	Results and Discussion.....	101
3.3.1	XRD, TEM, Surface Area, and Pore Volume Analysis.....	101
3.3.2	Pore Diameter Analysis	108
3.3.3	Method Analysis	112
3.4	Conclusions	114
3.5	Supplemental Information.....	115
3.6	References	116
Chapter 4:	Optimizing the Synthesis and Properties of Al-modified Anatase Catalyst Supports by Statistical Experimental Design.....	124
4.1	Introduction	124
4.2	Experimental	126
4.2.1	Sample Preparation	126
4.2.2	Sample Design	128
4.2.3	Sample Characterization	129
4.3	Results	130
4.3.1	XRD and TEM	130
4.3.2	Pore Diameter Calculations	130

4.3.3	Statistical Analysis.....	132
4.3.4	Confirmation Trials.....	141
4.4	Discussion	143
4.5	Conclusions	147
4.6	Supplemental Information.....	148
4.7	References	149
Chapter 5: Structure Analysis of Al-modified TiO ₂		153
5.1	Introduction	153
5.2	Experimental	155
5.2.1	Sample Preparation.....	155
5.2.2	Sample Characterization	156
5.3	Results	158
5.3.1	XRD, TEM, N ₂ Sorption, XANES, and ²⁷ Al MAS NMR	158
5.3.2	Heat Capacity Results	168
5.4	Discussion	171
5.4.1	Ti Coordination from XANES.....	172
5.4.2	Crystallite Growth and Phase Transformation of Pure Materials (TiO ₂ ,DRC and TiO ₂ ,DCR)	174
5.4.3	Structure of 22 mol% Al-modified TiO ₂	174
5.4.4	Al Stabilization Mechanisms	176

5.4.5	Effects of Rinsing on Pure and Doped TiO ₂	178
5.5	Conclusions	179
5.6	References	180
Chapter 6: One-pot Synthesis of Pt Catalysts Supported on 22-mol% Al-modified Anatase.....		186
6.1	Introduction	186
6.2	Experimental	188
6.2.1	Sample Preparation	188
6.2.2	Sample Characterization	189
6.3	Results and Discussion.....	191
6.3.1	6.8 – 8 wt% Pt Catalysts	191
6.3.2	0.5 wt% Pt Catalysts	202
6.3.3	Method Overview	203
6.4	Conclusions	204
6.5	References	205

Chapter 1: Introduction

1.1 Introduction

Titanium, the Earth's fourth most abundant metal and ninth most abundant element, can be found in many minerals including rutile, ilmenite, and leucoxene. Titanium is also found in living organisms and has been detected on the sun, moon, and several stars. TiO_2 is primarily used for white pigments. Other uses include welding rod coatings, fluxes, Ti metals, and TiO_2 (particularly nano TiO_2 materials) for catalytic applications.

Nanomaterials have attracted substantial attention in the area of catalysis due to the unique properties they exhibit such as high surface areas, intricate pore networks, and unique morphologies. TiO_2 has attracted attention as a catalyst since the discovery of its high photocatalytic activity by Fujishima and Honda in 1972.¹ Given its high thermal stability, low cost, low environmental impact, and versatility, TiO_2 is a widely used commercial catalyst and catalyst support. TiO_2 is used in many applications, including photocatalysis, photovoltaics, environmental cleanup, antibacterial agents, coatings, and pigments.¹⁻⁶

TiO_2 is an excellent support material for noble metals such as Pd, Pt, and Au in a number of oxidative synthesis and pollution-control reactions e.g. oxidation of CO at low temperatures,⁷ preferential oxidation of CO in H_2/CO mixtures,⁸ low-temperature, direct synthesis of hydrogen peroxide,⁹ selective oxidation of primary C-H bonds,¹⁰ oxidation of alcohols to aldehydes,¹¹ complete oxidation of volatile organic compounds,¹² and as a support and promoter for vanadium oxide in selective catalytic reduction of NO_x . For more information, several excellent reviews have been written on the synthesis and applications of TiO_2 .^{6, 13-17}

This dissertation focuses on the synthesis and characterization of high surface area, thermally stabilized TiO₂ catalyst supports and the synthesis and characterization of highly dispersed Pt catalysts supported on Al-modified TiO₂. An overview of TiO₂ crystal structures, morphologies, synthesis methods including the use of dopants to modify properties, and TiO₂ applications is presented in this chapter, followed by a summary of the dissertation work.

1.2 TiO₂ Crystal Structures

Four phases of titania can be found in nature: (1) anatase (tetragonal), (2) brookite (orthorhombic), (3) rutile (tetragonal), and (4) TiO₂ B (monoclinic) (see Figure 1.1).

Additionally, two high pressure forms have been synthesized from the rutile phase, TiO₂ (II) and TiO₂ (H).¹⁸ Anatase and rutile are the most commonly observed phases and will be discussed in detail as all TiO₂ materials presented in this work are either anatase, semi-amorphous anatase-like, or rutile.

The tetragonal structure of anatase is shown in Figure 1.1. The anatase crystal is made up of chains of octahedrons of a Ti atom surrounded by six oxygen atoms. The octahedrons share four edges to form eight-faced tetragonal dipyramids. Anatase has no corner sharing and the TiO₆ octahedra are linked together only through edge sharing.¹⁹ Anatase contains twelve atoms per unit cell. Information on the crystal structure and properties of anatase can be found in Table 1.1. Anatase is the stable phase at crystallite sizes less than approximately 11 – 13 nm.²⁰ Because stable, high surface area anatase can be obtained, it has traditionally been recognized as the best phase for catalysis. Anatase also exhibits higher photocatalytic reactivity than rutile due to its slightly higher Fermi level, lower oxygen adsorption capacity, increased hydroxylation, and longer lifetimes of the photo-excited h⁺/e⁻ carriers in the anatase lattice.^{19, 21}

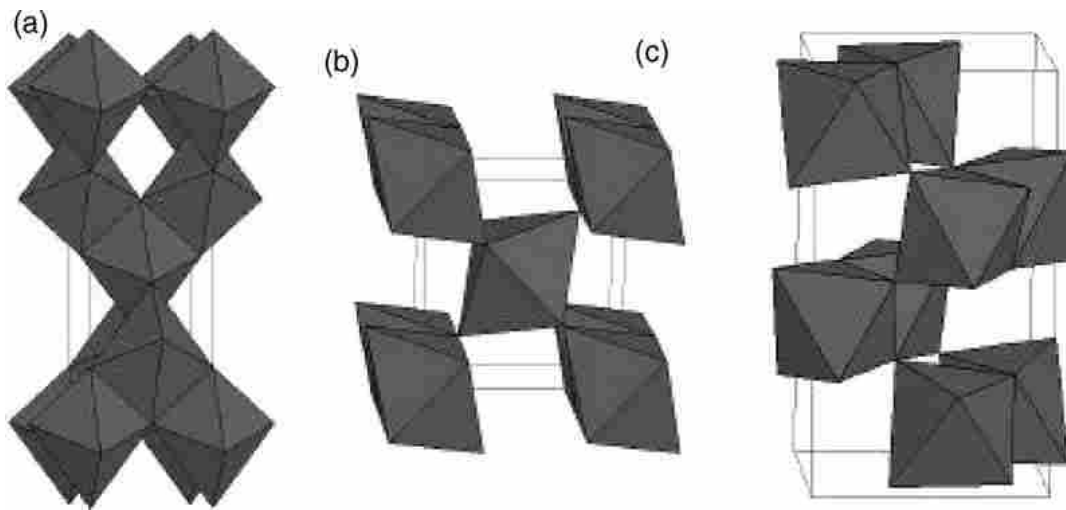


Figure 1.1 Models of a) anatase, b) rutile, and c) brookite polymorphs of TiO_2 . Image adapted from Carp et al.⁶

Table 1.1 Crystal structure data for anatase and rutile TiO_2 .^{6, 22-24}

Property	Anatase	Rutile
Crystal structure	Tetragonal	Tetragonal
Lattice constant (\AA)	$a = 3.784$ $c = 9.515$	$a = 4.5936$ $c = 2.9587$
Space group	$I4_1/amd$	$P4_2/mnm$
Volume/molecule (\AA^3)	34.061	31.2160
Density (g/cm^3)	3.79	4.13
Ti-O bond length (\AA)	1.937(3) 1.965(2)	1.949(4) 1.980(2)
O-Ti-O bond angle	77.7° 92.6°	81.2° 90.0°
Band gap (eV)	3.26	3.05
Refractive index	$n_g = 2.5688$ $n_p = 2.6584$	$n_g = 2.9467$ $n_p = 2.6506$

Like anatase, rutile exists in a tetragonal structure (Figure 1.1) The rutile structure is made up of parallel chains of TiO_6 octahedrons. Two edges of each octahedron are shared to

form linear chains along the [001] direction and the chains are linked together through corner connections.¹⁹ TiO_6 octahedrons are distorted in the rutile structure, though to a lesser degree than the distortion observed in the anatase structure.¹⁷ Rutile contains six atoms per unit cell. Information on the crystal structure of rutile and some properties can be found in Table 1.1.

The rutile phase has the highest density and is widely used in pigments and coatings. Rutile is also the stable phase at most temperatures and pressures up to 60 kbar at sizes above approximately 11 – 35 nm.^{20, 25} Therefore anatase and brookite structures often transform to rutile when calcined at elevated temperatures. Rutile obtained through heating anatase and brookite generally contains large crystallites (100 nm or larger). The increase in particle size is accompanied by a decrease in surface area, therefore large rutile crystallites are not particularly catalytically active. New synthesis methods, including the hydrolysis of titanium salts under acidic conditions at low temperatures, have been developed to yield high surface area, pure and stabilized nano rutile. High surface area rutile materials have become key catalysts in the electronics and semiconductor industries. Additionally, dopants can be used to tailor the band gap to increase the range of light absorption, increasing the activity of rutile photocatalysts.²⁶

Phase pure anatase is difficult to obtain; thus, in many synthesis techniques mixtures of amorphous TiO_2 , anatase, and rutile products are obtained. Degussa P25, one of the most common commercial titania catalyst and support products, is one such example, containing approximately 70% anatase to 30% rutile. Amorphous TiO_2 and anatase mixtures are also frequently used in various catalytic applications. Applications for TiO_2 are strongly correlated to the crystal structure, morphology, crystallite size, surface area, and pore properties. Therefore, significant attention has been given to the matter of controlling and thermally and hydrothermally stabilizing TiO_2 crystal structures and the associated properties.

1.3 Morphologies

TiO₂ can exist in many different morphologies. The most common are thin films, powders, and single crystals. Nanomaterials are also used for many applications, particularly as catalysts and catalyst supports. To utilize the unique pore structures and high surface areas of nanomaterials, many structures have been prepared, including nanoparticles,²⁷ nanorods,²⁸ nanowires,²⁹ nanotubes,³⁰ and nanoribbons.^{31, 32} Examples of some TiO₂ morphologies are shown in Figure 1.2.

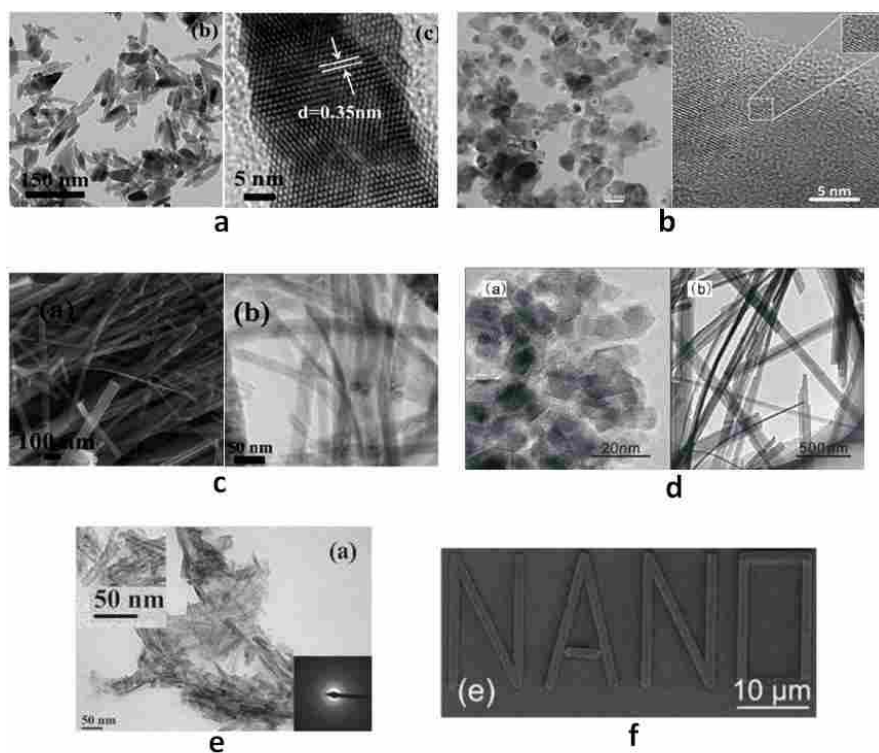


Figure 1.2 Transmission electron microscopy (TEM), high resolution TEM (HRTEM), and scanning electron microscopy (SEM) images of some interesting morphologies of TiO₂. (a) TEM and HRTEM images of TiO₂ nanorods,²⁸ (b) TEM and HRTEM images of TiO₂ nanoparticles,²⁷ (c) SEM and TEM images of TiO₂ nanowires,²⁹ (d) TEM and HRTEM images of nanoribbons,³² (e) TEM image of TiO₂ nanotubes,³⁰ and (f) SEM image of a complex structure made from TiO₂ nanoribbons.³¹

1.3.1 Nanomaterials

At small sizes of approximately 10 nm or less, charge carriers in semiconductor TiO_2 particles behave as particles in a box. Due to this quantum mechanical confinement, the band gap increases and the band edge shifts to yield larger redox potentials and increases the photoefficiency of systems.³³ TiO_2 with 1-D nanostructures, including rods, wires, fibers, and tubes, have a wide range of optical and electronic properties that can be controlled through the size and shape of the structure.

Porous structures are an important feature in nanomaterials, particularly in catalytic applications. The IUPAC has defined three types of pores: micropores (<2 nm), mesopores (2 – 50 nm), and macropores (>50 nm). As shown in Figure 1.3, pores may exist between crystallites or between agglomerates. Depending on the size of individual crystallites, mesopores are generally the spacing between crystallites. Mesoporous materials are used in many catalytic applications and the development and control of the pore structure of titania is currently the focus of much research.

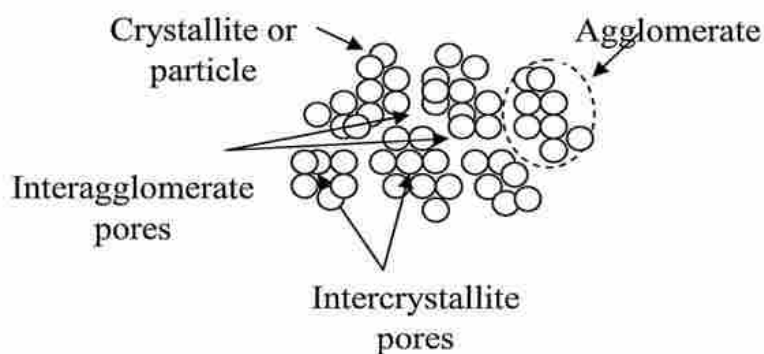


Figure 1.3 Interagglomerate pores refer to the spacing between agglomerates. Intercrystallite pores refer to the spacing between crystallites. Pore diameter and volume as measured by N_2 sorption generally refer to intercrystallite pores.

1.4 Synthesis of TiO₂

Many synthesis routes to the various morphologies and crystallite phases of TiO₂ have been reported in the literature. Among the most commonly used are solution methods: sol-gel, precipitation, solvothermal, combustion, and electrochemical and gas phase methods: chemical vapor deposition, physical vapor deposition, and spray pyrolysis. Methods are selected based on ease of procedure, cost, equipment requirements, and desired material properties including phase, crystallite size, morphology, porosity, and uniformity. Additionally, a variety of metals and inorganic oxides can be incorporated into titania to improve thermal stability, adjust pore diameter and volume, and otherwise render its properties suitable for various applications. Some of the most commonly employed synthesis techniques are discussed below.

1.4.1 Heat Treatment

It is widely reported in previous literature that increasing the calcination temperature leads to an increase in crystallinity, crystallite size, and agglomeration, and a decrease in the surface area of nanomaterials. Thermal treatment also affects the crystal phase and morphology of nanomaterials. Thermal stability, therefore, determines which application the material is suitable for and increasing the thermal stability of titania is the focus of much research. For practical reasons such as cost of procedure, reaction conditions are usually selected to be as mild as possible, however, starting materials or the synthesis procedure may necessitate high reaction temperatures to eliminate byproducts and to form TiO₂ materials. Additionally, as many applications require crystalline products, the material may need to be heated to increase crystallinity. Nano anatase transforms to the more stable rutile phase when heated, generally between 500-900°C, when a threshold crystallite size of approximately 13 nm is reached.^{34, 35} Zhang et al.³⁶ observed the appearance of rutile after heating anatase at 600°C. The material had

completely transformed to rutile by 900°C. Samples heated at 800°C for one and three hours resulted in the same amount of rutile, suggesting that mixed phases are not likely kinetic products. In contrast Zhu et al.³⁷ observed that heating samples for extended times at 600°C led to the formation of rutile, signifying that calcination time as well as temperature affect product crystal phase.

1.4.2 Solution Methods

Solution methods are popular, convenient methods to obtain homogeneous TiO₂ materials with controlled stoichiometry and/or complex morphology as well as composite materials. Solution methods, however, can require expensive materials and multiple, time-consuming steps, and therefore may be costly procedures. Some of the most common solution methods are presented below.

1.4.2.1 Sol-gel

The sol-gel method is used to synthesize thin films, membranes, and powders and is the most common technique to synthesize porous TiO₂ used in catalytic applications. Alkoxides and inorganic Ti salts are generally used as starting materials. In the case of inorganic salts, the removal of inorganic anions (such as Cl⁻) is generally required. The first step in a sol-gel process is to form a TiO₂ sol through hydrolysis and condensation reactions. Ti alkoxides and inorganic salts tend to be highly reactive with water; therefore the hydrolysis step is performed carefully in order to maintain control of the microstructure of the forming product. In the case of alkoxides, this can be done through the addition of ligands such as carboxylates that hydrolyze more slowly than the pure alkoxide.³⁸⁻⁴¹ Acid/base chemistry can be used to slow hydrolysis and control the rate of condensation, with acid generally promoting hydrolysis rates to form crystalline powder products and base generally promoting condensation to form amorphous powders.⁶ Alcohols

have also been used to prevent condensation.^{42,43} The formation of the sol may include an aging step, which can further promote or control polycondensation reactions, and a drying step.

Following the formation of the sol or precursor material, a calcination step can be incorporated to remove byproducts and promote crystallization of anatase or rutile. If alkoxides are used, organic byproducts are generally removed through calcination. In the formation of thin films, the sol can be treated in an autoclave to create a paste, with growth controlled through Oswald ripening. The paste is then deposited onto a substrate and calcined in air at elevated temperatures (i.e. 450°C) to remove byproducts. Slow heating and cooling rates as well as additives are used to prevent thin film cracking.⁶ Some examples of sol-gel syntheses are detailed elsewhere.^{37, 44-47}

Advantages of the sol gel method include a relatively simple process that allows for flexibility in dopant introduction, composition control, scalability, and high purity products. The sol-gel method is particularly useful in producing mixed oxides. Many different dopants have been incorporated into titania using this method and will be further discussed below.

1.4.2.2 Precipitation

Precipitation methods involve adding a base to a Ti containing starting material such as titanium chloride or titanium sulfate to precipitate a precursor, often followed by calcination to obtain a crystalline oxide product. Precipitation syntheses often lead to anatase and mixed phase products, though the room temperature hydrolysis of TiCl_4 under acidic conditions is a common method to obtain nano rutile TiO_2 . Precipitation methods are often used because they are fast and generally do not require expensive equipment or starting reagents. Drawbacks, however, include large particle sizes with large size distributions due to uncontrolled precipitation.⁶

1.4.2.3 Solvothermal

Solvothermal synthesis reactions are performed in an aqueous or organic (i.e. methanol or toluene) medium at low temperatures (generally 250°C or lower) under self-produced pressure. Ti inorganic salts and $\text{H}_2\text{TiO}(\text{C}_2\text{O}_4)_2$ are commonly used as starting materials.⁶ A calcination step is often included to form a crystalline solid. Many properties, including crystallite size, particle morphology, and phase can be controlled through regulating the reaction temperature and pressure, solvent choice, solution composition, additives, and aging times.

1.4.2.4 Combustion

In combustion syntheses, solutions are rapidly heated to form crystalline titanias through redox reactions. Combustion methods are used to produce large, crystalline particles.^{48, 49} Though high temperatures are employed, the high temperature period is short enough to minimize crystallite growth and therefore the anatase to rutile phase transition can be avoided if desired.

1.4.2.5 Electrochemical

Electrochemical methods are used to prepare complex thin film morphologies such as epitaxial thin films and quantum dot films. Acidic, oxygen-free, non-aqueous Ti solutions are used as starting materials.^{50, 51} Inorganic salts are avoided due to the tendency of salts to hydrolyze. Though some areas, such as the role of structure directing agents on electrochemical growth, need to be further investigated, properties of thin film products can be well controlled through control of pH, potential, current density, and temperature.

1.4.3 Gas Phase Methods

Gas methods are popular routes to synthesize TiO₂ thin films. The most common techniques are summarized below.

1.4.3.1 Chemical vapor deposition (CVD)

CVD involves the decomposition of a gaseous precursor to form a metal or oxide product.^{52, 53} Because CVD can be done as a fast, continuous process, it is a widely used technique to synthesize thin films and coatings, including ceramics and semiconductors.

1.4.3.2 Physical vapor deposition (PVD)

PVD, a process similar to CVD, is also used to synthesize thin films. As in CVD, thin films are formed in the gaseous phase. However, PVD does not involve a chemical reaction to form a product. Instead, products are commonly obtained through thermal evaporation of a TiO₂ material, followed by deposition onto a substrate. Reduced pressures are often used to minimize gas molecule collisions, which can lead to impurities in the deposited films. Though PVD is generally a slower, more difficult process compared with CVD, it can be used to obtain TiO₂ films with increased conductivity, purity, smoothness, and crystallinity.⁶

1.4.3.3 Spray pyrolysis deposition (SPD)

SPD is another technique to deposit TiO₂ thin films and powders onto substrates. Though similar to CVD and PVD, in SPD, an aerosol, not a vapor, is formed from the precursor solution and substrates are typically at ambient pressures. Metal-organic compounds or inorganic salts are generally used as starting materials for the precursor solution.^{54, 55} Reaction parameters, including precursor composition, substrate temperature, and gas flow rates, can be used to control crystallite size, particle morphology, and can also be utilized to obtain mixed oxides.

Though SPD faces difficulties creating uniform materials, it is a relatively easy, fast, and inexpensive process.

1.4.4 Other Specialized Methods

Many specialized methods to create unique morphologies with specific properties have been developed. A few of these include sputtering,^{56, 57} molecular beam epitaxy,^{58, 59} ion implantation,⁶⁰ radio frequency thermal plasma oxidizing,⁶¹ and dynamic ion beam mixing.⁶²

1.4.5 Industrial Techniques

Many commercial titanias are synthesized by sol-gel routes, sulfate hydrolysis, or by converting crude titanium ore to TiCl_4 that is then oxidized.^{6, 63} Though commercial products often have lower surface area and poor thermal and hydrothermal stabilities compared with materials reported in the literature, the commercial methods are economical and scalable. Therefore, further development of economically viable synthesis methods to obtain high surface area titanias with improved properties has received much attention. An additional drawback of commercial titanias is that it is more difficult to effectively add modifiers or stabilizers to the finished materials than during synthesis.

1.4.6 Synthesis of Supported Catalysts

Conventional methods to obtain supported catalysts involve impregnation or co-precipitation techniques, followed by drying and heating. In impregnation routes, the most common synthesis of supported catalysts, a high surface area support or support precursor (commonly a carbon or metal oxide) is placed in contact with a solution of a catalyst precursor. The resulting solution or slurry is dried, calcined to remove byproducts, and reduced to obtain an active metal catalyst (see Figure 1.4). Impregnation methods are classified according to the ratio

of volume of solution compared with volume of the support pore volume.⁶⁴ Some supported synthesis methods are briefly described below.

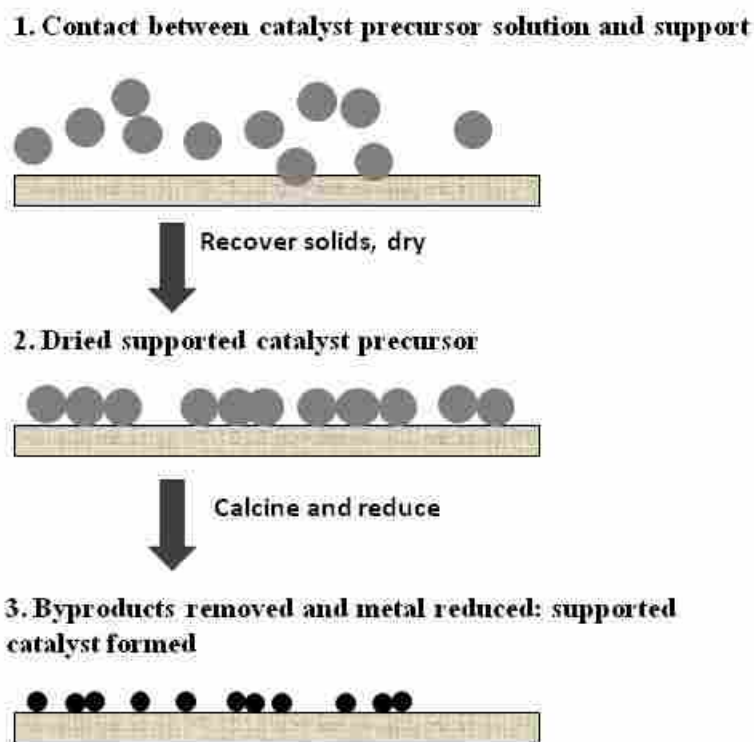


Figure 1.4 Stages of aqueous impregnation catalyst preparation.

1.4.6.1 Dry impregnation (DI)

In DI the volume of the metal catalyst solution is approximately equal to the pore volume of the support. The solution is mixed with the support or support precursor to form a thick paste that is then calcined and/or reduced. Capillary pressure is the dominant force behind pore filling. This method is simple; however, problems can arise when the support and catalyst precursor do not interact strongly and often results in non-uniform surface coverage.^{65, 66}

1.4.6.2 Wet impregnation (WI)

In WI the volume of the metal catalyst solution is larger than the pore volume of the support. The support or support precursor is mixed with a solution of the metal catalyst precursor for a certain period of time, after which the support and strongly interacting catalyst precursor are recovered through filtration. Any weakly adsorbed precursor is washed away and the solid is then calcined and/or reduced. Though WI can improve mixing (compared with DI), the catalyst may be lost through the filtration process. Additionally, the catalyst content must be determined through analysis of either the solid or liquid.⁶⁵

1.4.6.3 Ion exchange

In ion exchange the volume of the metal catalyst solution is larger than the pore volume of the support. The support material is immersed in the catalyst solution where concentration gradients and electrostatic interactions drive interactions between the support and catalyst precursor.⁶⁷ A net surface charge on the support attracts oppositely charged ions in the aqueous solution. Ion exchange can result in high dispersions, but, as with DI, can face drawbacks with uniform dispersion of the metal throughout the support.^{64, 66} Additionally, in recovering the support solid from solution, evaporation techniques are employed that can deposit solvent onto the support. Further removal of the solvent can cause the electrostatically bound catalyst to be expelled.⁶⁵

1.4.6.4 Deposition-precipitation

In deposition-precipitation the volume of the metal catalyst solution is larger than the pore volume of the support. The support material is suspended in a solution of the catalyst precursor. Solution properties are slowly altered (i.e. change of pH or concentration) to cause the catalyst to precipitate onto the support surface.⁶⁶ Though this method produces strong

interactions between the support and catalyst precursor, the mechanisms of deposition-precipitation are not always well understood, making it difficult to determine the appropriate solution conditions.^{65, 68}

1.4.6.5 Grafting

In grafting the volume of the metal catalyst solution is larger than the pore volume of the support. Surface functional groups (i.e. hydroxyl species) of the support and the catalyst precursor form covalent bonds.⁶⁹ The solid support and strongly interacting catalyst precursor are then washed to remove any weakly adsorbed catalyst precursor, followed by calcination and/or reduction. While grafting can result in homogeneous surface coverage, the catalyst loading is limited by the hydroxyl surface density.⁶⁵

1.4.6.6 Co-precipitation

In co-precipitation, a solution is made that contains precursors for both the support and catalyst. Agents to induce nucleation and precipitation are added and a solid precipitate is formed. Co-precipitation methods are limited by material solubilities. If the support and catalyst do not have similar solubilities, the precipitate is initially dominated by the less soluble species, leading to inhomogeneous compositions.⁶⁵

1.4.6.7 Other methods

Many other novel and/or complex methods have been reported, including sol-gel syntheses, organometallic precursor syntheses, microwave-assisted syntheses, dendrimer-metal precursor syntheses, solid state ion exchange by zeolites, and strong electrostatic adsorption. These and other syntheses of supported catalysts are reported elsewhere.⁶⁵

1.5 Dopants

Dopants are frequently introduced into titania to increase the thermal and hydrothermal stability, crystallinity, and surface area, and to control the pore properties, phase, and morphology of titanias used in catalysis. Dopants can also be used to modify the electronic structure, improve the light-absorption properties, and adjust the band gap of TiO₂ semiconductors and photocatalysts without loss of the TiO₂ crystal structure.

Dopants can be introduced at various stages in the synthesis, i.e., in the initial formation of a sol, after formation of a TiO₂ precursor before calcination, or after obtaining a TiO₂ product. Co-hydrolysis methods, which allow for precise control of dopant concentration and homogeneous mixing, have shown great promise in producing anatase stabilized with varying amounts of dopants.^{70, 71} For example, Kim et al.⁷² used co-hydrolysis to stabilize anatase with 5 – 40% Al, 10% Si, and 10% Zr.

Dopants can be incorporated in a number of ways, for example, as mixed metal oxides, substitutional or interstitial doping, or as surface species. It is expected that the manner in which dopants are incorporated into the crystal structure will result in different effects; therefore, in order to understand and predict dopant effects, the structure of doped nanomaterials should be understood. Characterizing the structure of doped nanomaterials is particularly difficult because traditional bulk techniques such as XRD, TEM, SEM, and XPS are limited in discerning finer details. In fact, using these techniques, many researchers have drawn contradictory conclusions from similar data.⁷³⁻⁷⁸ Evidence from these traditional techniques alone is not enough to determine the structure of nanomaterials, particularly small, 2 – 4 nm crystallites, however, development during the past 3 – 4 decades of sophisticated surface and high-energy spectroscopy

techniques such as X-ray absorption spectroscopy has enabled more in depth structural characterization.

Many different dopant species, including metal cations, nearly all non-metal anions, and noble metals, have been explored. Non-metal anions are frequently used to substitutionally replace oxygen anions resulting in a band gap shift towards the visible spectrum.¹³ Transition and rare earth metal cations can be used to substitutionally replace Ti cations and can also result in band gap adjustments. Noble metals are also often incorporated and TiO₂ is commonly used as a support material for noble metal catalysts.

1.5.1 Transition and Rare Earth Metal Dopants

Modifying the properties of TiO₂ using transition metal and rare earth metal dopants has been extensively studied. Many metal cations have been examined, including Cu, Ni, Co, Mn, Zn, Fe, Zr, Cr, V, Al, Ga, Sn, Sb, Nb, Mo, Ag, Ru, Rh, Re, Os, La, Ta, Ce, Nd, Sm, Eu, Gd, and Yb.^{44, 46, 61, 71, 72, 79-83}

Transition metals are used to adjust the band gap, provide additional energy levels within the band gap of semiconductors, and improve the photocatalytic properties of titanias. Transition metals can improve the trapping/recombination rate ratio to create more effective photocatalysts; however, impurities can also lead the formation of energy levels within the band gap that can cause increased rates of recombination between electron-hole pairs. Photocatalytic reactions occur when trapped electrons and holes are transferred to the surface of catalysts; therefore, the most efficient charge transfer occurs when metal ions are doped near the surface. In addition to the dopant location, dopant concentration affects the photocatalytic properties. Joshi et al.⁸⁴ found that high concentrations of dopants lead to the formation of localized d states that can act as sites to capture either electrons from the conduction band or holes from the valence band,

resulting in decreased photocatalytic activity. Dopant concentration also affects the space-charge region. As dopant concentration increases, the space-charge region narrows and the penetration depth of light greatly exceeds the width of the region. This results in an increase in recombination of electron-hole pairs and therefore a decrease in photocatalytic activity.¹⁶

Transition and rare earth metal metals are also used to modify the phase and increase the surface area, stability, and pore structure of titanias. Sibin et al.⁴⁶ concluded that substitutionally incorporating lanthanum into the structure of TiO₂ stabilized the Ti-O bonds and therefore retarded the anatase to rutile phase transition. Li et al.⁶¹ determined that increasing the concentration of a cobalt dopant in TiO₂ increased the number of oxygen vacancies, resulting in an increase in the amount of rutile phase present in the product. Bian et al.⁴⁴ found that surface lanthanum species prevented the collapse of mesoporous titania structures during thermal treatment and inhibited the formation of the rutile phase. The doped samples remained anatase at calcination temperatures above 600°C, compared to the pure sample, which began transforming to rutile at temperatures as low as 350°C. Periyat et al.⁴⁵ found that silicon prevented grain growth and stabilized the anatase phase up to 1000°C. Silicon incorporated into the TiO₂ lattice reduced contact between Ti atoms to prevent grain growth. Silicon incorporated on the surface of TiO₂ provided a framework that inhibited structural changes such as phase changes and grain growth. Periyat et al.⁴⁵ also found that the surface area increased with increasing concentration of silicon, with the pure TiO₂ having a surface area of 48 m²/g compared to a 15 mol% Si doped TiO₂, which had a surface area of 187 m²/g.

1.5.2 Noble Metal Dopants

Noble metals are added to TiO₂ to enhance photocatalytic activity. Fermi levels in noble metals are lower than those in TiO₂, allowing electron transfer from the conduction band of TiO₂

to the metal particles on the surface of TiO₂ while valence band holes remain on TiO₂. This electron transfer reduces the electron-hole recombination rate and therefore increases photocatalytic activity. Schubert et al.⁸⁵ demonstrated that the addition of Pt metal to TiO₂ enhanced the rate and extent of photo-decomposition of methyl formate.

TiO₂ is also used as a support material for noble metal catalysts. TiO₂ supported catalysts are discussed in the applications section.

1.5.3 Non-metal and Anion Dopants

Non-metal and anion dopants can increase the photocatalytic activity and adjust the structural properties of titania. Through the mixing of p states from oxygen and dopant anions, the valence band energy of TiO₂ can be shifted higher and the band gap energy of TiO₂ can be narrowed. Various non-metals, including C, N, F, P, and S have been used to substitute oxygen in the TiO₂ lattice.^{34, 86-91} Metal anions have been shown to better increase photocatalytic reactivity compared with cations as they are less likely to form recombination centers.⁹² Raj et al.⁹³ concluded that phosphates decreased the crystallinity and crystallite size of TiO₂ by as much as 50%, and delayed the anatase to rutile phase transition. Roy et al.³⁴ found that dopants affect the oxygen vacancy concentration, which in turn inhibits or accelerates phase transitions. The anatase to rutile phase transition was inhibited by phosphorous, which decreased the oxygen vacancy concentration.³⁴

1.6 Applications in Catalysis

TiO₂ is used in many applications including pigments, coatings, and catalytic applications. This work will focus on the use of TiO₂ in catalytic applications.

Nanomaterials have attracted substantial attention in the area of catalysis due to the properties they exhibit such as high surface areas, intricate pore networks and unique morphologies. TiO₂, in particular is a widely used catalyst and catalyst support because it is relatively inexpensive, environmentally friendly, stable, and versatile. It is most commonly used as a photocatalyst,^{34, 61, 94} but its broad range of applications include photovoltaics,^{34-36, 95} air and water purification,^{44, 96} environmental cleanup,^{44, 96} optical and antireflective coatings,⁹⁷ bactericide,^{34, 35, 44} water splitting,³⁴ and sensors.³⁴⁻³⁶ TiO₂ exists in many different phases, most commonly anatase and rutile. The anatase phase has traditionally been recognized as the best for catalysis because it is the stable low temperature phase for nano TiO₂ and generally has the highest surface area, an important property for catalysis.

Each catalytic application needs particles with distinct pore diameters, particle sizes, and surface areas and as many catalysts are used at elevated temperatures, thermal/hydrothermal stability is essential. Different synthesis variables such as the addition of dopants, the choice of starting materials, precursor treatment, and calcination temperature and time, will affect important catalytic properties including phase, surface area, particle size, porosity, agglomeration, morphology, thermal stability, and hydrothermal stability.

In addition to the need to finely control several properties, catalysts are often made from expensive materials via time-consuming and difficult processes. It is therefore, not surprising that catalysts are expensive. Due to the cost, catalysts are often affixed to a support that is used to (1) finely disperse the metal catalyst (dispersion defined as the number of surface metal atoms divided by the number of total metal atoms), maximizing available surface area and minimizing grain growth and sintering by inhibiting migration, (2) aid in catalyst recovery (helps to separate

the catalyst from the reaction stream), and (3) promote reactions. TiO_2 is a popular catalyst support, particularly for noble metals in oxidation reactions.

TiO_2 is a versatile material with many applications. Some of the most common catalytic applications are presented below.

1.6.1 Photocatalysis

The primary catalytic use of TiO_2 is in photocatalysis. When semiconductors absorb light of greater photonic energy than the band gap, electron-hole pairs are generated and redox reactions with surface species are initiated before recombination.⁹⁸ TiO_2 is an excellent photocatalyst because of its band gap width and position, high quantum efficiency, stability, and low cost.⁹⁸ TiO_2 photocatalysts are used in many ways including water purification, hydrogen production, air purification, and selective organic synthesis.

1.6.1.1 Water treatment

Increasing awareness of environmental hazards and downstream use of water has resulted in an interest in green, effective, low cost water treatment methods. TiO_2 photocatalysts are therefore promising materials for water treatment systems. Through photocatalysis, TiO_2 has been shown to degrade wastewater pollutants such as aliphatics, aromatics, polymers, dyes, surfactants, pesticides, and herbicides to CO_2 , H_2O , and mineral acids with no solid byproducts. TiO_2 photocatalysts are also particularly useful for reacting with inactive materials such as linear alkanes. TiO_2 photocatalysts can operate at normal temperatures and pressures to oxidize pollutants in the ppb range in a relatively short time.

Photocatalytic reactions are generally performed using either a TiO_2 suspension or an immobilized TiO_2 system.⁹⁹ TiO_2 powder in suspension is generally the most catalytically

efficient. TiO_2 is often coated onto beads and other structures to increase the surface area, inhibit aggregation, and ease the process of catalyst separation from the reaction stream.

Wastewater treatment can be performed through several processes. Processes are selected based on the pollutant.

Processes:⁶

1. Activated sludge process: use microorganisms and bacteria and is generally applied to biological wastewater treatment.

Drawbacks: slow reaction rates, sludge disposal, pollutants may be toxic to the bacteria.

2. Traditional adsorption processes: use activated carbon and are generally applied to degradation of organics.

Drawbacks: expensive, loss of adsorbent each cycle, non-selective adsorbents.

3. Air stripping: involves extracting volatile organics from water followed by further treatment.

Drawbacks: subsequent treatment of air is required.

4. Chemical oxidation: chlorination and ozonation.

Drawbacks: only economical at high pollutant concentrations, high equipment costs, potential formation of carcinogens.

5. Other advanced oxidation technologies: used in degrading industrial toxins and microorganisms through generation of oxidizing hydroxyl radicals.

Drawbacks: expensive reactants, only applicable to wastes with small chemical oxygen demands.

Prairie et al.¹⁰⁰ demonstrated the successful photocatalytic reduction of Ag(I), Cr(VI), Hg(II), and Pt(II) using TiO₂. Mahmoodi et al.⁹⁹ showed that TiO₂ could degrade and therefore reduce the toxicity of Acid Blue 25, a textile dye. Several researchers have also explored the degradation of phenol to reduce its toxicity.^{101, 102} Zhang et al.¹⁰³ demonstrated that catalytic degradation is increased when surface area and crystallinity are increased. Liu et al.¹⁰⁴ showed that doping can be used to enhance the photocatalytic activity of TiO₂ by increasing visible-light absorption through band gap adjustment. The presence of pesticides (including herbicides, fungicides, and insecticides) in water can present serious problems to humans and aquatic organisms. Examples of photocatalytic degradation of pesticides using TiO₂ are reviewed elsewhere.¹⁰⁵⁻¹¹⁰ Further examples of photocatalytic wastewater treatment are detailed elsewhere.^{111, 112}

Besides these examples, further information on the research of the degradation of bacteria, fungus, inorganic oxidants, carboxylic acids, benzoic acid, chlorine-containing compounds, nitrogen-containing compounds, sulfur-containing compounds, selenium-containing compounds, humic acids, cyanobacterial metabolites, oil derivatives, dyes, surfactants, pesticides, and inorganic compounds including the reduction of several metals through TiO₂ photocatalysis are reviewed elsewhere.⁶

1.6.1.2 Hydrogen production

Hydrogen has attracted interest as a clean and renewable energy source. Currently, the majority of hydrogen is produced from fossil fuels. For a sustainable hydrogen energy source, the photocatalytic splitting of water is an attractive process and TiO₂ is presently the most widely studied semiconductor for hydrogen production through solar photocatalysis.

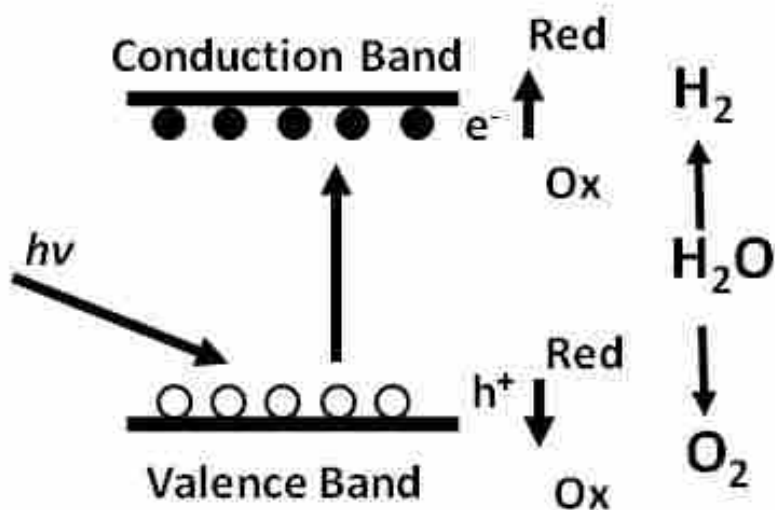


Figure 1.5 Photocatalytic splitting of water.

Figure 1.5 shows the mechanism of photocatalytic water splitting. Photon absorption by TiO_2 generates electron-hole pairs. Electrons migrate to the catalyst surface and H_2 and O_2 are produced through redox reactions. Fugishima et al.¹¹³ demonstrated the decomposition of water to oxygen and hydrogen using an n-type TiO_2 semiconductor. Zhang et al.¹¹⁴ showed that high surface area, mesoporous crystalline TiO_2 generated five times more H_2 compared with bulk TiO_2 . Fujihara et al.¹¹⁵ demonstrated the photochemical splitting of water using two photocatalytic reactions on TiO_2 catalysts: (1) reduction of water to hydrogen through the oxidation of bromide ions and (2) the oxidation of water to oxygen through the reduction of Fe^{3+} ions. Yoshida et al.¹¹⁶ showed that the photocatalytic reaction of CH_4 gas with H_2O vapor over a Pt/TiO_2 catalyst led to the formation of H_2 and CO_2 . Sreethawong et al.¹¹⁷ showed that increasing the crystallinity of TiO_2 catalysts increased H_2 production.

1.6.1.3 Air purification

Air pollutants, including volatile organic compounds (VOCs), NO_x compounds, and SO₂, produced largely from industrial processes and other human activity, can harm humans and other living organisms. As awareness of the harmful effects of air pollutants has increased, interest in developing green methods, including using TiO₂ photocatalysts, to reduce air pollution has also increased. In comparison with other air purification methods, photocatalytic air treatment processes using TiO₂ can operate at low temperatures and pressures and can oxidize low concentrations of pollutants. Additionally, with improvements to photocatalysts, the utilization of solar energy could reduce necessary energy costs. Drawbacks of TiO₂ photocatalytic air purification include catalyst deactivation, low oxidation of some materials including aromatics, and the potential formation of harmful, stable intermediates. TiO₂ photocatalytic oxidation has been used to degrade many pollutants, including hydrocarbons, chlorinated compounds, alcohols, nitrogen compounds, sulfur compounds, siloxane compounds, NO_x species, SO_x species, and ozone. Examples of these reactions have been reviewed elsewhere.⁶

1.6.1.4 Selective organic synthesis

Photocatalytic synthesis of organic materials, including oxidation, oxidative cleavage, reduction, isomerization, substitution, and polymerization, has gained interest as greener methods to replace traditional oxidation syntheses are explored. TiO₂ catalytic reactions have been used in the synthesis of alkanes, alkenes, alicyclic hydrocarbons, aromatics, alcohols, aldehydes, ketones, acids, amines, nitro compounds, and sulfides. Examples of reactions are summarized elsewhere.⁶

1.6.2 Solar Cells

Conventional silicon-based solar cells are currently too costly to compete with traditional power. Therefore, low cost dye sensitized solar cells (DSSCs) have attracted significant attention. Typical DSSCs are made of TiO_2 layers deposited on transparent conducting oxide glass (TCO), an electrolyte system, and a Pt electrode. To operate, TiO_2 adsorbs dye molecules, transferring electrons from the dye to the TCO (see Figure 1.6).

Currently, increasing the conversion efficiency is one of the main research focuses of DSSCs. Zukalova et al.¹¹⁸ found that ordered mesoporous TiO_2 films yielded higher photovoltaic conversion efficiency than randomly oriented TiO_2 films. Nedelcu et al.¹¹⁹ demonstrated that increasing the crystallinity of TiO_2 films increased the power conversion efficiency. Zhang et al.¹²⁰ reported that higher power conversion efficiency can be obtained using ordered TiO_2 mesostructures because fewer defects per charge combination are present.

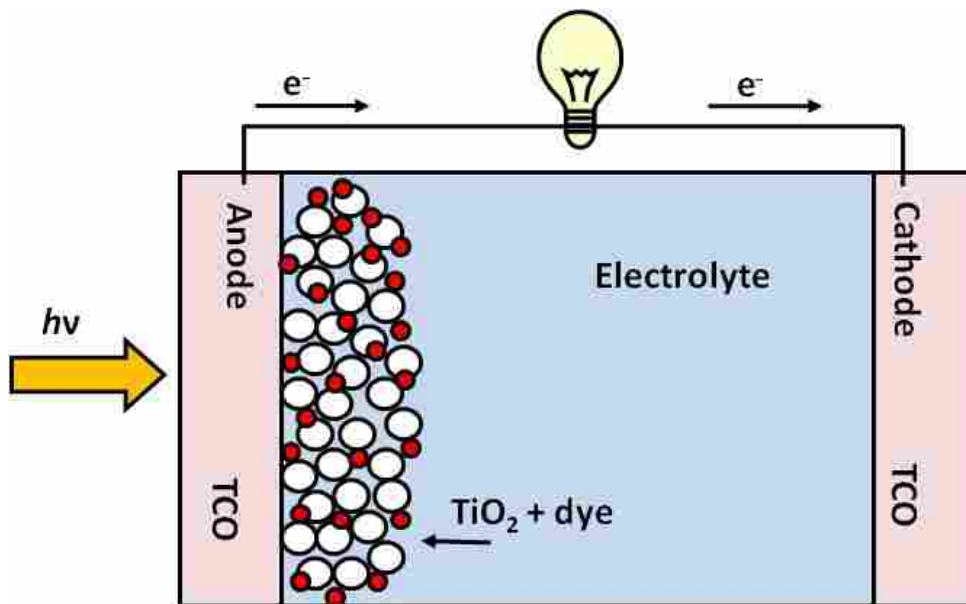


Figure 1.6 Example of a dye sensitized solar cell.

1.6.3 Sensors

Titanias can be used in sensors to detect various gases, and are particularly useful in the environmental protection applications. Varghese et al.¹²¹ demonstrated that sensors of TiO₂ nanotubes prepared through anodization were highly sensitive to H₂ gas at reasonably low temperatures (180°C). Devi et al.¹²² found that mesoporous TiO₂ sensors had increased sensitivities toward H₂ and CO gases compared with non-mesoporous commercial TiO₂ powders. The increased sensitivity was attributed to the increased surface area of mesoporous materials.

1.6.4 Lithium Ion Batteries

Rechargeable lithium-ion batteries generally utilize graphite anodes. TiO₂ is being investigated as an alternate anode material as it an inexpensive and nontoxic material with low volume change during the charge-discharge process, and increased overcharge protection.¹³ Wang et al.¹²³ reported large specific capacities for lithium batteries using TiO₂ nanotube electrodes. Yoon et al.¹²⁴ demonstrated that high battery capacities can also be obtained using hollow core-shell mesoporous TiO₂ spheres.

1.6.5 Catalyst Supports

TiO₂ is commonly used as a catalyst support due to its excellent thermal stability, low cost, low toxicity, high surface area, and pore structure. Noble metals supported on anatase TiO₂ are particularly useful in a number of oxidation reactions, e.g. oxidation of CO at low temperatures,⁷ preferential oxidation of CO in H₂/CO mixtures,⁸ low-temperature, direct synthesis of hydrogen peroxide,⁹ selective oxidation of primary C-H bonds,¹⁰ and oxidation of alcohols to aldehydes.¹¹ With increasing concerns about atmospheric pollution, there has been much interest expressed in using catalysts supported on TiO₂ in the complete oxidation of

volatile organic compounds to CO₂ and H₂O.¹² Examples of recent studies of catalysts supported on TiO₂ are presented below.

Haruta et al.⁷ demonstrated the low temperature oxidation of CO by Au nanocatalysts supported on TiO₂ and determined that the activity of Au nanocatalysts is size dependent. Zhao et al.¹²⁵ also examined catalyst activity size dependence; sub-1 nm Pt particles supported on TiO₂ demonstrated extremely high NO₂ conversion and high activity for the liquid phase oxidation of phenol. Pt supported on TiO₂ is known to be effective in oxidizing CO,^{126, 127} and TiO₂ supported Pt catalysts also show excellent activity for oxygen reduction and hydrogen oxidation in fuel cell applications. Elezovic et al.¹²⁸ reported that Pt supported on Ru-doped TiO₂ exhibited higher activity for oxygen reduction and hydrogen oxidation than Pt supported on carbon. In other applications, Green et al.¹²⁹ found that TiO₂ supported Au catalysts were effective in forming acetate from the partial oxidation of ethylene at relatively low temperatures of 97°C and Li et al.¹³⁰ demonstrated that TiO₂ supported Rh catalysts were highly active and selective for the production of ethanol from syngas.

The catalytic activity of noble metals is largely linked to crystallite size and dispersion. In the case of supported catalysts, these properties are controlled to some extent by support properties including surface area, pore structure, and stability. Therefore, the structure and properties of the TiO₂ support affect the performance of the catalyst. Ishihara et al.¹³¹ determined that Au-Pd catalysts supported on rutile TiO₂ were more active in the synthesis of H₂O₂ by oxidation of H₂ with air than Au-Pd catalysts supported on anatase or brookite TiO₂. Shi et al.¹³² demonstrated that increasing oxygen vacancies in the TiO₂ support increased the activity and stability of Pt in the oxidation of methanol. Shimura et al.¹³³ found that CO conversion rates in Fischer-Tropsch synthesis could be increased through (1) controlling the TiO₂ support crystal

phase or (2) modifying the TiO₂ support through the addition of dopants. CO conversions were highest when an anatase/rutile mixture modified with calcium was used as the support.

1.7 Dissertation Overview

TiO₂ is a widely used catalyst support, however currently available commercial titanias often have low surface area and poor thermal and hydrothermal stability. While several methods reported in literature produce materials of higher surface area and more ideal porosity relative to commercially available titanias, these procedures generally involve inherent drawbacks including time-consuming procedures, complicated processes, expensive materials and/or equipment, the use of organic reagents that generate waste and impurities, the addition of surfactants and capping agents that may need to be removed, and difficulties scaling up. Therefore, many processes reported in literature are not industrially viable. Cost-effective, large scale preparations of stable, high surface area, mesoporous TiO₂ need to be developed.

The work in this dissertation focuses on (1) producing high surface area stabilized TiO₂ supports of controlled pore diameters and (2) the preparation of well dispersed Pt on these supports using industrially viable processes. The characterization tools used in this dissertation are introduced in chapter two. A simple, industrially viable synthesis of high surface area, stabilized anatase TiO₂ with a range of pore diameters is presented in chapter three. Chapter four explores the range of anatase properties that can be obtained using this method through statistically designed process optimization.

The TiO₂ materials presented in this work have been modified with Al, La, Si, and Zr to control the thermal stability, surface area, and porosity. This is not unique as TiO₂ has traditionally been modified with various dopants, however, the structure of doped nanomaterials

and mechanisms of dopant stabilization are not well understood. Chapter five focuses on an analysis of Al-modified TiO₂ nanostructures using an advanced spectroscopic technique in combination with traditional characterization methods. Possible mechanisms of Al-stabilization are also discussed.

TiO₂ is commonly used to support Pt catalysts. Many methods of synthesizing supported Pt catalysts have been reported in the literature; however, many of these methods are time-consuming, difficult, and expensive processes that result in poor Pt size control and dispersion. Chapter six presents a facile one-pot method to synthesize highly dispersed Pt catalysts supported on Al-modified TiO₂.

1.7.1 Chapter Abstracts

Abstracts of chapters 3 – 6 are included below.

1.7.1.1 Chapter 3 abstract

The effects of dopants Al, La, Si, and Zr on the stability, surface area, and porosity of anatase were investigated. Anatase materials stabilized with 0 – 14 mol% La, Si, Zr, or 0 – 85 mol% Al were studied. Materials were characterized using XRD, TEM and N₂ sorption. Results show that (1) dopants increased the surface area and thermal stability of anatase through structural modifications and grain growth inhibition, (2) due to structural modifications it was important to select the appropriate hysteresis branch for pore diameter calculations, and (3) a thorough analysis of N₂ adsorption and TEM data provided additional insight into how stabilizing agents affected the mesoporous structure. Stabilized titanias produced by this method demonstrated equivalent or higher thermal stability and surface area compared with pure anatase and previously reported materials after treatment at 400°C and 700°C including 22 mol% Al-

TiO₂ calcined at 400°C which had a surface area of 479 ± 39 m²/g, a pore volume of 0.46 ± 0.04 cm³/g, and a pore diameter of 2.9 ± 0.2 nm.

1.7.1.2 Chapter 4 abstract

The important variables in the synthesis of stable, high surface area, aluminum-modified anatase TiO₂ catalyst supports were identified and optimized using statistically designed experiments (DOEs). The first DOE examined ten variables at two levels and a second DOE studied eight variables at three levels. Equations were developed to predict the conditions to obtain the highest surface area and pore volume at the desired pore diameter and predict the pore diameter range that may be obtained. Confirmation trials closely matched predicted surface areas, pore volumes, and pore diameters in all but one trial. Rinsing order (before or after calcination) was the most significant factor. Other important factors were calcination temperature, mole% aluminum, and water addition speed. The results of this study demonstrate (1) the power of DOEs in identifying and controlling synthesis variables in relatively few experiments and (2) how analysis of factor effects can provide insight into the formation mechanism.

1.7.1.3 Chapter 5 abstract

The structures of Al-modified anatase TiO₂ supports were analyzed using traditional analysis techniques of XRD, TEM, and N₂ sorption as well as XANES, ²⁷Al MAS NMR, and low temperature heat capacity. The combined results from these characterizations reveal that the Al dopant is incorporated either on the surface or in vacancies depending on the details of the synthetic method used. Alumina incorporated on the surface stabilizes TiO₂ by lowering the surface energy of anatase and stabilizing planes with high surface energy that would otherwise join to achieve a reduced surface energy. On the other hand, Al incorporated in TiO₂ vacancies

stabilize the structure through increasing lattice strain and limiting mass transport necessary for grain growth. 22 mol% Al-modified TiO₂ with Al on the surface had an average crystallite diameter of 6 nm, a surface area of 184 m²/g, a pore volume of 0.34 cm³/g, and a pore diameter of 6.4 nm compared with 22 mol% Al-modified TiO₂ with Al incorporated in vacancies and on the surface which had an average crystallite diameter of 2-3 nm, a surface area of 471 m²/g, a pore volume of 0.44 cm³/g, and a pore diameter of 4.4 nm. This work demonstrates the importance of structure analysis of doped nanomaterials in the development of stabilized catalysts and catalyst supports.

1.7.1.4 Chapter 6 abstract

A facile, industrially viable, one-pot synthesis of 0.5-8 wt% Pt supported on 22 mol% Al-modified anatase with high surface area and thermal stability is presented. Four pathways were studied to determine the effects of support properties on catalyst dispersion, and the highest dispersions were observed for high surface area materials containing 5-coordinate anatase. Systematic study of preparation variables shows that low drying temperatures, slow calcination ramp rates, and slow reduction ramp rates further increased Pt dispersion and resulted in a more uniform Pt size distribution. Pt dispersions as high as 54% have been obtained using the one-pot method and 59% for Pt catalysts synthesized by dry impregnation. Statistically designed studies are needed to more completely determine the effects of synthesis variables and to optimize the dispersion and reduction of Pt supported on Al-modified anatase. Results presented in this paper show that this one-pot method and dry impregnation method using our Al-modified anatase support are promising syntheses of highly dispersed Pt supported on stabilized titania. Our results demonstrate that the alumina-stabilized anatase support is superior to other anatase supports for (1) obtaining high Pt dispersions, i.e. more efficiently utilizing this expensive

precious metal and (2) processes in which thermal stability is important due to its constant phase and pore structures at high temperatures.

1.8 References

1. Fujishima, A.; Honda, K., Electrochemical photolysis of water at a semiconductor electrode. *Nature (London)* **1972**, *238* (5358), 37-8.
2. O'Regan, B.; Graetzel, M., A low-cost, high-efficiency solar cell based on dye-sensitized colloidal titanium dioxide films. *Nature (London)* **1991**, *353* (6346), 737-40.
3. Zou, Z.; Ye, J.; Sayama, K.; Arakawa, H., Direct splitting of water under visible light irradiation with an oxide semiconductor photocatalyst. *Nature (London, U. K.)* **2001**, *414* (6864), 625-627.
4. Zhang, Q.; Xu, H.; Yan, W., Highly ordered TiO₂ nanotube arrays: recent advances in fabrication and environmental applications - a review. *Nanosci. Nanotechnol. Lett.* **2012**, *4* (5), 505-519.
5. Tang, X.-h.; Wu, C.-z.; Li, B.-j.; Li, C.-w.; Lin, Y., New applications of nano titanium dioxide. *Meteorol. Environ. Res.* **2012**, *3* (1-2), 55-57.
6. Carp, O.; Huisman, C. L.; Reller, A., Photoinduced reactivity of titanium dioxide. *Prog. Solid State Chem.* **2004**, *32* (1-2), 33-177.
7. Haruta, M.; Tsubota, S.; Kobayashi, T.; Kageyama, H.; Genet, M. J.; Delmon, B., Low-temperature oxidation of carbon monoxide over gold supported on titanium dioxide, Î±-ferric oxide, and cobalt tetraoxide. *J. Catal.* **1993**, *144* (1), 175-92.

8. Imai, H.; Date, M.; Tsubota, S., Preferential Oxidation of CO in H₂-Rich Gas at Low Temperatures over Au Nanoparticles Supported on Metal Oxides. *Catal. Lett.* **2008**, *124* (1-2), 68-73.
9. Edwards, J. K.; Carley, A. F.; Herzing, A. A.; Kiely, C. J.; Hutchings, G. J., Direct synthesis of hydrogen peroxide from H₂ and O₂ using supported Au-Pd catalysts. *Faraday Discuss.* **2008**, *138* (Nanoalloys), 225-239.
10. Kesavan, L.; Tiruvalam, R.; Ab, R. M. H.; bin, S. M. I.; Enache, D. I.; Jenkins, R. L.; Dimitratos, N.; Lopez-Sanchez, J. A.; Taylor, S. H.; Knight, D. W.; Kiely, C. J.; Hutchings, G. J., Solvent-Free Oxidation of Primary Carbon-Hydrogen Bonds in Toluene Using Au-Pd Alloy Nanoparticles. *Science (Washington, DC, U. S.)* **2011**, *331* (6014), 195-199.
11. Enache, D. I.; Edwards, J. K.; Landon, P.; Solsona-Espriu, B.; Carley, A. F.; Herzing, A. A.; Watanabe, M.; Kiely, C. J.; Knight, D. W.; Hutchings, G. J., Solvent-Free Oxidation of Primary Alcohols to Aldehydes Using Au-Pd/TiO₂ Catalysts. *Science (Washington, DC, U. S.)* **2006**, *311* (5759), 362-365.
12. Tahir, S. F.; Koh, C. A., Catalytic oxidation for air pollution control. *Environ. Sci. Pollut. Res. Int.* **1996**, *3* (1), 20-3.
13. Zhang, R.; Elzatahry, A. A.; Al-Deyab, S. S.; Zhao, D., Mesoporous titania: From synthesis to application. *Nano Today* **2012**, *7* (4), 344-366.
14. Mills, A.; Le, H. S., An overview of semiconductor photocatalysis. *J. Photochem. Photobiol., A* **1997**, *108* (1), 1-35.
15. Lee, S. K.; Mill's, A., Platinum and palladium in semiconductor photocatalytic systems. Factors affecting the purification of water and air. *Platinum Met. Rev.* **2003**, *47* (2), 61-72.

16. Gupta, S. M.; Tripathi, M., A review of TiO₂ nanoparticles. *Chin. Sci. Bull.* **2011**, *56* (16), 1639-1657.
17. Chen, X.; Mao, S. S., Titanium Dioxide Nanomaterials: Synthesis, Properties, Modifications, and Applications. *Chem. Rev. (Washington, DC, U. S.)* **2007**, *107* (7), 2891-2959.
18. Latroche, M.; Brohan, L.; Marchand, R.; Tournoux, M., New hollandite oxides: titanium dioxide and potassium titanium oxide (K_{0.06}TiO₂). *J. Solid State Chem.* **1989**, *81* (1), 78-82.
19. Li, J. G.; Li, X.; Sun, X., *TiO₂ Nanocrystals: Synthesis and Enhanced Functionality*. Nova Science Publishers, Incorporated: 2010.
20. Zhang, H.; Banfield, J. F., Understanding Polymorphic Phase Transformation Behavior during Growth of Nanocrystalline Aggregates: Insights from TiO₂. *J. Phys. Chem. B* **2000**, *104* (15), 3481-3487.
21. Tanaka, K.; Capule, M. F. V.; Hisanaga, T., Effect of crystallinity of titanium dioxide on its photocatalytic action. *Chem. Phys. Lett.* **1991**, *187* (1-2), 73-6.
22. Cromer, D. T.; Herrington, K., The structures of anatase and rutile. *J. Am. Chem. Soc.* **1955**, *77*, 4708-9.
23. Baur, W. H., Atomic distances and bond angles in brookite, TiO₂. *Acta Crystallogr.* **1961**, *14*, 214-16.
24. Mo, S.-D.; Ching, W. Y., Electronic and optical properties of three phases of titanium dioxide: rutile, anatase, and brookite. *Phys. Rev. B: Condens. Matter* **1995**, *51* (19), 13023-32.

25. Zhang, Q.; Gao, L.; Guo, J., Effects of calcination on the photocatalytic properties of nanosized TiO₂ powders prepared by TiCl₄ hydrolysis. *Appl. Catal., B* **2000**, *26* (3), 207-215.
26. Li, W.; Bai, Y.; Liu, C.; Yang, Z.; Feng, X.; Lu, X.; van der Laak, N. K.; Chan, K.-Y., Highly Thermal Stable and Highly Crystalline Anatase TiO₂ for Photocatalysis. *Environ. Sci. Technol.* **2009**, *43* (14), 5423-5428.
27. Tobaldi, D. M.; Pullar, R. C.; Leoni, M.; Seabra, M. P.; Labrincha, J. A., Nanosized titania modified with tungsten and silver: Microstructural characterisation of a multifunctional material. *Appl. Surf. Sci.*, Ahead of Print.
28. Zhou, X.; Yang, F.; Jin, B.; Huang, Y.; Wu, Z., Hydrothermal fabrication of Ti³⁺ self-doped TiO₂ nanorods with high visible light photocatalytic activity. *Mater. Lett.* **2013**, *112*, 145-148.
29. Kiran, V.; Sampath, S., Facile synthesis of carbon doped TiO₂ nanowires without an external carbon source and their opto-electronic properties. *Nanoscale* **2013**, *5* (21), 10646-10652.
30. Nam, C. T.; Yang, W.-D.; Duc, L. M., Study on photocatalysis of TiO₂ nanotubes prepared by methanol-thermal synthesis at low temperature. *Bull. Mater. Sci.* **2013**, *36* (5), 779-788.
31. Wang, Y.; Wang, R.; Guo, C.; Miao, J.; Tian, Y.; Ren, T.; Liu, Q., Path-directed and maskless fabrication of ordered TiO₂ nanoribbons. *Nanoscale* **2012**, *4* (5), 1545-1548.
32. Chen, J.-Z.; Li, B.; Zheng, J.-F.; Jia, S.-P.; Zhao, J.-H.; Jing, H.-W.; Zhu, Z.-P., Role of One-Dimensional Ribbonlike Nanostructures in Dye-Sensitized TiO₂-Based Solar Cells. *J. Phys. Chem. C* **2011**, *115* (14), 7104-7113.

33. Han, H.; Bai, R., Buoyant Photocatalyst with Greatly Enhanced Visible-Light Activity Prepared through a Low Temperature Hydrothermal Method. *Ind. Eng. Chem. Res.* **2009**, *48* (6), 2891-2898.
34. Roy, B.; Ahrenkiel, S. P.; Fuierer, P. A., Controlling the size and morphology of TiO₂ powder by molten and solid salt synthesis. *J. Am. Ceram. Soc.* **2008**, *91* (8), 2455-2463.
35. Ambrus, Z.; Mogyorosi, K.; Szalai, A.; Alapi, T.; Demeter, K.; Dombi, A.; Sipos, P., Low temperature synthesis, characterization and substrate-dependent photocatalytic activity of nanocrystalline TiO₂ with tailor-made rutile to anatase ratio. *Appl. Catal., A* **2008**, *340* (2), 153-161.
36. Zhang, Z.; Brown, S.; Goodall, J. B. M.; Weng, X.; Thompson, K.; Gong, K.; Kellici, S.; Clark, R. J. H.; Evans, J. R. G.; Darr, J. A., Direct continuous hydrothermal synthesis of high surface area nanosized titania. *J. Alloys Compd.* **2009**, *476* (1-2), 451-456.
37. Zhu, J.; Yang, J.; Bian, Z.-F.; Ren, J.; Liu, Y.-M.; Cao, Y.; Li, H.-X.; He, H.-Y.; Fan, K.-N., Nanocrystalline anatase TiO₂ photocatalysts prepared via a facile low temperature nonhydrolytic sol-gel reaction of TiCl₄ and benzyl alcohol. *Appl. Catal., B* **2007**, *76* (1-2), 82-91.
38. Doeuff, S.; Dromzee, Y.; Taulelle, F.; Sanchez, C., Synthesis and solid- and liquid-state characterization of a hexameric cluster of titanium(IV): Ti₆($\mu_{4/2}$ -O)₂($\mu_{1/3}$ -O)₂($\mu_{1/2}$ -OC₄H₉)₂(OC₄H₉)₆(OCOCH₃)₈. *Inorg. Chem.* **1989**, *28* (25), 4439-45.
39. Doeuff, S.; Henry, M.; Sanchez, C., Sol-gel synthesis and characterization of titanium oxoacetate polymers. *Mater. Res. Bull.* **1990**, *25* (12), 1519-29.

40. Guillard, C.; Beaugiraud, B.; Dutriez, C.; Herrmann, J.-M.; Jaffrezic, H.; Jaffrezic-Renault, N.; Lacroix, M., Physicochemical properties and photocatalytic activities of TiO₂-films prepared by sol-gel methods. *Appl. Catal., B* **2002**, *39* (4), 331-342.
41. Campostrini, R.; Ischia, M.; Palmisano, L., Pyrolysis study of sol-gel derived TiO₂ powders. *J. Therm. Anal. Calorim.* **2004**, *75* (1), 13-24.
42. Takahashi, Y.; Matsuoka, Y., Dip-coating of titanium dioxide films using a sol derived from titanium tetraisopropoxide-diethanolamine-water-isopropyl alcohol system. *J. Mater. Sci.* **1988**, *23* (6), 2259-66.
43. Al-Salim, N. I.; Bagshaw, S. A.; Bittar, A.; Kemmitt, T.; James, M. A.; Mills, A. M.; Ryan, M. J., Characterisation and activity of sol-gel-prepared TiO₂ photocatalysts modified with Ca, Sr or Ba ion additives. *J. Mater. Chem.* **2000**, *10* (10), 2358-2363.
44. Bian, Z.; Zhu, J.; Li, H., Synthesis of well ordered crystalline TiO₂ photocatalyst with enhanced stability and photoactivity. *Stud. Surf. Sci. Catal.* **2007**, *165* (Recent Progress in Mesoporous Materials), 317-322.
45. Periyat, P.; Baiju, K. V.; Mukundan, P.; Pillai, P. K.; Warriar, K. G. K., High temperature stable mesoporous anatase TiO₂ photocatalyst achieved by silica addition. *Appl. Catal., A* **2008**, *349* (1-2), 13-19.
46. Sibin, C. P.; Kumar, S. R.; Mukundan, P.; Warriar, K. G. K., Structural Modifications and Associated Properties of Lanthanum Oxide Doped Sol-Gel Nanosized Titanium Oxide. *Chem. Mater.* **2002**, *14* (7), 2876-2881.
47. Yurdakal, S.; Palmisano, G.; Loddo, V.; Augugliaro, V.; Palmisano, L., Nanostructured Rutile TiO₂ for Selective Photocatalytic Oxidation of Aromatic Alcohols to Aldehydes in Water. *J. Am. Chem. Soc.* **2008**, *130* (5), 1568-1569.

48. Nagaveni, K.; Hegde, M. S.; Ravishankar, N.; Subbanna, G. N.; Madras, G., Synthesis and Structure of Nanocrystalline TiO₂ with Lower Band Gap Showing High Photocatalytic Activity. *Langmuir* **2004**, *20* (7), 2900-2907.
49. Nagaveni, K.; Sivalingam, G.; Hegde, M. S.; Madras, G., Solar photocatalytic degradation of dyes: high activity of combustion synthesized nano TiO₂. *Appl. Catal., B* **2004**, *48* (2), 83-93.
50. Kamada, K.; Mukai, M.; Matsumoto, Y., Electrodeposition of titanium(IV) oxide film from sacrificial titanium anode in I₂-added acetone bath. *Electrochim. Acta* **2002**, *47* (20), 3309-3313.
51. Zhitomirsky, I., Cathodic electrosynthesis of titanium and ruthenium oxides. *Mater. Lett.* **1998**, *33* (5,6), 305-310.
52. Jones, A. C.; Chalker, P. R., Some recent developments in the chemical vapour deposition of electroceramic oxides. *J. Phys. D: Appl. Phys.* **2003**, *36* (6), R80-R95.
53. Choy, K. L., Chemical vapor deposition of coatings. *Prog. Mater. Sci.* **2003**, *48* (2), 57-170.
54. Ahonen, P. P.; Tapper, U.; Kauppinen, E. I.; Joubert, J. C.; Deschanvres, J. L., Aerosol synthesis of Ti-O powders via in-droplet hydrolysis of titanium alkoxide. *Mater. Sci. Eng., A* **2001**, *A315* (1-2), 113-121.
55. Ahonen, P. P.; Kauppinen, E. I.; Joubert, J. C.; Deschanvres, J. L.; Van, T. G., Preparation of nanocrystalline titania powder via aerosol pyrolysis of titanium tetrabutoxide. *J. Mater. Res.* **1999**, *14* (10), 3938-3948.
56. Mardare, D.; Rusu, G. I., The influence of heat treatment on the optical properties of titanium oxide thin films. *Mater. Lett.* **2002**, *56* (3), 210-214.

57. Treichel, O.; Kirchoff, V., The influence of pulsed magnetron sputtering on topography and crystallinity of TiO₂ films on glass. *Surf. Coat. Technol.* **2000**, *123* (2-3), 268-272.
58. Ong, C. K.; Wang, S. J., In situ RHEED monitor of the growth of epitaxial anatase TiO₂ thin films. *Appl. Surf. Sci.* **2001**, *185* (1-2), 47-51.
59. Herman, G. S.; Gao, Y., Growth of epitaxial anatase (001) and (101) films. *Thin Solid Films* **2001**, *397* (1,2), 157-161.
60. Fromknecht, R.; Kubeis, I.; Massing, S.; Meyer, O., Ion implantation in TiO₂: damage production and recovery, lattice site location and electrical conductivity. *Nucl. Instrum. Methods Phys. Res., Sect. B* **1999**, *147* (1-4), 191-201.
61. Li, J.-G.; Buchel, R.; Isobe, M.; Mori, T.; Ishigaki, T., Cobalt-Doped TiO₂ Nanocrystallites: Radio-Frequency Thermal Plasma Processing, Phase Structure, and Magnetic Properties. *J. Phys. Chem. C* **2009**, *113* (19), 8009-8015.
62. Miyake, S.; Kobayashi, T.; Satou, M.; Fujimoto, F., Titanium oxide formation by dynamic ion beam mixing. *J. Vac. Sci. Technol., A* **1991**, *9* (6), 3036-40.
63. Lambourne, R.; Strivens, T. A.; Editors, *Paint and Surface Coatings--Theory and Practice, Second Edition (#9922)*. 1999; p 950 pp.
64. Marceau, E.; Carrier, X.; Che, M.; Clause, O.; Marcilly, C., Ion Exchange and Impregnation. In *Handbook of Heterogeneous Catalysis*, Wiley-VCH Verlag GmbH & Co. KGaA: 2008.
65. Regalbuto, J.; Editor, *Catalyst Preparation: Science and Engineering*. CRC Press LLC: 2007; p 474.

66. Geus, J. W.; van Dillen, A. J., Preparation of Supported Catalysts by Deposition–Precipitation. In *Handbook of Heterogeneous Catalysis*, Wiley-VCH Verlag GmbH & Co. KGaA: 2008.
67. Fierro, J. L. G., *Metal Oxides: Chemistry and Applications*. Taylor & Francis: 2005.
68. Moreau, F.; Bond, G. C.; Taylor, A. O., Gold on titania catalysts for the oxidation of carbon monoxide: control of pH during preparation with various gold contents. *J. Catal.* **2005**, *231* (1), 105-114.
69. Ertl, G.; Knözinger, H.; Weitkamp, J., *Preparation of Solid Catalysts*. Wiley: 2008.
70. Yang, J.; Ferreira, J. M. F., Inhibitory effect of the Al₂O₃-SiO₂ mixed additives on the anatase-rutile phase transformation. *Mater. Lett.* **1998**, *36* (5-6), 320-324.
71. Yang, J.; Ferreira, J. M. F., The effect of zirconia additive on the phase transition in a sol-gel-derived titania powder. *Mater. Res. Bull.* **1998**, *33* (3), 389-394.
72. Kim, J.; Song, K. C.; Foncillas, S.; Pratsinis, S. E., Dopants for synthesis of stable bimodally porous titania. *J. Eur. Ceram. Soc.* **2001**, *21* (16), 2863-2872.
73. Liao, L.; Ingram, C. W., Mesoporous I-Ag codoped titania and alumina modified titania catalysts: Synthesis, characterization and photocatalytic properties. *Appl. Catal., A* **2012**, *433-434*, 18-25.
74. Tsai, C.-Y.; Hsi, H.-C.; Bai, H.; Fan, K.-S.; Sun, H.-D., Single-step synthesis of Al-doped TiO₂ nanoparticles using non-transferred thermal plasma torch. *Jpn. J. Appl. Phys.* **2012**, *51* (1, Pt. 2), 01AL01/1-01AL01/6.
75. Smitha, V. S.; Baiju, K. V.; Perumal, P.; Ghosh, S.; Warriar, K. G., Hydrophobic, Photoactive Titania-Alumina Nanocrystallites and Coatings by an Aqueous Sol-Gel Process. *Eur. J. Inorg. Chem.* **2012**, *2012* (2), 226-233.

76. Zhou, Z.; Zeng, T.; Cheng, Z.; Yuan, W., Preparation and Characterization of Titania-Alumina Mixed Oxides with Hierarchically Macro-/Mesoporous Structures. *Ind. Eng. Chem. Res.* **50** (2), 883-890.
77. Lee, J. E.; Oh, S.-M.; Park, D.-W., Synthesis of nano-sized Al doped TiO₂ powders using thermal plasma. *Thin Solid Films* **2004**, *457* (1), 230-234.
78. Wang, L.-Y.; Sun, Y.-P.; Xu, B.-S., Comparison study on the size and phase control of nanocrystalline TiO₂ in three Ti-Si oxide structures. *J. Mater. Sci.* **2008**, *43* (6), 1979-1986.
79. Prasad, G. K.; Singh, B.; Ganesan, K.; Batra, A.; Kumeria, T.; Gutch, P. K.; Vijayaraghavan, R., Modified titania nanotubes for decontamination of sulphur mustard. *J. Hazard. Mater.* **2009**, *167* (1-3), 1192-1197.
80. El-Bahy, Z. M.; Ismail, A. A.; Mohamed, R. M., Enhancement of titania by doping rare earth for photodegradation of organic dye (Direct Blue). *J. Hazard. Mater.* **2009**, *166* (1), 138-143.
81. Choi, W.; Termin, A.; Hoffmann, M. R., The role of metal ion dopants in quantum-sized TiO₂: correlation between photoreactivity and charge carrier recombination dynamics. *J. Phys. Chem.* **1994**, *98* (51), 13669-79.
82. Wang, C.; Ao, Y.; Wang, P.; Hou, J.; Qian, J.; Zhang, S., Preparation, characterization, photocatalytic properties of titania hollow sphere doped with cerium. *J. Hazard. Mater.* **2010**, *178* (1-3), 517-521.
83. Reddy, B. M.; Ganesh, I.; Khan, A., Stabilization of nanosized titania-anatase for high temperature catalytic applications. *J. Mol. Catal. A: Chem.* **2004**, *223* (1-2), 295-304.

84. Joshi, M. M.; Labhsetwar, N. K.; Mangrulkar, P. A.; Tijare, S. N.; Kamble, S. P.; Rayalu, S. S., Visible light induced photoreduction of Methyl orange by N-doped mesoporous titania. *Appl. Catal., A* **2009**, *357* (1), 26-33.
85. Schubert, G.; Bansagi, T.; Solymosi, F., Photocatalytic Decomposition of Methyl Formate Over TiO₂-Supported Pt Metals. *J. Phys. Chem. C*, Ahead of Print.
86. Asahi, R.; Morikawa, T.; Ohwaki, T.; Aoki, K.; Taga, Y., Visible-light photocatalysis in nitrogen-doped titanium oxides. *Science (Washington, DC, U. S.)* **2001**, *293* (5528), 269-271.
87. Dong, L.; Cao, G.-x.; Ma, Y.; Jia, X.-l.; Ye, G.-t.; Guan, S.-k., Enhanced photocatalytic degradation properties of nitrogen-doped titania nanotube arrays. *Trans. Nonferrous Met. Soc. China* **2009**, *19* (6), 1583-1587.
88. Yu, J. C.; Yu, J. G.; Ho, W. K.; Jiang, Z. T.; Zhang, L. Z., Effects of F- Doping on the Photocatalytic Activity and Microstructures of Nanocrystalline TiO₂ Powders. *Chem. Mater.* **2002**, *14* (9), 3808-3816.
89. Sakthivel, S.; Kisch, H., Daylight photocatalysis by carbon-modified titanium dioxide. *Angew. Chem., Int. Ed.* **2003**, *42* (40), 4908-4911.
90. Sakthivel, S.; Kisch, H., Photocatalytic and photoelectrochemical properties of nitrogen-doped titanium dioxide. *ChemPhysChem* **2003**, *4* (5), 487-490.
91. Ang, T. P.; Toh, C. S.; Han, Y.-F., Synthesis, Characterization, and Activity of Visible-Light-Driven Nitrogen-Doped TiO₂-SiO₂ Mixed Oxide Photocatalysts. *J. Phys. Chem. C* **2009**, *113* (24), 10560-10567.

92. Ni, M.; Leung, M. K. H.; Leung, D. Y. C.; Sumathy, K., A review and recent developments in photocatalytic water-splitting using for hydrogen production. *Renewable and Sustainable Energy Reviews* **2007**, *11* (3), 401-425.
93. Raj, K. J. A.; Ramaswamy, A. V.; Viswanathan, B., Surface Area, Pore Size, and Particle Size Engineering of Titania with Seeding Technique and Phosphate Modification. *J. Phys. Chem. C* **2009**, *113* (31), 13750-13757.
94. Yan, J.; Tang, Z.; Zhang, Z.; Zhou, Z., Highly active rutile TiO₂ for photocatalysis. *Xiyou Jinshu Cailiao Yu Gongcheng* **2006**, *35* (Suppl. 3), 396-399.
95. Chen, Y.; Lin, A.; Gan, F., Preparation of nano-TiO₂ from TiCl₄ by dialysis hydrolysis. *Powder Technol.* **2006**, *167* (3), 109-116.
96. Jia, H.; Zheng, Z.; Zhao, H.; Zhang, L.; Zou, Z., Nonaqueous sol-gel synthesis and growth mechanism of single crystalline TiO₂ nanorods with high photocatalytic activity. *Mater. Res. Bull.* **2009**, *44* (6), 1312-1316.
97. Lee, J. H.; Yang, Y. S., Synthesis of TiO₂ nanoparticles with pure brookite at low temperature by hydrolysis of TiCl₄ using HNO₃ solution. *J. Mater. Sci.* **2006**, *41* (2), 557-559.
98. Zhang, R.; Elzatahry, A. A.; Al-Deyab, S. S.; Zhao, D., Mesoporous titania: From synthesis to application. *Nano Today* *7* (4), 344-366.
99. Mahmoodi, N. M.; Arami, M., Degradation and toxicity reduction of textile wastewater using immobilized titania nanophotocatalysis. *J. Photochem. Photobiol., B* **2009**, *94* (1), 20-24.
100. Prairie, M. R.; Evans, L. R.; Martinez, S. L., Destruction of organics and removal of heavy metals in water via TiO₂ photocatalysis. *Chem. Oxid.* **1994**, *2*, 428-41.

101. Matthews, R. W.; McEvoy, S. R., Photocatalytic degradation of phenol in the presence of near-UV illuminated titanium dioxide. *J. Photochem. Photobiol., A* **1992**, *64* (2), 231-46.
102. Sclafani, A.; Palmisano, L.; Schiavello, M., Influence of the preparation methods of titanium dioxide on the photocatalytic degradation of phenol in aqueous dispersion. *J. Phys. Chem.* **1990**, *94* (2), 829-32.
103. Davis, M. E., Ordered porous materials for emerging applications. *Nature* **2002**, *417* (6891), 813-21.
104. Liu, G.; Zhao, Y.; Sun, C.; Li, F.; Lu, G. Q.; Cheng, H.-M., Synergistic effects of B/N doping on the visible-light photocatalytic activity of mesoporous TiO₂. *Angew. Chem., Int. Ed.* **2008**, *47* (24), 4516-4520.
105. Dai, K.; Peng, T.; Chen, H.; Zhang, R.; Zhang, Y., Photocatalytic Degradation and Mineralization of Commercial Methamidophos in Aqueous Titania Suspension. *Environ. Sci. Technol.* **2008**, *42* (5), 1505-1510.
106. Dai, K.; Peng, T.; Chen, H.; Liu, J.; Zan, L., Photocatalytic degradation of commercial phoxim over lanthanum-doped titanium oxide nanoparticles in aqueous suspension. *Environ. Sci. Technol.* **2009**, *43* (5), 1540-1545.
107. Cao, Y.; Yi, L.; Huang, L.; Hou, Y.; Lu, Y., Mechanism and Pathways of Chlorfenapyr Photocatalytic Degradation in Aqueous Suspension of TiO₂. *Environ. Sci. Technol.* **2006**, *40* (10), 3373-3377.
108. Konstantinou, I. K.; Sakellariades, T. M.; Sakkas, V. A.; Albanis, T. A., Photocatalytic degradation of selected s-triazine herbicides and organophosphorus insecticides over aqueous TiO₂ suspensions. *Environ. Sci. Technol.* **2001**, *35* (2), 398-405.

109. Vulliet, E.; Emmelin, C.; Chovelon, J.-M.; Guillard, C.; Herrmann, J.-M., Photocatalytic degradation of sulfonylurea herbicides in aqueous TiO₂. *Appl. Catal., B* **2002**, *38* (2), 127-137.
110. Parra, S.; Olivero, J.; Pulgarin, C., Relationships between physicochemical properties and photoreactivity of four biorecalcitrant phenylurea herbicides in aqueous TiO₂ suspension. *Appl. Catal., B* **2002**, *36* (1), 75-85.
111. Hoffmann, M. R.; Martin, S. T.; Choi, W.; Bahnemann, D. W., Environmental Applications of Semiconductor Photocatalysis. *Chem. Rev. (Washington, D. C.)* **1995**, *95* (1), 69-96.
112. Fox, M. A.; Dulay, M. T., Heterogeneous photocatalysis. *Chem. Rev.* **1993**, *93* (1), 341-57.
113. Fujishima, A.; Kohayakawa, K.; Honda, K., Hydrogen production under sunlight with an electrochemical photocell. *J. Electrochem. Soc.* **1975**, *122* (11), 1487-9.
114. Zhang, Z.; Zuo, F.; Feng, P., Hard template synthesis of crystalline mesoporous anatase TiO₂ for photocatalytic hydrogen evolution. *J. Mater. Chem.* *20* (11), 2206-2212.
115. Fujihara, K.; Ohno, T.; Matsumura, M., Splitting of water by electrochemical combination of two photocatalytic reactions on TiO₂ particles. *J. Chem. Soc., Faraday Trans.* **1998**, *94* (24), 3705-3709.
116. Yoshida, H.; Hirao, K.; Nishimoto, J.-i.; Shimura, K.; Kato, S.; Itoh, H.; Hattori, T., Hydrogen Production from Methane and Water on Platinum Loaded Titanium Oxide Photocatalysts. *J. Phys. Chem. C* **2008**, *112* (14), 5542-5551.
117. Sreethawong, T.; Suzuki, Y.; Yoshikawa, S., Synthesis, characterization, and photocatalytic activity for hydrogen evolution of nanocrystalline mesoporous titania

- prepared by surfactant-assisted templating sol-gel process. *J. Solid State Chem.* **2005**, *178* (1), 329-338.
118. Zukalova, M.; Zukal, A.; Kavan, L.; Nazeeruddin, M. K.; Liska, P.; Graetzel, M., Organized Mesoporous TiO₂ Films Exhibiting Greatly Enhanced Performance in Dye-Sensitized Solar Cells. *Nano Lett.* **2005**, *5* (9), 1789-1792.
119. Nedelcu, M.; Lee, J.; Crossland, E. J. W.; Warren, S. C.; Orilall, M. C.; Guldin, S.; Huettner, S.; Ducati, C.; Eder, D.; Wiesner, U.; Steiner, U.; Snaith, H. J., Block copolymer directed synthesis of mesoporous TiO₂ for dye-sensitized solar cells. *Soft Matter* **2009**, *5* (1), 134-139.
120. Zhang, J.; Deng, Y.; Gu, D.; Wang, S.; She, L.; Che, R.; Wang, Z.-S.; Tu, B.; Xie, S.; Zhao, D., Ligand-assisted assembly approach to synthesize large-pore ordered mesoporous titania with thermally stable and crystalline framework. *Adv. Energy Mater.* **2011**, *1* (2), 241-248.
121. Varghese, O. K.; Gong, D.; Paulose, M.; Ong, K. G.; Grimes, C. A., Hydrogen sensing using titania nanotubes. *Sens. Actuators, B* **2003**, *93* (1-3), 338-344.
122. Devi, G. S.; Hyodo, T.; Shimizu, Y.; Egashira, M., Synthesis of mesoporous TiO₂-based powders and their gas-sensing properties. *Sens. Actuators, B* **2002**, *87* (1), 122-129.
123. Wang, K.; Wei, M.; Morris, M. A.; Zhou, H.; Holmes, J. D., Mesoporous titania nanotubes: their preparation and application as electrode materials for rechargeable lithium batteries. *Adv. Mater. (Weinheim, Ger.)* **2007**, *19* (19), 3016-3020.
124. Yoon, S.; Manthiram, A., Hollow Core-Shell Mesoporous TiO₂ Spheres for Lithium Ion Storage. *J. Phys. Chem. C* **2011**, *115* (19), 9410-9416.

125. Zhao, S.; Ramakrishnan, G.; Shen, P.; Su, D.; Orlov, A., The first experimental demonstration of beneficial effects of sub-nanometer platinum particles for photocatalysis. *Chem. Eng. J. (Amsterdam, Neth.)* **2013**, *217*, 266-272.
126. Hayden, B. E.; Pletcher, D.; Suchsland, J.-P.; Williams, L. J., The influence of support and particle size on the platinum catalysed oxygen reduction reaction. *Phys. Chem. Chem. Phys.* **2009**, *11* (40), 9141-9148.
127. Hayden, B. E.; Pletcher, D.; Suchsland, J.-P.; Williams, L. J., The influence of Pt particle size on the surface oxidation of titania supported platinum. *Phys. Chem. Chem. Phys.* **2009**, *11* (10), 1564-1570.
128. Elezovic, N. R.; Babic, B. M.; Radmilovic, V. R.; Vracar, L. M.; Krstajic, N. V., Novel Pt catalyst on ruthenium doped TiO₂ support for oxygen reduction reaction. *Appl. Catal., B* **2013**, *140-141*, 206-212.
129. Green, I. X.; McEntee, M.; Tang, W.; Neurock, M.; Yates, J. T., Jr., Direct formation of acetate from partial oxidation of ethylene on a Au/TiO₂ catalyst. *Top. Catal.* **2013**, *56* (15-17), 1512-1524.
130. Li, C.; Liu, J.; Gao, W.; Zhao, Y.; Wei, M., Ce-Promoted Rh/TiO₂ Heterogeneous Catalysts Towards Ethanol Production from Syngas. *Catal. Lett.*, Ahead of Print.
131. Ishihara, T.; Shigeta, K.; Ooishi, Y.; Matsuka, M.; Hagiwara, H.; Ida, S., Effects of fluorinated hydrocarbon addition on H₂O₂ direct synthesis from H₂ and air over an Au-Pd bimetallic catalyst supported on rutile-TiO₂. *Catal. Sci. Technol.* **2013**, *3* (11), 2971-2975.

132. Shi, F.; Baker, L. R.; Hervier, A.; Somorjai, G. A.; Komvopoulos, K., Tuning the electronic structure of titanium oxide support to enhance the electrochemical activity of platinum nanoparticles. *Nano Lett.* **2013**, *13* (9), 4469-4474.
133. Shimura, K.; Miyazawa, T.; Hanaoka, T.; Hirata, S., Fischer-Tropsch synthesis over TiO₂ supported cobalt catalyst: Effect of TiO₂ crystal phase and metal ion loading. *Appl. Catal., A* **2013**, *460-461*, 8-14.

Chapter 2: Characterization Techniques

2.1 Introduction

Catalyst materials, specifically nano catalyst materials, have interesting properties that are often linked to the material structure, including crystallite and agglomerate size, morphology, surface area, porosity, crystal phase, and electronic structure. For example, zeolites are excellent molecular sieves because of their porous nature, anatase TiO_2 is an excellent photocatalyst because of its band gap energy, and Au is catalytically active at small crystallite sizes of approximately 2 nm or less. Structural analysis is therefore essential in determining suitable applications for materials. Relating material properties to structural characteristics also enables researchers to understand catalytic performance and design improved catalysts and catalyst supports.

In this work, X-ray diffraction, X-ray absorption spectroscopy, and transmission electron microscopy were used to study the crystal structure, crystal size and phase, morphology, relative position of neighboring atoms, the identity and oxidation state of nearest neighbor atoms, and the coordination numbers and geometry of atoms in the structure. Physisorption and chemisorption techniques were used to study surface properties and porosity including the surface area, active metal surface area, pore diameter/width, pore geometry, and metal dispersion. In this chapter, a brief overview of these techniques is presented. This review is meant as a general introduction to these techniques and the included references should be referred to for more information on each technique.

2.2 X-ray Diffraction

X-ray diffraction (XRD) is one of the primary methods available to determine atomic structure, including crystallite size, phase, and phase composition. It is a nondestructive technique that is relatively fast and easy compared with techniques that give similar information such as transmission electron microscopy (TEM) (crystallite phase and size) and N₂ sorption (crystallite size estimated from surface area).

In XRD, a crystalline sample is bombarded by X-rays (produced by high speed electrons colliding with a metal source) as it is rotated through different angles. The intensity of X-rays scattered by electrons bound to atoms is measured, with waves canceling each other out in many directions through destructive interference. Due to the repeating array of atoms in crystalline materials, some waves will interfere with one another constructively and diffraction is observed. Each crystal structure is unique, with specific d-spacings for planes of atoms. X-rays are used to produce diffraction patterns because the wavelength of X-rays is comparable to the spacing between atomic planes in crystalline materials (1 – 100 Å).¹ Therefore, specific diffraction lines corresponding to particular angles are recorded when cones of diffracted beams intersect a detector. By comparing standard diffraction patterns to the intensity of diffraction lines and angles at which diffraction lines occur, the crystal phase of a sample can be determined (Figure 2.1).

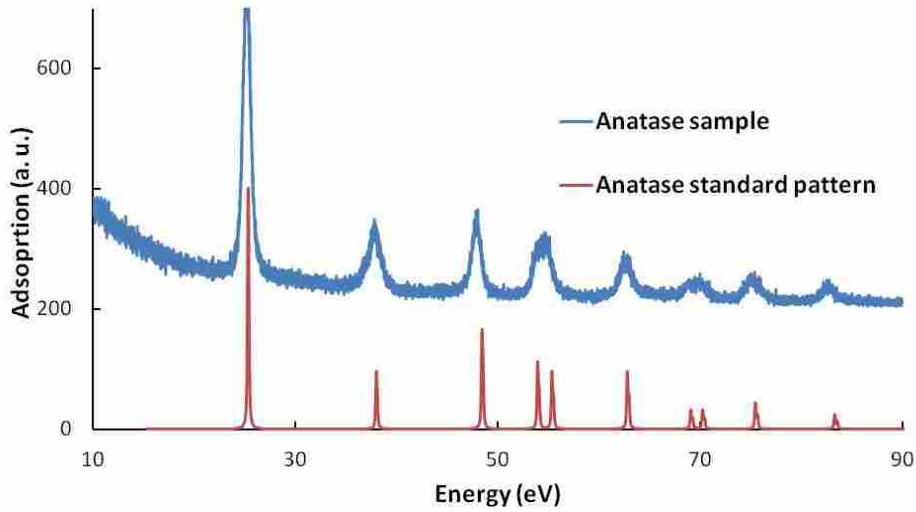


Figure 2.1 XRD patterns of anatase TiO_2 . Blue = experimental data and Red = a standard anatase pattern.

Crystalline solids are built of unit cells (the smallest repeating volume) which repeat in 3-dimensions to create a lattice. The lattice is defined by basis vectors \mathbf{a} , \mathbf{b} , and \mathbf{c} , and any point in the lattice may be described by the vector \mathbf{r} .²

$$\mathbf{r} = n_1\mathbf{a} + n_2\mathbf{b} + n_3\mathbf{c} \quad \text{Eq 2.1}$$

The unit cell is characterized by three lattice constants a , b , and c (the lengths of the basis vectors), and by three angles α (angle between \mathbf{b} and \mathbf{c}), β (angle between \mathbf{a} and \mathbf{c}), and γ (angle between \mathbf{a} and \mathbf{b}). The positions of atoms in the lattice can be described by the axis defined by the basis vectors \mathbf{a} , \mathbf{b} , and \mathbf{c} . Atom positions are then given in terms of

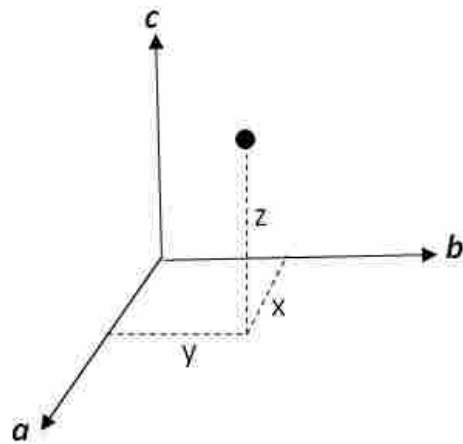


Figure 2.2 Atomic parameters in terms of the basis vectors.

fractional lattice constants a , b , and c (described in terms of x , y , and z coordinates). For example an atom in the center of the unit cell would be described as $(\frac{1}{2}, \frac{1}{2}, \frac{1}{2})$ (Figure 2.2).²

A simple crystal can be imagined with each unit cell containing one atom. The path difference between waves scattered by two lattice points along the a axis would therefore be defined as in the Laue equation, Eq 2.2.

$$a \cos\mu_\alpha + a \cos\theta_\alpha = n_1\lambda \tag{Eq 2.2}$$

Where a = distance between points, μ_a = angle of incidence, and θ_a = angle of scattering.

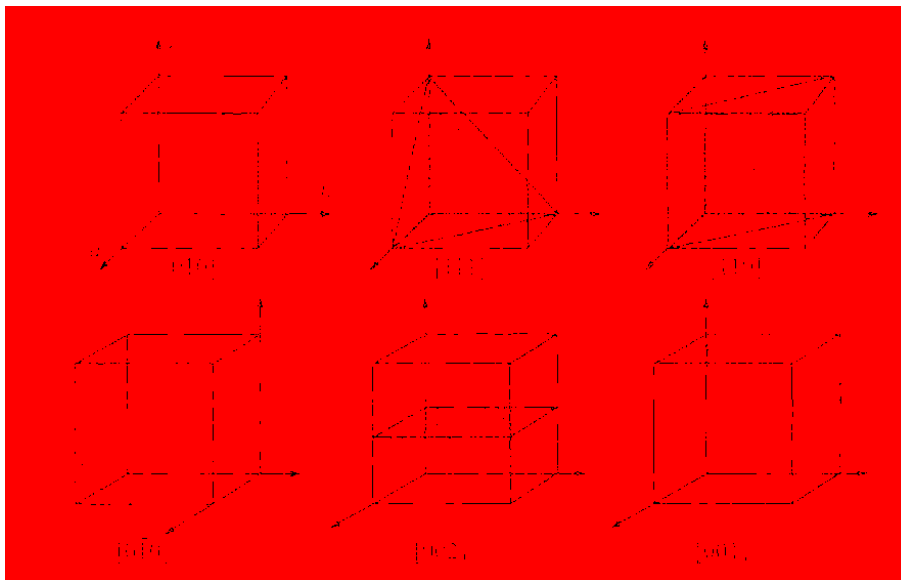


Figure 2.3 The Miller indices of some planes in cubic crystals. Image adapted from Rajagopal.⁴

For a row of points, for any defined μ_a and n_1 , scattered waves will be observed at a specific scattering angle. Because waves will be scattered in all directions, cones (with a half angle θ_a) are formed around the row of points,

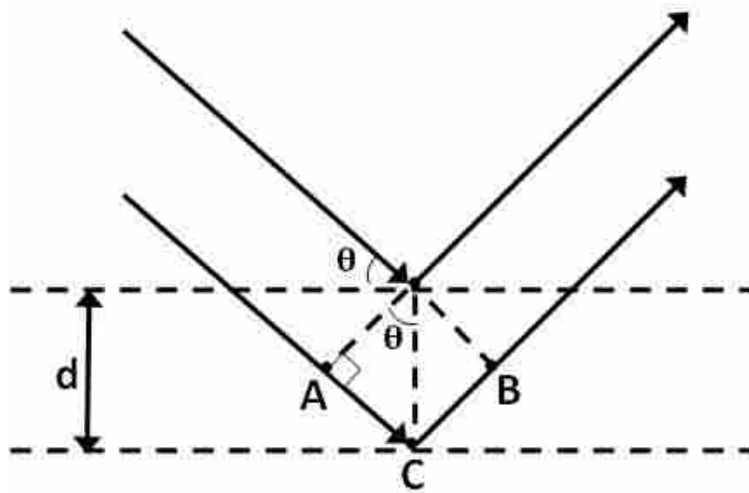
with one cone for each value of n . In a 3-dimensional system, X-rays will interact with rows of atoms along the a , b , and, c axes to create coaxial cones. Diffraction is observed when three Laue cones, one from each of the a , b , and, c axes, intersect each other in a single line (conditions for three Laue equations are met simultaneously).^{2,3} The planes that give rise to these diffractions

are known as lattice planes, and are defined by *Miller indices* with the values hkl (Figure 2.3).⁴ The hkl values relate the orientation of the lattice plane to the axis defined by the basis vectors \mathbf{a} , \mathbf{b} , and \mathbf{c} .

For constructive interference to occur (a) the angle of incidence must equal the angle of reflection, (b) this angle must have a value such that the three Laue equations for axes \mathbf{a} , \mathbf{b} , and \mathbf{c} are met, and (c) the entire set of lattice planes must scatter in phase. In 1913, physicists W. H. Bragg and W. L. Bragg (his son) developed the Bragg equation, Eq 2.3, to describe the angles at which diffraction will occur.⁵

$$n\lambda = 2d \sin\theta \quad \text{Eq 2.3}$$

d = distance between planes of atoms in the lattice, λ = wavelength of incident X-ray beam, n = integer



As shown in Figure 2.4, in order for waves reflected from different planes to be in phase and constructive interference to occur, the extra distance traveled by waves penetrating deeper into the structure must be an integral multiple of the wavelength. Therefore, using Bragg's law (Eq 2.3), the angles at

Figure 2.4 Illustration of X-rays reflected by lattice planes and the geometry used to derive Bragg's law.

which diffraction occurs for each set of lattice planes (hkl) can be determined.

Each set of lattice planes can be defined by Miller indices. Additionally, it is often useful to describe lattice planes in three dimensions using a vector \mathbf{d} , with a length related to the spacing of the lattice planes. In the case of a simple orthorhombic system, \mathbf{d} can be defined by Eq 2.4.^{2,3}

$$1/d^2 = h^2/a^2 + k^2/b^2 + l^2/c^2. \quad \text{Eq 2.4}$$

This can be further simplified if the equation is in the form of

$$d^{*2} = h^2 a^{*2} + k^2 b^{*2} + l^2 c^{*2} \quad \text{Eq 2.5}$$

With $d^* = 1/d$, $a^* = 1/a$, $b^* = 1/b$, and $c^* = 1/c$

A new coordinate system, called the reciprocal lattice, can thus be defined by basis vectors \mathbf{a}^* , \mathbf{b}^* , and \mathbf{c}^* which are normal to lattice planes in the direct lattice. Each set of lattice planes in the direct lattice corresponds to a vector in the reciprocal lattice. The reciprocal lattice was developed to represent what happens physically when crystals diffract. Just as the direct or real lattice describes the arrangement of unit cells in the crystal, the reciprocal lattice describes an array of points that correspond to a set of lattice planes in the crystal. Figure 2.5 shows a representation of the reciprocal lattice, where d^*_{hkl} vectors are described by points. Using d^* , the Bragg equation can be restated as in Eq 2.6.

$$\sin \theta = \frac{d^*/2}{1/\lambda} \quad \text{Eq 2.6}$$

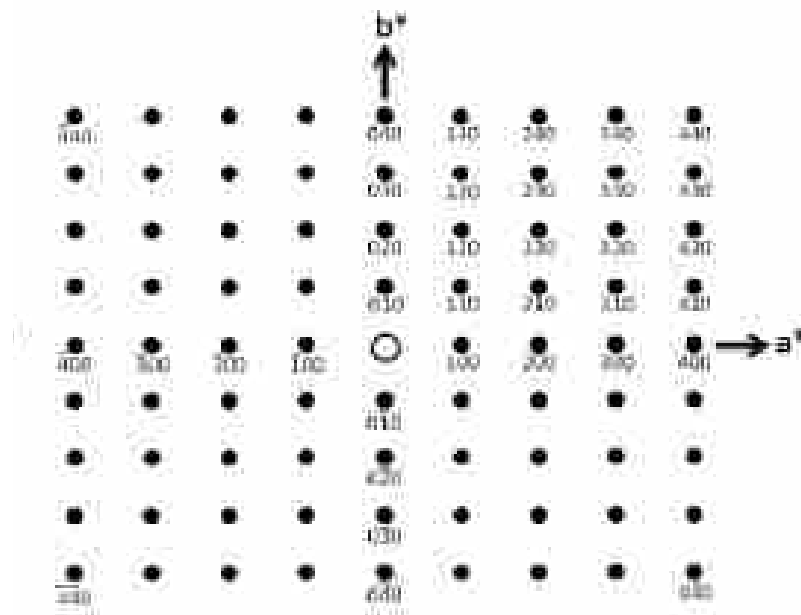


Figure 2.5 Plot of the reciprocal lattice with the vectors represented as points. Image adapted from Jenkins and Snyder.⁶

The relationship between the direct lattice and the reciprocal lattice was introduced and further discussed by Ewald in 1913 and 1921 using Ewald's sphere, a construct useful for further visualizing diffraction.^{7,8} An imaginary sphere of radius $1/\lambda$ is centered such that a beam of X-rays passes through the center of the sphere and the origin of the reciprocal lattice is placed on the edge of the sphere. The Bragg equation is satisfied when reciprocal lattice points fall on the surface of the Ewald sphere. As seen in Figure 2.6, rotating the crystal through different angles brings different sets of lattice planes into reflecting positions. Therefore, this sphere can be used to determine which lattice planes will be in a reflecting position at specific 2θ angles. The reflections at many 2θ angles are measured and recorded to create a diffraction pattern. Because the reciprocal lattice is directly related to the real crystal lattice, by measuring and recording the

reflections at many 2θ angles the structure of the real crystal can be determined.^{3,9}

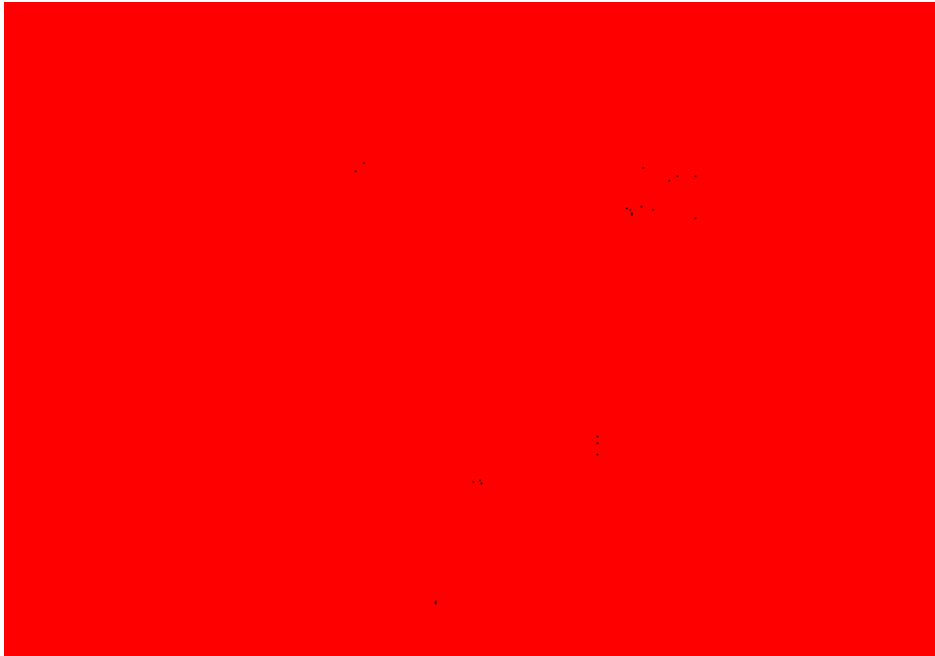


Figure 2.6 Ewald's sphere. O = the origin of the reciprocal lattice, K_1 = wave vector of the incident wave, k_D = wave vector of the diffracted wave. When one or more points in the reciprocal lattice fall on the surface of the Ewald sphere, the Bragg condition is satisfied and diffraction is observed. Image adapted from Williams and Carter.¹⁰

Unlike in bulk or well-ordered single crystals, nanoparticles have fewer unit cells, resulting in incomplete destructive interference of the reflected beams at angles near the Bragg angle. This is manifest in broader peaks in the diffraction patterns of nanomaterials, with the degree of broadening increasing as the crystallite size decreases. As long as size-related broadening is larger than instrumental broadening, the Scherrer formula¹¹ (Eq 2.7) can be used to estimate the average crystallite diameter from each peak.

$$d = \frac{K\lambda}{w \cos\theta} \quad \text{Eq 2.7}$$

Where K = a dimensionless shape factor (0.9 in this study), λ = wavelength of incident X-rays, w = peak width at half of the maximum height (full width at half maximum, FWHM,) and θ = the Bragg angle (angle of reflection)

It is important to note that while broad peaks with low intensities may be due to amorphism, they may also be due to small crystallite sizes (peak broadening). Transmission electron microscopy (TEM) can be used to verify crystallinity.

2.3 X-ray Absorption Spectroscopy

X-ray absorption spectroscopy (XAS) is a technique used for structure investigation. Many properties are determined by the interactions between neighboring atoms, and it is therefore important to know the relative positions of atoms close enough to interact, the identity and oxidation state of nearest neighbor atoms, and the coordination numbers and geometry of atoms in the structure.¹² XAS is particularly useful in examination of nanomaterials and can be used to gain insight into the structure of doped nanomaterials, the bonding between metal atoms in well-dispersed clusters, and the bonding between metal clusters and high surface area catalyst supports.

XAS was observed by several researchers in the early 1900's and many attempts to explain the experimental data were made. The interpretation of XAS theory published by Kronig in the early 1930s¹³ contains the basic concepts used in today's interpretations, but it was not until approximately 1970 that enough was known to use the technique for quantitative structure determination. Today, this technique can be used to obtain structural information such as bond

angles, oxidation states, coordination numbers,¹⁴⁻¹⁶ and the type and number of nearest neighbors¹⁷ in gases, liquids, and solids (amorphous or crystalline, buried or surface atoms).

XAS is the measurement of the X-ray absorption coefficient versus energy. XAS is element specific; each element has a set of unique absorption edges corresponding to the binding energies of its electrons. Scanning a few KeV before an absorption edge, a spectrum is collected and when the energy of the X-rays matches the binding energy of the electrons in the sample, photons are absorbed and the absorbance signal rapidly increases. When the X-ray is absorbed, a core electron is ejected and can interact with electrons in neighboring atoms. In XAS, electrons are treated as having a wave-like nature surrounded by point scatters (other atoms). The oscillations in the spectra are created by backscattered waves interfering with forward-propagating waves. The Fourier transform of the oscillations gives information on coordination, bond lengths, and oxidation states (Figure 2.7). XAS studies are done at synchrotron sources because this technique requires a tunable beam (tuned to the absorption edge of interest) with high intensity (flux > 10^6 /sec). Since synchrotrons produce brilliant X-rays, it is possible to look at low (ppm) concentrations of the absorbing element.

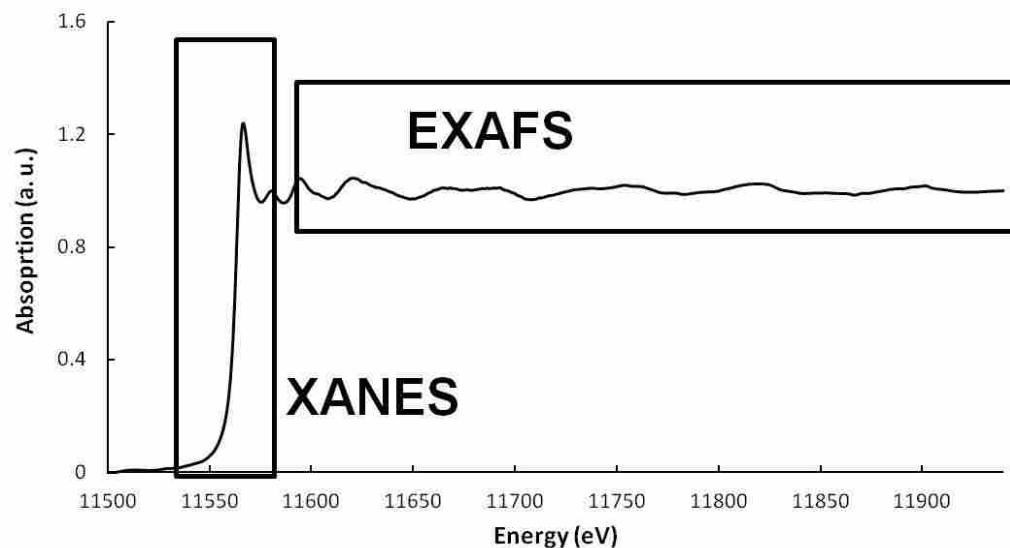


Figure 2.7 X-ray absorption spectrum of Pt metal.

As previously mentioned, XAS is element specific and there are several absorption edges for each element corresponding to the different shells of electrons such as the K and L-edges. The K edge corresponds to a 1s core electron s to p transition, the L1 edge corresponds to a 2s core electron s to p transition, and the L2 edge corresponds to a p to d transition. The edge results from dipole allowed transitions and is therefore very intense. The pre-edge results from mixing p and d orbitals or from quadrupolar allowed transitions that tend to be low in intensity. As seen from the Ti and Pt data below, the various edges occur at different energies and provide some experimental flexibility; you can choose which edge to use based on the energy range of the X-ray beam.

Data for Ti; Z = 22

K-edge at: 4.96500015 KeV

L-edges at: 0.531000018, 0.461199999, 0.453799993 KeV

Data for Pt; Z = 78

K-edge at: 78.3949966 KeV

L-edges at: 13.8920002, 13.2729998, 11.5640001 KeV

XAS spectra are often divided into two regions: X-ray absorption near edge structure (XANES) and extended X-ray absorption fine structure (EXAFS) (Figure 2.7).¹² XANES (sometimes called near edge X-ray absorption spectroscopy (NEXAFS), though this term generally refers to low Z elements), is the part of the spectrum within approx 50eV of the absorption edge (includes pre-edge, edge, and 50eV after the edge) (Figure 2.8). The absorption peaks in XANES are due to multiple scattering events and due to these effects, XANES analysis was developed after EXAFS analysis and is still not fully understood today. Despite these difficulties, XANES is becoming a widely accepted technique for structure analysis, with Scifinder showing several hundred publications a year since the early 1990s. The wiggles approx 150 eV after the edge comprise the EXAFS portion of the spectrum.

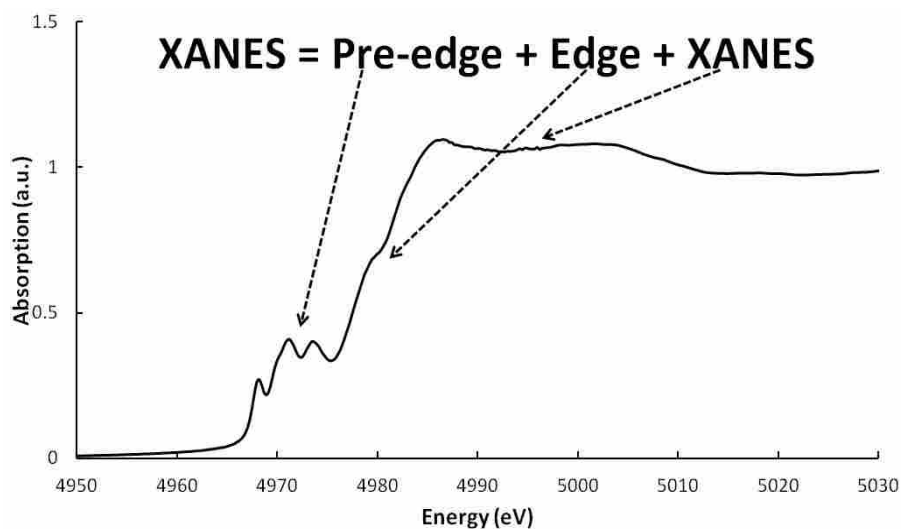


Figure 2.8 XANES spectrum of TiO₂.

XANES is easier to crudely interpret than EXAFS and can be used to determine the geometry, coordination, and oxidation state of the absorbing element, and to gain insight into the

hybridization of the molecular orbitals, the band structure, and how the electron scatters. EXAFS is easier to fully interpret than XANES and can be used to determine distances between and sometimes even types of nearest neighbors. Together these techniques can be used to determine the crystal structures of doped nanomaterials.

2.3.1 XANES

The XANES pre-edge arises due to electronic transitions to empty bound states (probability of a transition is determined by selection rules) and gives information on coordination and geometry of the absorbing element. It is sensitive enough that many elements of the same oxidation state will show significantly different pre-edges for various coordination numbers (Figure 2.9).

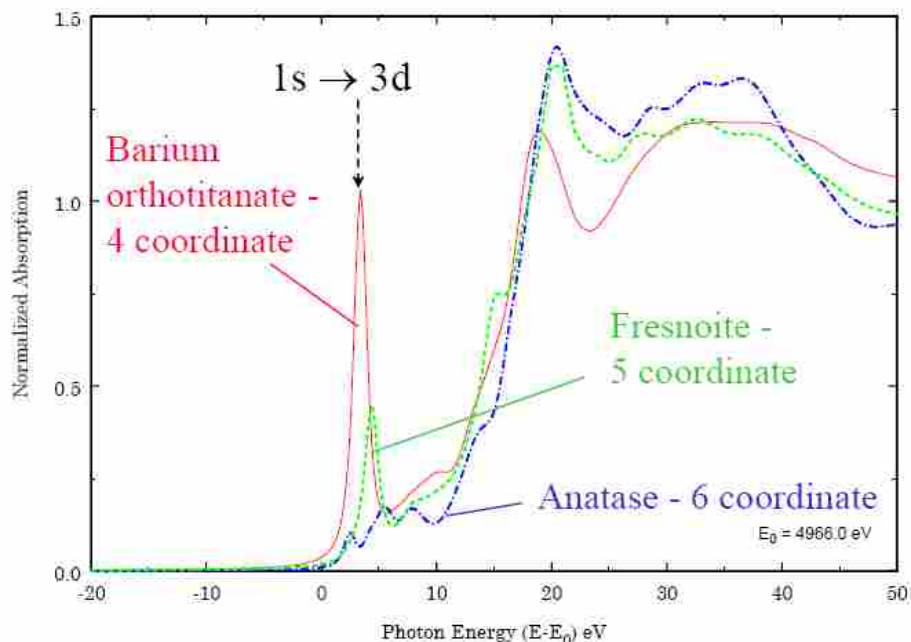


Figure 2.9 XANES spectra of 4, 5, and 6-coordinate Ti. Image adapted from the EXAFS data collection and analysis course, APS, 2005.

XANES is also used to determine the oxidation state of the element. Berengren¹⁸ observed in 1920 that the edge shift (the binding energy shift) is dependent on the oxidation state and generally the edge shifts to higher energies (1 – 5 eV per oxidation number change) as the oxidation state increases. In addition to the energy shift, the intensity of the pre-edge varies with oxidation state. For elements with full subshells such as Ag and Au, very low intensity or almost no peak will be observed. As the oxidation number increases, the intensity increases (Figure 2.10). The pre-edge is also useful for observing metal-ligand bonding since peaks arising from the ligand will appear in the pre-edge, allowing it to be used as a fingerprint to detect certain chemical species.

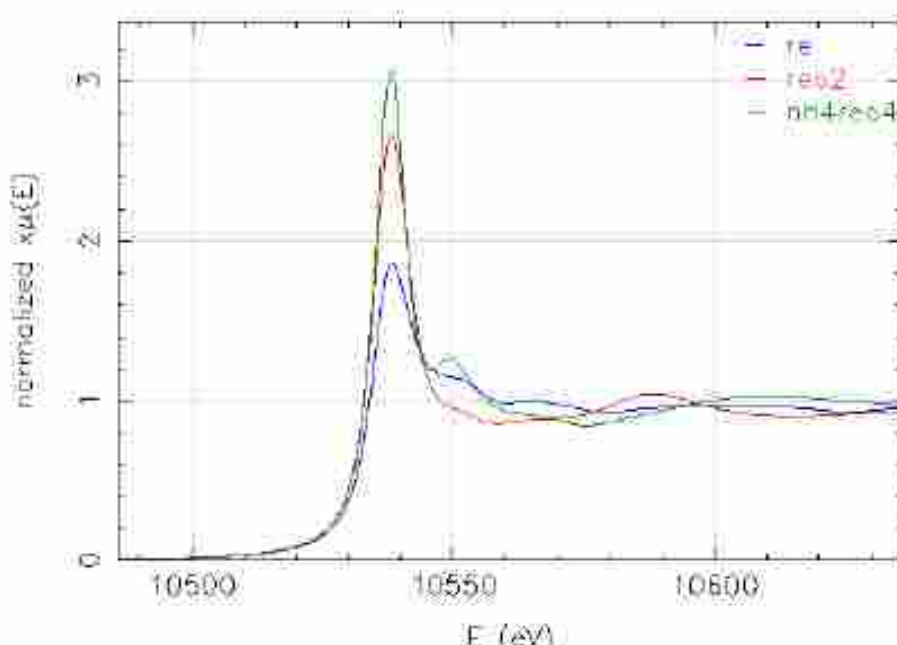


Figure 2.10 XANES spectra of Re metal (R^0), ReO_2 (R^{4+}), and NH_4ReO_4 (Re^{7+}). EXAFS data collection and analysis course, APS, 2005.

The wiggles after the absorption edge can be used to obtain information about the atomic positions (bond angles and distances) of neighboring atoms and it is essential to collect spectra of

standards with known coordination numbers and oxidation states to compare to the samples. Using linear combinations, the amount of the element in each oxidation state/coordination can be quantitatively determined relatively easily. It is possible to generate model structures and use ab initio calculations (Feff), but there are many difficulties associated with this and it is generally attempted only by experts, who often report it is difficult to interpret XANES spectra accurately, precisely, and reliably. While complete spectral interpretation is extremely complex, the XANES spectra are often easily interpreted qualitatively (much easier than EXAFS data) and linear combinations of standards are often sufficient for quantitative analysis as well. Despite the difficulties in data analysis, XANES is popular because it is generally easier to get high quality XANES data compared to EXAFS data (sample thickness is less of a concern, data collection time is faster because you do not need to collect the entire spectrum), and, because XANES has a larger signal than EXAFS, lower concentrations can be examined.

2.3.2 EXAFS

The EXAFS portion of the spectrum, the ‘wiggles’ approx 150 eV after the edge, arises from single backscattering events.

EXAFS data is used to determine inter-atomic distances (atomic pair distribution) between neighboring atoms as well as coordination

numbers. A basic XAS experimental setup is pictured in Figure 2.11.

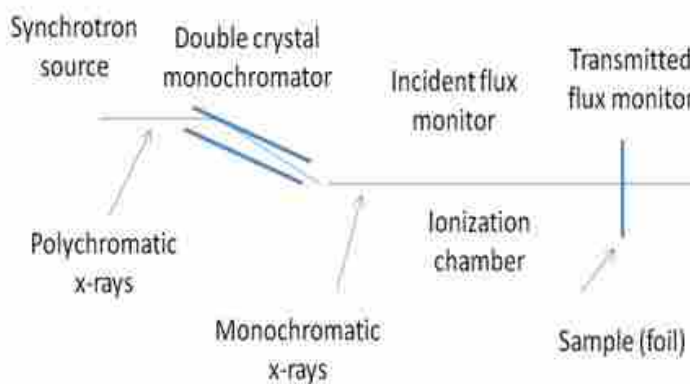


Figure 2.11 XAS experimental setup, transmission mode.

To collect EXAFS data you first identify and tune the beam to the energy of the edge for the element of interest using Eq 2.8.

$$E = \frac{-Z^2 \cdot \text{Rydberg}}{n^2} \quad \text{Eq 2.8}$$

Next, the absorption coefficient is calculated as in Eq 2.9.

$$\mu \propto |\langle f | \vec{\epsilon} \cdot \vec{r} | i \rangle|^2 \quad \text{Eq 2.9}$$

$$\Delta l = \pm 1$$

Then the electron wave number relates to X-ray photon energy by Eq 2.10.

$$E - E_0 = \frac{\hbar^2 \cdot k^2}{2 \cdot m} \quad \text{Eq 2.10}$$

Though the EXAFS phenomenon has been known and basically understood for more than 50 years, it was not until the 1970s that Stern, Sayers, and Lytle were able to make assumptions to derive the EXAFS equation, Eq 2.11.^{19, 20}

$$\chi(k) = \sum_i \chi_i(k)$$

$$\chi_i(k) = \left[\frac{(N_i S_0^2 F_i(k))}{k R_i^2} \cdot \sin(2k R_i + \varphi_i(k)) \cdot e^{(-2\sigma_i^2 k^2)} \cdot e^{\left(\frac{-2R_i}{\lambda(k)}\right)} \right] \quad \text{Eq 2.11}$$

$R_i = R_0 + \Delta R$

$k_2 = 2 m_e(E-E_0)/\hbar$

$F_i(k)$ = effective scattering amplitude

N_i = degeneracy of path

$\varphi_i(k)$ = effective scattering phase shift

S_0^2 = passive electron reduction factor

$\lambda(k)$ = mean free path

E_0 = energy shift

R_0 = initial path length

σ_i^2 = mean squared displacement

ΔR = change in half-path length

As with XANES, the simplest way of analyzing EXAFS data is to collect spectra of standards for comparison using linear combinations. It is also possible to model the data to determine the structure. To produce a theoretical model you must have a value for each variable for every path and computer programs can give estimates of where to start.

XANES data fitting can be done (using the Athena and Artemis free programs) by normalizing the spectra and using linear combinations of experimentally measured standards. Phase shifts, backscattering amplitudes, and XANES references should be obtained from reference compounds. EXAFS data can be extracted based on standard procedures (using the WINXAS97 software) including correcting for instrumental errors, determining the background, normalizing the pre and post edges, determining the edge step, using the edge step to scale $\chi(k)$, normalizing the absorption data, interpolating into K-space, selecting the correct weighting (generally 1, 2, or 3), Fourier transforming the data, selecting the range and inverting the transform to look at a single shell, and analyzing one shell for amplitude and phase. The data can then be fit to models built for structure analysis.

2.4 Transmission Electron Microscopy (TEM)

Microscopes constitute anything that reveals finer details than can be resolved by the eye. Classical Rayleigh criterion for light microscopy states that the smallest distance δ that can be resolved is approximately as seen in Eq 2.12.

$$\delta = 0.61\lambda/(\mu \sin\beta) \quad \text{Eq 2.12}$$

λ = radiation wavelength, μ = refractive index of the viewing medium, and β = semi-angle of collection of the magnifying lens

Resolution, the distance between two points that can be resolved, is therefore approximately equal to $\frac{1}{2} \lambda$. The resolution of a good light microscope is approximately 300 nm, well above atomic resolution. Therefore, fine details in samples and nanometer crystallites are not visible with light microscopes, which are limited by the wavelength of light.¹⁰

Experiments by de Broglie,²¹ Thompson and Reid,²² and Davisson and Germer²³ in the early 1900's showed that electrons have a wave-like nature and can therefore diffract. Because electrons are smaller than atoms, it is theoretically possible to obtain resolution below the atomic level using an electron microscope. Therefore, to overcome the limitations of light microscopes, the first electron microscope was built by Knoll and Ruska in the early 1930's.²⁴

The resolution of TEMs is approximately $1/1 - 0.61 \lambda/\beta$. The wavelength of an electron is related to its energy as seen in Eq 2.13.

$$\lambda \approx 1.22/E^{1/2} \quad \text{Eq 2.13}$$

For a 100 KeV electron, the wavelength = 4 pm, a resolution much smaller than the diameter of an atom. Due to imperfect lenses, the resolution has not reached picometer levels, however, TEMs can image at resolutions of approximately 0.1 nm and columns of atoms may be observed.¹⁰

TEMs are versatile instruments used to characterize materials, specifically nanomaterials, to determine properties such as morphology, particle size, crystallinity, and crystallite phase. TEM in combination with other techniques can also be used to gain information on elemental analysis, electronic structure, and atomic structure.

In TEM, a beam of electrons is passed through a sample to produce a magnified image. Electrons passing through the sample may be undeflected (no interaction with atoms), elastically scattered (no loss of energy), or inelastically scattered (loss of energy, excitation of secondary electrons or X-rays).²⁵ Regular TEM imaging utilizes elastically scattered electrons. When a significant amount of electrons are scattered, the scattered electron beam (a wave) will combine in some directions to produce constructive interference, while most waves will cancel out in destructive interference. As in XRD, this means that diffraction is observed at a few specific angles (twice the Bragg angle from the unscattered beam) and that heavy, crystalline materials are more likely to scatter electrons due to the regular array of atoms in the crystal structure.²⁵ In order to create the contrast needed to produce an image, scattered electrons are separated from unscattered electrons using an objective lens aperture. As scattered electrons are filtered out, the brightness of the image is proportional to the number of unscattered electrons allowed to pass through the aperture. Though it has a smaller impact than crystallinity and atomic weight, sample thickness also contributes to the image brightness.

TEM microscopes are similar to traditional light microscopes, with the following major components: an illumination source (electron gun), condenser system to collimate the illumination onto the specimen (condenser), objective lens to create the first focused image, projector system to magnify this image to the final size, viewing screen (fluorescent screen), and

a camera to record the image (plates, film, or detector) (see Figure 2.12).

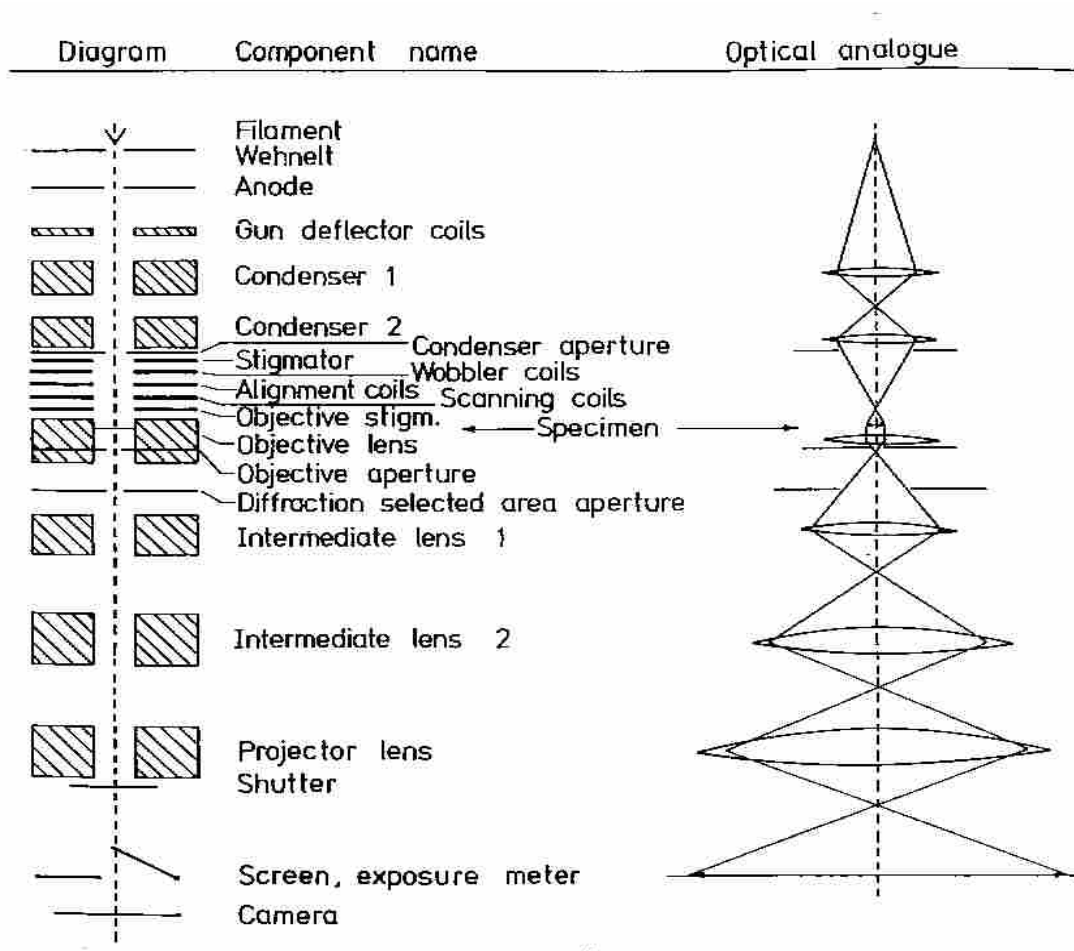


Figure 2.12 TEM instrument. Image adapted from Chescoe and Goodhew.²⁵

The electron gun, placed at the top of an evacuated column, produces an intense diverging beam of high energy electrons that is accelerated through a voltage, typically 100 – 500 kV, before traveling down the microscope to the illumination (condenser) system. The brightness of electron guns is limited and beam spot size decreases as current increases (a concern at very high currents). The gun produces the first image of the specimen (called the crossover), which then becomes the object for the illumination system. Gun deflector coils (gun tilt and gun shift) are used to deflect the beam onto the optical axis so that a focused beam of a

small spot size travels down to the illumination system. The illumination system consists of two or three condenser lenses (electromagnetic rings as opposed to the glass lenses used in a traditional light microscope). The first condenser lens (C1) produces a fine beam and controls the beam size that can be attained by the condenser system. The C1 lens forms a de-magnified or magnified (depending on the gun source) image of the gun crossover. The beam then travels down to the second condenser lens (C2), which projects the beam at the specimen and controls the illuminated area and the convergence angle.^{10, 25, 26}

A note on lenses: TEM lenses set up a symmetric electromagnetic field around the optical axis of the microscope. Electrons traveling down the optical axis experience no force and are undeflected, however, electrons traveling off axis experience a force, causing them to spiral about the optical axis. Changing the strength of the lenses (and therefore the focal length) adjusts the magnification and focus of the image. Two types of aberrations can affect the resolution of the image: (1) chromatic, resulting from variations in the energy of the electrons, and (2) spherical, resulting from the lens geometry. Solutions for each are to use thin specimens and small apertures. Astigmatism, another problem associated with lenses, can be controlled with stigmator controls, which are coils in the column that force the beam back into a symmetric configuration.^{10, 25}

A condenser aperture can be inserted below C2 to filter electrons out of the beam, thereby controlling beam intensity and the convergence angle (Figure 2.13). The convergence angle is linked to the depth of field (length of optical axis that a point in the object is not spread by the microscope into a spot larger than the microscope resolution limit). All points within the depth of field will appear at the same resolution (equally sharp) in the image. Large apertures are used for thicker samples, while small apertures are used to obtain greater depth of field and/or to

minimize beam damage to the sample. Due to trade off of beam strength and depth of field, medium apertures are used for most imaging.²⁵

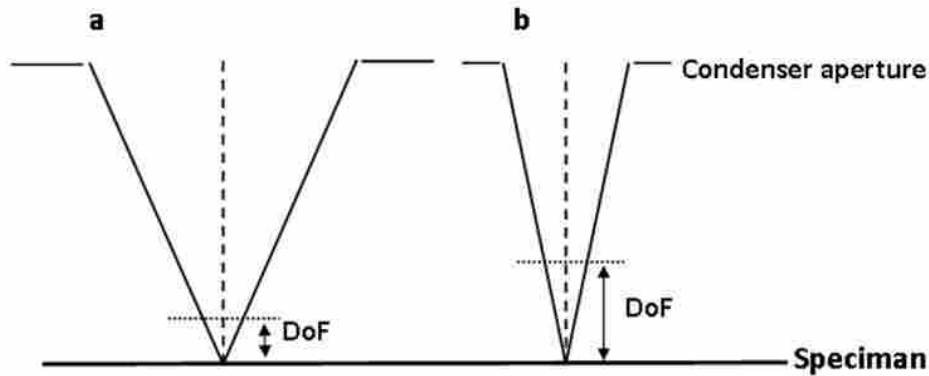


Figure 2.13 All points within the Depth of field (DoF) appear equally sharp in the image. DoF depends on the convergence angle. a. A larger aperture gives more electrons, a larger convergence angle, and a smaller DoF. b. A smaller aperture gives fewer electrons, a smaller convergence angle, and a larger DoF.

Following passage through the C2 lens and the condenser aperture, the beam travels through the condenser stigmator. The condenser stigmator counteracts any astigmatism in the illumination system by creating a circular beam at the specimen. Wobbler coils are used to aid in focusing and alignment coils are used to bring the beam onto the optical axis near the specimen. Scanning coils used in the scanning mode of TEM are also located in this area of the column. The objective lens, objective stigmator, objective aperture, and specimen are all located below the coils. The objective lens focuses on the specimen and forms an image approximately 50x magnification. The objective aperture, located in the back focal plane of the lens, can then be used to select which electrons form the final image. A selected area aperture (diffraction aperture) sits in the plane of the first image. In diffraction mode (selected area diffraction), it is possible to view the diffraction pattern that arises from the crystallinity of the specimen, similar to the ideas presented in the XRD section of this chapter. Figure 2.14 shows the two basic

imaging modes of TEM, projecting an image onto a screen versus projecting a diffraction pattern onto a screen.¹⁰ Below the selected area aperture several lenses magnify the image and project it onto the screen. Below the screen, a shutter and camera/detector are located for recording the image.

In regular TEM mode, or parallel beam mode, the beam is collimated by condenser lenses so that a parallel beam passes through the sample. The beam can also be focused more intensely on a specific area of the sample by focusing the C2 lens to form a convergent beam (small spot size, approximately 0.2 – 5 nm). The convergent beam mode is referred to as scanning transmission electron microscopy (STEM) mode. In STEM mode, a small beam probe is used to scan specific areas of the sample with higher resolution than may be obtained in regular TEM mode.^{10, 27}

Several modes of imaging are possible using TEM including low and high magnification, diffraction, and scanning modes. In high and low magnification imaging, different lenses are used. As a lens is turned on/off, the image on the screen rotates 180°, as one more/less inversion is taking place (see Figure 2.15). At low magnifications the intermediate lens is turned off and two inversions take place. At medium magnification all three lenses are used and three inversions take place. At high magnification, the three lenses are used at high strength and four inversions take place.²⁵

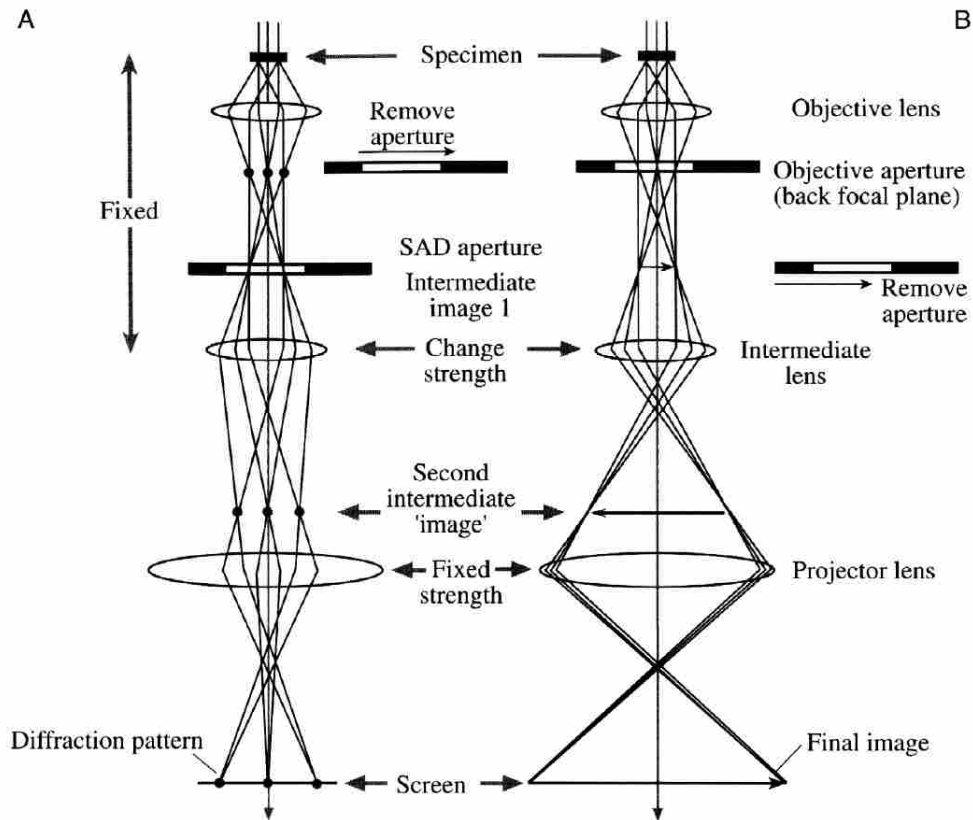
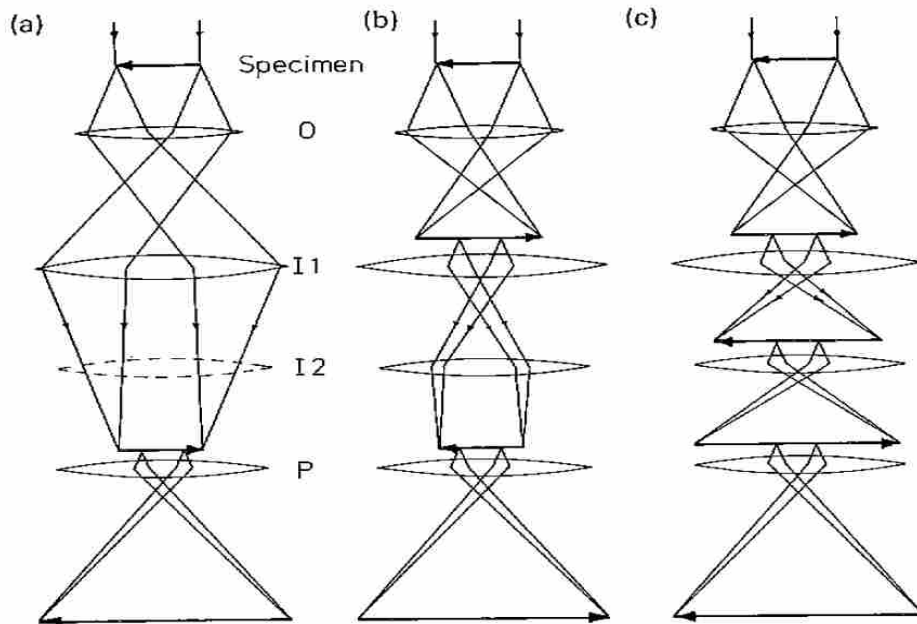


Figure 2.14 Two basic modes of TEM: (A) projecting the diffraction pattern onto the viewing screen and (B) projecting the image onto the screen. Image adapted from Williams and Carter.¹⁰



2.15 Three common configurations of TEM microscopes, representing image inversions. (a) At low magnification I2 (second intermediate lens) is switched off and two inversions occur. (b) At medium magnification all lenses are used and three inversions occur. (c) At high magnification all lenses are strongly excited and four inversions occur. Image adapted from Chescoe and Goodhew.²⁵

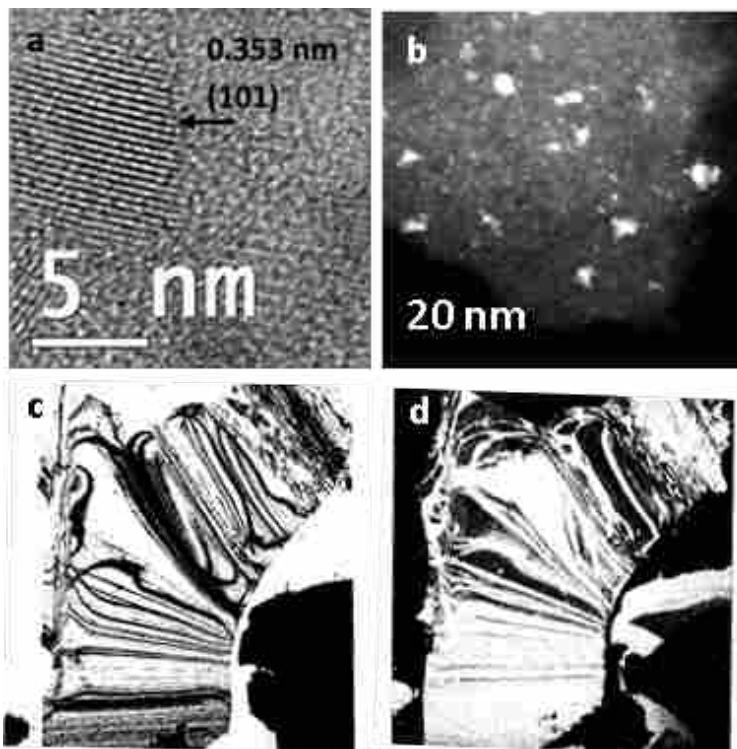


Figure 2.16 a. Fresnel lattice fringes arising from the 101 plane of anatase TiO_2 . b. Z-contrast STEM image of Pt supported on TiO_2 . c. A bright field image of a mica sample on a plastic and carbon-coated grid. d. A dark field image of the same mica sample. Images c and d adapted from Flegler et al.²⁸

Low magnification images are formed from virtual images, where the specimen is placed after the front focal plane and a magnified (but not inverted) virtual image is formed in front of the front focal plane. High magnification images are formed from real images, the specimen is placed in front of the front focal plane and a magnified and inverted real image is formed behind the back focal plane.²⁸ At high magnification columns of atoms are revealed, referred to as Fresnel or lattice fringes (see Figure 2.16a). As in XRD, the distance between lattice fringes can be measured and correlated to d-spacings characteristic of materials in order to characterize the material, phase, crystallinity, and crystal direction.

The primary source of contrast in TEM images is mass/thickness contrast, which occurs because thicker regions of a sample transmit fewer electrons. Other techniques to increase and enhance contrast include bright field, dark field, Z-contrast, and selected area diffraction (Figure 2.16 b, c, and d). To obtain bright field contrast, an objective aperture is used to filter out scattered electrons, so that weakly scattered electrons appear much brighter (Figure 2.16c). Conversely, dark field contrast utilizes the objective aperture to select strongly scattered electrons that appear much brighter than the weakly scattered electrons in the final image (Figure 2.16d). In STEM mode, an annular detector can be used to detect electrons scattered at high angles. At these angles, the scattering intensity exhibits a Z^2 dependence and therefore contrast between elements is observed (Figure 2.16b).^{28, 29}

Analyses involving inelastically scattered electrons include X-ray energy dispersive spectroscopy (XEDS) and electron energy loss spectra (EELS). XEDS spectra, detected using an energy dispersive spectrometer, show characteristic emission lines for each element in the sample. EELS spectra can be separated into energy-loss near-edge structure (ELNES) and extended energy-loss fine structure (EXELFS). Analogous to XANES and EXAFS, the EELS

spectrum contain information on nearest neighbor atoms, coordination, bonding, and electronic structure.^{28, 30}

2.5 Adsorption

Adsorption, the increase in density of the fluid in the area of the interface, occurs when a solid surface is exposed to a gas or liquid. Adsorption occurs to an appreciable extent on materials with large surface areas, high porosity, and very small particles. Adsorbents are used in many ways, including catalysis, separations, purification, environmental cleanup, desiccation, and biological reactions. Models by which the adsorbate (substance in the adsorbed state, also called adsorptive when in a fluid phase) and adsorbent (solid material on which adsorption occurs) interact have been proposed and can be used to gain information on surface area, pore volume, and pore size distribution of the solid. Adsorption techniques are therefore widely used to characterize the surface and porosity of solids. Adsorption onto a solid surface can occur with gas or liquid molecules. We will focus on gas adsorption, which applies to the adsorption techniques presented in this work.

Gas molecules can be either physisorbed or chemisorbed.

Physisorption vs chemisorption:³¹

1. Physisorption is a general phenomenon that occurs in any solid/fluid system.

Chemisorption is a chemically specific phenomenon that depends on the reactivity of the solid and fluid.

2. Physisorbed molecules maintain their chemical identity and remain unchanged through adsorption and desorption.

Chemisorbed molecules undergo chemical reactions or dissociation and therefore generally cannot be recovered through desorption.

3. Physisorption can occur as a multilayer (at high pressures).

Chemisorption is generally limited to a monolayer, since adsorbed molecules are bonded to adsorption surface sites.

4. Physisorption is always exothermic and the energy involved is on the same order of magnitude as the energy of condensation of the adsorptive (energy can be enhanced when taking place in very narrow pores).

Chemisorption is on the same order of magnitude as energy involved in a comparable chemical reaction.

5. In physisorption, equilibrium is generally rapidly attained.

In chemisorption, a large activation energy is generally required and equilibrium is attained slowly. Systems at low temperatures may not have sufficient thermal energy to attain thermodynamic equilibrium.

2.5.1 Physisorption

In physisorption, as a gas molecule approaches the surface of the solid it experiences London dispersion forces of attraction as well as short-range repulsion forces. At a particular distance from the surface, these forces balance each other to minimize potential energy and the gas molecule is physisorbed.³¹

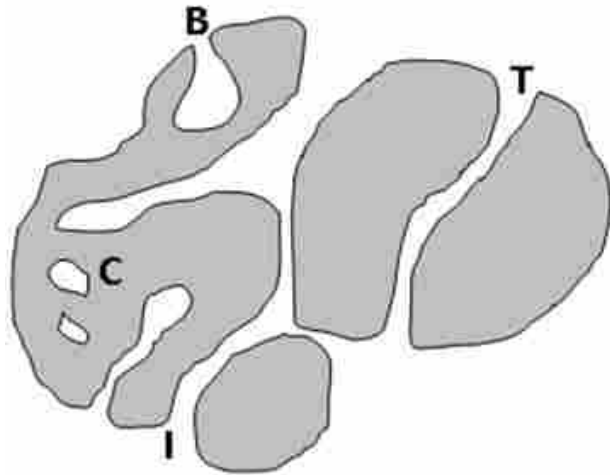
A solid sample is weighed and placed in a sample tube. It is useful to have some idea of the surface area of the material prior to measurement as most instruments operate best with 20 – 50 m² of surface area in the sample tube. The first mass measurement includes the sample mass

and any adsorbed gases such as H₂O and CO₂, therefore, the sample is degassed and reweighed prior to sorption measurements. Degassing is an important process to create a reproducible sample surface that is independent of storage and aging.

Adsorption is conventionally measured point-by point as successive amounts of adsorbate (i.e. N₂ (g)) gas are introduced into the sample tube. After sufficient time has passed to allow for the system to equilibrate, the pressure at each point is measured (most commonly by a membrane capacitance pressure transducer). Many data points are collected to create a sorption isotherm. To avoid pressure changes due to temperature changes, the temperature is maintained over the entire experiment. For example, sample tubes are often immersed in liquid N₂ to maintain a stable temperature of 77 K.

Gas can be adsorbed and subsequently desorbed at constant temperature and a sorption isotherm relates the amount adsorbed or desorbed to the equilibrium pressure. The porosity of a material (geometry and diameter/width), nature of the gas-solid system, and adsorption temperature all influence how adsorption and desorption occur, as reflected in the shape of the sorption isotherm. Inspection of the isotherm can give information on the physisorption mechanism of pore filling and emptying and therefore, the pore geometry.

The IUPAC defines three types of pores: micropores = pores of widths less than 2 nm, mesopores = pores of widths 2 to 50 nm, and macropores = pores of widths greater than 50 nm.³¹ As seen in Figure 2.17, pores can be described as open (open to the surface), blind (single connection to the surface), closed (no connection to the surface), through (both ends open to the surface), and interconnected/networked (connected to multiple pores). Pores can be further described in terms of the shape, such as cylindrical, slit-like, and ink-bottle.



2.17 A porous grain showing different types of pores: C = closed pores, B = blind or dead end pores, I = interconnected pores, and T = through pores.

In 1985 the IUPAC defined six types of gas physisorption isotherms and correlated them to specific pore geometries, or adsorption/desorption mechanisms.³² The various isotherms are shown in Figure 2.18.

1. Type I isotherms are reversible and concave to the P/P^0 axis, with a sharp rise at low pressures to a horizontal plateau. This type of isotherm is associated with microporous materials with a small external surface area, tight size distribution, and only a small amount of multilayer adsorption.
2. Type II isotherms are reversible and are concave to the P/P^0 axis at low pressures, almost linear to the P/P^0 axis at medium pressures, and convex to the P/P^0 axis at high pressures. This type of isotherm is associated with multilayer adsorption on an open and stable surface of a nonporous, macroporous, or possibly microporous material.

3. Type III isotherms are reversible and convex to the P/P^0 axis. These isotherms are uncommon and are indicative of weak adsorbent-adsorbate interactions (compared to the stronger adsorbate-adsorbate interactions).

4. Type IV isotherms are similar to Type II isotherms at low pressures. At higher pressures, hysteresis is observed. Hysteresis in the isotherm arises when the amount adsorbed is not brought to the same level at a given equilibrium pressure as the amount desorbed. The lower hysteresis

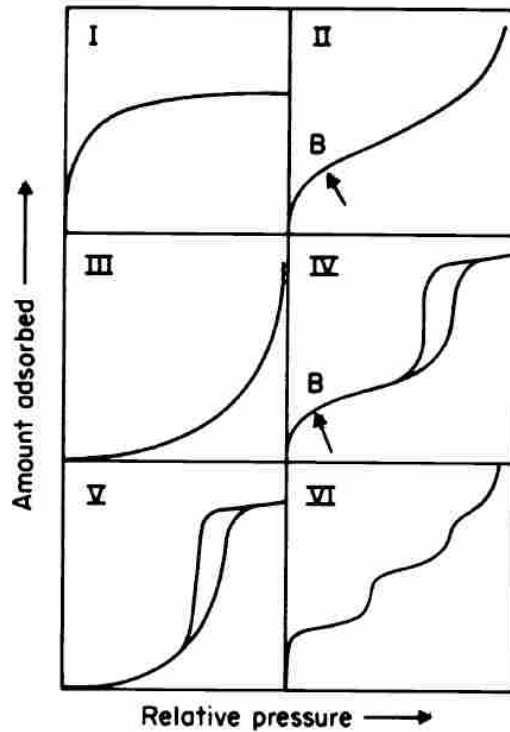


Figure 2.18 Six types of physisorption isotherms. Image adapted from Sing et al.³²

branch is associated with the adsorption, or the pore filling process, and the upper branch is associated with desorption, or withdrawal of fluids from the pores. This type of isotherm is associated with mesoporous materials.

5. Type V isotherms are convex to the P/P^0 axis at low pressures. Similar to Type III isotherms, they exhibit weak adsorbent-adsorbate interactions. Similar to Type IV, they exhibit hysteresis.

6. Type VI isotherms are stepped. This type of isotherm is associated with the relatively rare layer-by-layer adsorption on a highly uniform system.

All materials discussed in the present work are Type IV mesoporous materials. Analysis of the hysteresis loop observed in Type IV isotherms gives further insight into pore geometry. As shown in Figure 2.19, Type IV isotherms can be classified as H1, H2, H3, or H4 hysteresis loops.³²

H1 hysteresis loops are narrow with steep slopes and nearly parallel adsorption and desorption branches. H1 hysteresis is generally associated with materials having a uniform pore structure with a narrow size distribution. H4 hysteresis loops are nearly parallel to the P/P^0 axis and do not terminate at high pressures. H4 hysteresis often arises from microporous materials with slit-like pores. All of the materials presented in this work exhibit primarily H2 hysteresis, with a few examples of H3 hysteresis, therefore, these will be discussed in further detail.

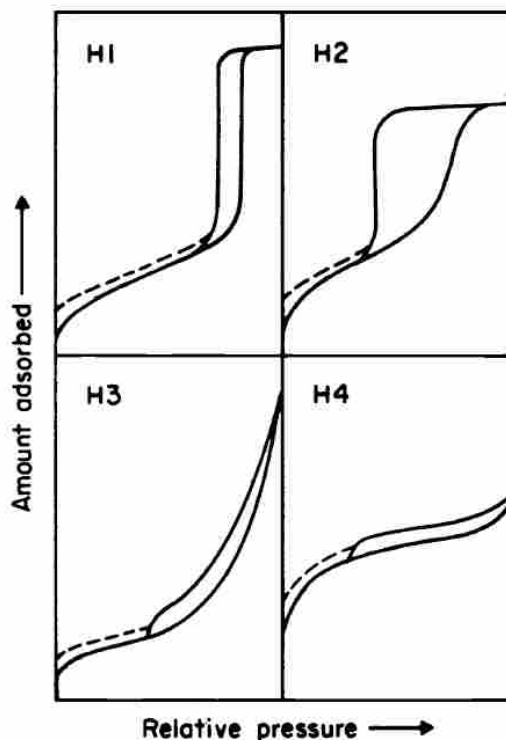


Figure 2.19 The four types of hysteresis. Image adapted from Sing et al.³²

H2 hysteresis loops exhibit a plateau at high P/P^0 and a steep desorption branch with a lower closure point around $0.42 P/P^0$ (see figure 2.19).³¹ H2 hysteresis is associated with complex interconnected networks of ink-bottle pores. The lower closure point is mainly dependent on the condensate for a given temperature. The triangular shape of the H2 loop is observed when evaporation/desorption of fluids from the main pore bodies is delayed (constrained by pore necks).^{33, 34} The steep slope around $0.4 P/P^0$ in the desorption branch,

characteristic of H2 hysteresis, signals that calculations of pore size from the desorption branch are probably questionable³¹ and the adsorption branch should be used to calculate pore diameters.^{34, 35}

Two evaporation mechanisms from H2 pores are: (1) delayed evaporation or entrapment and (2) percolation, a network effect in which liquid remains in constricted regions while vapor is formed in pore bodies; it may also involve spontaneous nucleation of a gas bubble.³⁴ When delayed evaporation occurs, the lower closure P/P^0 of the hysteresis loop may measure the ‘neck’ size.³⁴ This could be visualized in terms of a significant pressure drop across the neck leading to a non equilibrium between low pressure gas in the pore outlet and high pressure evaporating gas inside the pore. In the case of percolation, condensate is removed from wider pores while vapor filled pores form spanning clusters across the particle. The pressure is further reduced until the percolation threshold (which depends on the properties of the condensate (loop closure at $P/P^0 < 0.42$ is characteristic of N_2 at 77 K)³¹ rather than the ‘neck’ width) is reached and desorption becomes rapid.^{31, 34} It is thought that percolation confirms the structure of mesopores that can only be accessed by narrow meso and micropores or larger mesopore cavities embedded in a microporous matrix.³⁴ If there is no apparent microporosity, percolation may signal that mesopore cavities with a narrow constriction of small mesoporous dimensions are present.

H3 hysteresis loops exhibit delayed condensation in the adsorption branch, exhibit no limiting adsorption at high P/P^0 , and appear similar to Type II isotherms with hysteresis (Figure 2.19). Aggregates of plate-like particles with slit like pores give rise to H3 type loops.^{34, 35} The pseudo type II character is associated with the delayed capillary condensation caused by a low degree of pore curvature and non-rigidity of the aggregate structure.³⁵ The desorption branch is

preferred for H3 type hysteresis with slit-like pores due to delayed condensation observed in the adsorption process.³⁶⁻³⁹

Many porous oxide materials contain complex pore structures and therefore the associated sorption isotherms often contain features of several pore types, complicating the analysis. Analysis of pore geometry evident in TEM micrographs may be used to determine pore geometry and aid in selection of the best model to use in determining pore size distribution.

2.5.1.1 Pore diameter/width and volume calculations

The most widely used method to determine pore size is the Barrett, Joyner, and Halenda (BJH) method,⁴⁰ which was developed in the early 1950's and is based on the Kelvin equation, Eq 2.15. The Kelvin equation gives the mechanical equilibrium between two fluids at opposite sides of a meniscus at different pressures.

$$\ln \frac{P}{P^0} = -\frac{2\gamma(\cos\theta)V_L}{r_k RT} \quad \text{Eq 2.15}$$

where γ = surface tension, θ = contact angle between liquid and adsorbed layer on the wall, V_L = molar volume of the liquid, and r_k = radius of curvature of the meniscus.

The radius of curvature of the meniscus is dependent on the pore geometry. For a cylindrical pore open to the surface on one end, the pore radius, r_p , is given by Eq 2.16.

$$r_p = r_k + t \quad \text{Eq 2.16}$$

where t = the adsorbed multilayer thickness.

For a slit-shaped pore there are two layers of thickness t on each side of the meniscus, therefore, the pore width, w_p , is given by Eq 2.17.

$$w_p = r_k + 2t \quad \text{Eq 2.17}$$

The thickness of the adsorbed layer t can be calculated with the Halsey equation,⁴¹ seen in Eq 2.18.

$$t = -0.354 \left(\frac{5.00}{\ln\left(\frac{P}{P_0}\right)} \right)^{1/3} \quad \text{Eq 2.18}$$

Though the most popular pore analysis method, the BJH model assumes perfectly cylindrical pore geometry, and is therefore not applicable to slit-like pore systems and has been observed to underestimate pore diameters for systems with non-uniform cylindrical pores. To improve the calculation of pore widths a new SPG model, with structural corrections for area and volume, has been suggested.⁴² According to the SPG model, the pore width, w_p , may be calculated as shown in Eq 2.19.

$$w_p = \alpha \left(\frac{2\Delta V_p}{\Delta S_p} \right) \quad \text{Eq 2.19}$$

Where α = structural factor accounting for surface area changes, ΔV_p = adsorbed volume, and ΔS_p = specific surface area corresponding to ΔV_p .

Similar to Eq 2.19, a modified Pierce method including structural corrections for area and volume, can be used to calculate pore diameter, d_p (Eq 2.20).

$$d_p = \alpha \left(\frac{2\Delta V_p}{\Delta S_p} \right) \quad 2.20$$

w_p and d_p differ in the determination of ΔV_p . See Huang et al.⁴² for further discussion and more information on the SPG model.

Porosity is defined as the ratio of the volume of pores and voids to the volume occupied by the solid. At saturation pressures (i.e. 0.98), it is assumed that the pores have been filled with condensed adsorbate and pore volume can be measured.

2.5.1.2 Surface area determination

The Brunauer-Emmett-Teller (BET) theory⁴³ (an extension of the Langmuir adsorption theory⁴⁴) uses gas adsorption to determine surface area was proposed in 1938. BET has since become the most extensively used method to calculate surface area of adsorbent materials, including nanocatalysts and catalyst supports. BET theory assumes that gas molecules are adsorbed randomly onto a surface of equivalent sites with no interaction between adsorbed molecules in the same layer. It further assumes that each layer of gas molecules are essentially the ‘first’ layer on the adsorbent, with each subsequent adsorbed layer behaving as the surface of the adsorbent, therefore, the rate of adsorption and the heat of condensation do not change between subsequent layers.³¹

BET theory determines the surface area by first determining the monolayer capacity, then, with a value for the average area occupied by each adsorbent, the BET surface area (SA_{BET}) can be determined by Eqs 2.21 and 2.22.

$$\frac{P}{n(P^0-P)} = \frac{1}{n_m C} + \frac{C-1}{n_m C} \times \frac{P}{P^0} \quad \text{Eq 2.21}$$

Where n = number of moles, P = pressure, n_m = the monolayer capacity, and C = a constant

$$SA_{\text{BET}} = n_m L \sigma \quad \text{Eq 2.22}$$

Where L = Avogadro's constant, and σ = the cross-sectional area occupied by each adsorbate molecule

A linear relationship is obtained by graphing $\frac{P}{n(P^0 - P)}$ vs $\frac{P}{P^0}$ through which the slope and intercept are used to determine C and n_m . The cross-sectional area σ can be determined using Eq 2.23.

$$\sigma = f(M/\rho L)^{2/3} \quad \text{Eq 2.23}$$

where f = packing factor (hexagonal close-pack = 1.091), ρ = density of the adsorptive liquid at the operational temperature, M = molar mass of the adsorptive

For Nitrogen adsorbed at 77 K, $\sigma = 0.162$ is generally used.³¹

2.5.2 Chemisorption

Chemisorption is the most common technique used to measure active surface area. It is also used to characterize the reactivity of surfaces, catalyst surface area and dispersion, surface site energetics, acid-base surface properties, and weak/strong gas-solid interactions through well established techniques. Chemisorption is used extensively in catalysis, primarily to determine the number of active sites that are available to interact with a fluid phase.

In Chemisorption a reactive gas is allowed to react with a solid (i.e. metal catalyst). Several techniques are available including gas adsorption onto metals in the metallic state, hydrogen/oxygen titrations, and acid/base reactions. Prior to chemisorption, samples are generally first oxidized (calcined) and reduced (activated). Any H_2 chemisorbed during reduction

is removed by flowing an inert gas over the sample at an appropriate temperature. Following reduction, some samples experience surface blocking of active sites (decoration effect or strong metal support interaction).⁴⁵⁻⁴⁷ For example, in the case of Pt supported on TiO_2 , reduced TiO_x species formed at temperatures as low as 177°C migrate to form a thin film covering adsorption sites on the surface of Pt metal.⁴⁸ Surface blocks can often be reversed or removed through exposure to oxygen. Though sample pre-treatment depends on the synthesis method and the technique that will be used, a degassing step is necessary to remove adsorbed gases (a similar step is performed before physisorption measurements). Similar to physisorption, a gas is introduced into a sample chamber. The amount of adsorbed gas may be determined by several different methods. Unlike in physisorption, in which gas adsorbs in a multi-layer fashion, chemisorption is limited by the adsorption of a chemically bound monolayer. Therefore, chemisorption isotherms exhibit plateaus at lower pressures than physisorption isotherms, including those of microporous materials. Also unlike physisorption, chemisorption reactions may have long equilibration times and may react so slowly as to be undetectable. Therefore, reaction conditions must be tailored to each gas-solid reaction, and high temperatures or pressures may be required.³¹

The different methods through which gas can be adsorbed onto a solid include static volumetric, static gravimetric, and flow methods.⁴⁹ In static volumetric and gravimetric methods, known doses of gas are pulsed over the sample. In the volumetric method, the resulting equilibrium pressure between the sample and gaseous phase is measured. In the gravimetric method, weight changes of the sample during adsorption are used to measure the amount of adsorbed gas. For comparison, blank measurements (run under identical conditions using an inert gas instead of a reactive gas) are used. Both volumetric and gravimetric methods are known for

high precision and an accurate measurement of the true equilibrium state. However, because they both are performed under vacuum, and the gravimetric method requires a microbalance, these methods are associated with high instrumentation costs. Flow methods are performed at atmospheric pressures and use less expensive instrumentation. In flow methods, an inert carrier gas flows over the sample while a reactive gas is injected in pulses of known volumes. Any unadsorbed gas flows to a detector, most commonly a thermal conductivity detector (TCD). When the reactive gas reaches the TCD, the thermal conductivity difference between the reactive gas and inert reference gas is detected and a signal is produced. The amount of adsorbed gas is calculated by integrating the peaks generated by the detector signal as a function of time. Flow methods generate fast results and are relatively low cost, however, they are best for systems that have fast equilibrium times.⁴⁹

Several reactive gases are available and gas selection is dependent on the reactivity of the gas with the active surface. Included in the consideration are reaction time with the metal, equilibration time, spillover (discussed below), gas-gas interactions (multi-layer formation), an understanding of the stoichiometry of adsorbed gas, and gas purity (minimum = 99.99%).

The amount of chemisorbed gas is used to determine the active free surface area. The stoichiometric factor, the number of molecules of adsorbate per surface metal atom, is fundamental to this calculation and must be known. It is determined using other analytical methods, including infrared spectroscopy. The stoichiometry of several gases is listed in Table 2.1.

Table 2.1 Stoichiometric factors for different types of chemisorption reactions.⁴⁹

Method	Reaction (M = accessible metal atom)	Stoichiometry
H ₂ chemisorption	$M + \frac{1}{2} H_2 = M-H$	0.5
CO chemisorption	$M + CO = M-CO$	1
	$2 M + CO = M-CO-M$	0.5
H ₂ /O ₂ titration	$M-O + \frac{3}{2} H_2 = M-H + H_2O$	1.5
O ₂ /H ₂ titration	$M-H + \frac{3}{4} O_2 = M-O + \frac{1}{2} H_2O$	0.75

Hydrogen is the most commonly used chemisorption gas. It is frequently used to characterize noble metals, though it cannot be used with Ag or Pd. H₂ is generally adsorbed in a 1:1 H:M (M = metal) stoichiometry, however, other interactions between hydrogen and metals and supports are known and should be accounted for. Oxygen can be used to characterize metal surfaces; however, it is best used at low temperatures to avoid corrosion and the formation of oxide surface layers. It is the primary gas used to characterize Ag. CO can also be used to characterize metals, including Pd. Two adsorption stoichiometries are commonly observed and therefore it can be difficult to determine the exact stoichiometry. CO has also been observed to form carbonyl complexes with particular metals.⁴⁹

In chemisorption, an active species is chemisorbed onto an active phase (in the case of a catalysis, the metal is the active phase). Spillover occurs when the chemisorbed species migrates onto a second phase (i.e. the support) that it could not usually react with alone (Figure 2.20). Spillover is a problem because it leads to an increase in adsorbed gas beyond what can be adsorbed by the active phase alone, and therefore overestimates the active site surface area and dispersion. Conditions should be carefully selected to avoid spillover; in general, high temperatures and pressures promote spillover.^{49, 50}

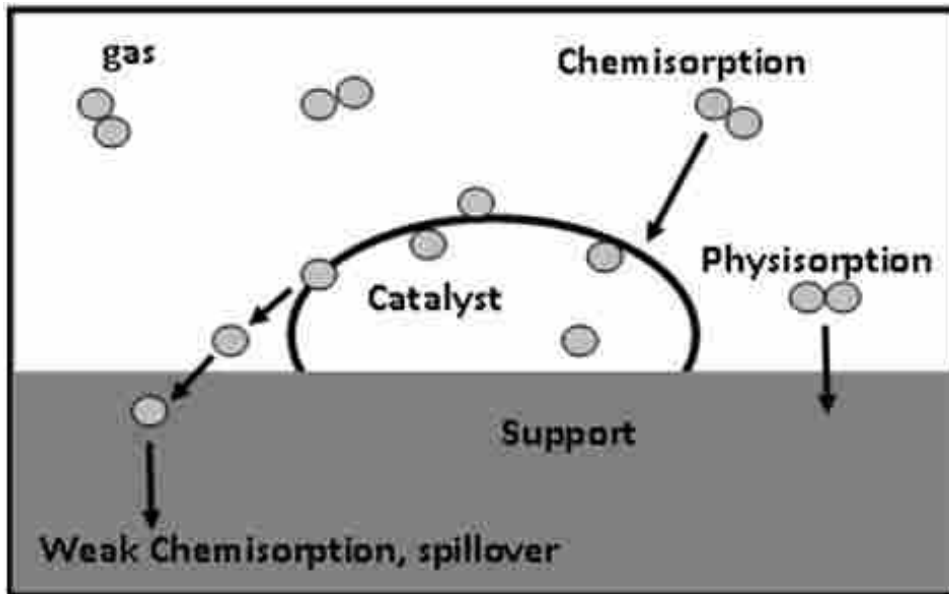


Figure 2.20 Spillover of dissociated gas atoms onto the support material surface following chemisorption on the catalyst surface.

The BET method, which utilizes physisorption, is the most popular method to determine total surface area. TEM can be used to estimate crystallite sizes and metal dispersion.

Chemisorption differs from these methods in that it can be used to determine the active surface area (area exposed and available for reactions). In the field of catalysis, chemisorption is utilized to selectively determine the active sites (the amount of reactive surface area of a catalyst), particularly of supported catalysts, as opposed to the total surface area of the support and catalyst. Active sites react with the gas and the metal specific surface area (MSA) can be determined by Eq 2.24.

$$MSA = \frac{V_m \times N_a}{S_f \times S_d} \quad \text{Eq 2.24}$$

Where V_m = gas adsorbed at monolayer (moles per gram of sample), N_a = Avogadro's number, S_f = stoichiometric factor (number of molecules of adsorbate per surface metal atom), and S_d = metal surface density (number of metals per square meter).

Parameters in Eq 2.24 are listed in Table 2.2

Table 2.2 Parameters of some metals with different gases.⁴⁹

Metal (M)	H ₂ /M	CO/M	O ₂ /M	Atomic Weight	S _d x 10 ²⁰ (atoms/m ²)	Notes
Pt	0.5	1 1.15	0.5	195.09	0.125	Spillover at T > 200°C
Pd	0.5	0.6	---	106.4	0.127	Absorption of H ₂
Ir				192.22	0.130	
D > 1.5 nm	0.5	1	0.5			
D < 1.5 nm	1	1	0.5			
Rh				102.905	0.133	
D > 1.5 nm	0.5	1	0.5			
D < 1.5 nm	0.5-1	2	0.5			
Ru				101.07	0.163	Spillover of H ₂ at T > 25°C and P > 100 Torr
D > 1.5 nm	0.5	1	0.5			
D < 1.5 nm	0.5	> 1	> 0.5			
Os	0.5	---	---	190.2	0.159	
Ni	0.5	---	---	58.71	0.154	Carbonyl formation
Co	0.5	---	---	55.993	0.151	
Fe	0.5	0.5	---	55.847	0.163	
Ag	---	---	0.4	107.868	0.115	At 420 K
Au	---	---	0.25 0.5	196.9665	0.115	At 470 K At 570 K

It is useful to talk about the metal or active phase dispersion, which is the ratio of free metal atoms to the total number of metal atoms fixed on the support (the fraction of metal that is free to react). Metal dispersion (D) can be calculated using Eq 2.25.

$$D = \frac{V_m \times AW \times 10^4}{W\% \times S_f} \quad \text{Eq 2.25}$$

Where V_m = volume of monolayer, AW = atomic weight, W% = weight % metal in the sample, and S_f = stoichiometric factor

2.6 References

1. Friedrich, W.; Knipping, P.; Laue, M., Interference Phenomena with R. overdot.ontgen Rays. *Sitzb. kais. Akad. Wiss., Munchen* **1912**, 303-22.
2. Massa, W.; Gould, R. O., *Crystal Structure Determination*. Gardners Books: 2010.
3. Dinnebier, R. E.; Billinge, S. J. L. In *Principles of powder diffraction*, Royal Society of Chemistry: 2008; pp 1-19.
4. Rajagopal, K., *Textbook Of Engineering Physics*. Prentice-Hall Of India Pvt. Limited: 2008.
5. Bragg, W. H.; Bragg, W. L., The Reflection of X-rays by Crystals. *Proc. R. Soc. London, Ser. A* **1913**, 88, 428-38.
6. Jenkins, R.; Snyder, R., *Introduction to X-Ray Powder Diffractometry*. Wiley: 2012.
7. Ewald, P. P., The Theory of the Interference of R. overdot.ontgen Rays in Crystals. *Phys. Z.* **1913**, 14, 465-72.
8. Ewald, P. P., *Z. Kristallogr.* **1921**, (56), 129.
9. Authier, A., *The Reciprocal Lattice*. International Union of Crystallography: 1981.
10. Williams, D. B.; Carter, C. B., *Transmission Electron Microscopy: A Textbook for Materials Science*. Springer: 2009.
11. Patterson, A. L., The Scherrer formula for x-ray particle-size determination. *Phys. Rev.* **1939**, 56, 978-82.
12. Koningsberger, D. C.; Prins, R., *X-Ray Absorption: Principles, Applications, Techniques of EXAFS, SEXAFS and XANES*. Wiley: 1988.
13. Kronig, R. d. L., *Zeit. Phys.* **1931**, 70, 317-323.

14. Frenkel, A.; Stern, E. A.; Voronel, A.; Qian, M.; Newville, M., Solving the structure of disordered mixed salts. *Phys. Rev. B: Condens. Matter* **1994**, *49* (17), 11662-74.
15. Frenkel, A. I.; Hills, C. W.; Nuzzo, R. G., A View from the Inside: Complexity in the Atomic Scale Ordering of Supported Metal Nanoparticles. *J. Phys. Chem. B* **2001**, *105* (51), 12689-12703.
16. Ravel, B.; Stern, E. A.; Vedrinskii, R. I.; Kraizman, V., Local structure and the phase transitions of BaTiO₃. *Ferroelectrics* **1998**, *206-207* (1-4/1-2), 407-430.
17. Kelly, S. D.; Kemner, K. M.; Fein, J. B.; Fowle, D. A.; Boyanov, M. I.; Bunker, B. A.; Yee, N., X-ray absorption fine structure determination of pH-dependent U-bacterial cell wall interactions. *Geochim. Cosmochim. Acta* **2002**, *66* (22), 3855-3871.
18. Stumm, v. B. R., A history of x-ray absorption fine structure. *Ann. Phys. (Paris)* **1989**, *14* (4), 377-466.
19. Stern, E. A., Theory of the extended x-ray-absorption fine structure. *Phys. Rev. B* **1974**, *10* (8), 3027-37.
20. Stern, E. A., Structure determination by x-ray absorption. *Contemp. Phys.* **1978**, *19* (4), 289-310.
21. de Broglie, L., *Annales de Physique* **1925**, *3* (22).
22. Thompson, G. P.; Reid, A., Diffraction of cathode rays by a thin film. *Nature (London, U. K.)* **1927**, *119*, 890.
23. Davisson, C.; Germer, L. H., Diffraction of electrons by a single crystal of nickel. *Phys. Rev.* **1927**, *30*, 705-40.
24. Knoll, M.; Ruska, E., The electron microscope. *Z. Phys.* **1932**, *78*, 318-39.

25. Chescoe, D.; Goodhew, P. J.; Society, R. M., *The Operation of Transmission and Scanning Electron Microscopes*. Oxford University Press, Incorporated: 1990.
26. De Graef, M., *Introduction to Conventional Transmission Electron Microscopy*. Cambridge University Press: 2003.
27. Nellist, P. D. In *Scanning transmission electron microscopy*, Springer: 2007; pp 65-132.
28. Flegler, S. L.; Heckman, J. W.; Klomparens, K. L., *Scanning and Transmission Electron Microscopy: An Introduction*. Oxford University Press: 1993.
29. Browning, N. D.; James, E. M.; Kishida, K.; Arslan, I.; Buban, J. P.; Zaborac, J. A.; Pennycook, S. J.; Xin, Y.; Duscher, G., Scanning transmission electron microscopy. An experimental tool for atomic scale interface science. *Rev. Adv. Mater. Sci.* **2000**, *1* (1), 1-26.
30. Reimer, L.; Kohl, H., *Transmission Electron Microscopy: Physics of Image Formation*. Springer: 2008.
31. Rouquerol, F.; Rouquerol, J.; Sing, K., *Adsorption by Powders and Porous Solids: Principles, Methodology and Applications*. Academic: 1999.
32. Sing, K. S. W.; Everett, D. H.; Haul, R. A. W.; Moscou, L.; Pierotti, R. A.; Rouquerol, J.; Siemieniewska, T., Reporting physisorption data for gas/solid systems with special reference to the determination of surface area and porosity (Recommendations 1984). *Pure Appl. Chem.* **1985**, *57* (4), 603-19.
33. Thommes, M.; Smarsly, B.; Groenewolt, M.; Ravikovitch, P. I.; Neimark, A. V., Adsorption Hysteresis of Nitrogen and Argon in Pore Networks and Characterization of Novel Micro- and Mesoporous Silicas. *Langmuir* **2006**, *22* (2), 756-764.

34. Thommes, M., Recent advances in the characterization of mesoporous materials by physical adsorption. *Annu. Rev. Nano Res.* **2010**, *3*, 515-555.
35. Sing, K. S. W.; Williams, R. T., Physisorption hysteresis loops and the characterization of nanoporous materials. *Adsorpt. Sci. Technol.* **2004**, *22* (10), 773-782.
36. Ball, P. C.; Evans, R., Temperature dependence of gas adsorption on a mesoporous solid: capillary criticality and hysteresis. *Langmuir* **1989**, *5* (3), 714-23.
37. Neimark, A. V.; Ravikovitch, P. I., Capillary condensation in MMS and pore structure characterization. *Microporous Mesoporous Mater.* **2001**, *44-45*, 697-707.
38. Neimark, A. V.; Ravikovitch, P. I.; Vishnyakov, A., Adsorption hysteresis in nanopores. *Phys. Rev. E: Stat. Phys., Plasmas, Fluids, Relat. Interdiscip. Top.* **2000**, *62* (2-A), R1493-R1496.
39. Monson, P. A., Contact Angles, Pore Condensation, and Hysteresis: Insights from a Simple Molecular Model. *Langmuir* **2008**, *24* (21), 12295-12302.
40. Barrett, E. P.; Joyner, L. G.; Halenda, P. P., The determination of pore volume and area distributions in porous substances. I. Computations from nitrogen isotherms. *J. Am. Chem. Soc.* **1951**, *73*, 373-80.
41. Halsey, G., Physical adsorption on nonuniform surfaces. *J. Chem. Phys.* **1948**, *16*, 931-7.
42. Huang, B.; Bartholomew, C., H.; Woodfield, B. F., Facile synthesis of mesoporous alumina with tunable pore size: Effects of alcohols in precursor formation and calcination. *Microporous Mesoporous Mater.* **2013**, *177*, 37-46.
43. Brunauer, S.; Emmett, P. H.; Teller, E., Adsorption of gases in multimolecular layers. *J. Am. Chem. Soc.* **1938**, *60*, 309-19.

44. Langmuir, I., Constitution and fundamental properties of solids and liquids. I. Solids. *J. Am. Chem. Soc.* **1916**, *38*, 2221-95.
45. Stevenson, S. A.; Dumesic, J. A.; Baker, R. T. K.; Ruckenstein, E.; Editors, *Metal-Support Interactions in Catalysis, Sintering, and Redispersion*. Van Nostrand Reinhold Co.: 1987; p 315 pp.
46. Baker, R. T. K.; Kim, K. S.; Emerson, A. B.; Dumesic, J. A., A study of the platinum-titanium oxide system for the hydrogenation of graphite: ramifications of strong metal-support interactions. *J. Phys. Chem.* **1986**, *90* (5), 860-6.
47. de la Pena O'Shea, V. A.; Consuelo, A. G. M.; Platero, P. A. E.; Campos-Martin, J. M.; Fierro, J. L. G., Direct evidence of the SMSI decoration effect: the case of Co/TiO₂ catalyst. *Chem. Commun. (Cambridge, U. K.)* **2011**, *47* (25), 7131-7133.
48. Pesty, F.; Steinrueck, H.-P.; Madey, T. E., Thermal stability of Pt films on TiO₂(110): evidence for encapsulation. *Surf. Sci.* **1995**, *339* (1/2), 83-95.
49. Fadoni, M.; Lucarelli, L., Temperature programmed desorption, reduction, oxidation and flow chemisorption for the characterization of heterogeneous catalysts. Theoretical aspects, instrumentation and applications. *Stud. Surf. Sci. Catal.* **1999**, *120A* (Adsorption and Its Applications in Industry and Environmental Protection, Vol. 1), 177-225.
50. Guerrero-Ruiz, A.; Rodriguez-Ramos, I., *Spillover and Mobility of Species on Solid Surfaces*. Elsevier Science: 2001.

Chapter 3: Synthesis and Characterization of Pure and Stabilized Mesoporous Anatase Titanias

3.1 Introduction

TiO₂ has attracted attention as a catalyst since the discovery of its high photocatalytic activity by Fujishima and Honda in 1972.¹ TiO₂ is used in many applications, including photocatalysis, photovoltaics, environmental cleanup, antibacterial agents, coatings, and pigments.¹⁻⁶ TiO₂ is also an excellent support material for noble metals such as Pd, Pt, and Au in a number of oxidative synthesis and pollution-control reactions.⁷⁻¹² These and other reactions involving catalysts supported on TiO₂ have been reviewed elsewhere.⁶

Many synthetic routes to TiO₂ have been reported in the literature, including sol-gel methods,¹³⁻¹⁶ templating, self-assembly routes,¹⁷⁻¹⁹ and hydrolysis reactions.²⁰⁻²³ Details of these methods are reviewed elsewhere.⁶ A variety of metals and nonmetals are incorporated into titania to improve thermal stability, adjust pore diameter and volume, and otherwise render its properties suitable for various applications.^{14-16, 24-28} While several of these methods produce materials of higher surface area and more ideal porosity relative to commercially available titanias, these procedures are largely time-consuming, complicated, expensive, or difficult to scale up and are therefore not industrially viable. Many commercial titanias are synthesized by sol-gel routes, sulfate hydrolysis, or by converting crude titanium ore to TiCl₄ that is then oxidized,^{6, 29} but the resulting products have low surface area and poor thermal and hydrothermal stabilities. Moreover, it is more difficult to effectively add modifiers or stabilizers to the finished materials than during synthesis.

Co-hydrolysis methods, which allow for precise control of dopant concentration and homogeneous mixing, have shown great promise in producing anatase stabilized with varying amounts of additives including Al, La, Si, and Zr. For example, Kim et al.²⁶ has used co-hydrolysis to stabilize anatase with 5 – 40% Al, and 10% Si or Zr to produce particles with high surface areas, slit-like pores, and bimodal pore size distributions. Yang et al.^{16,27} also used a sol-gel/co-hydrolysis method to stabilize anatase with 5 – 10% Zr, 10% Al or Si, and 5% Al/5% Si. While they were able to synthesize stabilized anatase, their process took several days to complete.^{16,27} These and other similar methods produce excellent materials but involve inherent drawbacks including the necessity to dissolve starting materials in various solvents, stir at specific temperatures for several hours to days, add surfactants and capping agents that may later need to be removed, and use organic reagents that generate waste and impurities.

In this paper we explore using a facile method to produce mesoporous anatase and anatase stabilized with various amounts of Al, La, Si, and Zr. While this method is similar to hydrolysis/co-hydrolysis techniques discussed above, this method provides a uniquely rapid, simple route to incorporate stabilizers into the Ti starting material in a solvent deficient environment without the need for templates. This method overcomes many of the difficulties previously mentioned, e.g. it involves a short mixing time, water solvent, simple equipment, low water requirements as rinse water can be recycled, and the process can easily be scaled up to industrial size batches. Of equally great significance are the unusual and highly-desirable properties of the nano-oxides produced by this method, including high thermal stability, surface area as high as or higher than most reported in literature, and narrow pore diameter distributions. For example, TiO₂ synthesized by this method has been modified with aluminum to obtain anatase particles stable to 400°C and 700°C with surface areas of $479 \pm 39 \text{ m}^2/\text{g}$ and 120 ± 27

m²/g; pore volumes of 0.46 ± 0.04 cm³/g and 0.3 ± 0.1 cm³/g; and pore diameters of 2.9 ± 0.2 nm and 7.81 ± 0.03 nm respectively. State of the art characterization methods for determining pore structure and their application to TiO₂ nanostructures are discussed.

3.2 Experimental

3.2.1 Sample Preparation

Samples were prepared following a general solvent deficient mixing method that can be used to synthesize many metal and mixed metal oxides.³⁰ Approximately 3.48 mL of TiCl₄, and either 0.63 g Al(NO₃)₃·9H₂O, 0.72 g La(NO₃)₃·6H₂O, 0.19 ml SiCl₄, or 0.39 g ZrCl₄ were mixed together in a mortar and pestle for one minute. (Amounts listed are for 5 mol% Al, La, Si, and Zr-modified anatase. Molar ratios of 0 – 14% La, Si and Zr, and 0 – 85% Al were also examined.) Next 10.54 g NH₄HCO₃ was added and mixed for an additional minute followed by the addition of 5 to 15 ml of distilled H₂O to facilitate mixing. The slurry was mixed at room temperature for 5 minutes to form a stabilized anatase precursor. The precursor was dried in air at 100°C for at least 24 hours and then rinsed with 2 L of distilled water using a vacuum filtration system at room temperature. The resulting product was found to be pure anatase by XRD analysis. The product was calcined in air at temperatures ranging from 400 – 900°C for 3 hours, with ramp rates of 18 – 30°/min. For ease of discussion and to compare different stabilizers, several synthesis parameters including mixing time, drying time, drying temperature, rinse water amounts, calcination time, and calcination ramp rate were held constant at the values previously mentioned. However, these parameters may be varied. Additionally, rinse water may be recycled.

3.2.2 Sample Characterization

X-ray diffraction patterns were collected using a PANalytical X'Pert Pro diffractometer (Cu-K $_{\alpha 1}$ radiation, $\lambda = 1.540598 \text{ \AA}$) at 45 kV and 40 mA over the 2θ range of $10 - 90^\circ$. Average crystallite diameters were estimated using the Scherrer equation³¹ and confirmed using transmission electron microscopy (TEM). TEM measurements were performed on a Tecnai F20 Analytical STEM operating at 200 keV. The samples were dispersed in ethanol and deposited on copper grids (lacey carbon fiber, 400 mesh copper grids, Ted Pella, Inc.).

Full-range N₂ sorption isotherms were collected at 77 K using a Micromeritics TriStar 3020 surface analyzer. Samples of 0.25 – 0.50 g were degassed at 200°C prior to data collection. Pore volumes were calculated from the adsorption isotherm at a relative pressure of 0.98 and specific surface areas were calculated using the Brunauer-Emmett-Teller (BET) method from a P/P^0 range of 0.05 to 0.2.

Pore diameters were calculated using a modified Pierce method^{32, 33} with corrections for pore area and volume. A structural factor α is introduced to account for the distortion of the ideal cylindrical model used in the Barrett-Joyner-Helenda (BJH) model. Similar to the SPG model reported by our group,³⁴ the structural factor is used to correct the calculated accumulative surface area. Pore diameters were calculated from either adsorption or desorption branches, depending on the shape of the hysteresis loop. For example, the adsorption branch calculations are considered more accurate for H2 type pores, since evaporation of the condensate in the desorption process is significantly constrained by the pore necks in an “ink-bottle” pore geometry and the connectivity of the network.³⁵⁻³⁸ For H3 type hysteresis with slit-like pores, the desorption branch is preferred due to delayed condensation observed in the adsorption process.³⁹⁻

⁴² In the present study, pore diameters calculated from both branches are reported to provide

additional information on pore structure. For example, in some instances of ink-bottle pores the adsorption branch may be used to calculate the diameter of the ‘bottles’ and the desorption branch may give information on the ‘necks’. Pore size distributions were calculated by fitting the adsorption and desorption data to a log normal distribution function.⁴³ Standard deviations are based on two sample preparations with a few exceptions as noted.

3.3 Results and Discussion

3.3.1 XRD, TEM, Surface Area, and Pore Volume Analysis

Surface area, pore volume, and pore diameter of the pure and modified anatase materials are listed in Table 3.1. Data in Table S3.1 in the supplemental information also reveals evidence of high surface area precursor materials. The XRD data in Figure 3.1 show that our pure anatase samples are stable up to 400°C, after which calcining from 500°C to 700°C leads to a mixture of anatase and bulk rutile and by 900°C the sample is entirely bulk rutile. While it is known that high surface area rutile can be prepared, it is associated with small crystallite sizes. In this study, when the pure anatase was heated at 500°C – 700°C, it underwent a phase change to bulk (99 nm) rutile. Therefore, the decreases in surface area and pore volume observed with increasing calcination temperature are due to grain growth and formation of bulk rutile. It is important to note that pure, crystalline anatase is formed after drying at 100°C (Figure 3.1), which is unusual since many researchers report higher temperatures are required to form crystalline anatase.

Table 3.1 Average crystallite diameters, surface areas, pore volumes and pore diameters calculated from adsorption and desorption branches of pure and modified anatase TiO₂ calcined at 400°C and 700°C.

Calcination Temp	Sample	^a Phase	^b Crystallite Diameter (nm)	Surface Area (m ² /g)	Pore volume (cm ³ /g)	^c d _{pore} (nm)	^d Width-Distribution 2σ (nm)
400°C	anatase	A	6	127 ± 14	0.18 ± 0.02	3.9 ± 0.4	3.6 ± 0.2
						3.59 ± 0.04	4.32 ± 0.03
	5 mol% Al	A	5	374 ± 2	0.32 ± 0.01	2.51 ± 0.08	3.4 ± 0.1
						3.39 ± 0.09	2.3 ± 0.2
	14 mol% Al	A	3	429 ± 55	0.5 ± 0.2	4 ± 2	3.8 ± 0.3
						4 ± 1	4.7 ± 0.4
	5 mol% Zr	A	6	384 ± 36	0.33 ± 0.03	2.57 ± 0.01	3.62 ± 0.06
						3.37 ± 0.06	2.3 ± 0.1
	5 mol% Si	A	7	149.9 ± 0.2	0.197 ± 0.004	3.6 ± 0.3	3.64 ± 0.06
						3.6 ± 0.2	2.19 ± 0.07
	5 mol% La	^f A	^f 5	351 ± 27	0.30 ± 0.06	2.3 ± 0.2	3.1 ± 0.1
						3.3 ± 0.2	2.3 ± 0.2
700°C	anatase	A/R	51-A, 99-R	5 ± 2	No measurable pore volume		
	5 mol% Al	A	10	70 ± 2	0.161 ± 0.003	8.6 ± 0.6	3.65 ± 0.01
						6.1 ± 0.5	2.4 ± 0.1
	14 mol% Al	A	8	100 ± 6	0.25 ± 0.02	10.4 ± 0.8	3.72 ± 0.08
						7.1 ± 0.3	2.28 ± 0
	5 mol% Zr	A	10	75 ± 10	0.20 ± 0.04	10.7 ± 0.08	3.6 ± 0.2
						7.2 ± 0.5	2.23 ± 0.04
	5 mol% Si	A/R	20	25 ± 4	No measurable pore volume		
5 mol% La	A	7	54 ± 9	0.12 ± 0.03	8.2 ± 0.5	3.42 ± 0.06	
					5.9 ± 0.6	2.1 ± 0.2	

a. A corresponds to anatase, R corresponds to rutile.

b. Crystallite diameter calculated using the Scherrer formula.

c. d_{pore} calculated from the adsorption branch is listed first and calculations from the desorption branch are listed second.

d. Represents the full width of the Gaussian distribution at half the maximum.

e. Standard deviations based on four sample preparations.

f. Determined by TEM.

Al, La, and Zr-modified anatase materials calcined at 700°C have higher surface areas and pore volumes than the pure and Si-modified anatase (Table 3.1). This is consistent with

XRD patterns (Figure 3.1) which show that the anatase phase is thermally stable to at least 700°C for 14 mol% Al and 5 mol% Al, La, and Zr-modified anatase while the Si-modified anatase calcined at 700°C demonstrated grain growth and the onset of the anatase to rutile phase transition was observed.

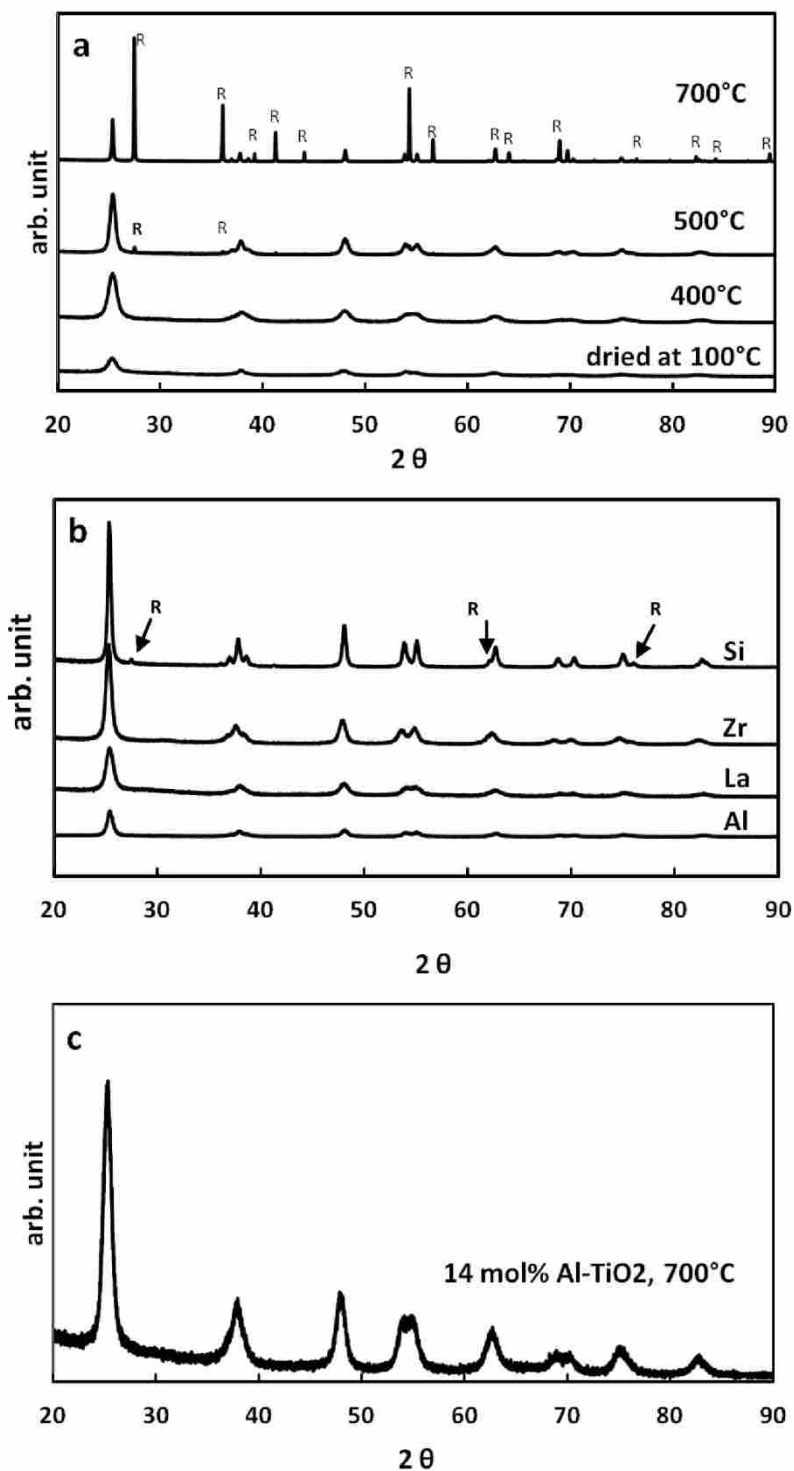


Figure 3.1 X-ray diffraction patterns of (a) pure TiO_2 dried and calcined at 400°C, 500°C, and 700°C, (b) 5 mol% modified anatase calcined at 400°C, and (c) 14 mol% Al-modified anatase calcined at 700°C. R corresponds to rutile peaks and all other peaks correspond to anatase.

The anatase structure consists of chains of distorted TiO_6 octahedra joined at two adjacent edges with half of the octahedral sites and all tetrahedral sites available for cationic doping. While the location and form of dopants in nanomaterials is largely unclear and XAS studies are needed to confirm the hypotheses discussed below, DFT studies⁴⁴ have shown that cationic dopants are typically most stable in lattice positions. Based on cation/anion ratios, we expect Zr^{4+} to be found in octahedral sites as seen in previous studies^{27, 45} and Si^{4+} to be found in tetrahedral sites. Al^{3+} could exist in tetrahedral or octahedral sites but, as the Al-modified anatase exhibits surface area and thermal stability similar to the Zr-modified anatase, we expect Al^{3+} to be found in octahedral sites. Similarly, Al^{3+} and Ti^{4+} ions are both located in octahedral sites in aluminum titanate, compared to Ti/Si oxide molecular sieve materials where Si^{4+} are in tetrahedral sites and Ti^{4+} ions are in octahedral sites. As mol% dopant is increased and lattice sites are filled, dopant species likely populate the surface of the anatase. Due to the large size of La^{3+} , we expect it to be found primarily on the surface as La-O species, similar to XAS findings by Chen et al. for Y-doped anatase.⁴⁶ Si did not increase the surface area and phase stability of anatase as much as Al, La, and Zr at 5 mol% or 14 mol% (Table 3.1) thus this leads us to conjecture that tetrahedral cation substitution does not stabilize the structure of anatase as effectively as octahedral and/or surface cation doping.

As seen by XRD and TEM (Table 3.1, Figures 3.1 and 3.2), 5-mol% Al, La, Si, and Zr-modified anatase materials calcined at 400°C have crystallite sizes and lattice parameters comparable with pure anatase but, with the exception of Si-modified anatase, the Al, La, and Zr-modified materials have much larger surface areas. The high surface areas are attributed to increased porosity. For La^{3+} and Al^{3+} , increased oxygen vacancies and/or increased protons and

OH^- groups necessary for charge compensation could also increase the surface area consistent with previous studies.^{44, 47}

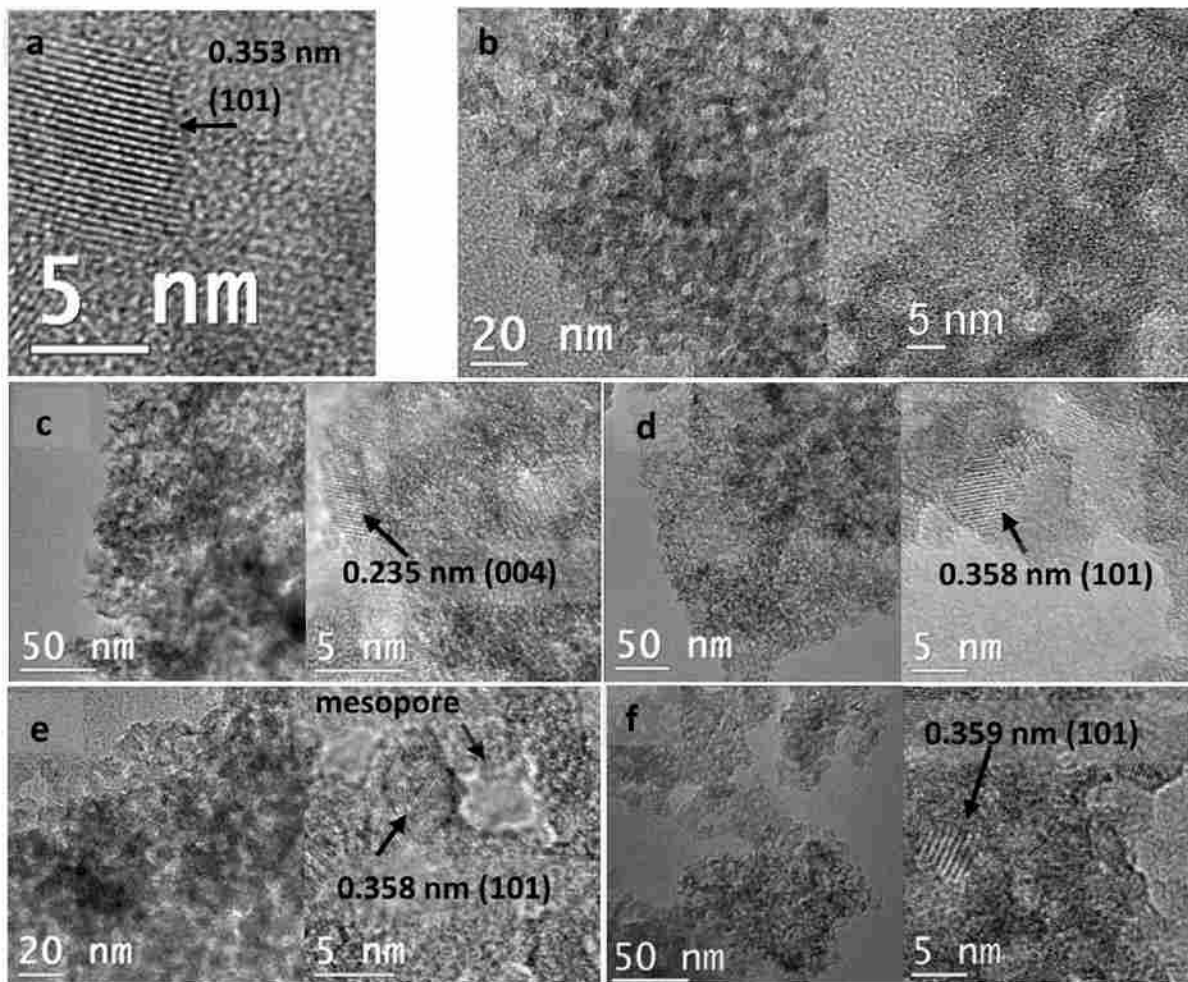


Figure 3.2 TEM images of anatase TiO₂ calcined at 400°C for 3 h. (a) pure, (b) 14 mol% Al, (c) 5 mol% Al (d) 5 mol% La, (e) 5 mol% Si, and (f) 5 mol% Zr. Low magnification images confirm mesoporosity. High magnification images confirm particle size and crystallinity.

Data in Figure 3.3 and TEM micrographs in Figure 3.2 show that increasing the amount of Al from 5 mol% to 14 mol% decreases order in the crystal structure and leads to smaller, less crystalline particles with higher surface areas. This may be due to structural changes induced by dopants.^{46, 48} A companion XANES study (manuscript in preparation) reveals a change in Ti-

coordination for anatase modified with 14 mol% and higher Al; the high surface area is attributed to lattice distortions due to differences in coordination.

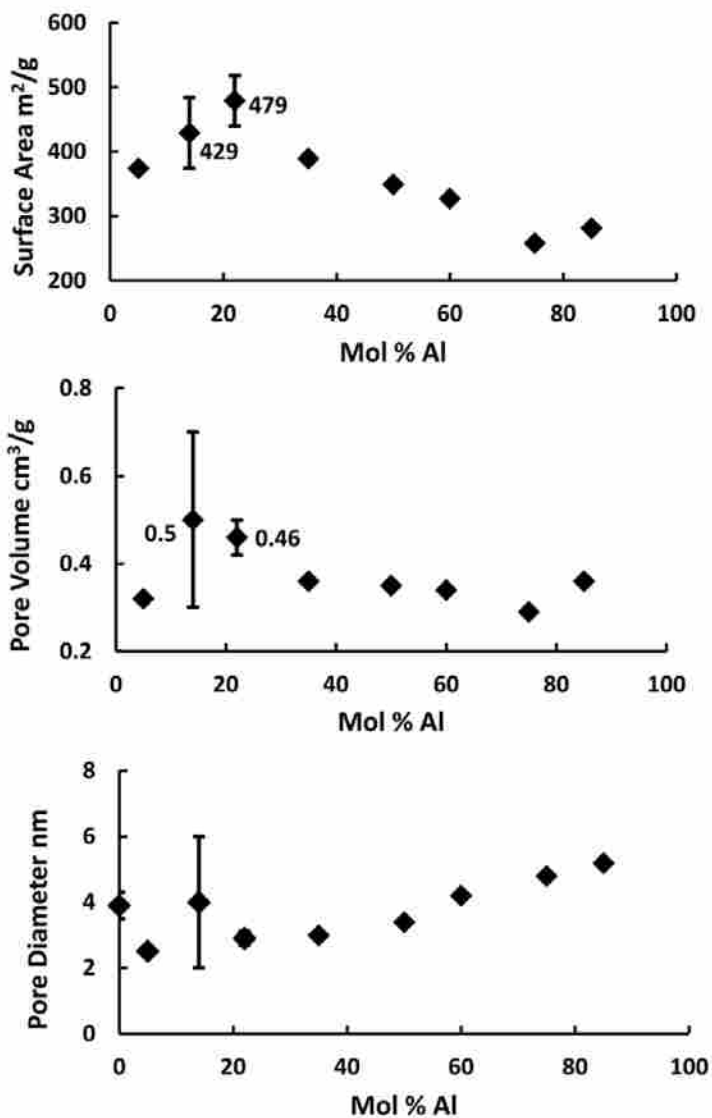


Figure 3.3 Surface area, pore volume, and pore diameter as a function of mol% Al in anatase TiO₂ calcined at 400°C.

The surface area continues to increase with increasing amounts of stabilizer until a critical level, approximately 22 mol% Al, is reached and the surface area is maximized.

Materials of higher Al content (35 – 85 mol% Al) could be considered mixed oxide systems of

anatase in an amorphous alumina matrix, with the surface area and porosity belonging to the mixed oxide system. However, since only the anatase phase is observed by XRD, there is no evidence of a mixed oxide system and no change in crystallite diameter. As the mol% Al increases, XRD patterns of 35 – 85 mol% Al calcined at 400°C – 700°C appear increasingly amorphous. From this evidence we conclude that after a critical level is reached, further addition of Al leads to short-range structural disorder. While the XRD evidence is consistent with a single phase system, we cannot rule out the existence of an additional, X-ray amorphous phase.

Several mechanisms have been suggested by which Al, La, Si, and Zr dopants inhibit grain growth and as a consequence the anatase to rutile phase transformation, thermally stabilizing anatase and preserving high surface areas. While further structural characterization is needed, we conclude that the following mechanisms previously reported are important for our materials: (1) dopants minimize anatase-anatase contact points;⁴⁹ (2) lattice distortions and vacancies previously discussed restrict atom movement;^{50, 51} and (3) dopants adsorb onto anatase planes of high surface energy to decrease interfacial free energies (these planes would otherwise join as part of the crystallite growth process).⁴⁶

3.3.2 Pore Diameter Analysis

The isotherms of pure TiO₂ and 5 mol% Al, La, Si, and Zr-TiO₂ calcined at 400°C are type IV, H2 loops (Figure 3.4).⁵² Similar isotherms were observed by Ragai and Sing for anatase with a well-defined mesoporous network.⁵³ H2 loops are associated with complex interconnected networks of ink-bottle pores. The steep slope around 0.4 P/P⁰ in the desorption branch is characteristic of H2 hysteresis signals that calculations of pore size from the desorption branch are probably questionable⁵³ and the adsorption branch should be used to calculate pore diameters.^{54, 55}

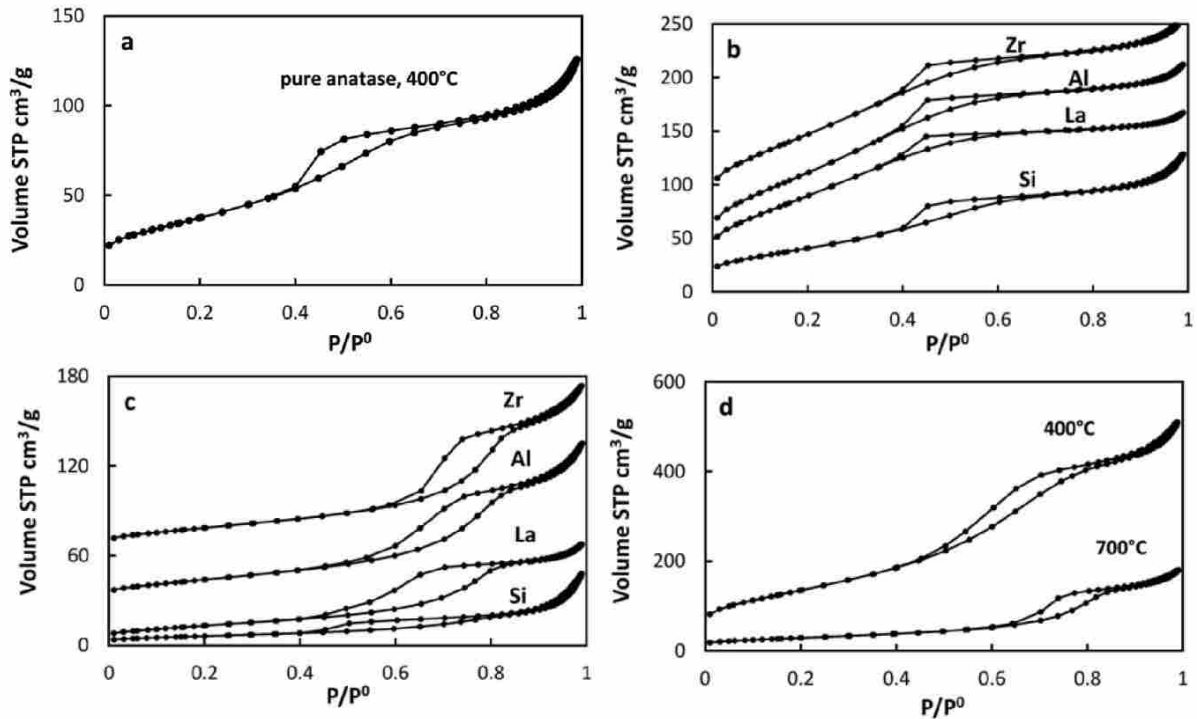


Figure 3.4 Full N_2 isotherms of (a) pure anatase calcined at 400°C , (b) 5 mol% modified anatase calcined at 400°C (y-axis offset by 10 units for Al and 50 units for Zr), (c) 5 mol% modified anatase calcined at 700°C (y-axis offset by 25 units for Al and 60 units for Zr), and (d) 14 mol% Al-modified anatase calcined at 400°C and 700°C .

Two evaporation mechanisms from pores are (1) delayed evaporation or entrapment and (2) percolation, a network effect in which liquid remains in constricted regions while vapor is formed in pore bodies; it may also involve spontaneous nucleation of a gas bubble.⁵⁵ When delayed evaporation occurs, the lower closure P/P^0 of the hysteresis loop may measure the ‘neck’ size;⁵⁵ this could be visualized in terms of a significant pressure drop across the neck leading to a non equilibrium between low pressure gas in the pore outlet and high pressure evaporating gas inside the pore. In the case of percolation, condensate is removed from wider pores while vapor filled pores form spanning clusters across the particle. The pressure is further reduced until the percolation threshold, which depends on the properties of the condensate (loop closure at $P/P^0 <$

0.42 is characteristic of N₂ at 77 K⁵³) rather than the ‘neck’ width, is reached and desorption becomes rapid.^{53,55} The lower closure points of the loops in Figure 3.4 and the calculated pore diameters ranging from 2.3 to 3.9 nm are consistent with percolation as the mechanism of evaporation for pure TiO₂ and 5 mol% Al, La, Si, and Zr-TiO₂ calcined at 400°C. Therefore, the adsorption branch should be used to calculate the pore diameter of the ‘bottle’ and the desorption branch may not be used to determine ‘neck’ width. Thommes concluded in his review that percolation confirms the structure of mesopores that can only be accessed by narrow meso and micropores or larger mesopore cavities embedded in a microporous matrix.⁵⁵ However, in this study, there is no apparent microporosity; hence percolation may signal that mesopore cavities with a narrow constriction of small mesopore dimensions are present.

The full isotherms of the 5 mol% Al, La, and Zr-TiO₂ materials calcined at 700°C and 14 mol% Al-TiO₂ calcined at 400°C and 700°C (Figure 3.4) represent type IV mesoporous particles with both H2 (ink-bottle) and H3 (plate-like) characteristics with gradual slopes for both hysteresis branches. Thus, the isotherms do not exhibit (1) rapid desorption characteristic of H2 loops, or (2) delayed condensation characteristic of H3 loops. In this case information is available from both branches, with the desorption branch giving information on the ‘neck’ or constricted regions and the adsorption branch giving information on the ‘body’ or larger diameter regions. The hybridization likely results from a distribution of pore widths and/or irregularly shaped pores caused by the incorporation of dopants and may signal a range of pores open to the surface and networked (branched) mesopores. The 14 mol% Al material is less crystalline than the pure titania and 5 mol% Al materials and we conjecture that the amorphous nature gives rise to small, irregularly shaped pore channels which causes the H2/H3 hybridized hysteresis. The changes in pore structure observed after calcination of the 5 mol% Al, La, and

Zr-titanias and the 14 mol% Al-titania at 700°C are consistent with grain growth leading to larger pore channels more open to the surface. The ‘neck’ diameters are also observed to be somewhat distributed with no limiting neck size. The small pore diameters and narrow pore size distributions of all samples (a selection of representative PSDs are shown in Figure 3.5) are consistent with the tightly packed faceted particles observed by TEM (Figure 3.2).

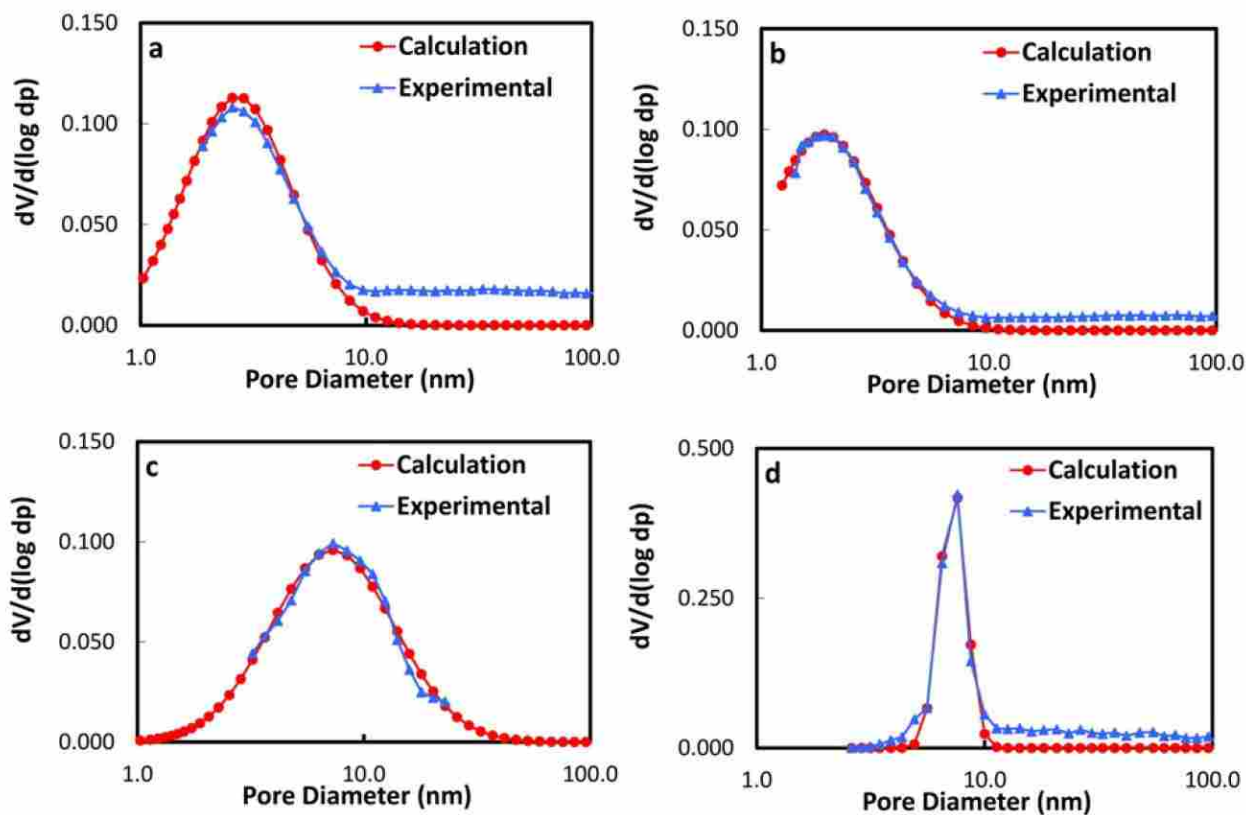


Figure 3.5 Pore size distributions of (a) pure anatase calcined at 400°C, (b) 5 mol% Al-modified anatase calcined at 400°C, (c) 14 mol% Al-modified anatase calcined at 700°C, and (d) 14 mol% Al-modified anatase calcined at 700°C. PSD for (a), (b), and (c) are based on the adsorption branch, PSD of (d) is based on the desorption branch.

Data in Figure 3.3 shows that as the amount of Al dopant increases the pore diameter generally decreases until a minimum was reached, around 22 mol% Al. After this the pore

diameter was seen to increase as more Al was incorporated. This is consistent with the observed surface area loss and is associated with the formation of larger particles.

It should be noted that it is difficult to evaluate the quality of previous work and compare samples from various sources because authors have neglected to state the method and the hysteresis branch used to calculate pore diameters as well as to provide statistical information. Careful analysis provides more accurate information on pore shape and size as well as method reproducibility.

3.3.3 Method Analysis

We have presented an industrially viable method to produce pure and stabilized anatase materials. This method is industrially viable because (a) only simple equipment, including a mixing bowl, an oven/kiln, and the optional drying oven and rinsing apparatus are used, (b) this method is fast, requiring only a 5 minute mixing step, an optional 24 hour drying step, an optional rinsing step (rinse water can be recycled), and a three hour calcination step, and (c) this method can be scaled to industrial-sized batches.

Table 3.2 compares our materials to commercially available anatase materials and materials reported in the literature. Our materials have surface areas, pore volumes, and thermal stabilities as high as or better than materials previously reported (Table 3.2). Compared with the most widely used, commercially-available titania support, Degussa P25, anatase prepared by this method has much higher surface areas, pore volumes, and thermal stabilities. Surface area is maximized by stabilizing TiO₂ with 22 mol% Al, which has surface areas and pore volumes of $479 \pm 39 \text{ m}^2/\text{g}$ and $0.46 \pm 0.04 \text{ cm}^3/\text{g}$ after calcining at 400°C; and $120 \pm 27 \text{ m}^2/\text{g}$ and $0.28 \pm 0.1 \text{ cm}^3/\text{g}$ after calcining at 700°C.

Table 3.2. 22 mol% Al-TiO₂ compared with stabilized anatase titanias reported in literature and commercially available products.

Calcination Temperature	Stabilizer/ dopant	Surface Area (m ² /g)	Pore volume (cm ³ /g)	d _{pore} (nm)	Ref
Low temperature calcination (300°C-500°C)	^a 22 mol% Al	479 ± 39	^d 0.46 ± 0.04	^d 3.52 ± 0.06	*
	50 mol% Al	470.72	0.59	4.5	56
	20 mol% Al	318	0.32	---	49
	10 mol% SiO ₂	290	0.26	3.9	15
	15 mol% Al	275	0.31	---	49
	15 mol% SiO ₂	187.3	0.17	3.6	14
	5 mol% Al	174	0.20	---	49
	5 mol% Zr	172	---	---	57
	10 mol% SiO ₂	163	---	---	24
	1 wt% La ₂ O ₃	160.52	0.26	---	58
	25 mol% Zr	148.9	0.13	---	59
	^b pure	127 ± 14	^d 0.18 ± 0.02	^d 3.9 ± 0.4	*
	16.7 mol% La ₂ O ₃	123	---	---	25
	pure	120	0.34	14.4	17
	pure	105	0.15	---	49
	19 wt% Al ₂ O ₃	79.1	---	---	60
	pure	72	0.24	10	61
High temperature calcination (700°C-900°C)	^c 22 mol% Al	120 ± 37	^d 0.28 ± 0.1	^d 6.2 ± 0.5	*
	pure	100	---	---	62
	15 mol% SiO ₂	93.30	0.11	4.6	14
	50 mol% Al	82.76	0.33	13.6	56
	25 mol% Zr	81.1	0.14	---	59
	16.7 mol% La ₂ O ₃	77	---	---	25
	pure	59.8	0.15	4.41–6.14	21
	1 wt% La ₂ O ₃	51.97	0.10	---	58
	19 wt% Al ₂ O ₃	45.7			60
	^c pure	12	0.06	20	61
Commercial samples	^e Degussa P25	50	^d 0.17	^d 96 ± 3	*
	MIRKAT 411	200	0.63	10-20 and larger	63

a. TiCl₄ and Al(NO₃)₃·9H₂O were mixed with ABC and a small volume of distilled H₂O, dried, rinsed with 2 L of distilled H₂O, and calcined at 400°C for three hours.

b. TiCl₄ was mixed with ABC and a small volume of distilled H₂O, dried, rinsed with 2 L of distilled H₂O, and calcined at 400°C for three hours.

c. TiCl₄ and Al(NO₃)₃·9H₂O were mixed with ABC and a small volume of distilled H₂O, dried, rinsed with 2 L of distilled H₂O, and calcined at 700°C for three hours.

d. Pore volume and diameter calculated from the adsorption branch.

e. Anatase and rutile phases present.

* reported in this study

Using our simple template-free method, materials with pore diameters ranging from 2.5 to 11 nm with narrow size distributions were synthesized by varying (1) the stabilizer material, (2) the amount of stabilizer, and/or (3), the calcination temperature. While the type and amount of stabilizer as well as calcination temperature lead to some variation in pore diameter, preliminary data shows that greater variation in pore diameter with a higher degree of control comes from varying synthesis parameters such as drying time, drying temperature, and precursor treatment. This work will be reported separately.

Sources of error in our experiments include (1) Ti:Al ratios and (2) variations in sample size and water amounts. Due to difficulties associated with dissolving the TiO₂, we have not determined Ti:Al ratios in all samples, however, the degree of accuracy in this study is sufficient to observe the trends. Future studies will include inductively coupled plasma (ICP) characterization to determine reproducibility of properties between samples of verified compositions. Additionally, we are currently using statistically designed experiments to identify other sources of error as well as determine the effects of synthetic variables such as mixing, drying, and rinsing.

3.4 Conclusions

This paper focuses on a simple, industrially viable method for synthesis of pure and stabilized mesoporous titanias of high surface area.

- 1) This work demonstrates that pure anatase and Al, La, Si, and Zr-stabilized titanias with pore diameters ranging from 2.5 to 11 nm were synthesized can be prepared using the solvent deficient method.

- 2) This method can be used to prepare a 22 mol% Al-TiO₂ calcined at 400°C having a surface area of 479 ± 39 m²/g which is apparently higher than previously reported for stabilized anatase products, including those that are commercially available. This product has a pore volume of 0.46 ± 0.04 cm³/g and a pore diameter of 2.9 ± 0.2.
- 3) Stabilized titanias demonstrate equivalent or higher thermal stability and surface area compared with pure anatase and previously reported pure and modified anatase materials after treatment at 400°C and 700°C.

3.5 Supplemental Information

Table S3.1 Average crystallite diameters, surface areas, pore volumes and pore diameters calculated from adsorption and desorption branches of ^adried and rinsed pure and modified anatase TiO₂.

Sample	^b Phase	Surface Area (m ² /g)	Pore volume (cm ³ /g)	^c d _{pore} (nm)	^d Width-Distribution 2σ (nm)
anatase	A	575	0.43	2.8	3.6
				6.4	2.6
5 mol% Al	A	384	0.44	4.6	3.9
				3.6	2.6
5 mol% Zr	A	369	0.43	4.5	4.0
				3.5	2.6
5 mol% Si	A	586	0.45	2.7	3.4
				3.2	2.7
5 mol% La	A	388	0.37	4.4	4.0
				3.5	2.5

a. Samples were dried at 100°C and degassed at 200°C

b. All materials are semi-amorphous anatase phase, with crystallites 2 nm or smaller

c. d_{pore} calculated from the adsorption branch is listed first and calculations from the desorption branch are listed second.

d. Represents the full width of the Gaussian distribution at half the maximum.

3.6 References

1. Fujishima, A.; Honda, K., Electrochemical photolysis of water at a semiconductor electrode. *Nature (London)* **1972**, *238* (5358), 37-8.
2. O'Regan, B.; Graetzel, M., A low-cost, high-efficiency solar cell based on dye-sensitized colloidal titanium dioxide films. *Nature (London)* **1991**, *353* (6346), 737-40.
3. Zou, Z.; Ye, J.; Sayama, K.; Arakawa, H., Direct splitting of water under visible light irradiation with an oxide semiconductor photocatalyst. *Nature (London, U. K.)* **2001**, *414* (6864), 625-627.
4. Zhang, Q.; Xu, H.; Yan, W., Highly ordered TiO₂ nanotube arrays: recent advances in fabrication and environmental applications - a review. *Nanosci. Nanotechnol. Lett.* **2012**, *4* (5), 505-519.
5. Tang, X.-h.; Wu, C.-z.; Li, B.-j.; Li, C.-w.; Lin, Y., New applications of nano titanium dioxide. *Meteorol. Environ. Res.* **2012**, *3* (1-2), 55-57.
6. Carp, O.; Huisman, C. L.; Reller, A., Photoinduced reactivity of titanium dioxide. *Prog. Solid State Chem.* **2004**, *32* (1-2), 33-177.
7. Haruta, M.; Tsubota, S.; Kobayashi, T.; Kageyama, H.; Genet, M. J.; Delmon, B., Low-temperature oxidation of carbon monoxide over gold supported on titanium dioxide, γ -ferric oxide, and cobalt tetraoxide. *J. Catal.* **1993**, *144* (1), 175-92.
8. Imai, H.; Date, M.; Tsubota, S., Preferential Oxidation of CO in H₂-Rich Gas at Low Temperatures over Au Nanoparticles Supported on Metal Oxides. *Catal. Lett.* **2008**, *124* (1-2), 68-73.

9. Edwards, J. K.; Carley, A. F.; Herzing, A. A.; Kiely, C. J.; Hutchings, G. J., Direct synthesis of hydrogen peroxide from H₂ and O₂ using supported Au-Pd catalysts. *Faraday Discuss.* **2008**, *138* (Nanoalloys), 225-239.
10. Kesavan, L.; Tiruvalam, R.; Ab, R. M. H.; bin, S. M. I.; Enache, D. I.; Jenkins, R. L.; Dimitratos, N.; Lopez-Sanchez, J. A.; Taylor, S. H.; Knight, D. W.; Kiely, C. J.; Hutchings, G. J., Solvent-Free Oxidation of Primary Carbon-Hydrogen Bonds in Toluene Using Au-Pd Alloy Nanoparticles. *Science (Washington, DC, U. S.)* **2011**, *331* (6014), 195-199.
11. Enache, D. I.; Edwards, J. K.; Landon, P.; Solsona-Espriu, B.; Carley, A. F.; Herzing, A. A.; Watanabe, M.; Kiely, C. J.; Knight, D. W.; Hutchings, G. J., Solvent-Free Oxidation of Primary Alcohols to Aldehydes Using Au-Pd/TiO₂ Catalysts. *Science (Washington, DC, U. S.)* **2006**, *311* (5759), 362-365.
12. Tahir, S. F.; Koh, C. A., Catalytic oxidation for air pollution control. *Environ. Sci. Pollut. Res. Int.* **1996**, *3* (1), 20-3.
13. Li, Y.; Liu, J.; Jia, Z., Morphological control and photodegradation behavior of rutile TiO₂ prepared by a low-temperature process. *Mater. Lett.* **2006**, *60* (13-14), 1753-1757.
14. Periyat, P.; Baiju, K. V.; Mukundan, P.; Pillai, P. K.; Warriar, K. G. K., High temperature stable mesoporous anatase TiO₂ photocatalyst achieved by silica addition. *Appl. Catal., A* **2008**, *349* (1-2), 13-19.
15. Calleja, G.; Serrano, D. P.; Sanz, R.; Pizarro, P., Mesoporous SiO₂-doped TiO₂ with enhanced thermal stability prepared by a soft-templating sol-gel route. *Microporous Mesoporous Mater.* **2008**, *111* (1-3), 429-440.

16. Yang, J.; Ferreira, J. M. F., Inhibitory effect of the Al₂O₃-SiO₂ mixed additives on the anatase-rutile phase transformation. *Mater. Lett.* **1998**, *36* (5-6), 320-324.
17. Liu, F.; Liu, C.-L.; Hu, B.; Kong, W.-P.; Qi, C.-Z., High-temperature hydrothermal synthesis of crystalline mesoporous TiO₂ with superior photo catalytic activities. *Appl. Surf. Sci.* **2012**, *258* (19), 7448-7454.
18. Lin, Y.-C.; Liu, S.-H.; Syu, H.-R.; Ho, T.-H., Synthesis, characterization and photocatalytic performance of self-assembled mesoporous TiO₂ nanoparticles. *Spectrochim. Acta, Part A* **2012**, *95*, 300-304.
19. Zimny, K.; Ghanbaja, J.; Carteret, C.; Stebe, M.-J.; Blin, J.-L., Highly ordered mesoporous titania with semi crystalline framework templated by large or small nonionic surfactants. *New J. Chem.* **2010**, *34* (10), 2113-2117.
20. Bian, Z.; Zhu, J.; Li, H., Synthesis of well ordered crystalline TiO₂ photocatalyst with enhanced stability and photoactivity. *Stud. Surf. Sci. Catal.* **2007**, *165* (Recent Progress in Mesoporous Materials), 317-322.
21. Chen, Y.; Lin, A.; Gan, F., Preparation of nano-TiO₂ from TiCl₄ by dialysis hydrolysis. *Powder Technol.* **2006**, *167* (3), 109-116.
22. Jia, H.; Zheng, Z.; Zhao, H.; Zhang, L.; Zou, Z., Nonaqueous sol-gel synthesis and growth mechanism of single crystalline TiO₂ nanorods with high photocatalytic activity. *Mater. Res. Bull.* **2009**, *44* (6), 1312-1316.
23. Li, Q.; Liu, B.; Li, Y.; Liu, R.; Li, X.; Li, D.; Yu, S.; Liu, D.; Wang, P.; Li, B.; Zou, B.; Cui, T.; Zou, G., Ethylene glycol-mediated synthesis of nanoporous anatase TiO₂ rods and rutile TiO₂ self-assembly chrysanthemums. *J. Alloys Compd.* **2009**, *471* (1-2), 477-480.

24. Ang, T. P.; Toh, C. S.; Han, Y.-F., Synthesis, Characterization, and Activity of Visible-Light-Driven Nitrogen-Doped TiO₂-SiO₂ Mixed Oxide Photocatalysts. *J. Phys. Chem. C* **2009**, *113* (24), 10560-10567.
25. Reddy, B. M.; Ganesh, I.; Khan, A., Stabilization of nanosized titania-anatase for high temperature catalytic applications. *J. Mol. Catal. A: Chem.* **2004**, *223* (1-2), 295-304.
26. Kim, J.; Song, K. C.; Foncillas, S.; Pratsinis, S. E., Dopants for synthesis of stable bimodally porous titania. *J. Eur. Ceram. Soc.* **2001**, *21* (16), 2863-2872.
27. Yang, J.; Ferreira, J. M. F., The effect of zirconia additive on the phase transition in a sol-gel-derived titania powder. *Mater. Res. Bull.* **1998**, *33* (3), 389-394.
28. Korosi, L.; Oszko, A.; Galbacs, G.; Richardt, A.; Zollmer, V.; Dekany, I., Structural properties and photocatalytic behavior of phosphate-modified nanocrystalline titania films. *Appl. Catal., B* **2007**, *77* (1-2), 175-183.
29. Lambourne, R.; Strivens, T. A.; Editors, *Paint and Surface Coatings--Theory and Practice, Second Edition (#9922)*. 1999; p 950 pp.
30. Woodfield, B. F.; Liu, S.; Boerio-Goates, J.; Liu, Q. Preparation of uniform nanoparticles of ultra-high purity metal oxides, mixed metal oxides, metals, and metal alloys. WO2007098111A2, 2012.
31. Patterson, A. L., The Scherrer formula for x-ray particle-size determination. *Phys. Rev.* **1939**, *56*, 978-82.
32. Pierce, C., Computation of pore sizes from physical adsorption data. *J. Phys. Chem.* **1953**, *57*, 149-52.
33. Orr, C., Jr.; Dallavalle, J. M., *Fine Particle Measurement-Size, Surface, and Pore Volume*. Macmillan Co.: 1959; p 353 pp.

34. Huang, B.; Bartholomew, C., H.; Woodfield, B. F., Facile synthesis of mesoporous alumina with tunable pore size: Effects of alcohols in precursor formation and calcination. *Microporous Mesoporous Mater.* **2013**, *177*, 37-46.
35. Liu, H.; Zhang, L.; Seaton, N. A., Sorption hysteresis as a probe of pore structure. *Langmuir* **1993**, *9* (10), 2576-82.
36. Rojas, F.; Kornhauser, I.; Felipe, C.; Esparza, J. M.; Cordero, S.; Dominguez, A.; Riccardo, J. L., Capillary condensation in heterogeneous mesoporous networks consisting of variable connectivity and pore-size correlation. *Phys. Chem. Chem. Phys.* **2002**, *4* (11), 2346-2355.
37. Niemark, A. V., Percolation theory of capillary hysteresis phenomena and its application for characterization of porous solids. *Stud. Surf. Sci. Catal.* **1991**, *62* (Character. Porous Solids 2), 67-74.
38. Parlar, M.; Yortsos, Y. C., Percolation theory of vapor adsorption-desorption processes in porous materials. *J. Colloid Interface Sci.* **1988**, *124* (1), 162-76.
39. Ball, P. C.; Evans, R., Temperature dependence of gas adsorption on a mesoporous solid: capillary criticality and hysteresis. *Langmuir* **1989**, *5* (3), 714-23.
40. Neimark, A. V.; Ravikovitch, P. I., Capillary condensation in MMS and pore structure characterization. *Microporous Mesoporous Mater.* **2001**, *44-45*, 697-707.
41. Neimark, A. V.; Ravikovitch, P. I.; Vishnyakov, A., Adsorption hysteresis in nanopores. *Phys. Rev. E: Stat. Phys., Plasmas, Fluids, Relat. Interdiscip. Top.* **2000**, *62* (2-A), R1493-R1496.
42. Monson, P. A., Contact Angles, Pore Condensation, and Hysteresis: Insights from a Simple Molecular Model. *Langmuir* **2008**, *24* (21), 12295-12302.

43. Nobe, K.; Hamidy, M.; Chu, C., Pore-size distributions of copper oxide-alumina catalysts. *J. Chem. Eng. Data* **1971**, *16* (3), 327-31.
44. Hanaor, D. A. H.; Assadi, M. H. N.; Li, S.; Yu, A.; Sorrell, C. C., Ab initio study of phase stability in doped TiO₂. *arXiv.org, e-Print Arch., Condens. Matter* **2012**, 1-21, arXiv:1210.7555v1 [cond-mat.mtrl-sci].
45. Hirano, M.; Nakahara, C.; Ota, K.; Inagaki, M., Direct formation of zirconia-doped titania with stable anatase-type structure by thermal hydrolysis. *J. Am. Ceram. Soc.* **2002**, *85* (5), 1333-1335.
46. Chen, B.; Zhang, H.; Gilbert, B.; Banfield, J. F., Mechanism of Inhibition of Nanoparticle Growth and Phase Transformation by Surface Impurities. *Phys. Rev. Lett.* **2007**, *98* (10), 106103/1-106103/4.
47. Smitha, V. S.; Baiju, K. V.; Perumal, P.; Ghosh, S.; Warriar, K. G., Hydrophobic, Photoactive Titania-Alumina Nanocrystallites and Coatings by an Aqueous Sol-Gel Process. *Eur. J. Inorg. Chem.* **2012**, *2012* (2), 226-233.
48. Wang, L.-Y.; Sun, Y.-P.; Xu, B.-S., Comparison study on the size and phase control of nanocrystalline TiO₂ in three Ti-Si oxide structures. *J. Mater. Sci.* **2008**, *43* (6), 1979-1986.
49. Rajesh, K. S.; Pillai, S. C.; Hareesh, U. S.; Mukundan, P.; Warriar, K. G. K., Synthesis of thermally stable, high surface area anatase-alumina mixed oxides. *Mater. Lett.* **2000**, *43* (5-6), 286-290.
50. Tsai, C.-Y.; Hsi, H.-C.; Bai, H.; Fan, K.-S.; Sun, H.-D., Single-step synthesis of Al-doped TiO₂ nanoparticles using non-transferred thermal plasma torch. *Jpn. J. Appl. Phys.* **2012**, *51* (1, Pt. 2), 01AL01/1-01AL01/6.

51. Lee, D.-W.; Park, S.-J.; Ihm, S.-K.; Lee, K.-H., One-Pot Synthesis of Pt-Nanoparticle-Embedded Mesoporous Titania/Silica and Its Remarkable Thermal Stability. *J. Phys. Chem. C* **2007**, *111* (21), 7634-7638.
52. Sing, K. S. W.; Everett, D. H.; Haul, R. A. W.; Moscou, L.; Pierotti, R. A.; Rouquerol, J.; Siemieniewska, T., Reporting physisorption data for gas/solid systems with special reference to the determination of surface area and porosity (Recommendations 1984). *Pure Appl. Chem.* **1985**, *57* (4), 603-19.
53. Rouquerol, F.; Rouquerol, J.; Sing, K., *Adsorption by Powders and Porous Solids: Principles, Methodology and Applications*. Academic: 1999.
54. Sing, K. S. W.; Williams, R. T., Physisorption hysteresis loops and the characterization of nanoporous materials. *Adsorpt. Sci. Technol.* **2004**, *22* (10), 773-782.
55. Thommes, M., Recent advances in the characterization of mesoporous materials by physical adsorption. *Annu. Rev. Nano Res.* **2010**, *3*, 515-555.
56. Zhou, Z.; Zeng, T.; Cheng, Z.; Yuan, W., Preparation and Characterization of Titania-Alumina Mixed Oxides with Hierarchically Macro-/Mesoporous Structures. *Ind. Eng. Chem. Res.* **2011**, *50* (2), 883-890.
57. Bineesh, K. V.; Kim, D.-K.; Park, D.-W., Synthesis and characterization of zirconium-doped mesoporous nano-crystalline TiO₂. *Nanoscale* **2010**, *2* (7), 1222-1228.
58. Sibü, C. P.; Kumar, S. R.; Mukundan, P.; Warriar, K. G. K., Structural Modifications and Associated Properties of Lanthanum Oxide Doped Sol-Gel Nanosized Titanium Oxide. *Chem. Mater.* **2002**, *14* (7), 2876-2881.
59. Ribeiro, M. A.; Neiva, L. S.; Kiminami, R. H. A.; de, O. J. B. L.; Gama, L., Evaluation of calcined temperature on the structural and morphological characterization of TiO₂ doped

- with Zr nanopowders obtained by the Pechini method. *Mater. Sci. Forum* **2012**, 727-728 (Pt. 2, Advanced Powder Technology VIII), 1393-1397.
60. Subramanian, V.; Ni, Z.; Seebauer, E. G.; Masel, R. I., Synthesis of High-Temperature Titania-Alumina Supports. *Ind. Eng. Chem. Res.* **2006**, 45 (11), 3815-3820.
61. Zhu, J.; Yang, J.; Bian, Z.-F.; Ren, J.; Liu, Y.-M.; Cao, Y.; Li, H.-X.; He, H.-Y.; Fan, K.-N., Nanocrystalline anatase TiO₂ photocatalysts prepared via a facile low temperature nonhydrolytic sol-gel reaction of TiCl₄ and benzyl alcohol. *Appl. Catal., B* **2007**, 76 (1-2), 82-91.
62. Roy, B.; Ahrenkiel, S. P.; Fuierer, P. A., Controlling the size and morphology of TiO₂ powder by molten and solid salt synthesis. *J. Am. Ceram. Soc.* **2008**, 91 (8), 2455-2463.
63. BV., E. S. Titanium and Zirconium Dioxides.
http://www.eurosupport.nl/pdf/titanium_zirconium_dioxides.pdf.

Chapter 4: Optimizing the Synthesis and Properties of Al- modified Anatase Catalyst Supports by Statistical Experimental Design

4.1 Introduction

TiO₂ is an excellent support material for metal and metal oxide catalysts in a number of oxidative synthesis and pollution-control reactions e.g. oxidation of CO at low temperatures,¹ preferential oxidation of CO in H₂/CO mixtures,² low-temperature, direct synthesis of hydrogen peroxide,³ complete oxidation of volatile organic compounds,⁴ and also as a support and promoter for vanadium oxide in selective catalytic reduction of NO_x.⁵ These and other reactions involving catalysts supported on TiO₂ have been reviewed elsewhere.⁶ Each application requires specific anatase or anatase/rutile properties such as surface area, pore volume, and pore diameter. Given the complexity involved in preparing catalyst supports, many synthesis variables are expected to affect these properties. Optimizing anatase supports has been the subject of much research; however, most studies have used a traditional approach of varying one factor at a time while holding all other factors constant. Results from the one factor at a time approach are often misleading and inconclusive because (a) only a small amount of the factor space is covered, (b) interactions between factors are unaccounted for, (c) statistical relevance of data is unknown, and (d) full analysis of all synthesis parameters using this approach is nearly impossible due to the large number of experiments required.

Statistically designed experiments (design of experiments or DOEs) are excellent tools to identify factor effects and interactions and determine conditions needed to obtain the desired

properties in a minimum number of experiments. A few DOEs have been used to study catalysts and catalyst supports, primarily to optimize catalytic processes or the synthesis and dispersion of the catalyst onto a support, as opposed to studying the properties of the support itself.⁷⁻¹³

While making an important contribution, these studies have nonetheless had a limited impact in the methodology used in the catalysis community. Thus, the majority of work on catalyst preparation continues to use a one factor at a time approach. The limited impact may be due to (a) narrow audiences of journals in which they were published, (b) the limited scope of variables studied (generally studying 4 variables or less) and therefore failed to demonstrate the advantages of DOEs relative to a conventional design, and (c) a general lack of knowledge of new statistical methods. Nevertheless, the benefits of using DOEs in the study of process variables are dramatic and clear, but this has yet to be demonstrated effectively in the literature. To our knowledge, there are no previously published studies using statistically designed experiments to optimize the synthesis of anatase catalyst supports.

We recently described a simple method which enables preparation of anatase catalyst supports of high surface area and unusually high thermally stable. Moreover, this method enables preparation of anatase having a wide range of pore properties.¹⁴ While this method is relatively simple, more than ten variables must be optimized to maximize surface area and pore volume, and to control pore diameter. Since analyzing variables individually is inefficient and ineffective, two DOEs, (1) a traditional fractional factorial design and (2) a definitive screening design, were used to optimize surface area and pore volume, and to control pore diameter in a reasonable number of experiments. Traditional fractional factorial designs are among the most widely used DOEs, however, main effect factors are often confounded with one or more two-factor interactions, requiring further experimentation (as observed in this work). Screening designs are

useful in assessing the relative impact of a large number of factors in relatively few trials; however, most screening models only allow for a two-level system (three-level is necessary to assess the curvature in the factor-response relationship) and also face problems with confounded interactions. The definitive screening design (DSD) used in this study is based on a new model proposed by Jones and Nachtsheim in 2011¹⁵ which allows for the study of many factors at three levels in only $2k + 1$ (k = number of factors) experiments. DSD is a one-step alternative to other two step DOEs because it can be used to estimate (1) main effects while avoiding any confounded second-order effects, (2) two factor interactions, and (3) the full quadratic model in any three factors, thereby rendering further experimentation unnecessary in most cases. DSD was awarded the American Statistical Association's 2012 Statistics in Chemistry Award for a collaboration using this design to optimize catalytic sequestration of CO₂ and one example of applying DSD to a physical system, characterizing a protein-cross linking reaction,¹⁶ has been published in the public literature, however, DSD is still generally unknown.

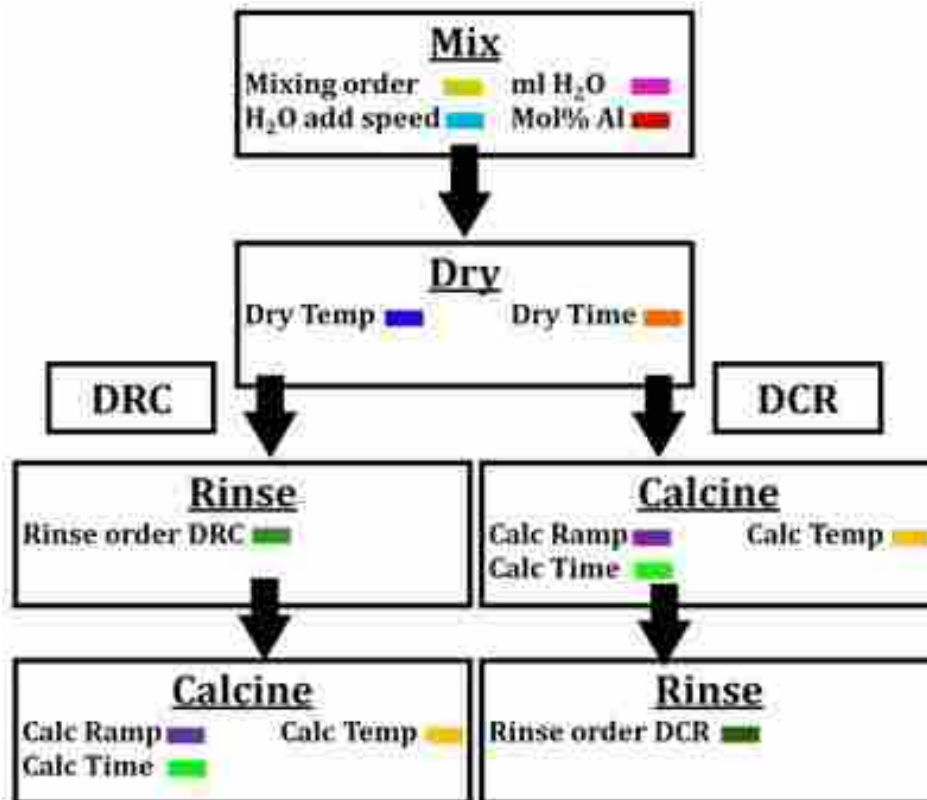
In this study we show that through the use of DOEs (a) the surface area and pore structure of anatase supports can be predicted and (b) unusually high surface areas and thermal stabilities can be realized. This work also demonstrates the successful use of DSD to separate and identify the effects of ten variables with no confounded interactions, an approach that is generally applicable to materials and process optimization.

4.2 Experimental

4.2.1 Sample Preparation

Samples were prepared following a general solvent deficient method that can be used to synthesize many metal and mixed metal oxides.^{14, 17} A schematic of the synthesis is found in

Scheme 4.1 Approximately 3.0 ml TiCl_4 , 0.54 g $\text{Al}(\text{NO}_3)_3 \cdot 9\text{H}_2\text{O}$ and 9.1 g NH_4HCO_3 (ABC) were mixed together (amounts listed are for a 5 mol% Al-modified anatase, 5 – 25 mol% Al ratios were examined). The order in which starting materials were mixed was varied in design of experiment (DOE) 1 but held constant in DOE 2 (TiCl_4 and $\text{Al}(\text{NO}_3)_3 \cdot 9\text{H}_2\text{O}$ mixed together in a mortar and pestle for one minute, after which ABC was added and mixed for an additional minute). Distilled H_2O was added in the amount and at the speed outlined in the DOEs 1 and 2. The slurry was then mixed for five minutes to form a stabilized anatase precursor. For DRC samples, the slurry was dried in air, rinsed with two liters of distilled water using a vacuum filtration system at room temperatures, and then immediately calcined. For DCR samples, the slurry was dried in air, calcined, rinsed with two liters of distilled water using a vacuum filtration system at room temperatures, and subsequently dried 100°C for 24 hours. Drying temperatures and times as well as calcination temperatures, times, and ramp rates were specified by DOEs 1 and 2 and are listed in Tables 4.2 – 4.4.



Scheme 4.1 Synthesis schematic. DRC rinsing order = dry, rinse, calcine. DCR rinsing order = dry, calcine, rinse.

4.2.2 Sample Design

4.2.2.1 DOE 1: preliminary screening experiments

Ten synthesis variables that may affect the surface area, pore diameter, and pore volume of Al-modified anatase were identified based on previous experiments and are listed in Table 4.1. To study all 10 factors at two levels each in a full factorial design would require $2^{10} = 1024$ experiments. Instead, a $1/64^{\text{th}}$ fractional factorial resolution III minimum aberration experiment (2_{III}^{10-6}) was used for screening.¹⁸ The design and resulting data are shown in Table 4.2. The design is listed in the standard order but experiments were performed in a random order to prevent biases and to justify the validity of results.

4.2.2.2 DOE 2: definitive screening experiments

Following the preliminary resolution III fractional factorial DOE 1, a definitive screening design was used.¹⁵ This design requires only $2k + 1$ experiments to study k factors at three levels. Based on results from DOE 1, Factor A, mixing order, was held constant (TiCl_4 was first mixed with $\text{Al}(\text{NO}_3)_3 \cdot 9\text{H}_2\text{O}$) and Factor D was separated into two trials, dry-rinse-calcine (DRC) and dry-calcine-rinse (DCR). The remaining eight factors (B, C, E, F, G, H, I, and J) were studied in 17 experiments for both levels of Factor D-order of rinsing. The design and results are shown Tables 4.3 and 4.4. Surface area, pore diameter, and pore volume were analyzed using Jmp Pro version 10.^{15, 19-21}

4.2.3 Sample Characterization

X-ray diffraction patterns were collected using a PANalytical X'Pert Pro diffractometer (Cu- $\text{K}_{\alpha 1}$ radiation, $\lambda = 1.540598 \text{ \AA}$) at 45 kV and 40 mA over the 2θ range of $10 - 90^\circ$ at scanning rates of $0.30 - 0.44^\circ/\text{min}$. Average crystallite diameters were estimated using the Scherrer equation and confirmed using transmission electron microscopy (TEM).²² TEM measurements were performed on a Tecnai F20 Analytical STEM operating at 200 keV. The samples were dispersed in ethanol and deposited on copper grids (lacey carbon fiber, 400 mesh copper grids, Ted Pella, Inc.).

Full-range N_2 sorption isotherms were collected at 77 K using a Micromeritics TriStar 3020 surface analyzer. Samples of 0.25 – 0.50 g were degassed at 200°C for 12 – 24 hours prior to collecting data. Pore volumes were calculated from the adsorption isotherm at a relative pressure of 0.98 and specific surface areas were calculated using the Brunauer-Emmett-Teller (BET) method from a P/P^0 range of 0.05 to 0.2. H2 type pore diameters were calculated using a modified Pierce method with structural corrections for pore area and volume.^{23, 24} H3 and H2/H3

hybridized pore widths were calculated using the newly developed SPG model involving slit geometry for the Kelvin equation, which also incorporates structural corrections for area and volume.²⁵ For a more detailed discussion see reference.²⁵ For ease of discussion, pore widths and pore diameters will both be referred to as pore diameters. Pore diameters were calculated from either adsorption or desorption branches, depending on the shape of the hysteresis loop. For example, adsorption branch calculations are considered more accurate for H2 type pores, since evaporation of the condensate during desorption is significantly constrained and delayed by the pore necks with “ink-bottle” pore geometry and the connectivity of the network.²⁶⁻²⁹ For H3 type hysteresis with slit-like pores, the desorption branch is preferred due to delayed condensation observed in the adsorption process.³⁰⁻³³

4.3 Results

4.3.1 XRD and TEM

XRD data confirms all materials are anatase TiO₂. Crystallite diameters calculated using the Scherrer formula range from 2 – 20 nm for different samples, each have a tight crystallite size distribution and are in good agreement with TEM micrographs (see Tables 4.2 – 4.4). XRD and TEM reveal changes in crystallite size and pore structure after samples are rinsed prior to rather than after calcination (Tables 4.2 – 4.4). These changes as well as the statistical analysis of DOE 1 led us to separate the DRC and DCR routes into separate experiments.

4.3.2 Pore Diameter Calculations

Pore diameters for DOE 1, DOE 2, and the confirmatory experiments are listed in Tables 4.2 – 4.5. All materials were Type IV mesoporous materials with no evident microporosity. Pore diameters in DOE 1 were calculated using the adsorption branch from the modified Pierce model

(cylindrical pore model).^{23, 24} Pore diameters in DOE 2 were calculated using either the cylindrical model or the newly developed SPG (slit) model based on the hysteresis of the isotherms as well as mesopore geometry evident in TEM micrographs.²⁵ In most cases, calculations from both models agreed well; however, data from several samples were clearly best fitted with either a cylindrical or slit model. Isotherms of DCR materials were mainly H3 associated with slit-like pores (Figure 4.1); thus, pore diameters were calculated from the desorption branch using the SPG model.^{25, 30-33} Two types of isotherms were observed for DRC, H2 (samples calcined at 400°C) and H2/H3 hybridized (samples calcined at 550°C and 700°C) (Figure 4.1). H2 hysteresis is associated with networked, ink-bottle pores; accordingly, these pore diameters were calculated from the adsorption branch using a cylindrical model to avoid problems associated with percolation encountered in the desorption branch.²⁶⁻²⁹ H2/H3 hybridized hysteresis is likely due to a connected, channel-like, irregular pore structure.¹⁴ There is no evidence in the isotherms of delayed condensation or percolation; therefore, pore diameters were calculated from both the adsorption branch and desorption branch using the SPG model. The adsorption branch gives information on the wider pore regions and the desorption branch gives information on constricted regions.¹⁴ To simplify the statistical analysis only the adsorption branch calculations were used. Three samples, DRC samples 5, 9, and 13, exhibited bimodal pore size distributions. Again, to simplify the statistical analysis, only the smaller diameter, which had the largest volume in each case, was used.

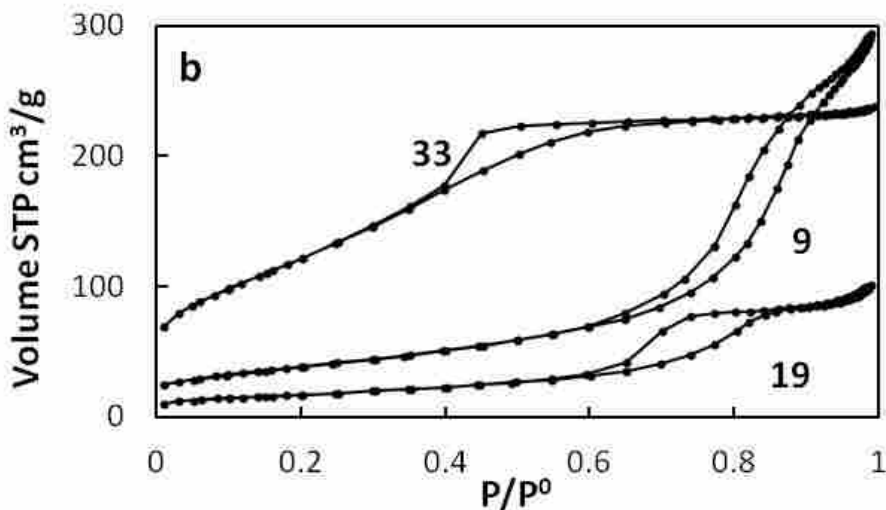


Figure 4.1 Isotherm examples. Sample 9 (H3 type, slit-like pores) is representative of DCR materials. Sample 19 (H2/H3 hybridized, irregular channel-like pores) and sample 33 (H2 type, ink-bottle pores) are representative of the two types of pore structures observed in DRC samples. The range of pore structures demonstrates the importance of model selection in pore diameter analysis.











4.3.3 Statistical Analysis

4.3.3.1 DOE 1

A set of traditional screening experiments (Table 4.2) was designed, conducted, and analyzed to identify which of the ten synthesis factors (Table 4.1) might have the largest effects on the surface area, pore diameter, and pore volume of Al-modified anatase supports. Factor effects and directions determined in DOE 1 can be found in the Supplementary Information, Table S4.1. A positive direction indicates increasing the factor level causes an increase in the response while a negative direction indicates increasing the factor level causes a decrease in the response. The factors with the largest effects were identified to be rinsing order (D), calcination temperature (H), amount of H₂O (C), speed of H₂O addition (B), and drying temperature (F), while mixing order (A) exhibited a negligible effect. Because of the highly fractional nature of

the design, many factors and two-factor interactions were confounded (i.e. inseparable) and follow-up experiments were necessary to fully confirm the presence, size, and direction of significant effects and to develop models to predict synthesis conditions necessary to produce anatase with various properties. Mixing order (A) was eliminated from further study and was held constant in DOE 2. Rinsing order (D) exhibited a large effect and therefore, two separate studies, in which rinsing order was held constant, were conducted in DOE 2.

Table 4.1 Factors and levels for DOE 1 and DOE 2.

Factor	Variables	Levels	
		DOE 1	DOE 2
^a A	 Mixing Order	Ti/Al, Al/ABC	Ti/Al
^b B	 Speed of H2O Addition	S, F	S, M, F
C	 ml H2O	7, 25	5, 20, 35
^c D	 Order of Rinsing	DRC, DCR	DRC, DCR
E	 Drying Time (hrs)	3, 24	3, 14, 24
F	 Drying Temp (°C)	25, 100	25, 63, 100
G	 Calcination Ramp rate (°C /min)	2, 20	2, 12, 22
H	 Calcination Temp (°C)	400, 700	400, 550, 700
I	 Calcination Time (hrs)	2, 20	2, 11, 20
J	 Mol% Al	5, 22	5, 15, 25

a. Ti/Al = TiCl₄ + Al(NO)₃·9H₂O, then ABC. Al/ABC = Al(NO)₃·9H₂O + ABC, then TiCl₄. ABC = NH₄HCO₃. Held constant in DOE 2 at TiCl₄/Al(NO)₃

b. S = slow, M = medium, F = fast

c. DRC = dry, rinse, calcine. DCR = dry, calcine, rinse. DOE 2 separated into DRC experiments and DCR experiments.

Table 4.2 DOE 1 design and results.

	A	B	C	D	E	F	G	H	I	J	Crystallite Diameter (nm)	Surface Area (m ² /g)	Pore Volume (cm ³ /g)	^b Pore Diameter (nm)
1	1	Slow	7	DRC	24	25	2	700	2	5	18	50	0.11	6.4
2	2	Slow	7	DRC	3	25	20	700	20	22	9	67	0.12	5.7
3	1	Fast	7	DRC	3	100	2	700	20	22	14	104	0.21	6.1
4	2	Fast	7	DRC	24	100	20	700	2	5	12	61	0.16	7.6
5	1	Slow	25	DRC	3	100	20	400	2	22	2	375	0.33	3.5
6	2	Slow	25	DRC	24	100	2	400	20	5	6	332	0.35	3.5
7	1	Fast	25	DRC	24	25	20	400	20	5	8	203	0.20	3.7
8	2	Fast	25	DRC	3	25	2	400	2	22	6	177	0.31	6.5
9	1	Slow	7	DCR	3	100	20	400	20	5	8	123	0.36	10.1
10	2	Slow	7	DCR	24	100	2	400	2	22	2	369	0.31	3.6
11	1	Fast	7	DCR	24	25	20	400	2	22	6	169	0.52	15.6
12	2	Fast	7	DCR	3	25	2	400	20	5	8	150	0.49	12.3
13	1	Slow	25	DCR	24	25	2	700	20	22	8	124	0.41	12.1
14	2	Slow	25	DCR	3	25	20	700	2	5	10	95	0.46	17.3
15	1	Fast	25	DCR	3	100	2	700	2	5	10	308	0.84	14.9
16	2	Fast	25	DCR	24	100	20	700	20	22	10	94	0.41	15.3

a. mixing order 1: ABC & AlNO₃, mixing order 2: TiCl₄ & AlNO₃

b. Pore diameters calculated from the adsorption branch using a cylindrical method.

Table 4.3 DOE 2 (rinsing order ^aDRC) design and results.

	B	C	E	F	G	H	I	J				
	H ₂ O add speed	H ₂ O (ml)	Dry Time (hrs)	Dry Temp (°C)	Calc Ramp (°C/min)	Calc Temp (°C)	Calc Time (hrs)	Mol% Al	^b Crystallite Diameter (nm)	Surface Area (m ² /g)	Pore Volume (cm ³ /g)	^c Pore Diameter (nm)
1	Medium	20	14	63	12	550	11	0.15	8	246	0.31	5.4
2	Fast	5	24	63	22	700	2	0.05	11	63	0.15	11.4
3	Medium	35	3	25	22	400	2	0.05	2-3, A	219	0.23	4.4
4	Medium	5	24	100	2	700	20	0.25	9	194	0.25	5.4
5	Fast	20	24	25	2	400	2	0.25	2, A	363	0.28	3.8
6	Fast	35	3	100	12	700	2	0.25	8	130	0.26	11.4
7	Slow	35	24	25	22	700	11	0.25	8	128	0.25	9.5
8	Slow	35	24	100	2	550	2	0.05	7	142	0.23	5.9
9	Fast	35	24	100	22	400	20	0.15	6	334	0.39	3.9
10	Fast	5	3	25	22	550	20	0.25	9	112	0.23	10.1
11	Slow	5	24	25	12	400	20	0.05	9	240	0.22	3.6
12	Slow	5	3	25	2	700	2	0.15	9	83	0.13	8.1
13	Slow	35	3	63	2	400	20	0.25	2, A	394	0.37	4.3
14	Fast	5	3	100	2	400	11	0.05	9	209	0.21	4.5
15	Fast	35	14	25	2	700	20	0.05	12	58	0.16	14.1
16	Slow	5	14	100	22	400	2	0.25	2, A	450	0.36	4.2
17	Slow	20	3	100	22	700	20	0.05	12	60	0.16	12.9

a. Dry, rinse, calcine synthesis route.

b. A = fairly amorphous according to XRD due to small crystallite sizes. TEM ring patterns confirm some level of crystallinity.

c. Pore diameters of samples 3, 5, 9, 11, 13, 14, and 16 were calculated from the adsorption branch using a cylindrical model. All other pore diameters were calculated from the desorption branch using the SPG (slit) model.

Table 4.4 DOE 2 (rinsing order ^aDCR) design and results.

	B	C	E	F	G	H	I	J				
	H ₂ O add speed	H ₂ O (ml)	Dry Time (hrs)	Dry Temp (°C)	Calc Ramp (°C/min)	Calc Temp (°C)	Calc Time (hrs)	Mol% Al	Crystallite Diameter (nm)	Surface Area (m ² /g)	Pore Volume (cm ³ /g)	^b Pore Diameter (nm)
1	Fast	5	3	100	2	400	11	0.05	8	127	0.38	10
2	Slow	5	14	100	22	400	2	0.25	6	190	0.33	6.6
3	Fast	5	3	25	22	550	20	0.25	11	102	0.34	11.2
4	Slow	20	3	100	22	700	20	0.05	10	82	0.36	14.6
5	Slow	35	24	25	22	700	11	0.25	10	133	0.34	8.5
6	Slow	35	24	100	2	550	2	0.05	8	137	0.39	9.3
7	Medium	35	3	25	22	400	2	0.05	7	139	0.41	10.3
8	Fast	35	24	100	22	400	20	0.15	7	138	0.44	18.6
9	Slow	5	24	25	12	400	20	0.05	7	140	0.45	11.0
10	Fast	5	24	63	22	700	2	0.05	11	81	0.34	15.3
11	Slow	5	3	25	2	700	2	0.15	8	126	0.40	11.8
12	Fast	35	14	25	2	700	20	0.05	13	97	0.41	13.3
13	Medium	5	24	100	2	700	20	0.25	6	148	0.38	9.0
14	Medium	20	14	63	12	550	11	0.15	7	119	0.34	12.5
15	Slow	35	3	63	2	400	20	0.25	6	192	0.44	7.8
16	Fast	20	24	25	2	400	2	0.25	6	182	0.56	16.9
17	Fast	35	3	100	12	700	2	0.25	7	137	0.52	14.0

a. Dry, calcine, rinse synthesis route.

b. Pore diameters were calculated from the desorption branch using the SPG (slit) model.

4.3.3.2 DOE 2

DOE 2 was designed and conducted to clarify ambiguity observed in DOE 1. A definitive screening design was used because they are particularly efficient at separating large effect factors from many small effect factors without any confounded interactions in a small number of experiments. Eight factors (B, C, E, F, G, H, I, and J) were studied at three levels, with 17 trials for both mixing orders DRC and DCR, totaling 34 trials. Experimental design and results are listed in Tables 4.3 (DRC) and 4.4 (DCR).

Regression subset selection methods were used to develop prediction Equations (4.1) – (4.6) for surface area, pore diameter, and pore volume which can be used with the solver or goal-seek function in an Excel® spreadsheet to identify conditions needed to produce the desired surface area and porosity. These equations are valid within the range of the factors tested and predictions outside these ranges may be inaccurate. R^2 measures the variation in observed responses. Standard deviations of the experimental errors were estimated from the mean squared errors. Figure 4.2 shows the relative importance of the factors in the prediction equations. Results from DOE 1 agree well with results from DOE 2 with some additions. Specific factor effects are discussed below.

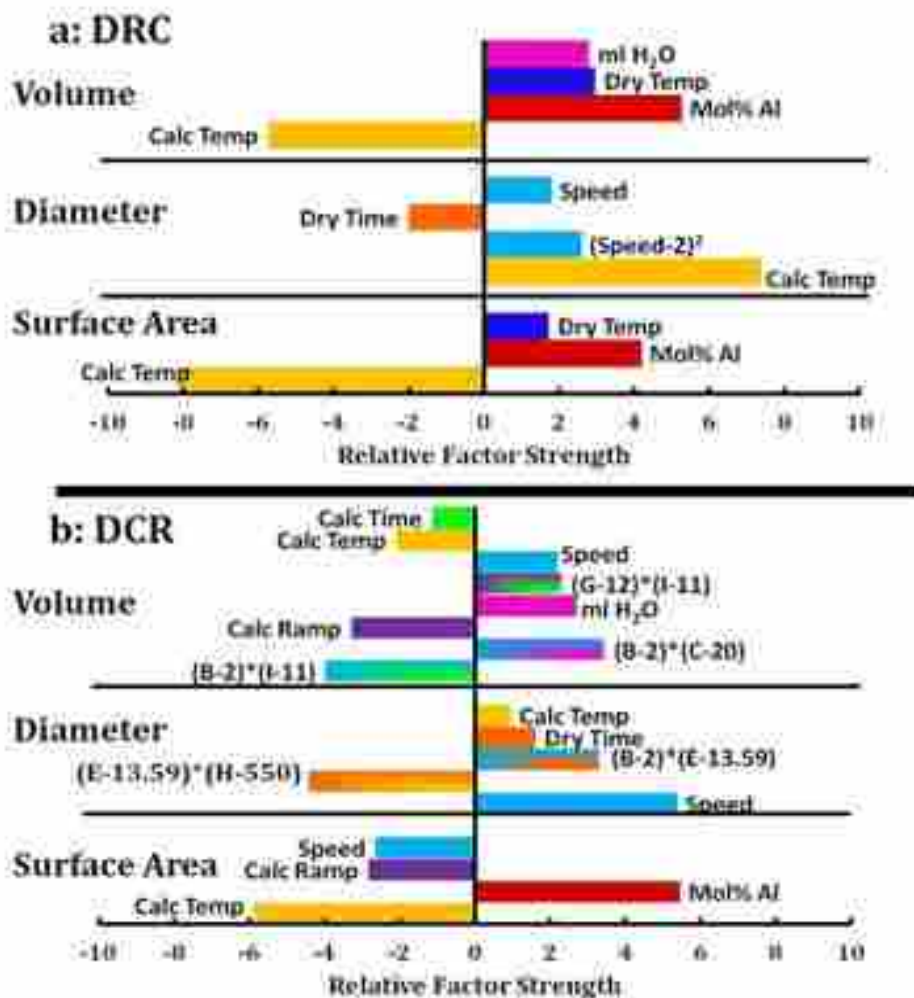


Figure 4.2 Factors and interactions that significantly affect the surface area, pore diameter, and pore volume of (a) DRC and (b) DCR materials based on DOE 2 results. A positive direction indicates increasing the factor level causes an increase in the response while a negative direction indicates increasing the factor level causes a decrease in the response. Factor labels: B, speed = H₂O addition speed, C = ml H₂O, E = dry time, G = calcination ramp rate, H = calcination temperature, I = calcination time.

Surface Area

Relative factor strengths and directions are summarized in Figure 4.2 and maximum surface areas are predicted to be 389 m²/g (DRC route) and 195 m²/g (DCR route) (Eqs 4.1 and 4.2). Surface area increased with increasing mol% Al or decreasing calcination temperature for

both DRC and DCR samples. In addition to these factors, surface area of DRC samples increased with increasing drying temperature, and surface area of DCR samples increased with decreasing H₂O addition speed or decreasing calcination ramp rate. No other factors or interactions significantly affected surface area. Prediction equations (4.1) and (4.2) can be used to predict the surface area expected under various synthesis conditions.

$$\begin{aligned} \text{DRC Surface Area (m}^2/\text{g)} &= 471.33 + 0.06024 (\text{drying temp}) - 0.71074 (\text{calc temp}) + \\ &555.99 (\text{mol\% Al}) \\ R^2 &= 0.866 \quad \text{standard deviation} = \pm 118 \quad (4.1) \end{aligned}$$

$$\begin{aligned} \text{DCR Surface Area (m}^2/\text{g)} &= 215.0751 - 9.7753 (\text{H}_2\text{O add speed}) - 1.0464 (\text{calc ramp}) - \\ &0.14456 (\text{calc temp}) + 199.946 (\text{mol\% Al}) \\ R^2 &= 0.868 \quad \text{standard deviation} = \pm 46 \quad (4.2) \end{aligned}$$

Pore Diameter

Figure 4.2 shows the relative factor strengths and directions. Predicted pore diameters that may be obtained using this technique range from 1 – 12 nm (DRC) and 8 – 18 nm (DCR) (Eqs 4.3 and 4.4). Pore diameters for DCR materials are expected to be larger on average compared with DRC materials. In addition to rinsing order, calcination temperature, H₂O addition speed, and drying time significantly affected pore diameter. A quadratic effect for H₂O addition speed was significant for DRC samples, while interactions between drying temperature and H₂O addition speed, and drying temperature and calcination temperature were observed for DCR samples. Pore diameters of DRC samples are predicted to be minimized using a medium

H₂O addition speed, long drying time, and low calcination temperature. Pore diameters of DCR samples are predicted to be minimized using a slow H₂O addition speed, short dry time, and low calcination temperature. Prediction equations (4.3) and (4.4) and may be used to understand interactions between factors and predict the pore diameter expected for various synthesis conditions.

$$\begin{aligned} \text{DRC Pore Diameter (nm)} &= -6.962 + 0.7664 (\text{H}_2\text{O add speed}) - 0.0871 (\text{dry time}) + \\ &0.02104 (\text{calc temp}) + 2.6467 (\text{H}_2\text{O add speed} - 2)^2 \\ R^2 &= 0.85 \quad \text{standard deviation} = \pm 3.96 \quad (4.3) \end{aligned}$$

$$\begin{aligned} \text{DCR Pore Diameter (nm)} &= 5.3702 + 2.1347 (\text{H}_2\text{O add speed}) + 0.06015(\text{dry time}) + \\ &0.000244 (\text{calc temp}) + 0.1364473 (\text{H}_2\text{O add speed} - 2) \times (\text{dry time} - 13.5882) - \\ &0.001222(\text{dry time} - 13.5882) \times (\text{calc temp} - 550.0) \\ R^2 &= 0.861 \quad \text{standard deviation} = \pm 3.8 \quad (4.4) \end{aligned}$$

Pore Volume

The relative factor strengths and directions can be seen in Figure 4.2 maximum pore volumes are predicted to be 0.39 cm³/g (DRC route) and 0.59 cm³/g (DCR route) (Eqs 4.5 and 4.6). The order of rinsing exhibited a large effect on pore volume and pore volumes of DCR materials are expected to be larger on average compared with DRC materials. In addition to the order of rinsing, calcination temperature, ml H₂O, drying temperature, and the amount of Al dopant were found to be statistically significant in maximizing the pore volume of DRC samples. The pore volume of DCR samples was affected by order of rinsing, calcination temperature, ml H₂O, H₂O addition speed, calcination ramp rate, and calcination time, as well as several

interactions between these factors (Figure 4.2). Pore volumes of DRC samples are predicted to be maximized using the maximum ml of H₂O, a high drying temperature, and a low calcination temperature. Pore volumes of DCR samples are predicted to be maximized using the maximum amount of H₂O, a fast H₂O addition speed, a slow ramp rate, a low calcination temperature, and a short calcination time. Prediction equations (4.5) and (4.6) can be used to understand factor interactions and determine the pore volume expected under various synthesis conditions.

$$\begin{aligned} \text{DRC Pore Volume (cm}^3/\text{g)} &= 0.28646 + 0.001619 (\text{ml H}_2\text{O}) + 0.0006842 (\text{dry temp}) - \\ &0.000334 (\text{calc temp}) + 0.45857 (\text{mol\% Al}) \\ R^2 &= 0.865 \quad \text{standard deviation} = \pm 0.08 \quad (4.5) \end{aligned}$$

$$\begin{aligned} \text{DCR Pore Volume (cm}^3/\text{g)} &= 0.44548 + 0.01862 (\text{H}_2\text{O add speed}) + 0.001532 (\text{ml H}_2\text{O}) - \\ &0.002819 (\text{calc ramp}) - 0.00012 (\text{calc temp}) - 0.0011 (\text{calc time}) + \\ &0.002155 (\text{H}_2\text{O add speed} - 2.0) \times (\text{ml H}_2\text{O} - 20) - 0.004226 (\text{H}_2\text{O} - 2.0) \times (\text{calc time} - 11) + \\ &0.0002402 (\text{calc ramp} - 12) \times (\text{calc time} - 11) \\ R^2 &= 0.873 \quad \text{standard deviation} = \pm 0.10 \quad (4.6) \end{aligned}$$

4.3.4 Confirmation Trials

Confirmation trials were run to verify the accuracy of the prediction equations. The conditions used are listed in Table 4.5 and the observed and predicted surface areas, pore volumes, and pore diameters (each based on two sample preparations) are shown in Figure 4.3. With the exception of the pore diameter of sample 3, the observed values for all trials were within the 95% confidence interval of the predicted values. Prediction equations for DCR

materials were slightly more accurate and more precise (based on the standard deviations of the experimental errors) than the equations for DRC materials. Smaller pore diameter ranges of 2.93 – 6.16 nm and larger pore volume ranges of 0.12 – 0.43 cm³/g were observed in the DRC confirmatory experiments, compared with the pore diameter ranges of 3.56 – 14.05 nm and pore volume ranges of 0.13 – 0.39 cm³/g observed in DOE 2 (Table 4.3, used to fit equations (4.3) and (4.5)). The different ranges of pore volumes and diameters between DOE 2 trials and the confirmation trials suggest extra variability in the DRC experiments, unaccounted for by the prediction limits of equations (4.3) and (4.5), due to unknown changes between DOE 2 trials and confirmatory experiments. Accuracy and precision of the prediction equations could be improved by incorporating additional trials and considering additional synthesis factors.

Table 4.5 Experimental conditions for confirmatory trials.

^a Route	Trial	B	C	E	F	G	H	I	J
DRC	1	1	35	24	100	22	400	2	17
	2	1	35	24	100	22	400	2	25
	3	3	35	3	25	22	700	2	17
	4	2	35	24	25	22	400	2	17
	5	1	35	13	65	22	552	2	17
DCR	6	1	35	24	100	22	400	2	17
	7	1	35	24	100	22	400	2	25
	8	3	35	3	25	22	700	2	17
	9	2	35	24	25	22	400	2	17
	10	1	35	13	65	22	552	2	17

a. DRC = dry, rinse, calcine. DCR = dry, calcine, rinse

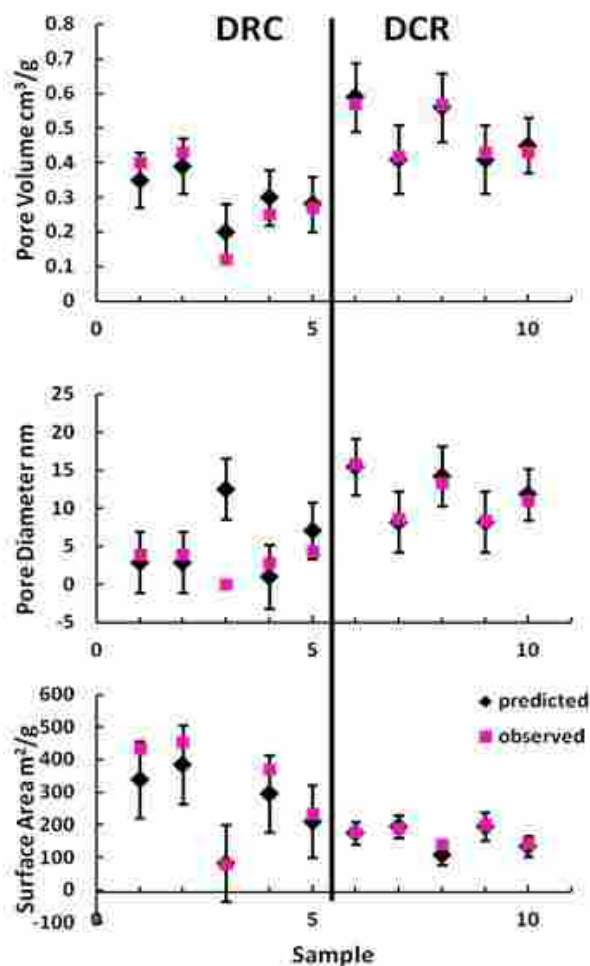


Figure 4.3 Pink squares correspond to surface areas, pore diameters, and pore volumes observed in confirmation trials and black diamonds correspond to predicted values. Error bars represent the standard deviation of the predictions. Observed values are based on two sample preparations. All values, except pore diameter of Sample 3, were within the 95% CI of the predictions. Conditions for confirmation trials are listed in Table 4.5.

4.4 Discussion

The results of this study illustrate the power of using DOEs to (1) optimize the surface area, pore volume, and pore diameter of catalyst supports in a minimum number of experiments and (2) provide a basis for predicting these properties based on experimental conditions. The predictive capability allows for tailoring of the anatase support properties for different

applications and an understanding of the range of properties that can be obtained using this synthesis method. The results of this study also provide new insights into the roles of variables in the preparation of aluminum-stabilized anatase.

The role of preparation variables

The mechanism of the formation of a high surface area material is a complex process involving several steps: nucleation, crystallite growth, polymerization, and agglomeration. In our preparation of anatase, we observed crystallization almost immediately, suggesting that nucleation is a rapid, almost instantaneous process. We observed that much of the crystallization occurs during the short mixing process, but continues to a lesser extent during the drying process. Growth, polymerization, and agglomeration occur throughout the drying and calcination processes. The results of this work provide significant insights into the effects of preparation variables in these important steps in the formation of anatase.

Mixing: The availability of water (Factor B, H₂O addition speed) controls the rates of nucleation and crystallization of anatase. Since water availability affects crystallite formation, H₂O addition speed affected surface area, pore volume, and pore diameter. Slow H₂O addition apparently leads to slower nucleation and controlled growth resulting in small crystallites, small pore diameters, high surface areas, and small pore volumes. Smaller quantities of water (Factor C, ml H₂O) are also associated with low pore volumes. We hypothesize that water adsorbs onto surfaces and stabilizes planes of higher surface energy; however, if less water is available to adsorb onto the surface, high-energy faces are joined in a connected structure to increase stability, resulting in lower pore volumes. In addition, hydrogen bonding is thought to affect self-organization; thus, with less water available and less hydrogen bonding, a more tightly packed and more networked structure with a lower pore volume is formed, while a greater amount of

water leads to a more open structure with larger pore volume. The amount of water (Factor C) did not affect the crystallite diameter and consequently did not affect surface area or pore diameter.

Drying: Increasing the drying time (Factor E) leads to larger pores in DCR materials and smaller pores in DRC materials. We hypothesize that gel stiffness and strength increase as drying time increases (due to cross-linking and condensation reactions) and consequently, gels better withstand capillary pressure, which can cause pores to collapse during calcination. Therefore, longer drying times are associated with larger pore diameters, while shorter drying times lead to weaker gels which collapse into smaller pore diameter materials during calcination with no significant change in pore volume. Pore diameters of DRC materials decrease as drying time increases because the large pores formed after long dry times redistribute into smaller, networked pores during rinsing (discussed below). Increasing the drying temperature (Factor F) slightly increases surface area and pore volume of DRC materials. We suspect the amount of dehydration, which occurs during drying and continues during calcination, affects how DRC particles redistribute (discussed below) during the rinsing process. Within the experimental limits tested, the drying temperature had no significant effect on properties of DCR materials (Figure 4.2), which were calcined (and further dehydrated) following the drying step.

After drying, crystalline anatase approximately 6 – 7 nm in diameter is formed. Surface area increases as the amount of Al (Factor J) increases and we therefore hypothesize Al is present as an AlO_x species on the anatase surface. The Al stabilizes anatase by preventing grain growth and rearrangement, thereby delaying the anatase to rutile phase transition.

DCR

Calcining: Increasing the calcination temperature (Factor H) decreases surface area and pore volume and increases pore diameter because the high calcination temperatures lead to (1) increased crystallinity, densification, grain growth, and agglomeration and (2) loss of surface OH⁻ species. The effects of calcination temperature on the pore volume and pore diameter were less significant for DCR materials than DRC materials (Figure 4.2), indicating that DCR materials are more thermally stable compared with DRC materials. We hypothesize that the larger (6 – 7 nm) DCR precursors have lower surface energies and therefore sinter less during calcination compared with the smaller (2 – 3 nm) DRC precursors. Slow calcination ramp rates (Factor G), with slower removal of NH₄Cl and water from the pores (which could act as pillars to support the pore structure at the beginning of the calcination process), resulted in controlled growth and minimally higher surface area and pore volume. Increasing calcination time (Factor I) caused a minimal decrease in pore volume as a result of pores collapsing during prolonged heat treatment.

Rinsing: Rinsing and subsequent drying of calcined anatase materials (DCR materials) does not appear to have any significant effect on the surface area or porosity.

DRC

Rinsing: Rinsing anatase precursors (DRC route) decreases average crystallite size (from approx 6 nm to 2 nm). We hypothesize that the smaller crystallites of DRC samples (relative to DCR samples), result from a dissolution and redistribution process during rinsing. Rinsing also affects the location of Al, apparently allowing Al ions to move into empty octahedral sites located in the anatase lattice; this hypothesis is based on observations that increasing Al mol% (Factor J) increases pore volume of DRC materials but does not affect pore volume of DCR

materials. Surface Al species and Al³⁺ ions located in octahedral sites apparently stabilize anatase to 400°C; heat treatment above 400°C results in grain growth and loss of surface area. XAS studies are needed and presently being pursued to provide information on the mechanism of stabilization in the Al-modified anatase structure.

Calcining: Calcination temperature (Factor H) is the most important factor in the DRC route (Figure 4.2). Increasing the calcination temperature results in loss of surface area and pore volume and an increase in pore diameter due to grain growth. Ramp rate and calcination time (Factors G and I) did not significantly impact the properties of DRC materials.

4.5 Conclusions

We have shown that statistical experimental designs (a) reduce the number of experiments necessary to determine factors and factor interactions that affect surface area, pore volume, and pore diameter, (b) provide a basis for predicting the optimal conditions to obtain the highest surface area and pore volume at the desired pore diameter, and (c) provide inherent statistical measures of confidence in the data obtained.

- 1) The new definitive screening design used in this study showed correlations among variables and was used to conclusively determine the effects of many different variables while avoiding confounded variables, a drawback of traditional fractional factorial designs.
- 2) The prediction equations developed in this study match values obtained in confirmatory experiments very well, providing a high level of predictive capability. Nevertheless, additional experiments could improve the accuracy and precision of the prediction equations. Future studies could include other factors, e.g. analysis of the reaction

temperature, reaction pH, aging, rinsing agents, and batch size, as well as extend the limits of the variables examined in this study. We also recognize that a mechanical mixing method would be preferable to the hand grinding method used in this study.

- 3) Based on the results of this work we can predict and tune the surface area, pore volume, and pore diameter of Al-modified anatase. Both the DRC and DCR routes produce desirable materials with excellent thermal stability. In general, the DRC route produces materials of higher surface area, smaller pore diameter, and smaller pore volume relative to the DCR route, which produces materials of higher pore volume, larger pore diameter, and smaller surface area.

4.6 Supplemental Information

Table S4.1 Factor effects and directions determined in DOE 1.

Response	Largest Factor Effects	Effect Direction	Confounded Interactions
Surface Area	H (calcination temp.)	negative	BF + IJ + CD + AG
	F (drying temperature)	positive	BH + AE
	C (amount of H ₂ O)	positive	DH + EI
Pore Diameter	D*(rinsing order)		EJ + CH
	H (calcination temp.)	positive	BF + IJ + CD + AG
	B (speed of addition of H ₂ O)	positive	EG + FH
Pore Volume	D* (rinsing order)		EJ + CH
	C (amount of H ₂ O)	positive	DH + EI
	BC (speed × amount H ₂ O)		AJ + DF + GI
	H (calcination temp.)	negative	BF + IJ + CD + AG

*significant at ($\alpha=0.05$ level)

4.7 References

1. Haruta, M.; Tsubota, S.; Kobayashi, T.; Kageyama, H.; Genet, M. J.; Delmon, B., Low-temperature oxidation of carbon monoxide over gold supported on titanium dioxide, γ -ferric oxide, and cobalt tetraoxide. *J. Catal.* **1993**, *144* (1), 175-92.
2. Imai, H.; Date, M.; Tsubota, S., Preferential Oxidation of CO in H₂-Rich Gas at Low Temperatures over Au Nanoparticles Supported on Metal Oxides. *Catal. Lett.* **2008**, *124* (1-2), 68-73.
3. Edwards, J. K.; Carley, A. F.; Herzing, A. A.; Kiely, C. J.; Hutchings, G. J., Direct synthesis of hydrogen peroxide from H₂ and O₂ using supported Au-Pd catalysts. *Faraday Discuss.* **2008**, *138* (Nanoalloys), 225-239.
4. Tahir, S. F.; Koh, C. A., Catalytic oxidation for air pollution control. *Environ. Sci. Pollut. Res. Int.* **1996**, *3* (1), 20-3.
5. Shyue, J.-J.; De, G. M. R., Single-step preparation of mesoporous, anatase-based titanium-vanadium oxide and its application. *J. Am. Chem. Soc.* **2005**, *127* (36), 12736-12742.
6. Carp, O.; Huisman, C. L.; Reller, A., Photoinduced reactivity of titanium dioxide. *Prog. Solid State Chem.* **2004**, *32* (1-2), 33-177.
7. Xu, J.; Bartholomew, C. H.; Sudweeks, J.; Eggett, D. L., Design, Synthesis, and Catalytic Properties of Silica-Supported, Pt-Promoted Iron Fischer-Tropsch Catalysts. *Top. Catal.* **2003**, *26* (1-4), 55-71.
8. Nele, M.; Vidal, A.; Bhering, D. L.; Carlos, P. J.; Salim, V. M. M., Preparation of high loading silica supported nickel catalyst: simultaneous analysis of the precipitation and aging steps. *Appl. Catal., A* **1999**, *178* (2), 177-189.

9. Chiang, Y.-D.; Lian, H.-Y.; Leo, S.-Y.; Wang, S.-G.; Yamauchi, Y.; Wu, K. C. W., Controlling Particle Size and Structural Properties of Mesoporous Silica Nanoparticles Using the Taguchi Method. *J. Phys. Chem. C* **2011**, *115* (27), 13158-13165.
10. McNamara, C. A.; King, F.; Bradley, M., Experimental design and the optimization of a polymer supported palladium complex for use in the Heck reaction. *Tetrahedron Lett.* **2004**, *45* (44), 8239-8243.
11. Naderi, M.; Shamirian, A.; Edrisi, M., Synthesis, characterization and photocatalytic properties of nanoparticles CuAl₂O₄ by Pechini method using Taguchi statistical design. *J. Sol-Gel Sci. Technol.* **2011**, *58* (2), 557-563.
12. Sakkas, V. A.; Islam, M. A.; Stalikas, C.; Albanis, T. A., Photocatalytic degradation using design of experiments: A review and example of the Congo red degradation. *J. Hazard. Mater.* **2010**, *175* (1-3), 33-44.
13. Vanyorek, L.; Loche, D.; Katona, H.; Casula, M. F.; Corrias, A.; Konya, Z.; Kukovecz, A.; Kiricsi, I., Optimization of the Catalytic Chemical Vapor Deposition Synthesis of Multiwall Carbon Nanotubes on FeCo(Ni)/SiO₂ Aerogel Catalysts by Statistical Design of Experiments. *J. Phys. Chem. C* **2011**, *115* (13), 5894-5902.
14. Olsen, R. E.; Bartholomew, C. H.; Huang, B.; Simmons, C.; Woodfield, B. F., Synthesis and characterization of pure and stabilized mesoporous anatase titanias. *Microporous Mesoporous Mater.* **2013**, *Ahead of print*.
15. Jones, B.; Nachtsheim, C. J., A class of three-level designs for definitive screening in the presence of second order effects. *Journal of Quality Technology* **2011**, *43*, 1-14.

16. Erler, A.; Mas, N.; Ramsey, P.; Henderson, G., Efficient biological process characterization by definitive-screening designs: the formaldehyde treatment of a therapeutic protein as a case study. *Biotechnol. Lett.* **2013**, *35* (3), 323-329.
17. Woodfield, B. F.; Liu, S.; Boerio-Goates, J.; Liu, Q. Preparation of uniform nanoparticles of ultra-high purity metal oxides, mixed metal oxides, metals, and metal alloys. WO2007098111A2, 2007.
18. Wu, C.; Hamada, M., *Experiments: Planning, Analysis, and Parameter Design Optimization*. New York: John Wiley and Sons, Inc: 2000.
19. Lawson, J., *Design and Analysis of Experiments with SAS*. CRC Press, Boca Raton.: 2010.
20. Lawson, J.; Grimshaw, S.; Burt, J., A quantitative method for identifying active contrasts in unreplicated factorial experiments based on the half-normal plot. *Computational Statistics and Data Analysis* **1998**, *26* (425-436).
21. Daniel, C., Locating outliers in factorial experiments. *Technometrics* **1960**, *2* (149-156).
22. Patterson, A. L., The Scherrer formula for x-ray particle-size determination. *Phys. Rev.* **1939**, *56*, 978-82.
23. Pierce, C., Computation of pore sizes from physical adsorption data. *J. Phys. Chem.* **1953**, *57*, 149-52.
24. Orr, C., Jr.; Dallavalle, J. M., *Fine Particle Measurement-Size, Surface, and Pore Volume*. Macmillan Co.: 1959; p 353 pp.
25. Huang, B.; Bartholomew, C., H.; Woodfield, B. F., Facile synthesis of mesoporous alumina with tunable pore size: Effects of alcohols in precursor formation and calcination. *Microporous Mesoporous Mater.* **2013**, *177*, 37-46.

26. Liu, H.; Zhang, L.; Seaton, N. A., Sorption hysteresis as a probe of pore structure. *Langmuir* **1993**, *9* (10), 2576-82.
27. Rojas, F.; Kornhauser, I.; Felipe, C.; Esparza, J. M.; Cordero, S.; Dominguez, A.; Riccardo, J. L., Capillary condensation in heterogeneous mesoporous networks consisting of variable connectivity and pore-size correlation. *Phys. Chem. Chem. Phys.* **2002**, *4* (11), 2346-2355.
28. Niemark, A. V., Percolation theory of capillary hysteresis phenomena and its application for characterization of porous solids. *Stud. Surf. Sci. Catal.* **1991**, *62* (Charact. Porous Solids 2), 67-74.
29. Parlar, M.; Yortsos, Y. C., Percolation theory of vapor adsorption-desorption processes in porous materials. *J. Colloid Interface Sci.* **1988**, *124* (1), 162-76.
30. Ball, P. C.; Evans, R., Temperature dependence of gas adsorption on a mesoporous solid: capillary criticality and hysteresis. *Langmuir* **1989**, *5* (3), 714-23.
31. Neimark, A. V.; Ravikovitch, P. I., Capillary condensation in MMS and pore structure characterization. *Microporous Mesoporous Mater.* **2001**, *44-45*, 697-707.
32. Neimark, A. V.; Ravikovitch, P. I.; Vishnyakov, A., Adsorption hysteresis in nanopores. *Phys. Rev. E: Stat. Phys., Plasmas, Fluids, Relat. Interdiscip. Top.* **2000**, *62* (2-A), R1493-R1496.
33. Monson, P. A., Contact Angles, Pore Condensation, and Hysteresis: Insights from a Simple Molecular Model. *Langmuir* **2008**, *24* (21), 12295-12302.

Chapter 5: Structure Analysis of Al-modified TiO₂

5.1 Introduction

TiO₂ is an excellent support material for metal and metal oxide catalysts in a number of oxidative synthesis and pollution-control reactions e.g. oxidation of CO at low temperatures,¹ preferential oxidation of CO in H₂/CO mixtures,² low-temperature, direct synthesis of hydrogen peroxide,³ complete oxidation of volatile organic compounds,⁴ and also as a support and promoter for vanadium oxide in selective catalytic reduction of NO_x.⁵ These and other reactions involving catalysts supported on TiO₂ have been reviewed elsewhere.⁶

TiO₂ materials are often modified with dopants such as Al to control the thermal stability, surface area, and porosity, however, it is unclear how Al stabilizes and modifies the crystal phase and properties of anatase TiO₂ because the structures of doped nanomaterials are not well understood. Dopants can be incorporated in a number of ways, for example, as solid solutions, as surface species, or in lattice vacancies. It is expected that the manner in which dopants are incorporated into the crystal structure will result in different effects; therefore, in order to understand and predict dopant effects, the structure of doped nanomaterials should be understood. A detailed understanding of doped nanomaterial structures should also provide insight into the stabilization mechanism of Al in TiO₂. Because the mechanisms of dopant stabilization have not been understood, previous studies have used laborious trial and error methods to find more stable support materials and catalysts. Catalyst development is an expensive endeavor and with limitless possibilities we must move away from an empirical system to a more effective process of understanding how dopants stabilize and change the

behavior of the support and catalyst in order to efficiently design stable, high surface area materials.

Characterizing the structure of doped nanomaterials is particularly difficult because traditional bulk techniques such as XRD, TEM, SEM, and XPS are limited in discerning fine details. In fact, using these techniques, many researchers have drawn contradictory conclusions from similar data. For example, the absence of separate oxide peaks in the X-ray diffraction data of Al-TiO₂ suggests a solid solution, but, this is not conclusive evidence. Many researchers interpret this to suggest the stabilizer/dopant is interstitially or substitutionally incorporated while others report that it is found on the surface or is a separate phase that either consists of small highly dispersed particles or is amorphous.⁷⁻¹² Evidence from these traditional techniques alone is not enough to determine the structure of nanomaterials, particularly small, 2 to 4 nm or smaller crystallites. Development during the past 3 to 4 decades of sophisticated surface and spectroscopy techniques such as ²⁷Al MAS NMR spectroscopy and X-ray absorption spectroscopy have enabled more in depth structural characterization of nanomaterials. Additionally, techniques not generally used for structural characterization such as low temperature heat capacity can provide insight into the structure of doped nanomaterials.

We recently presented a method to prepare Al-modified anatase TiO₂ catalyst supports of unusually high surface area and thermal stability. This method enables the preparation of anatase having a wide range of properties.^{13,14} Previous work has shown that synthesis variations including the order of rinsing affect the thermal stability and final properties of the catalyst supports.¹⁴ In this study we examine the structure of Al-modified anatase supports to gain insight into the possible mechanisms of Al stabilization. Structural information was obtained using a variety of analysis techniques including XRD, TEM, N₂ sorption, as well as XANES, ²⁷Al MAS

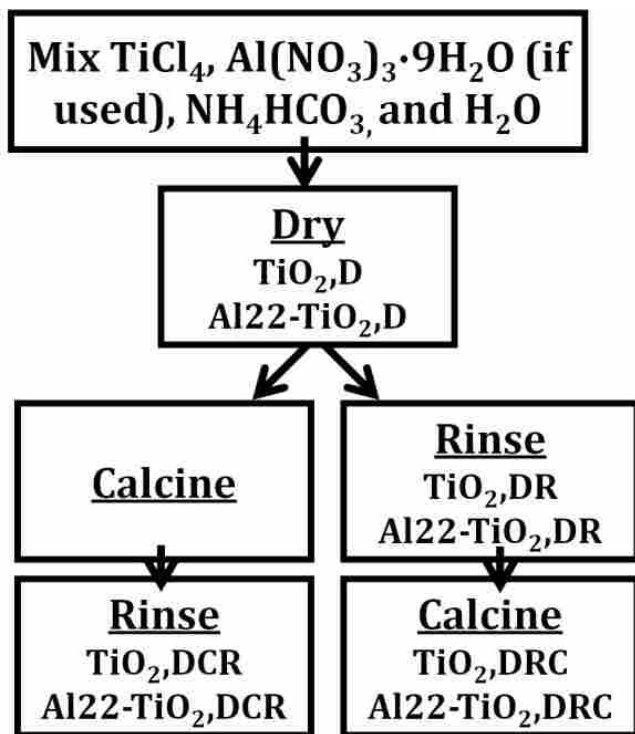
NMR, and low temperature heat capacity data. Results presented in this paper show that (1) our unique synthesis method allows dopants to be incorporated either on the surface or in vacancies, leading to different pore structures, surface area, and thermal stability, and (2) in addition to the choice and amount of dopant (which have already been widely studied), the manner in which dopants are incorporated is an important factor in creating a high surface area stable support.

5.2 Experimental

5.2.1 Sample Preparation

Anatase and anatase modified with Al samples were prepared following a general solvent deficient method that can be used to synthesize many metal and mixed metal oxides.^{13,15} A schematic of the synthesis is found in Scheme 5.1. Approximately 3.7 ml TiCl_4 was mixed with 10.54 g NH_4HCO_3 (ABC) mixed for one minute. For Al-modified anatase materials, 2.75 g $\text{Al}(\text{NO}_3)_3 \cdot 9\text{H}_2\text{O}$, 2.86 ml TiCl_4 , and 10.54 g ABC were mixed together for one minute (amounts listed are for 22 mol% Al, 5 to 50 mol% Al ratios were examined). Ten ml distilled water was added slowly while stirring to start the reaction and facilitate mixing. The slurry was mixed for five minutes to form an anatase precursor. The precursor was then dried in air at 100°C for 24 hours. Samples were rinsed with 2 L distilled water using a vacuum filtration system at room temperature and calcined at 400°C or 700°C for three hours in air (ramp rate = $19^\circ\text{C}/\text{min}$) in the order specified in the synthesis schematic, either dry, rinse, calcine (DRC), or dry, calcine, rinse (DCR).

Sample notation: D = dried, R = rinsed, C = calcined. TiO_2 = pure TiO_2 . Al22- TiO_2 = 22 mol% Al-modified anatase TiO_2 .



Scheme 5.1 Synthesis routes. D= dry, R = rinse, C = calcine. Al22= 22 mol% Al-modified TiO₂.

5.2.2 Sample Characterization

X-ray diffraction patterns were collected using a PANalytical X'Pert Pro diffractometer (Cu-K_{α1} radiation, $\lambda = 1.540598 \text{ \AA}$) at 45 kV and 40 mA over the 2θ range of 10 to 90° at scanning rates of 0.44 to 1.3°/min. Average crystallite diameters were estimated using the Scherrer equation¹⁶ and confirmed using transmission electron microscopy (TEM). TEM measurements were performed on a Tecnai F20 Analytical STEM operating at 200 keV. The samples were dispersed in ethanol and deposited on copper grids (400 mesh copper grids, Ted Pella, Inc.).

The Ti K edge X-ray absorption spectroscopy spectra (X-ray absorption near edge, XANES, and extended X-ray absorption fine structure, EXAFS) were obtained using the 12-BM-B beamline of the Advanced Photon Source at Argonne National Laboratory. Spectra were

collected using a Si(111) crystal monochromator in either fluorescence or transmission mode and the spectra were calibrated using Ti foil as a reference.

Full-range N₂ sorption isotherms were collected at 77 K using a Micromeritics TriStar 3020 surface analyzer. Samples of 0.25 to 0.50 g were degassed at 200°C for 12 to 24 hours prior to collecting data. Pore volumes were calculated from the adsorption isotherm at a relative pressure of 0.98 and specific surface areas were calculated using the Brunauer-Emmett-Teller (BET) method from a P/P⁰ range of 0.05 to 0.2. H2 type pore diameters were calculated using a modified Pierce method^{17,18} with structural corrections for pore area and volume. Pore diameters were calculated from the adsorption branch for H2 type pores, since evaporation of the condensate during desorption is significantly constrained and delayed by the pore necks with “ink-bottle” pore geometry and by the connectivity of the network.¹⁹⁻²² H3 pore widths were calculated using the newly developed SPG model^{23,24} involving slit geometry for the Kelvin equation, which also incorporates structural corrections for area and volume. For H3 type hysteresis with slit-like pores, the desorption branch is preferred due to delayed condensation observed in the adsorption process.²⁵⁻²⁸ For ease of discussion pore widths and pore diameters will both be referred to as pore diameters.

Heat capacities were measured from 1.9 to 300 K using a Quantum Design Physical Property Measurement System (PPMS), which utilizes a relaxation technique. Prior to measurements, the samples were dried in a vacuum oven at 100°C for six hours and stored under Ar to prevent re-adsorption of water until measurements were made. Following drying, 10 to 20 mg of sample was mixed with approximately 20 mg of Cu flakes (to increase thermal contact) and pressed into pellets. Information on pellet preparation and mounting are detailed elsewhere.^{29,30} Data measurement increments are as follows: data below 10K were measured

every 0.14 K, data from 10 to 100 K were measured logarithmically and data from 100 to 300 K were measured in 10 K increments. Accuracies of the heat capacity data on the PPMS using this measurement technique were found to be $\pm 2\%$ and $\pm 0.6\%$ in the temperature ranges from 2 to 20 K and from 20 to 300 K, respectively, for a high-purity copper pellet.^{29,30} The copper contribution was subtracted from the obtained data to determine the raw sample molar heat capacity. This data was then corrected for the water heat capacity.³¹ The TiO₂ water heat capacity³¹ was used to produce an anhydrous heat capacity of the Al-modified TiO₂ material. Theoretical functions were fit to the data and the quality of fit was determined by the %RMS and a plot of the deviations. Heat capacity measurements and fitting techniques are further discussed in a companion heat capacity study (manuscript in preparation).

²⁷Al MAS NMR spectra were obtained on a Bruker Avance III 600 (14.6 T) spectrometer using a 4 mm broadband MAS probe. All spectra were obtained at room temperature at a spinning speed of 12.5 kHz using a single pulse Bloch decay, and high-power ¹H decoupling. The ²⁷Al chemical shift were referenced to the external 1M Al(H₂O)₆⁺ standard, $\delta = 0.0$ ppm. Spectral simulations were performed using DMFIT³² and utilized the Czjzek distribution of the ²⁷Al quadrupolar interaction to model the NMR spectra.³³

5.3 Results

5.3.1 XRD, TEM, N₂ Sorption, XANES, and ²⁷Al MAS NMR

5.3.1.1 Unrinsed precursors

In Figure 5.1, XRD patterns are shown for dried, unrinsed pure anatase and 22 mol% Al-modified anatase precursors (TiO₂,D and Al22-TiO₂,D). In the pattern for TiO₂,D, both sharp ammonium chloride peaks and broad, somewhat X-ray amorphous anatase-like peaks (inset) are

apparent. In the inset pattern for Al₂₂-TiO₂,D, crystalline anatase of approximately 6 nm in diameter (from the Scherrer formula) and a small amount of ammonium chloride are evident. Lattice fringes evident in TEM micrographs of Al₂₂-TiO₂,D (Figure 5.2A) reveal the presence of small, 2 to 4 nm crystallites that are not observed by XRD. The larger 6 nm crystallites observed in the XRD pattern are also observed (Figure 5.2B) by TEM. XANES analysis reveals primarily 5-coordinate Ti in the Al₂₂-TiO₂,D sample. Solid state ²⁷Al MAS NMR reveals primarily 6-coordinate Al (Table 5.1) is present in Al₂₂-TiO₂,D.

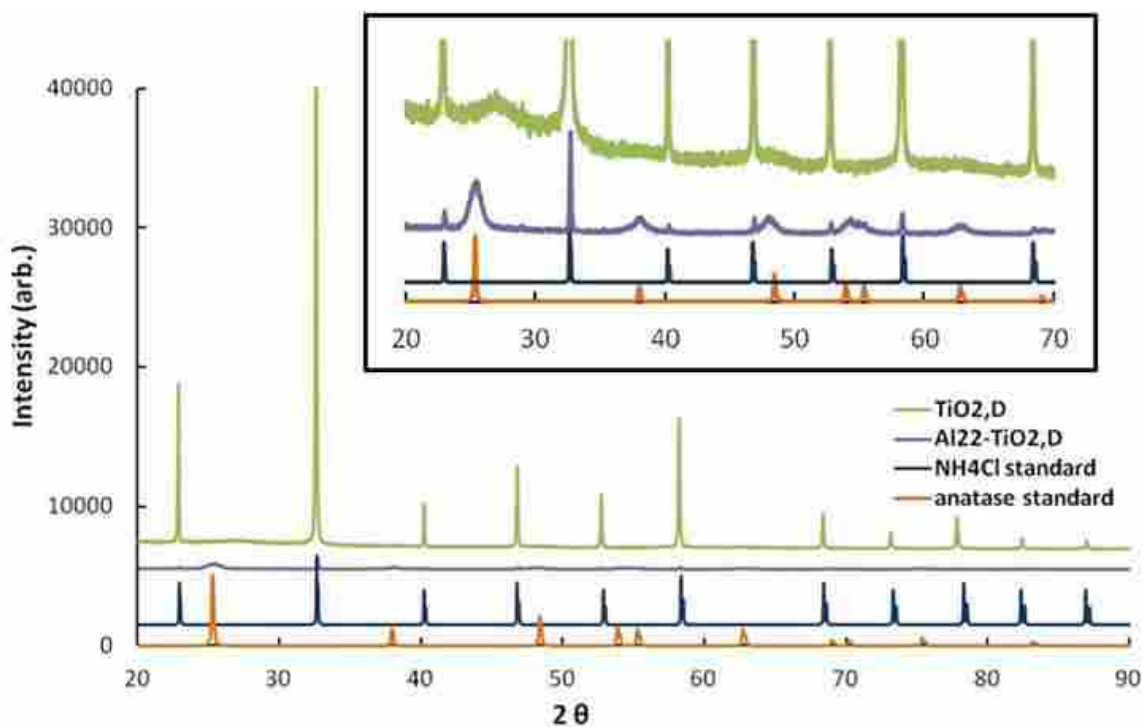


Figure 5.1 XRD patterns of unrinsed, dried precursors. TiO₂,D = pure anatase precursor. Al₂₂-TiO₂,D = 22 mol% Al-modified anatase precursor. The inset shows details in the baseline. NH₄Cl and anatase TiO₂ standards are included in both the full pattern and the inset for comparison.

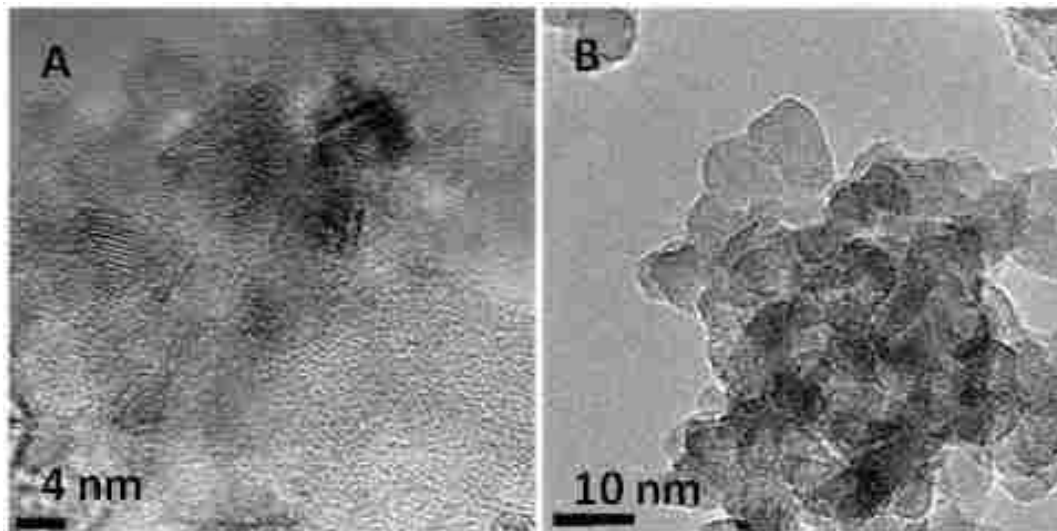


Figure 5.2 TEM micrographs of the unrinsed Al-modified anatase precursor, Al₂₂-TiO₂,D. Lattice fringes in the TEM image reveal (A) small 2 – 4 nm crystallites and (B) large 6 nm crystallites.

Table 5.1 Solid state ²⁷Al MAS NMR site concentration.

Calcination Temp	^a Sample	Al(IV) %	Al(V) %	Al(VI) %
Not calcined	Al ₂₂ -TiO ₂ ,D	4%	<1%	96%
	Al ₂₂ -TiO ₂ ,DR	5%	8%	87%
400°C	Al ₂₂ -TiO ₂ ,DCR	12%	11%	^b 77%
	Al ₂₂ -TiO ₂ ,DRC	14%	15%	71%

a. See Scheme 5.1 for information on sample preparation.

b. Al(VI) shows a reduced disorder in this material, indicating it is approaching a crystalline material.

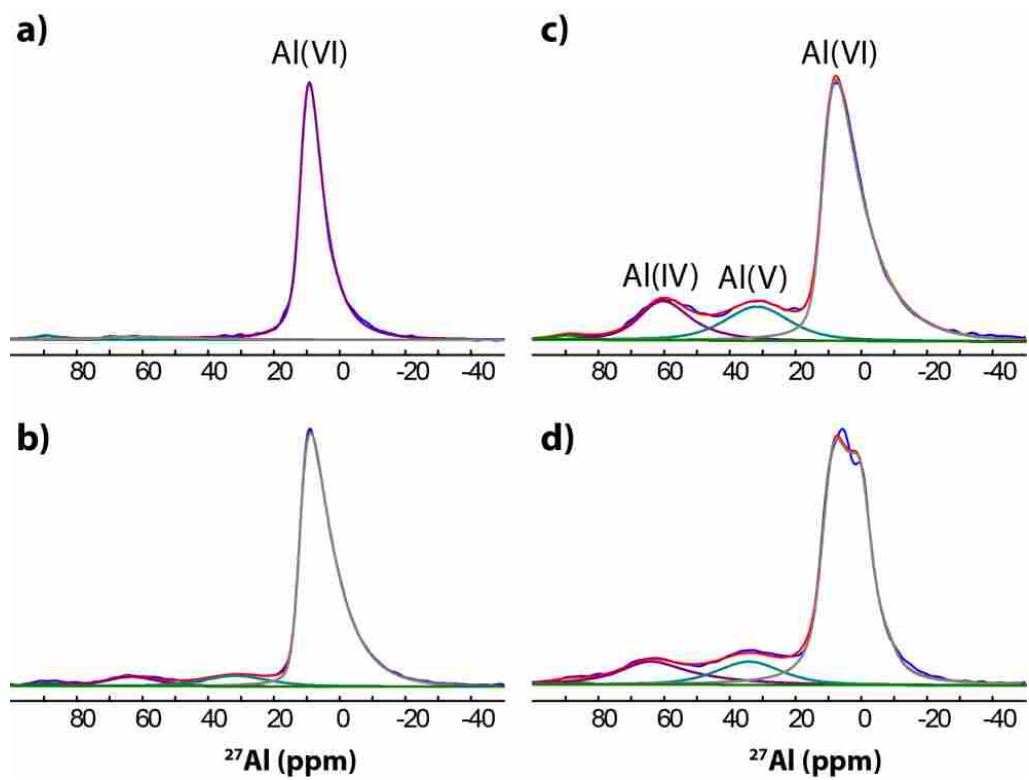


Figure 5.3 Solid state ^{27}Al MAS NMR spectra of a) Al₂₂-TiO₂,D, b) Al₂₂-TiO₂,DR, c) Al₂₂-TiO₂,DRC, and d) Al₂₂-TiO₂,DCR.

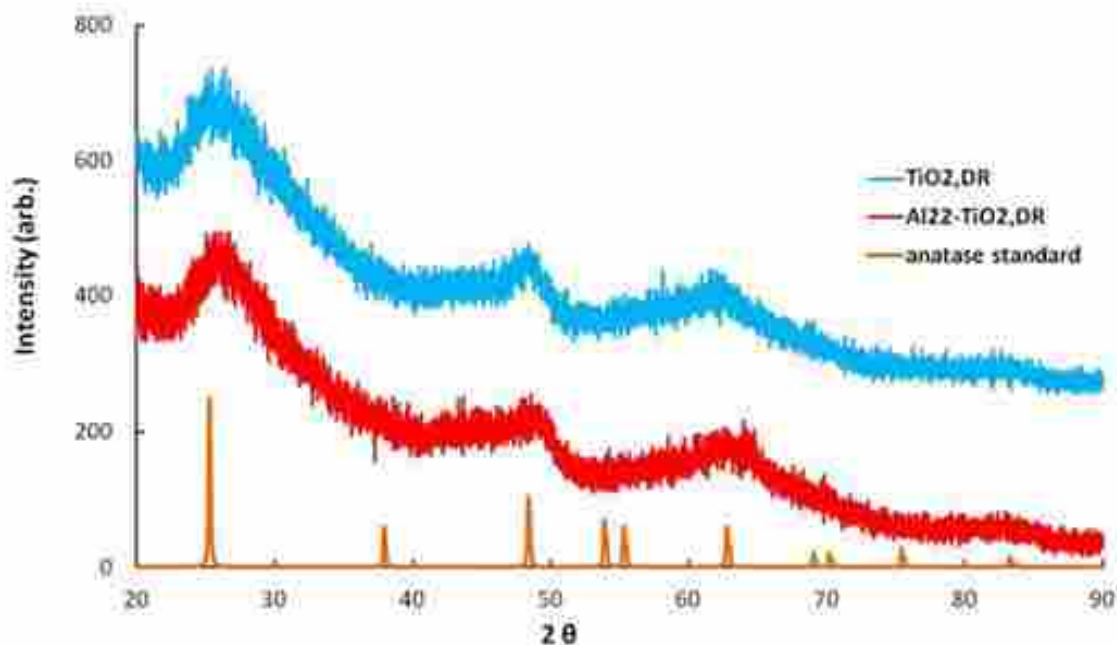


Figure 5.4 XRD patterns of dried and rinsed precursors. TiO_2,DR = pure anatase precursor. $\text{Al}_{22}\text{-TiO}_2,\text{DR}$ = 22 mol% Al-modified anatase precursor. An anatase standard pattern is included for comparison.

5.3.1.2 Rinsed precursors before calcination

Dried and rinsed pure anatase and 22 mol% Al-modified anatase precursors (TiO_2,DR and $\text{Al}_{22}\text{-TiO}_2,\text{DR}$) appear to be structurally similar according to XRD, TEM, and N_2 sorption analyses. In Figure 5.4, XRD patterns are shown for TiO_2,DR and $\text{Al}_{22}\text{-TiO}_2,\text{DR}$. Rinsing the TiO_2 precursor removes ammonium chloride but does not appear to greatly affect the crystallinity and crystallite size of the anatase-like phase (Figures 5.1 and 5.3). By contrast, rinsing the $\text{Al}_{22}\text{-TiO}_2,\text{DR}$ precursor results in small crystallites that give rise to broad, nearly X-ray amorphous peaks (Figure 5.4) and the 6 nm anatase crystallites present in the unrinsed $\text{Al}_{22}\text{-TiO}_2,\text{D}$ precursor are no longer observed. TEM analysis reveals that the rinsed precursors with XRD-amorphous looking peaks are not truly amorphous, but are very small crystallites of 2 nm

or less (Al₂₂-TiO₂,DR shown in Figure 5.5A). Analysis of N₂ sorption data for rinsed precursors (Table 5.2) reveals materials of very high surface area and small pore diameter (≥ 2 nm). Little hysteresis is evident in N₂ sorption isotherms (Figure 5.6A), suggesting that the majority of pores are similar in size and accessible to the surface; therefore there is little difference in the adsorption and desorption processes. Solid state ²⁷Al MAS NMR reveals primarily 6-coordinate Al (Table 5.1, Figure 5.3) is present in Al₂₂-TiO₂,D. Previous work has shown that rinsing does not remove Al.¹³

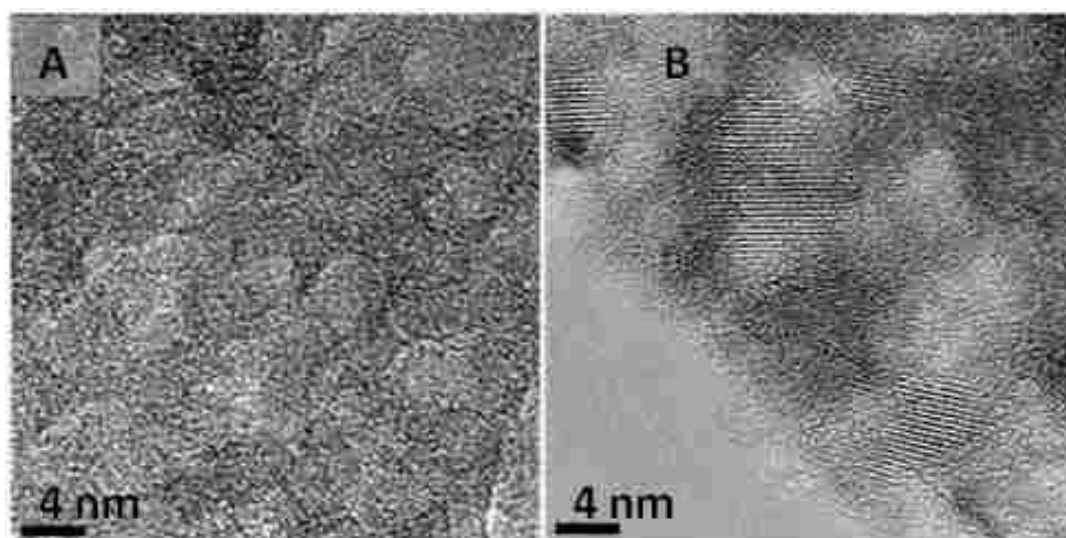


Figure 5.5 TEM micrographs of (A) 22 mol% Al-modified anatase dried and rinsed precursor (Al₂₂-TiO₂,DR) and (B) 22 mol% Al-modified anatase dried, rinsed, and calcined at 400°C (Al₂₂-TiO₂,DRC). A small increase in crystallization and crystallite size is seen after Al₂₂-TiO₂,DR crystallites (2 nm and smaller) are calcined at 400°C and grow to 2 – 3 nm crystallites.

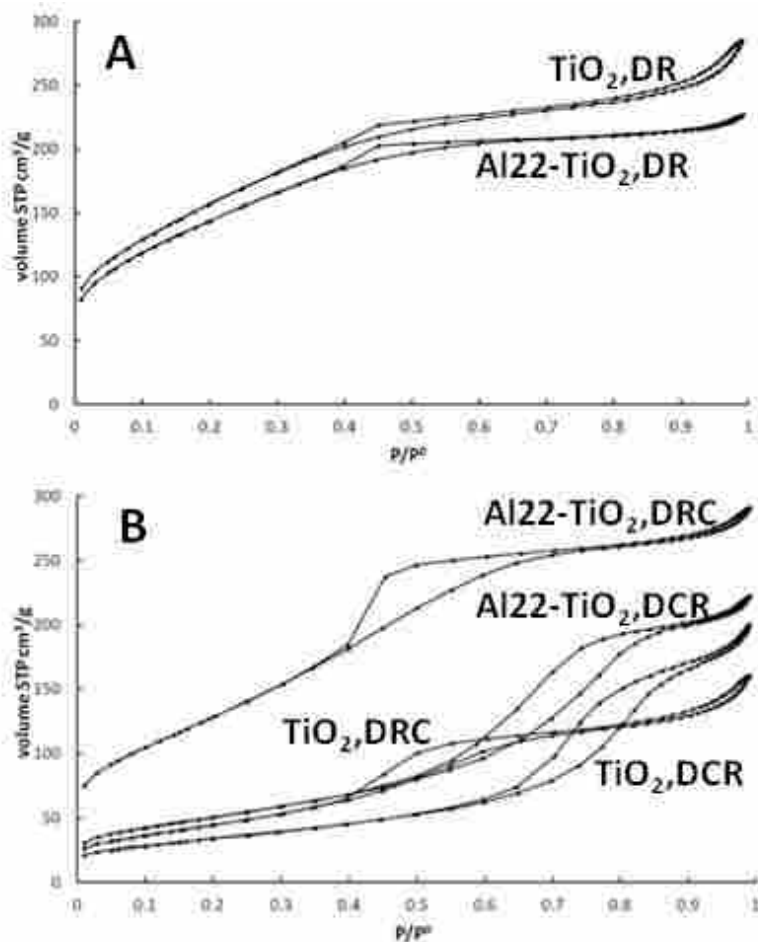


Figure 5.6 N₂ sorption isotherms of (A) dried and rinsed precursors and (B) materials calcined at 400°C. Isotherms of the rinsed precursors (A) are H₂ type with little hysteresis. Isotherms of products calcined at 400°C (B) are either (1) H₂ type (TiO₂,DRC and Al₂₂-TiO₂,DRC) or (2) H₃ type (TiO₂,DCR and Al₂₂-TiO₂,DCR).

Table 5.2 Crystallite size, N₂ sorption properties, and Ti coordination of pure TiO₂ and 22 mol% Al-modified TiO₂ calcined at different temperatures.

Calcination Temp (°C)	^a Sample	^b Crystallite Diameter (nm)	Surface Area (m ² /g)	Pore Volume (cm ³ /g)	Pore Diameter (nm)	Isotherm Type	^c Ti Coordination
Not calcined	TiO ₂ ,D	2 – 4, 6	Not measurable				
	Al22-TiO ₂ ,D	A, ≥2	Not measurable				5
	TiO ₂ ,DR	A, ≥2	575	0.43	2.8	H2-like	
	Al22-TiO ₂ ,DR	A, ≥2	526	0.35	2.8	H2-like	
400	TiO ₂ ,DCR	7	124	0.30	7.8	H3	6
	Al22-TiO ₂ ,DCR	6	184	0.34	6.3	H3	6
	TiO ₂ ,DRC	7	163.6	0.24	4.7	H2	6
	Al22-TiO ₂ ,DRC	A, 2 – 3	471	0.44	4.4	H2	5
700	TiO ₂ ,DCR	29-An, 63-Ru	11	No measureable porosity			
	Al22-TiO ₂ ,DCR	6	129	0.34	8.3	H3	
	TiO ₂ ,DRC	36-An, 56-Ru	4	No measureable porosity			6
	Al22-TiO ₂ ,DRC	7	131	0.24	6.9	H2	^d 6

a. See Scheme 5.1 for information on sample preparation.

b. A = X-ray amorphous and crystallite sizes were estimated from TEM. All other crystallite sizes estimated from the Scherrer formula. An = anatase phase, Ru = rutile phase.

c. Determined from XANES Ti K edge.

d. A 14 mol% Al modified sample contains 6-coordinate Ti and we expect the 22 mol% Al modified sample to have a similar structure.

5.3.1.3 Materials calcined at 400°C

Figure 5.7A shows the XRD patterns of materials calcined at 400°C. Following calcination at 400°C, TiO₂,DCR and Al22-TiO₂,DCR (Scheme 5.1) are clearly crystalline 6 nm anatase (Figure 5.7A) and contain the 6-coordinate Ti expected for anatase (representative

XANES spectrum in Figure 5.8). Data in Table 5.1 (Figure 5.3) reveal the 6-coordinate environment of Al in Al₂₂-TiO₂,DCR materials is approaching that of a crystalline material. N₂ sorption isotherms (Figure 5.6B) for TiO₂,DCR and Al₂₂-TiO₂,DCR are Type IV H3 isotherms, indicating mesoporous materials with slit-like pore geometry. N₂ sorption data in Table 5.2 reveal that Al₂₂-TiO₂,DCR has a higher surface area and pore volume and a smaller pore diameter compared with TiO₂,DCR.

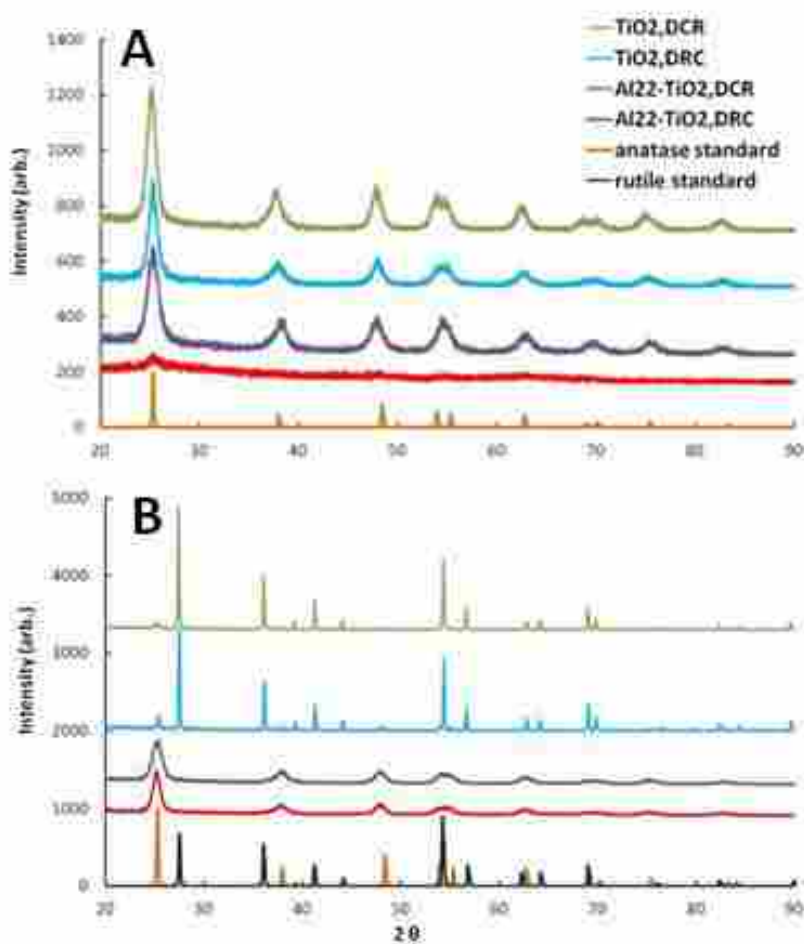


Figure 5.7 XRD patterns of samples calcined at (A) 400°C and (B) 700°C for 3 hours.

TiO₂,DRC undergoes morphological changes following calcination at 400°C from a somewhat XRD-amorphous anatase-like structure to pure crystalline anatase. Thus, from the

XRD pattern in Figure 5.7A, increases in crystallinity and crystallite size are apparent. Compared with the rinsed precursor (TiO_2, DR), TiO_2, DRC has a much lower surface area and pore volume and a larger pore diameter (Table 5.2). A typical H_2 isotherm (Figure 5.6B) indicative of networked, ink-bottle pores is observed for this sample with greater hysteresis compared with the rinsed precursor. A 6-coordinate Ti, which matches standard anatase patterns, is evident for TiO_2, DRC from XANES data (Figure 5.8).

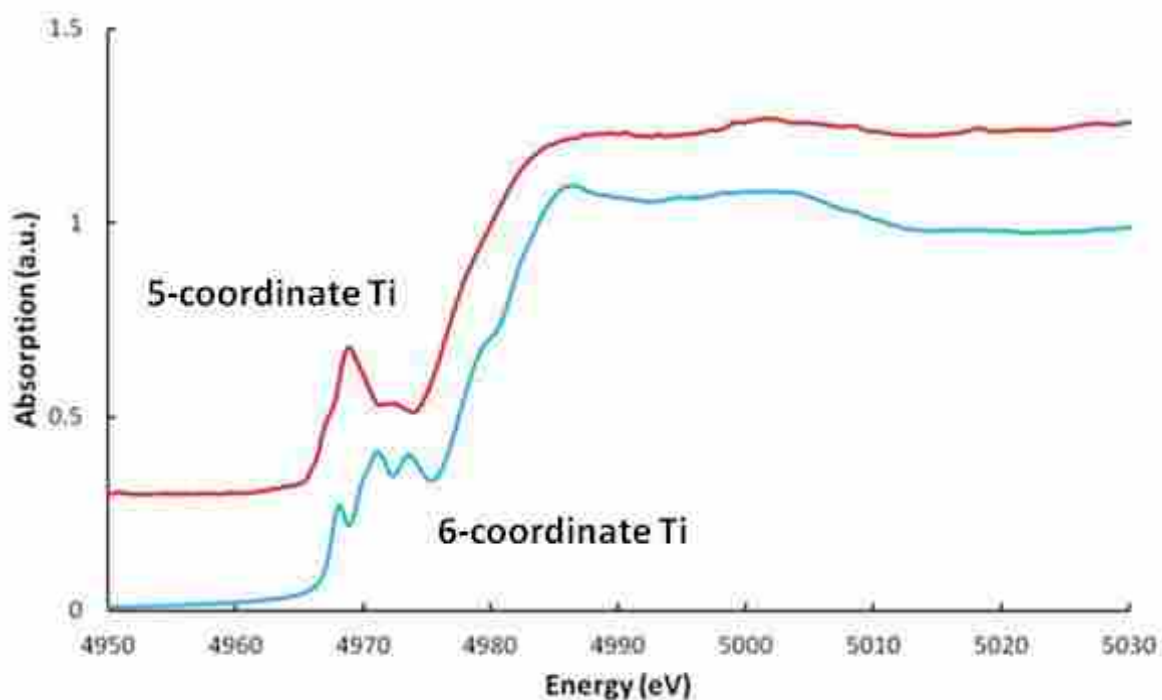


Figure 5.8 Representative XANES spectra of 5 and 6-coordinate Ti.

In contrast to the pure rinsed TiO_2 calcined at 400°C (TiO_2, DRC), $\text{Al}_{22}\text{-TiO}_2, \text{DRC}$ calcined at 400°C has properties very similar to its precursor. Thus, following calcination at 400°C , only a slight increase in crystallite size is observed in TEM micrographs (Figure 5.5). The increase in crystallite size is accompanied by a small loss of surface area and a modest increase in pore diameter (Table 5.2). Though some surface area is lost, $\text{Al}_{22}\text{-TiO}_2, \text{DRC}$ calcined at

400°C has a very high surface area with small, H2-type pores (Figure 5.6B) and, according to XANES analysis, contains primarily 5-coordinate Ti (Figure 5.8). According to Solid state ²⁷Al MAS NMR analysis (Table 5.1), the majority of Al in Al22-TiO₂,DRC calcined at 400°C is 6-coordinated.

5.3.1.4 Materials calcined at 700°C

Figure 5.7B shows the XRD patterns for materials calcined at 700°C. Calcining TiO₂,DCR and TiO₂,DRC at 700°C leads to complete loss of surface area and porosity as grain growth occurs and the materials transition to large crystallites of rutile (Figure 5.7B, Table 5.2). Following calcination at 700°C, Al22-TiO₂,DCR remains pure 6 nm anatase with only a slight decrease in surface area and increase in pore diameter (Figure 5.7B, Table 5.2). The pore structure remains the same H3-type geometry. TiO₂,DRC calcined at 700°C still contains 6-coordinate Ti (expected for both anatase and rutile TiO₂ crystal structures) and we expect that TiO₂,DCR and Al22-TiO₂,DCR also still contain primarily 6-coordinate anatase. Following calcination at 700°C, Al22-TiO₂,DRC increases in crystallinity and crystallite size and the XRD pattern matches pure anatase (Figure 5.7B). While the H2 type geometry is maintained, a loss of surface area and an increase in pore diameter is observed (Table 5.2). XANES analysis reveals a change from 5-coordinate Ti to the 6 coordinate structure of anatase for an analogous 14 mol% Al-modified anatase sample calcined at 700°C and we expect a similar Ti-coordination for Al22-TiO₂,DRC calcined at 700°C (representative spectrum in Figure 5.8).

5.3.2 Heat Capacity Results

A material's specific heat (*C*) is a measure of all occupied energy states (vibrational, electronic, magnetic, etc.) at a given temperature and its dependence on temperature has been modeled with theoretical functions for each type of contribution. All solids exhibit a Debye

dependence from phonons which at low temperatures ($T < 10$ K) approximates to odd powers in T starting with T^3 .³⁴ A linear contribution to the heat capacity, $C_{lin} = \gamma T$, is a well known contribution due to the conduction electrons in metals, however linear contributions have also been observed for non-metallic materials and have been attributed to a density of localized states associated with amorphous solids or ion vacancies.³⁵ For example, the linear dependence of the high temperature superconductor $\text{YBa}_2\text{Cu}_3\text{O}_7$ (YBCO) has been attributed to both intrinsic superconductivity³⁶ and to BaCuO_2 impurities.³⁷ Several studies have shown a direct correlation between linear terms (the slope of the linear contribution to the heat capacity) and lattice vacancies.³⁵ Therefore, a measurement of an insulating material's linear term is expected to give a measure of lattice vacancies.

Linear terms (the slope of the linear contribution to the heat capacity) were determined for pure anatase and 5, 14, 22, and 50 mol% Al-modified anatase samples calcined at 400°C prepared by both the DCR and DRC routes. The associated N_2 sorption, XANES, and XRD results for these samples are found in Table 5.3. For comparison, theoretical linear terms for mixtures of Al_2O_3 and TiO_2 were estimated using the experimentally determined linear terms for pure TiO_2 (DRC and DCR samples from this study) and Al_2O_3 (nano Al_2O_3 , see Huang et al.²³ for details on sample preparation). Linear terms of anatase and 5 – 50 mol% Al-modified anatase (DCR and DRC) are plotted against the $\text{TiO}_2/\text{Al}_2\text{O}_3$ estimated linear terms in Figure 5.9. A companion heat capacity study should be referred to for more information on the heat capacities, fitting procedures, and the origination of linear terms (manuscript in preparation).

Figure 5.9A reveals a sharp increase in the linear terms for pure TiO_2 ,DCR to Al5- TiO_2 ,DCR, after which the linear terms for 5 – 50 mol% Al-modified TiO_2 DCR samples follow a linear trend parallel to the predicted linear terms for the $\text{TiO}_2/\text{Al}_2\text{O}_3$ mixtures. Figure 5.9B

reveals that the linear terms for DRC materials below 50 mol% Al deviate largely from the predicted linear terms for TiO₂/Al₂O₃ mixtures. At 50 mol% Al, the linear term closely matches the predicted linear term for the TiO₂/Al₂O₃ mixture.

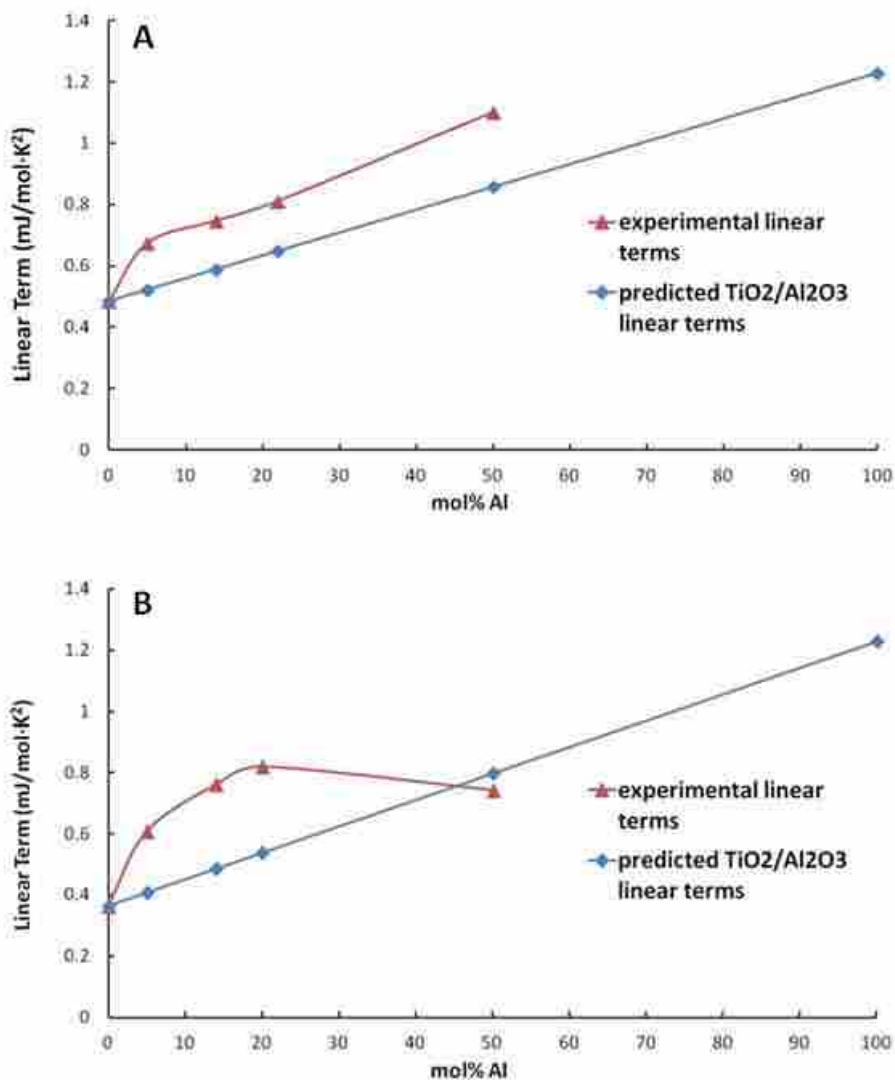


Figure 5.9 Experimentally determined linear terms of pure, 5, 14, 22, and 50 mol% Al-modified anatase calcined at 400°C synthesized by (A) dry, calcine, rinse (DCR) and (B) dry, rinse, calcine (DRC) synthesis routes.

Table 5.3 Crystallite size, N₂ sorption properties, and Ti coordination of materials calcined at 400°C with varying amounts of Al-modifier.

^a Route	Mol% Al	^b Crystallite Diameter (nm)	Surface Area (m ² /g)	Pore Volume (cm ³ /g)	Pore Diameter (nm)	Isotherm Type	^b Ti Coordination
DRC	0	7	163.6	0.24	4.7	H2	6
	5	5	375	0.33	4	H2	6ish
	14	A, 2 – 3	490	0.77	5.7	H2	5
	22	A, 2 – 3	471	0.44	4.4	H2	5
	50	A, 2 – 3	349	0.34	4.4	H2	5
DCR	0	7	124	0.30	7.8	H3	6
	5	7	138	0.25	3.8	H3	
	14	6	172	0.35	7.4	H3	
	22	6	184	0.34	6.3	H3	6
	50	5	307	0.37	4.3	H3	

- DRC = dry, rinse, calcine. DCR = dry, calcine, rinse.
- A = X-ray amorphous and crystallite sizes were estimated from TEM. All other crystallite sizes estimated from the Scherrer formula.
- Determined from XANES Ti k-edge.

5.4 Discussion

The results of this study illustrate how sophisticated techniques, including XANES and low temperature heat capacity in tandem with traditional techniques (XRD, TEM, and N₂ sorption) can provide new insights into the nano crystalline structure of doped materials. The results of this study also provide new insights into the mechanisms of stabilization of titania by dopants. As precursor structures are infrequently studied, our work provides new insights into precursor structure and how it relates to the synthesis process and the effects of rinsing. This study also reveals that the manner in which dopants are incorporated into the structure affects the stabilization and modification of support materials.

Table 5.4 includes a summary of structural information for 22 mol% Al-TiO₂ calcined at 400° synthesized by DRC and DCR pathways and should be referred to throughout the discussion as needed.

Table 5.4 Summary of structural information for 22 mol% Al-TiO₂ calcined at 400°C.

^a Route	Mol% Al	^b Crystallite Diameter (nm) and XRD Results	Surface Area (m ² /g)	Pore Structure	^c Ti Coordination	^d Al Coordination	Heat Capacity Results suggest:
DRC	22	A, 2 – 3	471	Networked, ink-bottle	5	Primarily 6	Separate TiO ₂ and Al ₂ O ₃ -like phases
DCR	22	6 little NH ₄ Cl in precursor, suggests surface Al coordinating Cl ⁻	184	Slit-like	6	Primarily 6 Approaching a crystalline environment	Strong interaction between Ti-Al, similar to predicted TiO ₂ /Al ₂ O ₃ mixture at 50 mol% Al-TiO ₂

a. DRC = dry, rinse, calcine. DCR = dry, calcine, rinse.

b. A = X-ray amorphous, therefore crystallite sizes were estimated from TEM. All other crystallite sizes estimated from the Scherrer formula.

c. Determined from XANES Ti k-edge analysis.

d. Determined from ²⁷Al MAS NMR analysis.

5.4.1 Ti Coordination from XANES

XANES Ti K edge data reveal that the unrinsed Al-modified precursor, Al22-TiO₂,D, contains primarily 5-coordinate Ti. While no XANES data were collected for precursors TiO₂,D, TiO₂,DR, and Al22-TiO₂,DR, the crystallinity and N₂ sorption properties of these precursors are very similar to Al22-TiO₂,DRC calcined at 400°C, a sample containing primarily 5-coordinate Ti. From these results, we suggest that TiO₂,D, TiO₂,DR, and Al22-TiO₂,DR also contain primarily 5-coordinate Ti. Though precursors TiO₂,D, TiO₂,DR, and Al22-TiO₂,DR appear

largely amorphous to XRD (i.e., observed as broad, low intensity peaks), TEM micrographs reveal that these materials are not truly amorphous, but instead consist of very small crystallites of approximately 2 nm or smaller.

Low coordinate Ti materials have been reported for amorphous and ultrafine titania particles based on XAS studies. Chen et al.^{38,39} observed a decrease in the Ti coordination number as crystallite size decreased, with a Ti coordination number of 4.8 for 3 nm titania crystallites. Luca et al.⁴⁰ reported that small titania xerogels likely have low Ti coordination numbers. Yeung et al.⁴¹ reported a Ti coordination number of 4.5 for a 3 nm TiO₂ sample. Zhang et al.⁴² determined that X-ray amorphous titania consisted of a strained anatase-like core with a highly distorted shell. A reduced coordination number of approximately 5 was attributed primarily to Ti atoms in the outer (surface) shell (6 coordinate in the crystallite core).⁴² These previous studies conclude that reduced Ti coordination in amorphous and ultrafine titanias mainly occurs in surface TiO₂.³⁸⁻⁴² Therefore, the structure of amorphous and ultrafine clusters is apparently dominated by the surface structure because the fraction of Ti atoms exposed to the surface is very high in these small clusters. The reduced coordination of surface Ti is a result of incomplete coordination by oxygen and distortion of TiO₆ octahedra due to the anisotropic surface environment. Therefore, we propose that 5-coordinate Ti is inherent to small anatase and anatase-like crystallites, which have a large fraction of surface Ti and is not an effect of incorporating the Al-modifier. Though Al₂₂-TiO₂,D appears to contain large and small crystallites, based on the 5-coordinate Ti, we propose that the sample more likely consists of 2 to 4 nm crystallites, some of which are joined through hydrogen bonding between surface Al-OH groups to create larger 6 nm particles.

5.4.2 Crystallite Growth and Phase Transformation of Pure Materials

(TiO₂,DRC and TiO₂,DCR)

We expect that unrinsed and rinsed precursor crystallites have very high surface energies due to the small (≥ 2 nm) crystallites they contain. In the case of unstabilized (pure) anatase, surface planes join during calcination to increase stability and crystallites grow together to form larger, more stable, Ti particles of lower surface energy. The increase in Ti coordination number from 5 to 6 is consistent with the formation of larger crystallites with a reduced number of surface Ti atoms. Our observations also demonstrate that following calcination at temperatures above 400°C, unstabilized titanias undergo a phase transition to bulk rutile accompanied by loss of surface area and porosity as observed in much of the previous literature.

5.4.3 Structure of 22 mol% Al-modified TiO₂

Al₂₂-TiO₂,DRC is the only calcined material to retain the small 2 nm crystallites (with 5-coordinate Ti) present in the precursor materials. While surface AlO_x species could stabilize small crystallites, preventing grain growth and the accompanying formation of 6-coordinate Ti, it can clearly be seen from the heat capacity data that Al is present in different surface or bulk environments in the DRC and DCR materials.

5.4.3.1 Al₂₂-TiO₂,DCR

No alumina phases are observed by XRD in the unrinsed precursor (Al₂₂-TiO₂,D) and therefore Al could be incorporated into the anatase structure or located on the surface in the form of AlO_x or Al(Cl)_x complexes. Given that very little ammonium chloride is observed in the XRD pattern for the Al₂₂-TiO₂,D precursor we conclude that the aluminum complexes with Cl⁻ ions to

inhibit the formation of ammonium chloride. Thus, Al is logically present on the surface of titania crystallites after drying.

It was shown from heat capacity measurements that as Al is added to DCR materials, the linear terms in the heat capacity increase parallel to the predicted linear terms for simple $\text{TiO}_2/\text{Al}_2\text{O}_3$ mixtures. This linear increase suggests that DCR samples behave like a mixture of two separate phases, i.e., TiO_2 and Al_2O_3 . As discussed earlier, the linear terms indicate a higher concentration of defects and vacancies in the DCR mixed oxides compared to the predicted linear terms for the simple $\text{TiO}_2/\text{Al}_2\text{O}_3$ mixtures, and XRD data suggest that AlO_x is present as an XRD amorphous, surface species. We therefore conclude the structure of $\text{Al}_{22}\text{-TiO}_2\text{,DCR}$ is a TiO_2 core coated with an AlO_x layer that is higher in defects and vacancies than Al_2O_3 . Al could be present as clusters of Al_xO_y , however, as observed by Chen et al.,⁴³ the significant changes in surface area and pore structure of Al-modified TiO_2 suggest multi-atom Al clusters should be relatively rare compared with single atom Al molecules. ^{27}Al NMR data reveals that the majority of Al (77%) in $\text{Al}_{22}\text{-TiO}_2\text{,DCR}$ is 6-coordinate and that Al NMR shows a reduced disorder in DCR materials, demonstrating that the local Al environment is approaching a crystalline material. Therefore, NMR data is consistent with an octahedrally coordinated surface Al species approaching a semi-ordered separate crystalline phase in DCR materials.

5.4.3.2 $\text{Al}_{22}\text{-TiO}_2\text{,DRC}$

The linear terms from heat capacity data for DRC materials deviate largely from the linear terms predicted for $\text{TiO}_2/\text{Al}_2\text{O}_3$ mixtures below 50 mol% Al. This suggests a strong interaction between Al and TiO_2 with increased vacancies or defects in the TiO_2 lattice. Furthermore, ^{27}Al NMR data indicates the lack of crystallinity of the Al environment in $\text{Al}_{22}\text{-TiO}_2\text{,DRC}$. Accordingly, there is no evidence from the heat capacity and NMR data for the

formation of separate TiO_2 and Al_2O_3 phases below 50 mol% Al. We hypothesize that Al is incorporated in TiO_2 lattice vacancies during rinsing which, due to charge differences, creates a substantial number of oxygen vacancies in the lattice. Based on cation/anion ratios, Al^{3+} could occupy tetrahedral or octahedral positions. From ^{27}Al MAS NMR data, we conclude that the majority of lattice incorporated Al is located in octahedral sites, with a smaller amount (14% or less for Al22- TiO_2 ,DRC) incorporated into tetrahedral sites. This is consistent with previous work¹³ where we observed similarities between Zr (likely to be found in octahedral positions) and Al-modified TiO_2 . It should be noted that it is difficult to distinguish between surface and bulk atoms in 2 nm crystallites. Therefore, the 4 and 5-coordinate Al observed by NMR for Al22- TiO_2 ,DRC could also be due to the effects of surface Al atoms with incomplete coordination.

At high concentrations of Al (i.e. 50 mol%), our heat capacity data are consistent with a physical mixture of TiO_2 and Al_2O_3 , strongly suggestive of separate phases. We hypothesize that at high concentrations of Al, the solubility of Al into the anatase crystal structure is exceeded and a surface AlO_x species is formed.

5.4.4 Al Stabilization Mechanisms

5.4.4.1 Al22- TiO_2 ,DCR

We previously concluded that Al is mostly present as AlO_x molecules on the surface of TiO_2 in Al22- TiO_2 ,DCR materials. Surface dopants are generally seen to inhibit grain growth, thereby inhibiting crystal phase transitions, e.g. anatase to rutile.⁴³ Phase transitions can be initiated through nucleation at interfaces between aggregates. Therefore, surface dopants may stabilize phases by altering the surface energies at interfaces and activation energies of

transformations. Chen et al.⁴³ found that surface yttrium clusters inhibited coarsening and the anatase to rutile phase transition in nano titania. This retardation of particle growth and phase transitions is important in catalysis because coarsening and phase changes can result in loss of catalytic properties. Our results are in agreement with previous findings; the incorporation of Al completely inhibits the anatase to rutile transition at temperatures as high as 700°C.⁶ In fact, calcination at 700°C results in little change in N₂ sorption properties, phase, crystallite size, and pore structure. We therefore conclude that Al inhibits coarsening of anatase by lowering the surface energy of one or more anatase surfaces, thereby stabilizing planes of high surface energy, which would otherwise join as part of the crystallite growth process to achieve stabilization.⁴³ Surface AlO_x species also increase surface area; hence Al-modified DCR titanias (Table 5.3) have higher surface area than unmodified TiO₂,DCR.^{9,44}

5.4.4.2 Al₂₂-TiO₂,DRC

We previously hypothesized that in Al₂₂-TiO₂,DRC materials, Al is present as AlO_x surface species and Al³⁺ ions in primarily octahedral sites. As previously discussed, surface AlO_x species adsorb onto and stabilize high-energy surface planes of TiO₂.⁴³ It is expected that Al³⁺ ions in octahedral lattice sites increase lattice strain, thereby limiting mass transport which is necessary for grain growth.^{8,45} Therefore, both surface and lattice vacancy incorporated Al inhibit grain growth and the formation of large titania crystallites (with 6-coordinate Ti). Following calcination at 400°C, Al₂₂-TiO₂,DRC retains the 2 nm crystallites (with 5-coordinate Ti), high surface area, and small pore diameter observed in its precursor.

Al apparently has a limited ability to stabilize the 2 nm anatase-like crystallites. After calcination at 700°C, grain growth and 6-coordinate Ti are observed for Al₂₂-TiO₂,DRC materials. We expect that by 700°C, the high surface energies of small 2 to 3 nm crystallites

overcome the stabilization of Al. The change from 5 to 6 coordinate Ti is attributed to grain growth and not structural rearrangement, as the pore geometry is maintained.

5.4.5 Effects of Rinsing on Pure and Doped TiO₂

Effects of rinsing on the pore structure

N₂ sorption analysis reveals that DRC materials have H2-type hysteresis (indicative of networked, ink-bottle pores) and DCR materials have H3-type hysteresis (indicative of slit-like pores). Due to the presence of byproducts, N₂ sorption analysis of unrinsed precursors is not possible. However, N₂ sorption analysis reveals that rinsed precursors have H2-like hysteresis, similar to the DRC materials, indicating that the pore structure changes only slightly during calcination. Therefore, we suspect that unrinsed precursors have H3-type hysteresis similar to the DCR materials. We conclude that rinsing leads to a change in pore structure from H3-type pores, to H2-type pores. We suspect the removal of byproduct salts which have stabilized the slit-like H3 precursor structure and interactions of rinse water with the unstable, exposed surfaces causes partial collapse of slit-like pores and opens channels between pores to create the H2-networked pore structure observed in the rinsed materials.

Effects of rinsing on crystallite size and Al incorporation

As previously discussed, Al₂₂-TiO₂,D consists of 2 to 4 nm anatase crystallites, some of which are joined through hydrogen bonding to create larger 6 nm particles. During rinsing, we suspect hydrogen bonds between hydroxyl surface groups are broken, resulting in the small 2 – 3 nm crystallites observed in Al₂₂-TiO₂,DR, and Cl⁻ is removed, resulting in an increase in 5-coordinate surface Al species. Based on heat capacity conclusions, we suspect that during rinsing

some surface Al is incorporated into the TiO₂ lattice. Further experiments are needed to determine how this occurs.

5.5 Conclusions

- 1) The results of this study reveal that 5-coordinate Ti is inherent to ultrafine ≥ 2 nm anatase crystallites due to the large concentration of surface Ti atoms and is not a consequence of incorporating Al into anatase.
- 2) Results of this work reveal that the order of rinsing affects the final structure of Al-modified anatase; we conclude that (1) Al is incorporated into lattice vacancies and present as surface AlO_x species in materials rinsed prior to calcination; and (2) Al is present as surface AlO_x species in materials rinsed only after calcination.
- 3) Heat capacity measurements in combination with other analysis techniques provide new and unique insights into the understanding of doped nanostructures and possible stabilization mechanisms. Two mechanisms of Al-stabilization and modification are present: (1) surface Al stabilizes anatase TiO₂ by lowering the surface energy of anatase surfaces, stabilizing planes of high surface energy which would otherwise join to achieve stabilization, thereby retarding crystallite growth; and (2) vacancy-incorporated Al stabilizes anatase TiO₂ by increasing lattice strain and limiting mass transport necessary for grain growth.
- 4) This work demonstrates that in addition to dopant identity and amount, the method of incorporation greatly affects the stability and properties of a doped oxide support. For example, 22 mol% Al-modified TiO₂ stabilized with surface Al has an average crystallite diameter of 6 nm, a surface area of 184 m²/g, a pore volume of 0.34 cm³/g, and a pore

diameter of 6.4 nm compared with 22 mol% Al-modified TiO₂ stabilized with surface and vacancy-incorporated Al which has an average crystallite diameter of 2-3 nm, a surface area of 471 m²/g, a pore volume of 0.44 cm³/g, and a pore diameter of 4.4 nm.

5.6 References

1. Haruta, M.; Tsubota, S.; Kobayashi, T.; Kageyama, H.; Genet, M. J.; Delmon, B., Low-temperature oxidation of carbon monoxide over gold supported on titanium dioxide, ferric oxide, and cobalt tetraoxide. *J. Catal.* **1993**, *144* (1), 175-92.
2. Imai, H.; Date, M.; Tsubota, S., Preferential Oxidation of CO in H₂-Rich Gas at Low Temperatures over Au Nanoparticles Supported on Metal Oxides. *Catal. Lett.* **2008**, *124* (1-2), 68-73.
3. Edwards, J. K.; Carley, A. F.; Herzing, A. A.; Kiely, C. J.; Hutchings, G. J., Direct synthesis of hydrogen peroxide from H₂ and O₂ using supported Au-Pd catalysts. *Faraday Discuss.* **2008**, *138* (Nanoalloys), 225-239.
4. Tahir, S. F.; Koh, C. A., Catalytic oxidation for air pollution control. *Environ. Sci. Pollut. Res. Int.* **1996**, *3* (1), 20-3.
5. Shyue, J.-J.; De, G. M. R., Single-step preparation of mesoporous, anatase-based titanium-vanadium oxide and its application. *J. Am. Chem. Soc.* **2005**, *127* (36), 12736-12742.
6. Carp, O.; Huisman, C. L.; Reller, A., Photoinduced reactivity of titanium dioxide. *Prog. Solid State Chem.* **2004**, *32* (1-2), 33-177.
7. Liao, L.; Ingram, C. W., Mesoporous I-Ag codoped titania and alumina modified titania catalysts: Synthesis, characterization and photocatalytic properties. *Appl. Catal., A* **2012**, *433-434*, 18-25.

8. Tsai, C.-Y.; Hsi, H.-C.; Bai, H.; Fan, K.-S.; Sun, H.-D., Single-step synthesis of Al-doped TiO₂ nanoparticles using non-transferred thermal plasma torch. *Jpn. J. Appl. Phys.* **2012**, *51* (1, Pt. 2), 01AL01/1-01AL01/6.
9. Smitha, V. S.; Baiju, K. V.; Perumal, P.; Ghosh, S.; Warriar, K. G., Hydrophobic, Photoactive Titania-Alumina Nanocrystallites and Coatings by an Aqueous Sol-Gel Process. *Eur. J. Inorg. Chem.* **2012**, *2012* (2), 226-233.
10. Zhou, Z.; Zeng, T.; Cheng, Z.; Yuan, W., Preparation and Characterization of Titania-Alumina Mixed Oxides with Hierarchically Macro-/Mesoporous Structures. *Ind. Eng. Chem. Res.* **2011**, *50* (2), 883-890.
11. Lee, J. E.; Oh, S.-M.; Park, D.-W., Synthesis of nano-sized Al doped TiO₂ powders using thermal plasma. *Thin Solid Films* **2004**, *457* (1), 230-234.
12. Wang, L.-Y.; Sun, Y.-P.; Xu, B.-S., Comparison study on the size and phase control of nanocrystalline TiO₂ in three Ti-Si oxide structures. *J. Mater. Sci.* **2008**, *43* (6), 1979-1986.
13. Olsen, R. E.; Bartholomew, C. H.; Huang, B.; Simmons, C.; Woodfield, B. F., Synthesis and characterization of pure and stabilized mesoporous anatase titanias. *Microporous Mesoporous Mater.* **2013**, *Accepted*.
14. Olsen, R. E.; Bartholomew, C. H.; Enfield, D. B.; Lawson, J. S.; Rohbock, N.; Scott, B. S.; Woodfield, B. F., Optimizing the synthesis and properties of Al-modified anatase catalyst supports by statistical experimental design. *Chemical Engineering Science* **2013**, *submitted*.

15. Woodfield, B. F.; Liu, S.; Boerio-Goates, J.; Liu, Q. Preparation of uniform nanoparticles of ultra-high purity metal oxides, mixed metal oxides, metals, and metal alloys. WO2007098111A2, 2007.
16. Patterson, A. L., The Scherrer formula for x-ray particle-size determination. *Phys. Rev.* **1939**, *56*, 978-82.
17. Pierce, C., Computation of pore sizes from physical adsorption data. *J. Phys. Chem.* **1953**, *57*, 149-52.
18. Orr, C., Jr.; Dallavalle, J. M., *Fine Particle Measurement-Size, Surface, and Pore Volume*. Macmillan Co.: 1959; p 353 pp.
19. Liu, H.; Zhang, L.; Seaton, N. A., Sorption hysteresis as a probe of pore structure. *Langmuir* **1993**, *9* (10), 2576-82.
20. Rojas, F.; Kornhauser, I.; Felipe, C.; Esparza, J. M.; Cordero, S.; Dominguez, A.; Riccardo, J. L., Capillary condensation in heterogeneous mesoporous networks consisting of variable connectivity and pore-size correlation. *Phys. Chem. Chem. Phys.* **2002**, *4* (11), 2346-2355.
21. Niemark, A. V., Percolation theory of capillary hysteresis phenomena and its application for characterization of porous solids. *Stud. Surf. Sci. Catal.* **1991**, *62* (Charact. Porous Solids 2), 67-74.
22. Parlar, M.; Yortsos, Y. C., Percolation theory of vapor adsorption-desorption processes in porous materials. *J. Colloid Interface Sci.* **1988**, *124* (1), 162-76.
23. Huang, B.; Bartholomew, C., H.; Woodfield, B. F., Facile synthesis of mesoporous alumina with tunable pore size: Effects of alcohols in precursor formation and calcination. *Microporous Mesoporous Mater.* **2013**, *177*, 37-46.

24. Huang, B. B., C.; Woodfield, B.F., Improved calculations of pore size distribution for relatively large, irregular slit-shaped mesopore structure. *Microporous Mesoporous Mater.* **2014**, *184*, 112-121.
25. Ball, P. C.; Evans, R., Temperature dependence of gas adsorption on a mesoporous solid: capillary criticality and hysteresis. *Langmuir* **1989**, *5* (3), 714-23.
26. Neimark, A. V.; Ravikovitch, P. I., Capillary condensation in MMS and pore structure characterization. *Microporous Mesoporous Mater.* **2001**, *44-45*, 697-707.
27. Neimark, A. V.; Ravikovitch, P. I.; Vishnyakov, A., Adsorption hysteresis in nanopores. *Phys. Rev. E: Stat. Phys., Plasmas, Fluids, Relat. Interdiscip. Top.* **2000**, *62* (2-A), R1493-R1496.
28. Monson, P. A., Contact Angles, Pore Condensation, and Hysteresis: Insights from a Simple Molecular Model. *Langmuir* **2008**, *24* (21), 12295-12302.
29. Shi, Q.; Snow, C. L.; Boerio-Goates, J.; Woodfield, B. F., Accurate heat capacity measurements on powdered samples using a Quantum Design physical property measurement system. *J. Chem. Thermodyn.* **2010**, *42* (9), 1107-1115.
30. Shi, Q.; Boerio-Goates, J.; Woodfield, B. F., An improved technique for accurate heat capacity measurements on powdered samples using a commercial relaxation calorimeter. *J. Chem. Thermodyn.* **2011**, *43* (8), 1263-1269.
31. Boerio-Goates, J.; Li, G.; Li, L.; Walker, T. F.; Parry, T.; Woodfield, B. F., Surface Water and the Origin of the Positive Excess Specific Heat for 7 nm Rutile and Anatase Nanoparticles. *Nano Lett.* **2006**, *6* (4), 750-754.

32. Massiot, D.; Fayon, F.; Capron, M.; King, I.; Le Calvé, S.; Alonso, B.; Durand, J. O.; Bujoli, B.; Gan, Z.; Hoatson, G., Modelling One and Two-Dimensional Solid-State NMR Spectra. *Magn. Reson. Chem.* **2002**, *40*, 70-76.
33. Neuville, D. R.; Cormier, L.; Massiot, D., Al environment in tectosilicate and peraluminous glasses: A ^{27}Al MQ-MAS NMR, Raman, and XANES investigation. *Geochimica et Cosmochimica Acta* **2004**, *68* (24), 5071-5079.
34. Gopal, E. S. R., *Specific Heats at Low Temperatures (International Cryogenics Monograph Series)*. Plenum: 1966; p 226 pp.
35. Coey, J. M. D.; Von, M. S.; Torressen, A., Low-temperature specific heat of bismuth strontium calcium copper oxide ($\text{Bi}_2\text{Sr}_2\text{CaCu}_2\text{O}_8$): comparison with some other layered oxides. *J. Less-Common Met.* **1989**, *151*, 191-4.
36. Wright, D. A.; Emerson, J. P.; Woodfield, B. F.; Gordon, J. E.; Fisher, R. A.; Phillips, N. E., Low-temperature specific heat of $\text{YBa}_2\text{Cu}_3\text{O}_{7-\delta}$, $0 \leq \delta \leq 0.2$: evidence for d-wave pairing. *Phys. Rev. Lett.* **1999**, *82* (7), 1550-1553.
37. Fisher, R. A.; Wright, D. A.; Emerson, J. P.; Woodfield, B. F.; Phillips, N. E.; Wang, Z. R.; Johnston, D. C., Low-temperature specific heat of BaCuO_2 and $\text{BaCuO}_{2.14}$ in magnetic fields to 7 T. *Phys. Rev. B: Condens. Matter Mater. Phys.* **2000**, *61* (1), 538-548.
38. Chen, L. X.; Rajh, T.; Wang, Z.; Thurnauer, M. C., XAFS Studies of Surface Structures of TiO_2 Nanoparticles and Photocatalytic Reduction of Metal Ions. *J. Phys. Chem. B* **1997**, *101* (50), 10688-10697.
39. Chen, L. X.; Rajh, T.; Jager, W.; Nedeljkovic, J.; Thurnauer, M. C., X-ray absorption reveals surface structure of titanium dioxide nanoparticles. *J. Synchrotron Radiat.* **1999**, *6* (3), 445-447.

40. Luca, V.; Djajanti, S.; Howe, R. F., Structural and Electronic Properties of Sol-Gel Titanium Oxides Studied by X-ray Absorption Spectroscopy. *J. Phys. Chem. B* **1998**, *102* (52), 10650-10657.
41. Yeung, K. L.; Maira, A. J.; Stolz, J.; Hung, E.; Ho, N. K.-C.; Wei, A. C.; Soria, J.; Chao, K.-J.; Yue, P. L., Ensemble Effects in Nanostructured TiO₂ Used in the Gas-Phase Photooxidation of Trichloroethylene. *J. Phys. Chem. B* **2002**, *106* (18), 4608-4616.
42. Zhang, H.; Chen, B.; Banfield, J. F.; Waychunas, G. A., Atomic structure of nanometer-sized amorphous TiO₂. *Phys. Rev. B: Condens. Matter Mater. Phys.* **2008**, *78* (21), 214106/1-214106/12.
43. Chen, B.; Zhang, H.; Gilbert, B.; Banfield, J. F., Mechanism of Inhibition of Nanoparticle Growth and Phase Transformation by Surface Impurities. *Phys. Rev. Lett.* **2007**, *98* (10), 106103/1-106103/4.
44. Hanaor, D. A. H.; Assadi, M. H. N.; Li, S.; Yu, A.; Sorrell, C. C., Ab initio study of phase stability in doped TiO₂. *arXiv.org, e-Print Arch., Condens. Matter* **2012**, 1-21, arXiv:1210.7555v1 [cond-mat.mtrl-sci].
45. Lee, D.-W.; Park, S.-J.; Ihm, S.-K.; Lee, K.-H., One-Pot Synthesis of Pt-Nanoparticle-Embedded Mesoporous Titania/Silica and Its Remarkable Thermal Stability. *J. Phys. Chem. C* **2007**, *111* (21), 7634-7638.

Chapter 6: One-pot Synthesis of Pt Catalysts Supported on 22-mol% Al-modified Anatase.

6.1 Introduction

Noble metals such as Pt supported on anatase TiO₂ are used in a number of oxidation reactions, e.g. oxidation of CO at low temperatures,¹ preferential oxidation of CO in H₂/CO mixtures,² low-temperature, direct synthesis of hydrogen peroxide,³ selective oxidation of primary C-H bonds,⁴ and oxidation of alcohols to aldehydes.⁵ With increasing concerns about atmospheric pollution, there has been significant interest in using catalysts supported on TiO₂ for the complete oxidation of volatile organic compounds to CO₂ and H₂O.⁶ A comprehensive review⁷ addresses other reactions involving catalysts supported on TiO₂.

In typical syntheses of supported Pt catalysts (i.e. wet and dry impregnation, ion exchange, and strong electrostatic adsorption) an aqueous Pt precursor is prepared and deposited onto a catalyst support, followed by calcination and then reduction to obtain a Pt metal catalyst.⁸⁻¹¹ Complex synthesis methods may include (1) solution based reductions of Pt precursors¹² and (2) gaseous chemical vapor deposition on supports.¹³ These latter complex syntheses may improve catalytic performance; however, they are often time-consuming and expensive processes, which may include multiple steps, low metal loadings per step, and the use of templates which may need to be removed.

Simplified one-pot syntheses of supported Pt catalysts have been previously reported.¹⁴⁻¹⁹ However, many of these one-pot methods encounter difficulties including the formation of large metal crystallites with a broad size distribution and formation of mixed phases between the

support and active metal. Therefore, advances in simple, efficient, and industrially viable synthesis methods of supported noble metal catalysts are needed.

The efficiency of Pt use (i.e. Pt dispersion), catalyst activity and selectivity, and catalyst durability are largely dependent on support properties, including crystallite size, surface area, porosity, pore diameter, and stability. For example, increasing the surface area and controlling the porosity and morphology of the support can lead to improved supported catalysts. While previous studies have examined effects of support type (e.g. Al₂O₃, SiO₂, TiO₂), few have examined the effects of altering the properties of a single support, likely due to the availability of commercial supports. The ability to tailor a commercial support to improve its properties is limited.

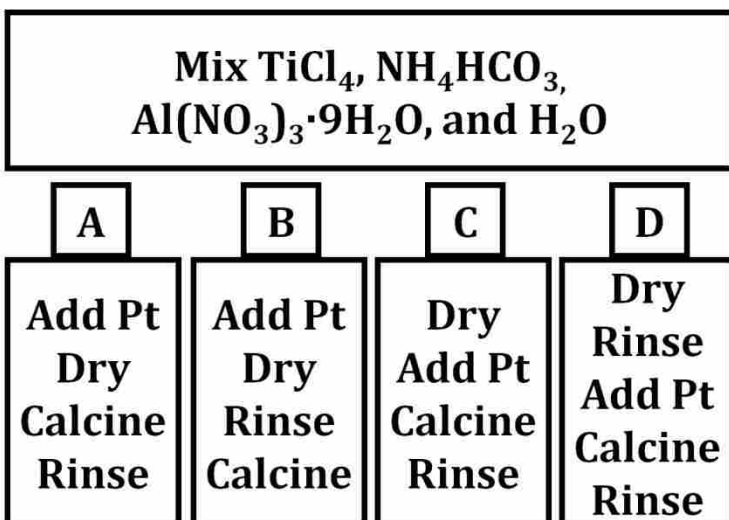
We previously reported a facile method to synthesize pure and modified anatase TiO₂ with high surface area, thermal stability, and pore volume while controlling pore diameter over a significant range. We report here a “one-pot” synthesis of supported Pt catalysts which involves an adaptation to the previous method. In this study we examine four pathways in a one-pot synthesis method and compare the resulting Pt dispersions with traditional Pt loading methods including dry impregnation (DI) and strong electrostatic adsorption (SEA). Each pathway influences the properties of both the anatase support and the Pt dispersion. Two promising one-pot pathways and the DI method were further examined to determine how the drying temperature, calcination ramp rate, and reduction ramp rate affected the Pt dispersion, crystallite size, and crystallite size distribution. Results presented in this paper show that this simple, fast, industrially viable, one-pot synthesis and the DI method using our Al-modified anatase support are promising syntheses of highly dispersed Pt supported on stabilized titania. Further studies, including statistically designed experiments are needed to (1) more completely determine the

effects of synthesis variables, (2) optimize the dispersion and reduction of Pt supported on 22 mol% Al-modified anatase, and (3) determine the activity and selectivity of these catalysts.

6.2 Experimental

6.2.1 Sample Preparation

0.5 – 8 wt% Pt catalysts supported on anatase and anatase modified with 22 mol% Al samples were prepared following a general solvent deficient method that can be used to synthesize many metal and mixed metal oxides.^{20, 21} A schematic of the synthesis is found in Scheme 6.1. Approximately 2.86 ml TiCl_4 , 2.75 g $\text{Al}(\text{NO}_3)_3 \cdot 9\text{H}_2\text{O}$, and 10.54 g NH_4HCO_3 (ABC) were mixed together. $\text{PtCl}_4 \cdot \text{XH}_2\text{O}$ was added when specified in the schematic, with the amount of $\text{PtCl}_4 \cdot \text{XH}_2\text{O}$ chosen to obtain the desired Pt loading. Ten ml distilled water was added slowly while stirring to start the reaction and facilitate mixing. The slurry was mixed for five minutes to form a stabilized anatase precursor. The precursor was then dried in air at temperatures of 21°C or 100°C for 24+ hours. Samples were rinsed using a vacuum filtration system at room temperature and calcined at 400°C for three hours in air (ramp rates of 1, 19 °C/min) in the order specified in the synthesis schematic. Samples synthesized via pathways A, C, and D were rinsed with 2 L of distilled water while samples synthesized via pathway B were rinsed with 500 ml dilute NH_4OH (1:4 NH_4OH :distilled H_2O) to prevent loss of Pt. Samples were also prepared by dry impregnation (DI) and strong electrostatic adsorption (SEA)⁹ for comparison. Anatase supports used for the DI and SEA supported catalysts were synthesized following pathway B, without adding Pt. Supports were rinsed with 2 L distilled H_2O before calcination. Details of the support preparation are available elsewhere.²¹



Scheme 6.1 Synthesis routes of 3 wt% Pt catalysts supported on 22 mol% Al-modified anatase. Pt = $\text{PtCl}_4 \cdot \text{XH}_2\text{O}$.

6.2.2 Sample Characterization

X-ray diffraction patterns were collected using a PANalytical X'Pert Pro diffractometer (Cu- $K_{\alpha 1}$ radiation, $\lambda = 1.540598 \text{ \AA}$) at 45 kV and 40 mA over the 2θ range of $10 - 90^\circ$ at scanning rates of $1.3^\circ/\text{min}$. Average crystallite diameters were estimated using the Scherrer equation²² and confirmed using transmission electron microscopy (TEM). TEM measurements were performed on a Tecnai F20 Analytical STEM operating at 200 keV. The samples were dispersed in ethanol and deposited on copper grids (lacey carbon fiber, 400 mesh copper grids, Ted Pella, Inc.).

The Ti K edge and Pt L_3 edge X-ray absorption spectroscopy spectra (X-ray absorption near edge, XANES, and extended X-ray absorption fine structure, EXAFS) were obtained using the 12-BM-B beamline of the Advanced Photon Source at Argonne National Laboratory. Spectra were collected using a Si(111) crystal monochromator in transmission mode and the spectra were calibrated using Ti or Pt foils as references.

Full-range N_2 sorption isotherms were collected at 77 K using a Micromeritics TriStar 3020 surface analyzer. Samples of 0.25 – 0.50 g were degassed at 200°C for 12 – 24 hours prior

to collecting data. Pore volumes were calculated from the adsorption isotherm at a relative pressure of 0.98 and specific surface areas were calculated using the Brunauer-Emmett-Teller (BET) method from a P/P^0 range of 0.05 to 0.2. H2 type pore diameters were calculated using a modified Pierce method^{23,24} with structural corrections for pore area and volume. Pore diameters were calculated from the adsorption branch for H2 type pores, since evaporation of the condensate during desorption is significantly constrained and delayed by the pore necks with “ink-bottle” pore geometry and by the connectivity of the network.²⁵⁻²⁸ H3 pore widths were calculated using the newly developed SPG model²⁹ involving slit geometry for the Kelvin equation, which also incorporates structural corrections for area and volume. For H3 type hysteresis with slit-like pores, the desorption branch is preferred due to delayed condensation observed in the adsorption process.³⁰⁻³³ For ease of discussion, pore widths and pore diameters will both be referred to as pore diameters.

H₂ chemisorption capacity was measured using a Quantachrome ChemBET TPR/TPD chemisorption Flow Analyzer instrument. Prior to measurements, samples were reduced under H₂ at 250°C (reduction ramp rates specified in Tables 6.1 – 6.3) for 75 min. Pt reduction temperature was selected based on temperature programmed reductions (TPRs) carried out on a Netzsch STA 409PC instrument. Following reduction, the temperature was reduced to 240°C under Ar, where samples were held for 30 min to remove loosely bound hydrogen. Samples were cooled in Ar to room temperature. H₂ chemisorption was measured at room temperature. To reverse the suppression of H₂ adsorption by TiO_x species (discussed below), samples were exposed to oxygen at room temperature, following which the oxygen was titrated by H₂. Pt dispersion was calculated using the following stoichiometry:

Reduced and cooled in Ar: $\text{H}_2 + 2 \text{ Pt} = 2 \text{ Pt-H}$

After exposure to oxygen: $\text{H}_2 = 2 \text{ H}$

$\text{PtO} + 3 \text{ H} = \text{Pt-H} + \text{H}_2\text{O}$

6.3 Results and Discussion

6.3.1 6.8 – 8 wt% Pt Catalysts

Characterizing supported catalysts is a challenge, as complex mixtures or structures often result from the synthesis, which may be further complicated by small crystallite sizes. As seen in Figure 6.1, Pt peaks are evident in the XRD patterns, with no evidence of an intermetallic compound Pt_3Ti . The presence of Pt peaks reveal crystalline Pt particles large enough to be observed by XRD (approx 4 – 9 nm for pathways B, D, DI, and SEA, approx 28 nm for pathways A and C, determined by the Scherrer formula²²) in addition to the small and finely dispersed Pt crystallites observed by TEM. The TiO_2 supports for samples synthesized via pathways A and C match anatase TiO_2 . The TiO_2 supports for samples synthesized via pathways B, D, DI, and SEA appear nearly amorphous according to XRD. However, TEM analysis reveals crystalline materials of very small (2 nm or smaller) crystallite sizes. No phase associated with the Al modifier is observed in XRD. We conjecture that the Al is present as (a) surface AlO_x species, and/or (b) Al^{3+} incorporated into empty octahedral sites in the anatase lattice. The structure of the modified anatase support will be further examined in an XAS study.

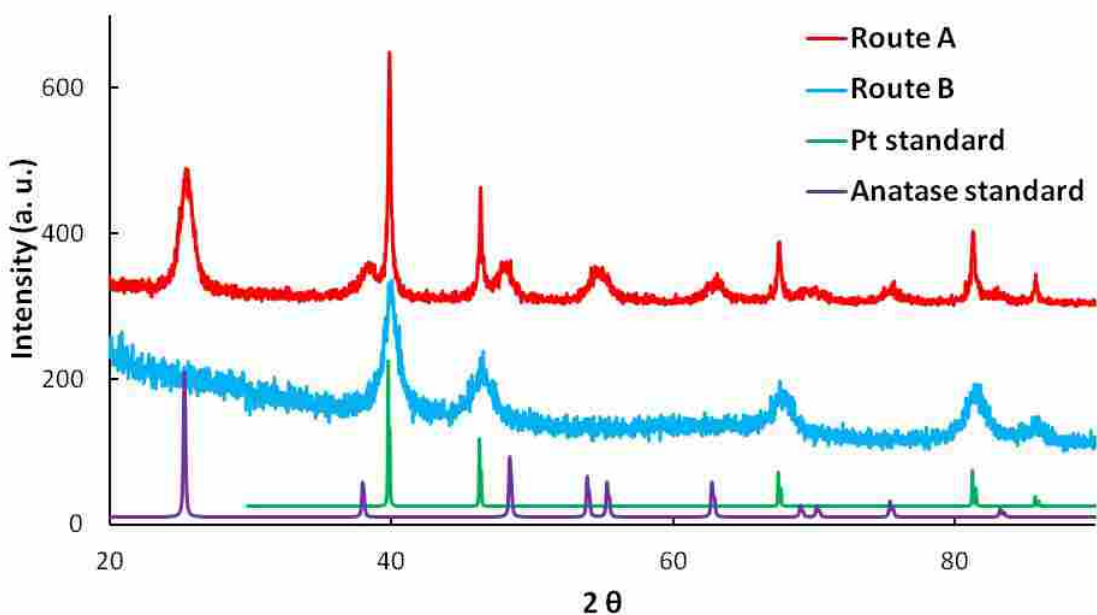


Figure 6.1 Representative X-ray diffraction patterns of 3 wt% Pt supported on 22 mol% Al synthesized via (a) route B (rinsed prior to calcination) and (b) route A (rinsed after calcination).

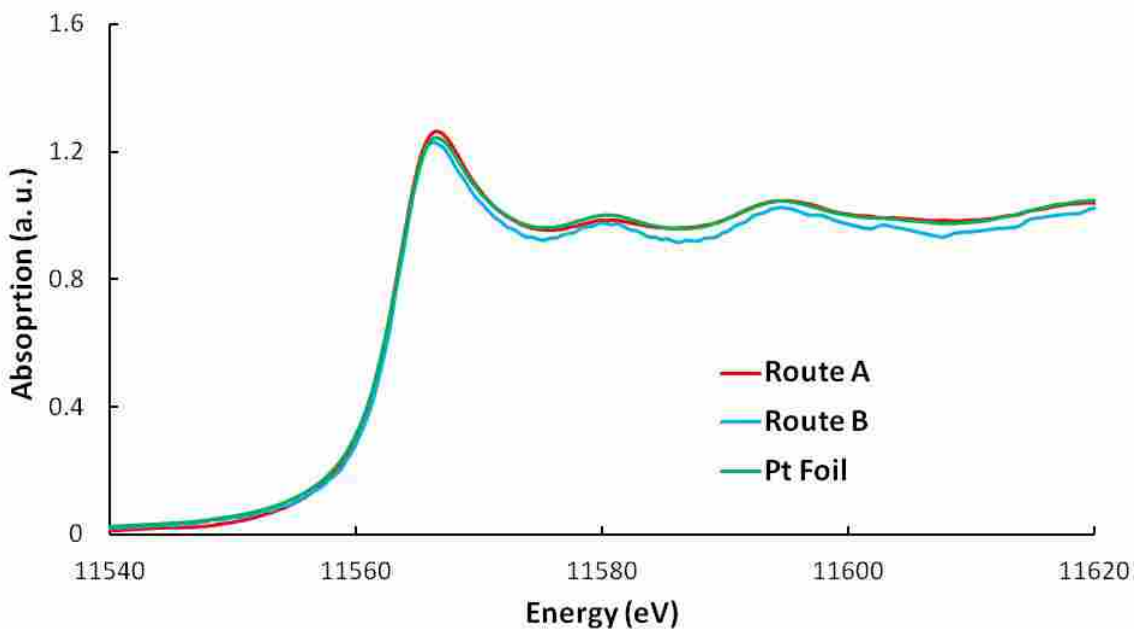


Figure 6.2 Representative XAS spectra of the Pt L₃ edge of 3 wt% Pt supported on 22 mol% Al-modified anatase synthesized via (a) route B (rinsed prior to calcination), (b) route A (rinsed after calcination) and (c) Pt foil. XAS spectroscopy was used to confirm the reduction of Pt.

Temperature programmed reductions were conducted to determine the temperature necessary to fully reduce the Pt catalyst. The reduction profile varied between sample pathways, however, to simplify the comparison between sample pathways and synthesis variables, 250°C, the highest temperature needed to fully reduce Pt, was selected. XAS spectroscopy confirmed the complete reduction of Pt to the metallic state. Representative spectra compared with a Pt foil standard are shown in Figure 6.2.

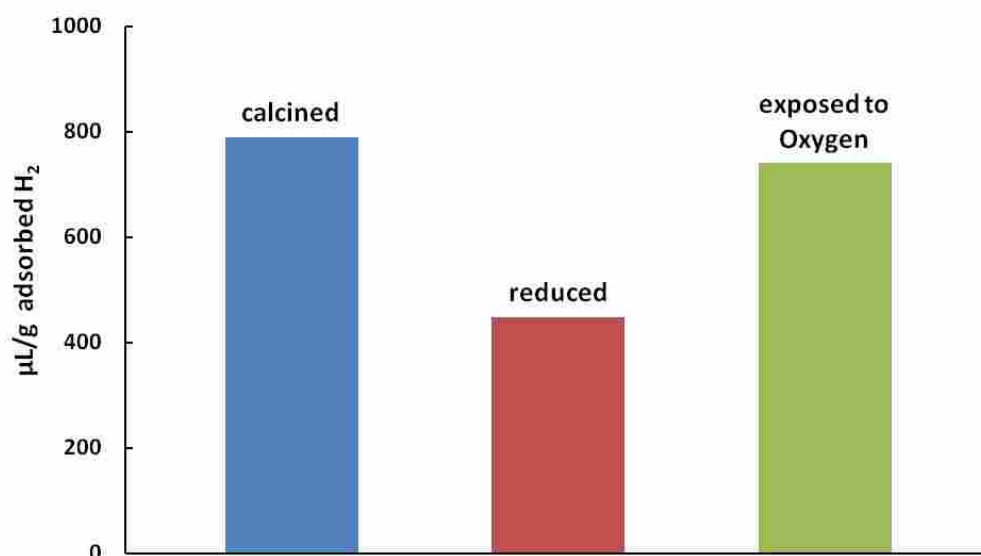


Figure 6.3 H₂ chemisorption uptakes. Considerable H₂ was adsorbed following calcination. H₂ adsorption was suppressed following reduction due to the SMSI effect. Sample was exposed to oxygen to reverse the SMSI effect and subsequently titrated with H₂. Chemisorption capacity was restored.

Following calcination, H₂ chemisorption capacity was measured. Due to the small and finely dispersed nature, Pt crystallites were formed during calcination at 400°C, probably due to decomposition of Pt oxide, and chemisorbed considerable H₂ (Figure 6.3). Following reduction at 250°C, H₂ chemisorption was almost completely suppressed for samples synthesized via pathways B, D, DI, and SEA, and partially suppressed for samples synthesized pathways A and C. However, following subsequent treatment with oxygen, the H₂ chemisorption capacity was

restored (Figure 6.3). The suppression of H₂ uptake after high temperature reduction and the restoration of H₂ chemisorption capacity on Pt and other Group VIII metals after exposure to oxygen have been widely reported in the literature, although the mechanism by which it occurs is not well understood.³⁴⁻⁴⁰ Previous reports postulate that H atoms, which spill over to the support from Pt crystallites, reduce TiO₂ to TiO_x ($x < 2$) species that migrate to the surface and form thin films that block adsorption sites on Pt metal particles.^{35, 36, 38-40} Exposure to oxygen reoxidizes the TiO_x thin films to 3-dimensional TiO₂ crystallites, thereby re-exposing most of the Pt. This interaction is referred to as a strong metal-support interaction (SMSI) or more properly, a decoration effect (i.e. decoration of the Pt surface by reduced TiO_x species).

In the present study, the SMSI effect is observed after reducing the samples at 250°C, though most researchers do not report observing the complete SMSI effect below reduction temperatures of 500°C.³⁴ While Paal et al.⁴⁰ observed complete H₂ chemisorption suppression only after reduction at or above 500°C, they observed reduced TiO_x species at reduction temperatures as low as 300°C.⁴⁰ Pesty et al.³⁹ however, reported the appearance of partially reduced TiO_x species as well as the initiation of the SMSI effect at temperatures as low as 177°C, and the SMSI effect became increasingly apparent as the reduction temperature was increased. We hypothesize that the generally low temperature at which the SMSI effect is observed in the present study could be due to the small crystallite sizes of the anatase support. Additionally, Al modifiers incorporated into the support are likely to induce oxygen defects in order to achieve charge balance. Many researchers have found that oxygen vacancies (or other defects) act as nucleation centers that strongly bind the catalyst, which could therefore lead to interactions between the support and the metal at lower temperatures. Less chemisorption suppression is observed for materials that were not rinsed prior to calcination (pathways A and C). We suspect

this is due to the larger anatase and Pt crystallite sizes as well as the different Al-modified anatase crystal structure (discussed below) present in these materials compared with those from the other synthesis pathways (B, D, DI, and SEA). However, SMSI states are complex and not fully understood and more studies examining the effects of dopants and the crystallite size of the support on the SMSI effect would be useful.

The SMSI (or decoration) effect has received attention because the partial coverage of the catalyst by mobile TiO_x species can lead to deactivation of the catalyst for some reactions. Several researchers have presented methods to reverse the SMSI effect through metal catalyst loading techniques and multi-step reduction methods.^{36, 37} In the present study, we observed the SMSI effect to be easily reversed by oxygen and therefore these catalysts are of potential use in applications where exposure to oxygen (or water) following reduction is acceptable.

While XRD observations indicate separate metal and support phases present in the reduced catalysts prepared by the one-pot method, hydrogen uptake results in Table 6.1 reveal, in addition, that (a) Pt metal crystallites are largely accessible to the gas phase and (b) higher Pt dispersions are observed for synthesis pathways B, D, DI, and SEA.

Table 6.1 Hydrogen uptake by 3 wt% Pt supported on 22 mol% Al-TiO₂ after calcination, reduction, and exposure to O₂.^a

Synthesis Route	^b Pt % Dispersion	Surface Area (m ² /g)	Pore Volume (cm ³ /g)	^c Pore Diameter (nm)	Ti Coordination
A	7	136	0.32	8	6
B	15	329	0.26	3.2	5
C	13	163	0.33	8.1	6
D	19	371	0.33	3.2	5
Dry Impregnation (DI)	24	375	0.33	3.2	5
Strong Electrostatic Adsorption (SEA)	18	394	0.35	3.3	5

a. Samples were dried at 100°C, calcined at 400°C for 3 hours, ramp = 19°C/min, reduced at 250°C in H₂ for 75 min, ramp = 2°C/min, exposed to oxygen, and titrated with H₂ at room temperature.

b. Samples A and B = 8 wt% Pt, all other samples = 6.5 wt% Pt.

c. Pore diameters for materials synthesized via routes A and C were calculated from the desorption branch using the SPG (slit) method, while pore diameters for materials from B, D, DI, and SEA routes were calculated from the adsorption branch using a cylindrical model.

BET data was collected following reduction of the catalyst (Table 6.1). All materials are Type IV mesoporous materials, and two types of isotherms, H2 and H3, are observed.⁴¹

Representative N₂ sorption isotherms are shown in Figure 6.4. Pore diameters were calculated using either a cylindrical model^{23,24} or the SPG (slit) model^{29,42} based on the hysteresis of the isotherms as well as mesopore geometry evident in TEM micrographs. Isotherms of materials synthesized via pathways A and C (not rinsed prior to calcination) are H3-type, which are associated with slit-like pores (Figure 6.4); thus pore diameters were calculated from the desorption branch using the SPG model.^{29-33,42} Isotherms for materials synthesized via pathways B, D, DI, and SEA (anatase supports were rinsed prior to calcination) are mainly H2-type,

associated with networked, ink-bottle pores; accordingly, these pore diameters were calculated from the adsorption branch using a cylindrical model to avoid problems associated with percolation encountered in the desorption branch.²⁵⁻²⁸ It should be noted that while the H3-type materials fit the model quite well, the H2-type materials did not. We suspect the H2-type pores are irregularly shaped with a distribution of pore widths and a range of pores either open to the surface and/or networked (branched).

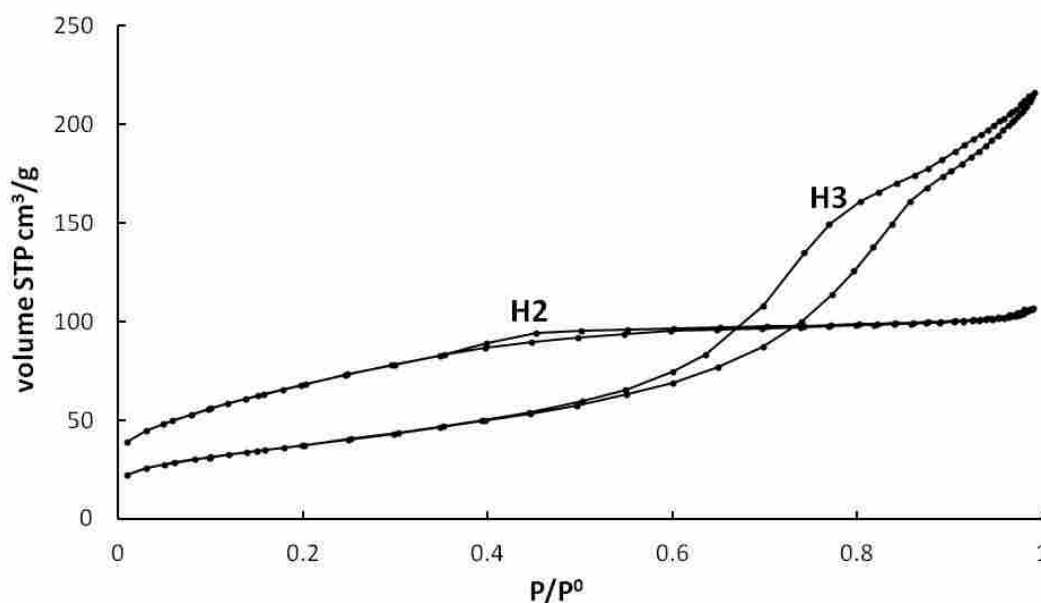


Figure 6.4 N₂ sorption isotherm examples. H3 type (slit-like pores) is representative of materials synthesized via routes A and C. H2 type (networked pores) are representative of materials synthesized via routes B, D, DI, and SEA. The types of pore structures demonstrates the effect of rinsing on the pore structure.

As seen in Table 6.1, synthesis pathways B, D, DI, and SEA, (anatase supports rinsed prior to calcination, H2-type pores), lead to higher levels of Pt dispersion than synthesis pathways A and C (anatase supports not rinsed prior to calcination, H3-type pores), likely due to the higher surface areas and smaller pore diameters observed for B, D, DI, and SEA materials (Scheme 6.1). Further structural analysis using XANES spectroscopy reveals that pathways leading to high Pt dispersions and high surface areas (B, D, DI, and SEA) contain primarily 5-

coordinate Ti, while the Ti environment in pathways leading to lower Pt dispersions and lower surface areas (A and C) matched a standard anatase environment, with a Ti-coordination of 6 (see Figure 6.5). Therefore, we conclude that rinsing affects the pore structure, surface morphology, and crystal structure of anatase supports. A 5-coordinate semi-amorphous precursor to anatase has been reported in the literature.⁴²⁻⁴⁶ We hypothesize that during the rinsing process, some Al migrates from the surface of TiO₂ into empty octahedral sites to stabilize and maintain this 5-coordinate precursor structure during and after calcination. In precursors that are not rinsed before calcination aluminum ions could remain bound to the surface and therefore cannot inhibit grain growth and structural rearrangement to the 6-coordinate structure of anatase during calcination. Although the 5-coordinate materials presented in this study appear largely amorphous to XRD (i.e., observed as broad, low intensity peaks), TEM micrographs reveal that these materials are not truly amorphous, but instead are very small crystallites of approximately 2 nm or less. Moreover, from the XRD patterns, these 5-coordinate materials appear to be anatase-like. We conclude that 5-coordinate Ti is inherent to small crystallites with limited 3D connectivity and which therefore contain a large percentage of surface Ti atoms. Lattice changes induced by the Al modifier, including strain and oxygen deficiency to achieve charge balance, could also affect the Ti-coordination. In a companion study we will further analyze the structure of the modified anatase using X-ray absorption spectroscopy.

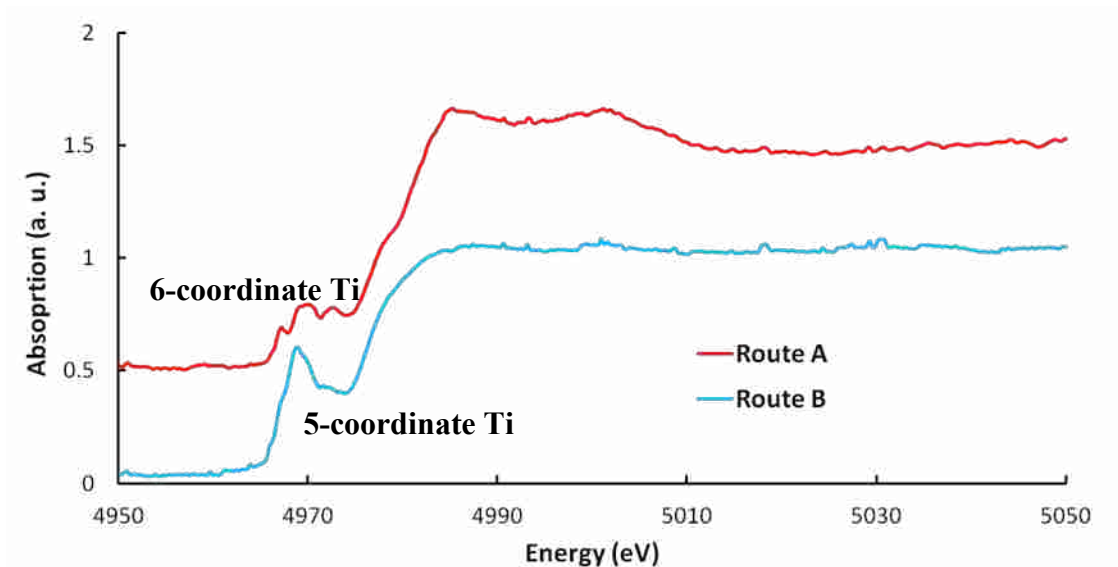


Figure 6.5 Representative XANES spectra of the Ti K-edge 3 wt% Pt supported on 22 mol% Al-modified anatase synthesized via (a) route B (rinsed prior to calcination) and (b) route A (rinsed after calcination). XANES spectra reveal 5-coordinate Ti for samples rinsed prior to calcination and 6-coordinate Ti for samples only rinsed after calcination.

Though initial Pt dispersions obtained using our method were promisingly high for such high Pt wt% loadings, large Pt crystallites are also observed by TEM among small and finely dispersed Pt crystallites. Thus, Pt was not fully utilized. Therefore, three synthesis pathways, B, D, and DI, were further studied to determine if variations in drying temperature, calcination ramp rate, and reduction ramp rate affect Pt crystallite size and dispersion. Results in Table 6.2 show that low drying temperatures (slow drying rates) and slow calcination ramp rates lead to smaller Pt crystallites and higher Pt dispersions compared with high drying temperatures and fast calcination ramp rates. We hypothesize that at slower drying rates smaller Pt nuclei are formed, while at slower calcination ramp rates the water partial pressure is lower enabling formation of smaller crystallites and decreased cluster and crystallite migration rates. The effects of reduction rates are inconclusive from these limited experiments. In the case of the DI pathway, increasing the reduction ramp rate increases Pt dispersion, while in pathway D, the reduction ramp rate did

not affect Pt dispersion. More studies are needed to determine the effect of reduction ramp rate, although a wealth of previous literature indicates that slow reduction rates are associated with higher dispersion.⁴⁷ While the highest dispersions obtained were achieved using a low drying temperature, a slow calcination ramp rate, and a slow reduction ramp rate, combinations of fast reduction ramp rates with low drying temperatures and slow calcination ramp rates, which have not yet been examined, may facilitate higher Pt dispersion, although this is unlikely.

Table 6.2 Effects of drying temperature, calcination ramp rate, and reduction ramp rate on Pt dispersion of a 6.5 – 8 wt% Pt catalyst supported on 22 mol% Al-TiO₂ after calcination, reduction, and exposure to O₂.^a

^a Synthesis Route	Drying Temp (°C)	Calcination Ramp Rate (°C/min)	Reduction Ramp Rate (°C/min)	^b Pt % Dispersion
B	21	1	1	25%
	100	19	2	15%
DI	21	1	1	30%
	100	19	1	20%
	100	19	2	24%
D	100	19	1	19%
	100	19	2	19%

- a. Samples were dried at 25°C or 100°C, calcined at 400°C for 3 hours, ramp = 1 or 19°C/min, reduced at 250°C in H₂ for 75 min, ramp = 1 or 2°C/min, exposed to oxygen, and titrated with H₂ at room temperature.
- b. Sample B = 8 wt% Pt, Samples DI and D = 6.5 wt% Pt

TEM micrographs confirm the changes in Pt dispersion with synthesis variations. Figure 6.6 compares 3 wt% Pt supported on 22 mol% Al-modified anatase prepared via pathway B with (1) a drying temperature of 25°C, a calcination ramp rate of 1°C/min, and a reduction ramp rate of 1°C/min, and (2) a drying temperature of 100°C, a calcination ramp rate of 19°C/min, and a reduction ramp rate of 2°C/min. Both preparations led to areas of small (approx 2 nm or less), highly dispersed Pt crystallites (Figure 6.6 1a and 2a) and some larger Pt crystallites (Figure 6.6

1b and 2b). However, conditions used for sample 2 led to a less uniform Pt size distribution, with more prevalent large Pt crystallites of larger diameters (compared with large Pt crystallites in sample 1), and, while the majority of micrographs for sample 1 contained areas of finely dispersed Pt observed in micrographs 1a and 1c, sample 2 has areas with little to no small (2 nm or less) Pt particles and only medium (approx 5 nm) Pt particles present (Figure 6.6 2c).

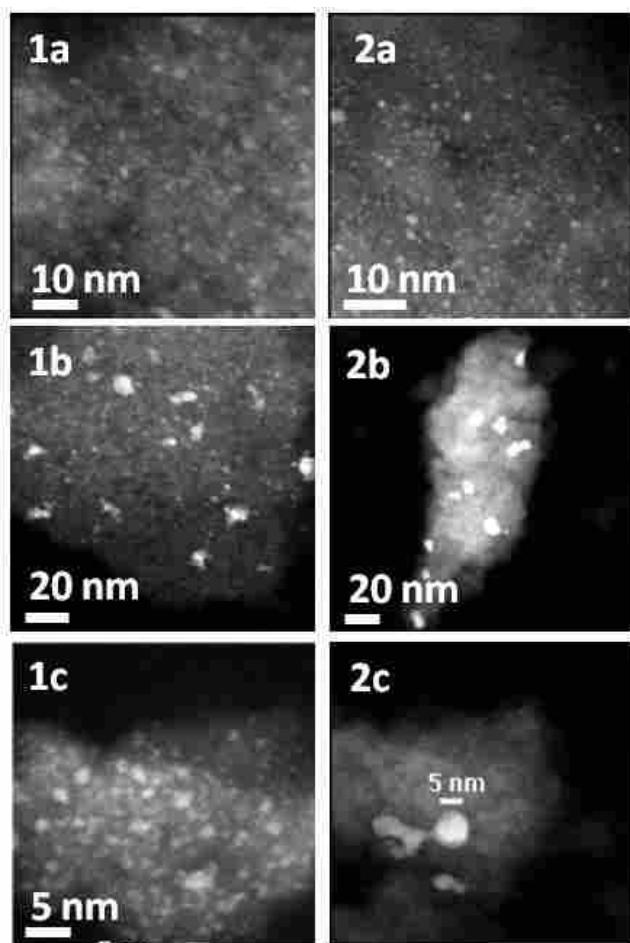


Figure 6.6 TEM images of 3 wt% Pt supported on 22 mol% Al-modified anatase synthesized via route B. (1) drying temperature = 25°C, calcination ramp rate = 1°C/min, and reduction ramp rate = 1°C/min. (2) drying temperature = 100°C, calcination ramp rate = 19°C/min, and reduction ramp rate = 2°C/min.

6.3.2 0.5 wt% Pt Catalysts

Based on results from the 6.5 – 8 wt% Pt samples, 0.5 wt% Pt catalysts supported on TiO₂ synthesized via pathways, B, D, and DI, using a drying temperature of 25°C, a calcination ramp rate of 1°C/min, and a reduction ramp rate of 1°C/min were examined. Results in Table 6.3 reveal that this method results in very high Pt dispersions for samples prepared via dry impregnation, demonstrating the excellent properties of the Al-modified TiO₂ support. While pathway D resulted in only moderate Pt dispersions, pathway B resulted in high Pt dispersions. The decoration effect (SMSI) was not as strongly observed for pathway B 0.5 wt% Pt samples as in prior 6.5-8 wt% Pt samples. In the case of pathway B (0.5 wt% Pt samples), Pt dispersions prior to O₂ exposure were significantly higher than after O₂ exposure. Further experimentation is needed to understand this phenomenon.

Table 6.3 Pt dispersion of a 0.5 wt% Pt catalyst supported on 22 mol% Al-TiO₂ after calcination, reduction, and exposure to O₂.^a

^a Synthesis Route	Drying Temp (°C)	Calcination Ramp Rate (°C/min)	Reduction Ramp Rate (°C/min)	Pt % Dispersion
DI	21	1	1	59%
B	21	1	1	^b 45%
D	100	19	1	30%

a. Samples were dried at 25°C, calcined at 400°C for 3 hours, ramp = 1°C/min, reduced at 250°C in H₂ for 75 min, ramp = 1°C/min, exposed to oxygen, and titrated with H₂ at room temperature.

b. Prior to oxygen exposure Pt dispersion = 54%

Table 6.4 compares Pt dispersions of 0.5 wt% Pt materials presented in this paper with dispersions of Pt supported on TiO₂ reported with documented methods in the recent literature. Samples (1) and (2) in Table 6.4 have unusually high Pt dispersions, however these samples contain K and Na making it difficult to compare the products. Additionally, these materials were obtained through a multi-step process which could present difficulties in an industrial setting. Pt

dispersions obtained using DI and the one-pot pathway B are higher than the majority of other dispersions reported for similar Pt wt% loadings. The one pot method shows initial promise, though it must be further optimized to control and increase Pt dispersion and decrease Pt crystallite/cluster size. For example, it is expected that variables such as reaction pH, mixing time, and drying time could affect Pt dispersion.

Table 6.4 Pt dispersion comparison.

	Sample	Wt % Pt	Pt % Dispersion	Source
1	Pt/Na/TiO ₂	0.5	94 ^c	10
2	Pt/Li/TiO ₂	0.5	89 ^c	10
3	Pt/TiO ₂	0.6	68.5 ^{d1}	48
4	Pt,TiO₂,Al₂O₃,DI	0.5	59^{d1}	*
5	^a Pt,TiO₂,Al₂O₃,Route B	0.5	54^{d1}	*
6	TiO ₂	1-3	51-54 ^c	12
7	Pt/TiO ₂	1	52 ^c	49
8	Pt-Re/TiO ₂	0.8	51.9 ^c	50
9	Pt/K/TiO ₂ -Al ₂ O ₃	1	51 ^d	51
10	^b Pt,TiO₂,Al₂O₃,Route B	0.5	45^{d1}	*
11	Pt/TiO ₂	1	39.1 ^{d1}	48
12	Rh/Pt/MgO/TiO ₂	1	36 ^e	52
13	Pt-Ba/Al-Ti	2.3	18 ^{b1}	11

a. Dispersion calculated prior to O₂ exposure

b. Dispersion calculated following O₂ exposure

c.CO chemisorption, stoichiometry used was not reported

d. H₂ chemisorption, stoichiometry used was not reported

d1. H₂ chemisorption, stoichiometry = 1 Pt : 1 H

e. method of determining Pt dispersion unknown.

*This paper

6.3.3 Method Overview

Results presented in this paper show that the simple, convenient one-pot method and the DI method using our Al-modified anatase support are promising for syntheses of highly

dispersed 0.5 – 8 wt% Pt supported on stabilized titania. Our results demonstrate that the stabilized anatase support is superior to other anatase supports for (1) obtaining high Pt dispersions, i.e. more efficiently utilizing this expensive precious metal and (2) processes in which thermal stability is important due to its constant phase and pore structures at high temperatures. Initial SEA results (Table 6.1) indicate promise for this method, and further study of this synthesis pathway is planned. Our systematic study of preparation variables shows that drying temperature, calcination ramp rate, and reduction ramp rate clearly affect the size and dispersion of Pt crystallites on the anatase support (see Table 6.2). It is expected that other synthesis variables (e.g. pH during impregnation) can affect Pt dispersion, activity, and selectivity. Statistically designed studies are needed to more completely determine the effects of synthesis variables and to optimize the dispersion and reduction of Pt supported on 22 mol% Al-modified anatase. Further work will also include catalytic activity and selectivity tests.

6.4 Conclusions

This paper focuses on a simple, industrially viable method for synthesis of pure and stabilized mesoporous titanias of high surface area.

- 1) We have presented a simple, fast, industrially viable, one-pot synthesis that can be used to prepare 0.5 – 8 wt% Pt supported on Al-modified anatase with high surface area and thermal stability. Dispersions for 0.5 wt% Pt catalysts as high as 54% for a one-pot preparation and 59% for DI on the stabilized anatase support have been obtained which are higher than most previously reported in literature for Pt of comparable loadings.
- 2) The SMSI (or decoration) effect, causing blocking of H₂ adsorption sites during H₂ chemisorption, is observed at an unusually low temperature (250°C) for most samples.

The low temperature onset may be due to the small crystallite sizes of the anatase support, as well as defects induced by the Al-modifier which could lead to support-metal interactions at lower temperatures. The SMSI effect was easily reversed by oxygen and therefore these catalysts are of potential use in applications where exposure to oxygen (or water) following reduction is acceptable.

- 3) Our work shows that support structure due to its preparation by different pathways and a number of synthesis variables affects Pt dispersion. The highest dispersions were observed for samples containing 5 coordinate anatase supports of high surface area, synthesized using a low drying temperature, a slow calcination ramp rate, and a slow reduction ramp rate. Statistically designed studies are needed to more completely understand the effects of drying temperature, calcination ramp rate, reduction ramp rate, and other variables, as well as to optimize the dispersion of Pt onto anatase supports..

6.5 References

1. Haruta, M.; Tsubota, S.; Kobayashi, T.; Kageyama, H.; Genet, M. J.; Delmon, B., Low-temperature oxidation of carbon monoxide over gold supported on titanium dioxide, $\hat{I}\pm$ -ferric oxide, and cobalt tetraoxide. *J. Catal.* **1993**, *144* (1), 175-92.
2. Imai, H.; Date, M.; Tsubota, S., Preferential Oxidation of CO in H₂-Rich Gas at Low Temperatures over Au Nanoparticles Supported on Metal Oxides. *Catal. Lett.* **2008**, *124* (1-2), 68-73.
3. Edwards, J. K.; Carley, A. F.; Herzing, A. A.; Kiely, C. J.; Hutchings, G. J., Direct synthesis of hydrogen peroxide from H₂ and O₂ using supported Au-Pd catalysts. *Faraday Discuss.* **2008**, *138* (Nanoalloys), 225-239.

4. Kesavan, L.; Tiruvalam, R.; Ab, R. M. H.; bin, S. M. I.; Enache, D. I.; Jenkins, R. L.; Dimitratos, N.; Lopez-Sanchez, J. A.; Taylor, S. H.; Knight, D. W.; Kiely, C. J.; Hutchings, G. J., Solvent-Free Oxidation of Primary Carbon-Hydrogen Bonds in Toluene Using Au-Pd Alloy Nanoparticles. *Science (Washington, DC, U. S.)* **2011**, *331* (6014), 195-199.
5. Enache, D. I.; Edwards, J. K.; Landon, P.; Solsona-Espriu, B.; Carley, A. F.; Herzing, A. A.; Watanabe, M.; Kiely, C. J.; Knight, D. W.; Hutchings, G. J., Solvent-Free Oxidation of Primary Alcohols to Aldehydes Using Au-Pd/TiO₂ Catalysts. *Science (Washington, DC, U. S.)* **2006**, *311* (5759), 362-365.
6. Tahir, S. F.; Koh, C. A., Catalytic oxidation for air pollution control. *Environ. Sci. Pollut. Res. Int.* **1996**, *3* (1), 20-3.
7. Carp, O.; Huisman, C. L.; Reller, A., Photoinduced reactivity of titanium dioxide. *Prog. Solid State Chem.* **2004**, *32* (1-2), 33-177.
8. Wegener, S. L.; Marks, T. J.; Stair, P. C., Design Strategies for the Molecular Level Synthesis of Supported Catalysts. *Acc. Chem. Res.* **45** (2), 206-214.
9. Regalbuto, J.; Editor, *Catalyst Preparation: Science and Engineering*. CRC Press LLC: 2007; p 474.
10. Panagiotopoulou, P.; Kondarides, D. I., Effects of alkali promotion of TiO₂ on the chemisorptive properties and water-gas shift activity of supported noble metal catalysts. *J. Catal.* **2009**, *267* (1), 57-66.
11. Pieta, I. S.; Epling, W. S.; Garcia-Dieguez, M.; Luo, J. Y.; Larrubia, M. A.; Herrera, M. C.; Alemany, L. J., Nanofibrous Pt-Ba Lean NO_x trap catalyst with improved sulfur resistance and thermal durability. *Catal. Today* **175** (1), 55-64.

12. Kimura, K.; Einaga, H.; Teraoka, Y., Preparation of highly dispersed platinum catalysts on various oxides by using polymer-protected nanoparticles. *Catal. Today* **164** (1), 88-91.
13. Banis, M. N.; Sun, S.; Meng, X.; Zhang, Y.; Wang, Z.; Li, R.; Cai, M.; Sham, T.-K.; Sun, X., TiSi₂O_x Coated N-Doped Carbon Nanotubes as Pt Catalyst Support for the Oxygen Reduction Reaction in PEMFCs. *J. Phys. Chem. C* **117** (30), 15457-15467.
14. Rebrov, E. V.; Berenguer-Murcia, A.; Johnson, B. F. G.; Schouten, J. C., Gold supported on mesoporous titania thin films for application in microstructured reactors in low-temperature water-gas shift reaction. *Catal. Today* **2008**, *138* (3-4), 210-215.
15. Muraza, O.; Rebrov, E. V.; Berenguer-Murcia, A.; de, C. M. H. J. M.; Schouten, J. C., Selectivity control in hydrogenation reactions by nanoconfinement of polymetallic nanoparticles in mesoporous thin films. *Appl. Catal., A* **2009**, *368* (1-2), 87-96.
16. Cao, Y.; Zhai, W.; Zhang, X.; Li, S.; Feng, L.; Wei, Y., Mesoporous SiO₂-supported Pt nanoparticles for catalytic application. *ISRN Nanomater.*, 745397, 8 pp.
17. Yacou, C.; Ayrat, A.; Giroir-Fendler, A.; Baylet, A.; Julbe, A., Catalytic membrane materials with a hierarchical porosity and their performance in total oxidation of propene. *Catal. Today* **156** (3-4), 216-222.
18. Liu, S.-H.; Chiang, C.-C.; Wu, M.-T.; Liu, S.-B., Electrochemical activity and durability of platinum nanoparticles supported on ordered mesoporous carbons for oxygen reduction reaction. *Int. J. Hydrogen Energy* **35** (15), 8149-8154.
19. Teoh, W. Y.; Maedler, L.; Beydoun, D.; Pratsinis, S. E.; Amal, R., Direct (one-step) synthesis of TiO₂ and Pt/TiO₂ nanoparticles for photocatalytic mineralization of sucrose. *Chem. Eng. Sci.* **2005**, *60* (21), 5852-5861.

20. Olsen, R. E.; Bartholomew, C. H.; Huang, B.; Simmons, C.; Woodfield, B. F., Synthesis and characterization of pure and stabilized mesoporous anatase titanias. *Microporous Mesoporous Mater.* **2013**, *Ahead of print*.
21. Woodfield, B. F.; Liu, S.; Boerio-Goates, J.; Liu, Q. Preparation of uniform nanoparticles of ultra-high purity metal oxides, mixed metal oxides, metals, and metal alloys. WO2007098111A2, 2007.
22. Patterson, A. L., The Scherrer formula for x-ray particle-size determination. *Phys. Rev.* **1939**, *56*, 978-82.
23. Pierce, C., Computation of pore sizes from physical adsorption data. *J. Phys. Chem.* **1953**, *57*, 149-52.
24. Orr, C., Jr.; Dallavalle, J. M., *Fine Particle Measurement-Size, Surface, and Pore Volume*. Macmillan Co.: 1959; p 353 pp.
25. Liu, H.; Zhang, L.; Seaton, N. A., Sorption hysteresis as a probe of pore structure. *Langmuir* **1993**, *9* (10), 2576-82.
26. Rojas, F.; Kornhauser, I.; Felipe, C.; Esparza, J. M.; Cordero, S.; Dominguez, A.; Riccardo, J. L., Capillary condensation in heterogeneous mesoporous networks consisting of variable connectivity and pore-size correlation. *Phys. Chem. Chem. Phys.* **2002**, *4* (11), 2346-2355.
27. Niemark, A. V., Percolation theory of capillary hysteresis phenomena and its application for characterization of porous solids. *Stud. Surf. Sci. Catal.* **1991**, *62* (Character. Porous Solids 2), 67-74.
28. Parlar, M.; Yortsos, Y. C., Percolation theory of vapor adsorption-desorption processes in porous materials. *J. Colloid Interface Sci.* **1988**, *124* (1), 162-76.

29. Huang, B.; Bartholomew, C., H.; Woodfield, B. F., Facile synthesis of mesoporous alumina with tunable pore size: Effects of alcohols in precursor formation and calcination. *Microporous Mesoporous Mater.* **2013**, *177*, 37-46.
30. Ball, P. C.; Evans, R., Temperature dependence of gas adsorption on a mesoporous solid: capillary criticality and hysteresis. *Langmuir* **1989**, *5* (3), 714-23.
31. Neimark, A. V.; Ravikovitch, P. I., Capillary condensation in MMS and pore structure characterization. *Microporous Mesoporous Mater.* **2001**, *44-45*, 697-707.
32. Neimark, A. V.; Ravikovitch, P. I.; Vishnyakov, A., Adsorption hysteresis in nanopores. *Phys. Rev. E: Stat. Phys., Plasmas, Fluids, Relat. Interdiscip. Top.* **2000**, *62* (2-A), R1493-R1496.
33. Monson, P. A., Contact Angles, Pore Condensation, and Hysteresis: Insights from a Simple Molecular Model. *Langmuir* **2008**, *24* (21), 12295-12302.
34. Tauster, S. J.; Fung, S. C.; Garten, R. L., Strong metal-support interactions. Group 8 noble metals supported on titanium dioxide. *J. Am. Chem. Soc.* **1978**, *100* (1), 170-5.
35. Stevenson, S. A.; Dumesic, J. A.; Baker, R. T. K.; Ruckenstein, E.; Editors, *Metal-Support Interactions in Catalysis, Sintering, and Redispersion*. Van Nostrand Reinhold Co.: 1987; p 315 pp.
36. Baker, R. T. K.; Kim, K. S.; Emerson, A. B.; Dumesic, J. A., A study of the platinum-titanium oxide system for the hydrogenation of graphite: ramifications of strong metal-support interactions. *J. Phys. Chem.* **1986**, *90* (5), 860-6.
37. Bonanni, S.; Ait-Mansour, K.; Brune, H.; Harbich, W., Overcoming the strong metal-support interaction state: CO oxidation on TiO₂(110)-supported Pt nanoclusters. *ACS Catal.* *1* (4), 385-389.

38. de la Pena O'Shea, V. A.; Consuelo, A. G. M.; Platero, P. A. E.; Campos-Martin, J. M.; Fierro, J. L. G., Direct evidence of the SMSI decoration effect: the case of Co/TiO₂ catalyst. *Chem. Commun. (Cambridge, U. K.)* **2011**, 47 (25), 7131-7133.
39. Pesty, F.; Steinrueck, H.-P.; Madey, T. E., Thermal stability of Pt films on TiO₂(110): evidence for encapsulation. *Surf. Sci.* **1995**, 339 (1/2), 83-95.
40. Paal, Z.; Menon, P. G.; Editors, *Hydrogen Effects in Catalysis. Fundamentals and Practical Applications. [In: Chem. Ind. (Dekker), 1988; 31]*. Marcel Dekker, Inc.: 1988; p 753 pp.
41. Sing, K. S. W.; Everett, D. H.; Haul, R. A. W.; Moscou, L.; Pierotti, R. A.; Rouquerol, J.; Siemieniewska, T., Reporting physisorption data for gas/solid systems with special reference to the determination of surface area and porosity (Recommendations 1984). *Pure Appl. Chem.* **1985**, 57 (4), 603-19.
42. Huang, B. B., C.; Woodfield, B.F., Improved calculations of pore size distribution for relatively large, irregular slit-shaped mesopore structure. *Microporous Mesoporous Mater.* **2014**, 184, 112-121.
43. Chen, L. X.; Rajh, T.; Wang, Z.; Thurnauer, M. C., XAFS Studies of Surface Structures of TiO₂ Nanoparticles and Photocatalytic Reduction of Metal Ions. *J. Phys. Chem. B* **1997**, 101 (50), 10688-10697.
44. Chen, L. X.; Rajh, T.; Jager, W.; Nedeljkovic, J.; Thurnauer, M. C., X-ray absorption reveals surface structure of titanium dioxide nanoparticles. *J. Synchrotron Radiat.* **1999**, 6 (3), 445-447.

45. Luca, V.; Djajanti, S.; Howe, R. F., Structural and Electronic Properties of Sol-Gel Titanium Oxides Studied by X-ray Absorption Spectroscopy. *J. Phys. Chem. B* **1998**, *102* (52), 10650-10657.
46. Yeung, K. L.; Maira, A. J.; Stolz, J.; Hung, E.; Ho, N. K.-C.; Wei, A. C.; Soria, J.; Chao, K.-J.; Yue, P. L., Ensemble Effects in Nanostructured TiO₂ Used in the Gas-Phase Photooxidation of Trichloroethylene. *J. Phys. Chem. B* **2002**, *106* (18), 4608-4616.
47. Zhang, H.; Chen, B.; Banfield, J. F.; Waychunas, G. A., Atomic structure of nanometer-sized amorphous TiO₂. *Phys. Rev. B: Condens. Matter Mater. Phys.* **2008**, *78* (21), 214106/1-214106/12.
48. Bartholomew, C. H.; Farrauto, R. J., *Fundamentals of Industrial Catalytic Processes*. John Wiley & Sons: 2003; p 700 pp.
49. Peng, J.; Wang, S., Performance and characterization of supported metal catalysts for complete oxidation of formaldehyde at low temperatures. *Appl. Catal., B* **2007**, *73* (3-4), 282-291.
50. Kimura, K.; Einaga, H.; Teraoka, Y., Catalytic Properties of Platinum Supported on Titanium Dioxide by Liquid-Phase Adsorption of Colloidal Nanoparticles. *Catal. Lett.* *139* (1-2), 72-76.
51. Iida, H.; Yonezawa, K.; Kosaka, M.; Igarashi, A., Low-temperature water gas shift reaction over Pt-Re/TiO₂ catalysts prepared by a sub-critical drying method. *Catal. Commun.* **2009**, *10* (5), 627-630.
52. Li, Z.; Meng, M.; You, R.; Ding, T.; Li, Z., Superior Performance of Mesoporous TiO₂-Al₂O₃ Supported NSR Catalysts with the Support Synthesized Using Nonionic and Cationic Surfactants as Co-Templates. *Catal. Lett.* *142* (9), 1067-1074.

53. Karatzas, X.; Jansson, K.; Gonzalez, A.; Dawody, J.; Pettersson, L. J., Autothermal reforming of low-sulfur diesel over bimetallic RhPt supported on Al₂O₃, CeO₂-ZrO₂, SiO₂ and TiO₂. *Appl. Catal., B* 106 (3-4), 476-487.